Thomas Kannengiesser
Sudarsanam Suresh Babu
Yu-ichi Komizo · Antonio J. Ramirez
Editors

In-situ Studies with Photons, Neutrons and Electrons Scattering II

Springer

In-situ Studies with Photons, Neutrons and Electrons Scattering II

Thomas Kannengiesser
Sudarsanam Suresh Babu
Yu-ichi Komizo · Antonio J. Ramirez
Editors

In-situ Studies with Photons, Neutrons and Electrons Scattering II

Springer

Editors
Thomas Kannengiesser
Bundesanstalt für Materialforschung
und—prüfung (BAM)
Berlin, Berlin
Germany

Sudarsanam Suresh Babu
Department of Materials Science and
Engineering
Ohio State University
Columbus, OH
USA

Yu-ichi Komizo
Joining and Welding Research Institute
Osaka University
Ibaraki, Osaka
Japan

Antonio J. Ramirez
Laboratório de Microscopia Eletronica
Brasileira de Tecnologia de Luz Sincrotron
Campinas, São Paulo
Brazil

ISBN 978-3-319-06144-3 ISBN 978-3-319-06145-0 (eBook)
DOI 10.1007/978-3-319-06145-0
Springer Cham Heidelberg New York Dordrecht London

Library of Congress Control Number: 2010934638

© Springer International Publishing Switzerland 2014
This work is subject to copyright. All rights are reserved by the Publisher, whether the whole or part of the material is concerned, specifically the rights of translation, reprinting, reuse of illustrations, recitation, broadcasting, reproduction on microfilms or in any other physical way, and transmission or information storage and retrieval, electronic adaptation, computer software, or by similar or dissimilar methodology now known or hereafter developed. Exempted from this legal reservation are brief excerpts in connection with reviews or scholarly analysis or material supplied specifically for the purpose of being entered and executed on a computer system, for exclusive use by the purchaser of the work. Duplication of this publication or parts thereof is permitted only under the provisions of the Copyright Law of the Publisher's location, in its current version, and permission for use must always be obtained from Springer. Permissions for use may be obtained through RightsLink at the Copyright Clearance Center. Violations are liable to prosecution under the respective Copyright Law.
The use of general descriptive names, registered names, trademarks, service marks, etc. in this publication does not imply, even in the absence of a specific statement, that such names are exempt from the relevant protective laws and regulations and therefore free for general use.
While the advice and information in this book are believed to be true and accurate at the date of publication, neither the authors nor the editors nor the publisher can accept any legal responsibility for any errors or omissions that may be made. The publisher makes no warranty, express or implied, with respect to the material contained herein.

Printed on acid-free paper

Springer is part of Springer Science+Business Media (www.springer.com)

Preface

Today's researchers and developers need to gain ever more precise insight into complex systems and materials. The reason is that trial and error based development of new materials is in many instances no longer feasible in the face of the increasingly demanding requirements for modern materials. In-depth understanding of material performance and processes is seen as the key to success. Study of fundamental processes increasingly calls for elaborated experiments at dedicated instruments and/or large-scale research facilities where intense photons and neutrons beams are available.

Investigation using high flux and high-energy photons (synchrotron radiation) or neutrons has therefore become an irreplaceable method in materials research. The resulting findings cannot be obtained by other methods such as classical materials testing.

Most of all, in-situ studies with photons, neutrons, and electrons are steadily gaining in importance in scientific engineering disciplines. One of the major goals of in situ experiments is always high spatial and time resolution, e.g., for deliberate examination of effects acting at the surface or in the volume of materials.

Continuous work is necessary for new experimentation techniques at the beamlines in order to rapidly develop materials with outstanding processability (e.g., weldability) and performance and to study und ultimately understand material-fundamentals. This is the reason why recently a variety of experimental stations were made available at major research facilities all over the world. Synchrotron radiation sources provide high photons flux in a wide spectral range that can advantageously be used for in-situ experiments. High-energy synchrotron radiation or neutrons make it possible to gain unique insight into the internal structure of materials. A particularly efficient method of producing neutrons is nowadays spallation. A number of such highly efficient spallation sources are already available to material scientists around the word.

The scientist will frequently find himself faced with the difficult task of finding the beamline explicitly tailored to his issue offering the necessary specific infrastructure. The aim in the coming years is thus to cooperate still closer on international level in the fields of materials science and engineering to further share and spread knowledge on the platform of workshops or by exchange of scientists. Above all, systematic description, international classification, and transparent display of the respective beamline opportunities and features are necessary which are often still lacking.

This book provides an insight into current research topics, focusing special attention exactly on materials science, metallurgy, and welding issues. The presented research work demonstrates that application of synchrotron and neutron radiation in combination with other techniques enables the basic understanding of material-related processes to be extended appreciably. It also shows ways of how to improve new materials and their use in industry.

Following on from the first workshop in 2009 at BAM Berlin, a second workshop dealing with this subject matter was held from 28 to 30 November 2012 in Osaka/Japan lasting several days with international participation of scientists from 16 countries. The book includes selected contributions from the various subject blocks, precisely covering issues of practical and immediately implementable benefit to industrial enterprises. Therefore, peer-reviewed papers dealing with the following topics are contained as well:

- Phase transformation during welding, metallurgy and material development
- Evolution and significance of residual stresses
- Investigations into laser and electron beam welding

We wish to express our thanks to the many assistants who have contributed to the success of this very interesting workshop. Special thanks go to the team around Prof. Y. Komizo and Assoc. Prof. H. Terasaki from the Joining and Welding Research Institute of the Osaka University for their great commitment and survey of the experiments at Synchrotronring SPring 8.

Thomas Kannengiesser
Sudarsanam Suresh Babu
Yu-ichi Komizo
Antonio J. Ramirez

Contents

Hybrid System for In Situ Observation of Microstructure Evolution in Steel Materials

Yu-ichi Komizo, Xin Fang Zhang and Hidenori Terasaki

Abstract A new technique, based on the combination of time-resolved X-ray diffraction (TRXRD) and high-temperature laser scanning confocal microscopy (LSCM), was developed for direct observation of morphological evolution and simultaneous identification of the phases. TRXRD data and LSCM images under the desired thermal cycles were measured simultaneously. As several observation examples, the microstructural evolutions in the steel materials were observed to investigate the phase transformation kinetics under the thermal cycle including the rapid heating and cooling.

1 Introduction

Over the past decade, two synchrotron based techniques have been developed at Lawrence Livermore National Laboratory for direct observation of phase transformations induced by welding. These techniques are spatially resolved X-ray diffraction (SRXRD), which was developed to map the phases that exist in the HAZ [1–6], and time-resolved X-ray diffraction (TRXRD).

Elmer et al. [7–12] showed that TRXRD could track phase transformation during welding in real time. Synchrotron radiation makes time-resolved diffraction measurements possible in local areas; phases that exist in the HAZ and fusion zone (FZ) of metal can be identified in real time. This technique was used to analyse the phase transformation during solidification of carbon–manganese (C–Mn) steel, and Babu et al. [10] verified the existence of non-equilibrium phases directly in the rapid cooling cycle of spot welds. In addition, TRXRD can be applied in tracking the phase evolution in the HAZ. The formation of the microstructures of duplex stainless steel (DSS) [11] and C–Mn [8] steel were observed in the HAZ during the

---

Y. Komizo (✉) · X. F. Zhang · H. Terasaki
Osaka University, Osaka, Japan
e-mail: komizo@jwri.osaka-u.ac.jp

T. Kannengiesser et al. (eds.), *In-situ Studies with Photons, Neutrons and Electrons Scattering II*, DOI: 10.1007/978-3-319-06145-0_1,

thermal cycle using TRXRD system. In experiments with DSS, the phase balance between ferrite and austenite was estimated, and the precipitation of the sigma phase in the thermal cycle of the HAZ was assessed. In TRXRD experiments with C–Mn steel, the effect of transformation strain on the diffraction pattern profile during martensitic transformation was discussed.

Our research group began TRXRD experiments for welding by developing a new technology for the system [13–26]. We focussed on the details of the weld solidification phenomena in the directional solidification process under rapid cooling because the influence of a preferred orientation was important for observing directional solidification along the $\langle 100 \rangle$ direction towards the moving heat source. First, the solidification process was confirmed by SRXRD as a function of the distance from the weld pool, which was melted by an arc of the quenched metals after welding [13, 14]. However, the crystallisation at a lateral resolution corresponding to a time resolution of 0.1 s was impossible to observe. That is, because the microstructure was ultimately dynamic, understanding the crystallography during heating and cooling was not possible. For instance, the eutectic microstructure is formed in the liquid phase during solidification in a short period; the displacement of interplanar spacing by thermal expansion and shrinkage could not be observed. Next, the phase transformation was dynamically observed along a certain direction on the reciprocal space using an imaging plate [15–17]. A crystallinity change was observed with a temperature drop, and the growth of dendrites was captured. We assumed the rotation of dendrites from the discontinuous diffraction pattern recorded by the imaging plates along one direction of reciprocal space. However, eutectic growth in the remaining liquid phase was confirmed, though peritectic growth of the hetero phase on the primary phase was expected. Therefore, it was difficult to simultaneously observe the primary phase and the hetero phase along a certain direction because interfaces have coherency and preferred crystal orientation.

With the availability of intense X-ray beams from synchrotron storage rings, it is now possible to directly observe phase transformation and microstructural evolution in situ and in real time as a function of welding time. Therefore, we developed a two-dimensional time-resolved X-ray Diffraction (2D-TRXRD) system for real welding [18–28]. Weld metal rapid solidification was then dynamically observed at a time resolution of 0.01–0.1 s.

The monochromatic X-ray is used as a probe with the incident beam from one direction in the study described above. Detecting a wider area of the Debye circle is very important. For analysing the solidification process, the weak and broad halo pattern is clear sign of the existence of liquid. Thus, detecting halo patterns with a high S/N ratio detector indicates the beginning and the end of solidification [22].

Further, a combination of analyses methods (the in situ phase identification system, morphological observation by high-temperature laser scanning confocal microscopy (LSCM) and observation of the microstructure at room temperature with an optical microscope, scanning electron microscope and micro diffraction system) was suggested for analysing the phase transformation during welding [20–22, 24–30].

The TRXRD data obtained during welding needs to be combined with the appropriate temperature history to obtain the phase transformation kinetic data. The LSCM technique can give us information such as the morphological development of microstructures and precise temperature [31, 32].

Then a new technique based on the TRXRD and LSCM system was developed in the present study. As some observation examples, the microstructural evolutions in the steel materials were observed to investigate the phase transformation kinetics under the thermal cycle including the rapid heating and cooling.

2 Hybrid System for In Situ Observation in Real and Reciprocal Space

2.1 Overview of System

Figure 1 shows a photograph of the experimental setup on the 46XU beam line at SPring-8 in Hyogo, Japan. The infrared furnace was set on the theta-axis of a goniometer situated within the hatch of the beam line. In this system, the head of the laser scanning confocal microscope (LSCM) was also set by fitting it to the theta-axis, as shown in the photograph. The focus point of the LSCM is on the surface of the observed sample which is set in the furnace. A two-dimensional pixel detector was placed on the two-theta axis. The incident beam, i.e., an ultra bright X-ray, was introduced to the furnace and the diffractions were recorded by the pixel detector with high time resolution. Simultaneously, the microstructural changes were observed through the LSCM in situ.

2.2 Detailed Experimental Procedures

Figure 2 shows a schematic illustration of the control flow for the experiment of in situ observations in real and reciprocal space [31]. The specimens, 5 mm in diameter and 1 mm thick, were place in the boron-nitride (BN) crucible in which the X-ray absorption is quite small, and held in a platinum holder, which was inserted in the furnace. The temperature was measured by a thermocouple incorporated into the crucible holder. The specimens were placed at the focal point of halogen lamp. The temperature controller, which was connected to a personal computer (PC), the thermocouple and the halogen lamp in the furnace were placed inside of the beam line hatch. When the thermal cycles that simulate welding were developed on the PC, the profiles were sent to the temperature controller, which reproduced the desired thermal cycles by switching the halogen lamp on and off, based on the measured temperature. The LSCM head makes it possible to carry out in situ observations of microstructural changes at a rate of 30 frames/s, at high

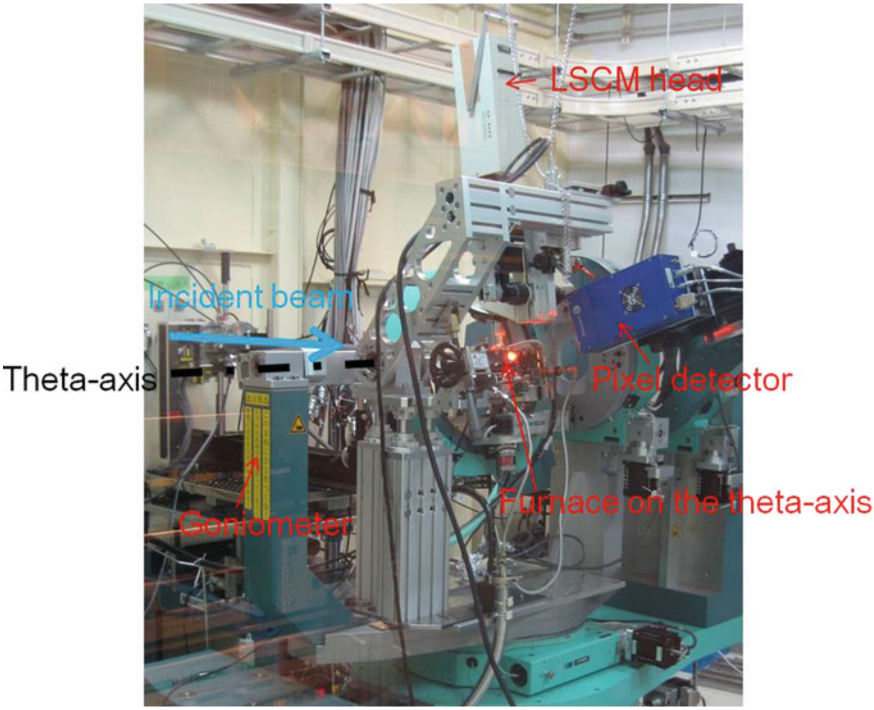

Fig. 1 Photograph of the experimental setup at the 46XU beamline at SPring-8 in Hyogo, Japan

temperature [21, 22, 27]. A CCD camera was connected to the PC located outside the hatch through the monitor, and the images were stored at a rate of 30 frames/s. The control program could trigger the temperature controller, the X-ray shutter, the x-y-z stages on θ-axis, goniometer-axis control and the exposure of the pixel detector.

Before the measurements, the specimen position was adjusted in the manner explained in the following section. Then, the θ-axis was tilted to a fixed angle (10° in the present study). The temperature controller was then triggered at a set timing and, the exposure of the detector was activated with the time resolution of 0.2 s. TRXRD data and LSCM images under the desired thermal cycles were measured simultaneously.

2.3 Scattering Geometry of X-rays in the Experimental Setup

Figure 3 shows the scattering geometry of the TRXRD part of system. The undulator beam was monochromatized by the double Si-crystal, and 30 keV of X-ray energy was used. The X-ray was introduced into the hatch through a mirror—the

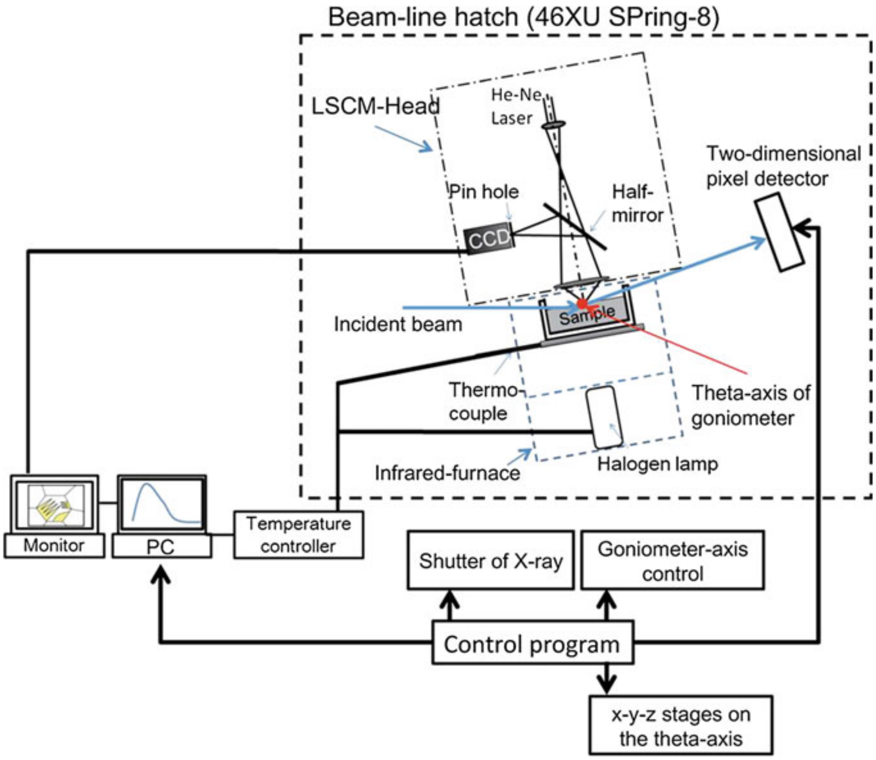

Fig. 2 Hybrid in situ observation system in real and reciprocal lattice space [31]

incident beam shown in Figs. 1 and 2. The X-ray was shaped by the slit. In the present study, the beam is shaped into dimensions of 0.5 mm height and width. The X-ray beam was introduced into the furnace through an X-ray window made with polyimide film. Before the measurements, the position of the sample surface was adjusted. By controlling the z-stage, the sample surface is forced to be at the half position of the beam height as indicated by the dashed line in Fig. 3 the θ-axis was then rotated to the angle of 10° in the present study. The resulting irradiated area was 1.4397 mm^2. The penetration depth is calculated using Eq. (1) [33]:

$$\int_0^t \frac{I_0}{\sin\gamma} e^{-\mu x(1/\sin\gamma + 1/\sin\beta)}\,dx = G \cdot \int_0^\infty \frac{I_0}{\sin\gamma} e^{-\mu x(1/\sin\gamma + 1/\sin\beta)}\,dx \tag{1}$$

where I_0 is the intensity of the incident beam, γ is the angle between the incident beam and the sample surface and β is the angle between the diffracted beam and sample surface.

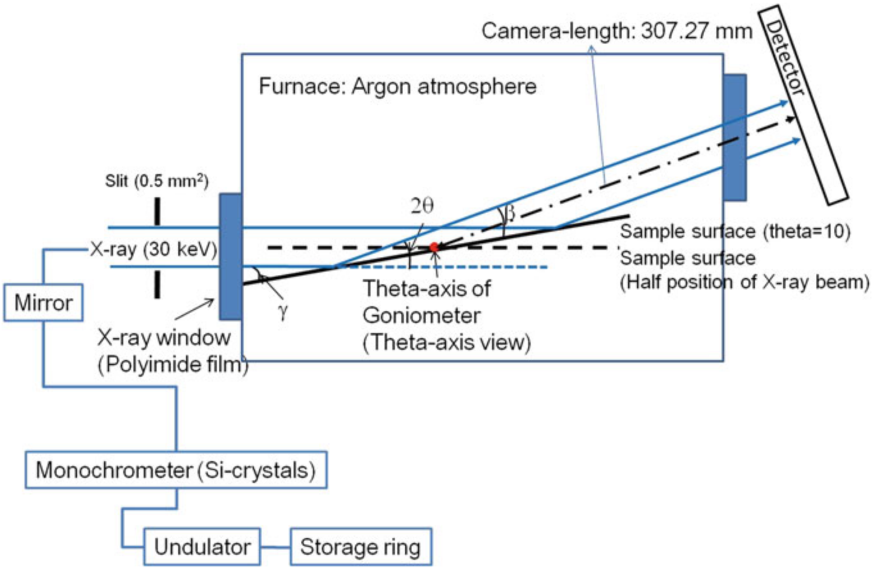

Fig. 3 Scattering geometry of X-rays in the experimental setup

Table 1 Chemical compositions of the studied metals (in mass %) with balance Fe

Sample	C	Si	Mn	Cr	Ni	Al	O	N
Iron	0.0018	0.06	0.17	0.05	0.02	0.001	0.0018	0.0026
Steel	0.1000	0.80	1.76	0.07	2.49	0.046	0.0140	0.0056

3 In Situ Investigation of the Allotropic Transformation in Iron

3.1 *In Situ Observations of the $\alpha \rightarrow \gamma$ and $\gamma \rightarrow \delta$ Transformations Using LSCM*

Two types of metals, iron and steel whose chemical compositions were shown in Table 1 were studied to provide more kinetics information about the phase transformation [34]. The aim is to differentiate between the two types of transformation because there are no any composition changes between parent and product phases during the allotropic and martensitic transformations. Figure 4 displays the microstructural evolution of the iron sample during the heating process (indicated by Fig. 7). The snapshots of the LSCM images for $\alpha \rightarrow \gamma$ transformation are shown in Fig. 4a–e. At the temperature of 1,202.2 K (Fig. 4a), a microstructural change was observed on the ferrite grain boundary as indicated by the arrow. It can be supposed that this is austenite phase. Austenite phases then spread to the surrounding areas (as designated by the arrows) with increasing temperature to 1,205.8 K (Fig. 4b). Subsequently (Fig. 4c), the austenite phases quickly spread throughout the region by half the sample. In the temperature of 1,218.4 K (Fig. 4d), the phase transformation in the other half sample can be also observed clearly. The transformation spreads to the center from all directions, and eventually is completed at the point, as presented in the Fig. 4e. By calculation, the $\alpha \rightarrow \gamma$ transformation is completed within 2.5 s (see Fig. 7). It is obviously seen the microstructural evolution during the $\alpha \rightarrow \gamma$ transformation even the transformation is rapid.

Figure 4f–j show the snapshots of the LSCM images for the $\gamma \rightarrow \delta$ transformation. The iron is further heated to 1,689.2 K (Fig. 4f). No changes are observed in the surface morphology of the austenite since 1,222.9 K, which can be seen from the Fig. 4e, f. When the temperature is increased to 1,689.6 K (Fig. 4g), the transformation of austenite to δ-ferrite begins, as indicated by the arrow. Within 1 s (Fig. 4h–j), this $\gamma \rightarrow \delta$ transformation (indicated by the arrows) can be completed. However, this contrast is concealed by the product generated during the previous heating transformation. Thus the image contrast of the δ product is weak. On the other hand, one cannot observe the austenite grain boundary during austenitizing process due to the short holding time at high temperature. So, it is hard to distinguish the nucleation sites before the onset of the allotropic δ-ferrite formation.

3.2 In Situ Observations of the δ → γ and γ → α Transformations Using LSCM

Figure 5 presents the morphological evolution in iron sample at the micron scale under the cooling cycle (indicated by Fig. 7) [34]. The snapshots of the LSCM images for the $\delta \rightarrow \gamma$ transformation are shown in Fig. 5a–d. When the temperature drops to 1,646.1 K (Fig. 5a), no changes are observed in the surface morphology of the δ-ferrite compared to the Fig. 4j. In the case of the $\delta \rightarrow \gamma$ transformation (Fig. 5b–d), it can be completed within 1 s during the temperature span of 4.8 K. The arrows in Fig. 5b–d indicate the austenite growth process. Similarly, the contrast is also concealed by the product generated during the previous heating transformation. In addition, the austenite grain boundary during the $\delta \rightarrow \gamma$ transformation cannot be observed due to the short holding time at high temperature.

Figure 5e–h show the snapshots of the LSCM images for the $\gamma \rightarrow \alpha$ transformation. When the temperature is cooled to 1,083.8 K, two austenite grain boundaries can be observed in Fig. 5e. The thick arrows indicate the locations of the grain boundaries. Subsequently, the nucleated ferrite spreads across the austenite grain boundary A, as indicated by the small arrow (Fig. 5f, g). When encountering the grain boundary B, the ferrite crosses it (Fig. 5h) and continues to

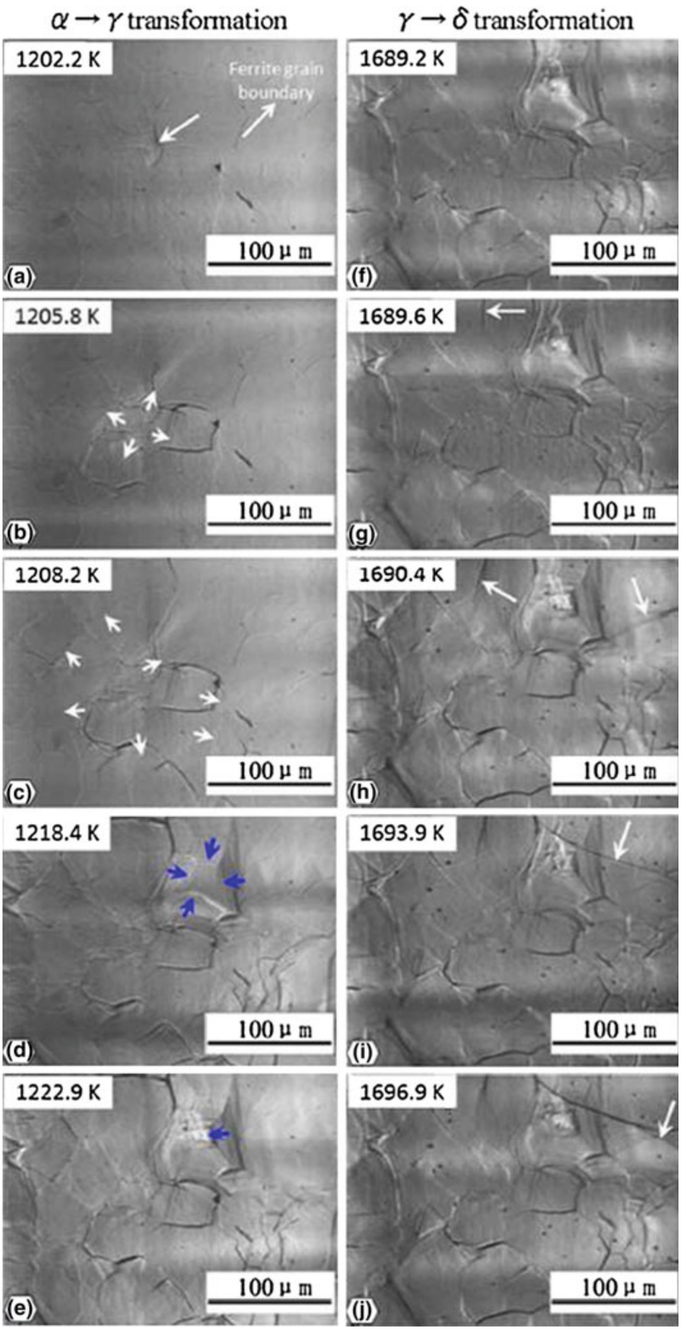

Fig. 4 The microstructural evolution of iron during the heating process, **a**–**e** the snapshots of the LSCM mages for $\alpha \rightarrow \gamma$ transformation, and **f**–**j** the snapshots for $\gamma \rightarrow \delta$ transformation [34]

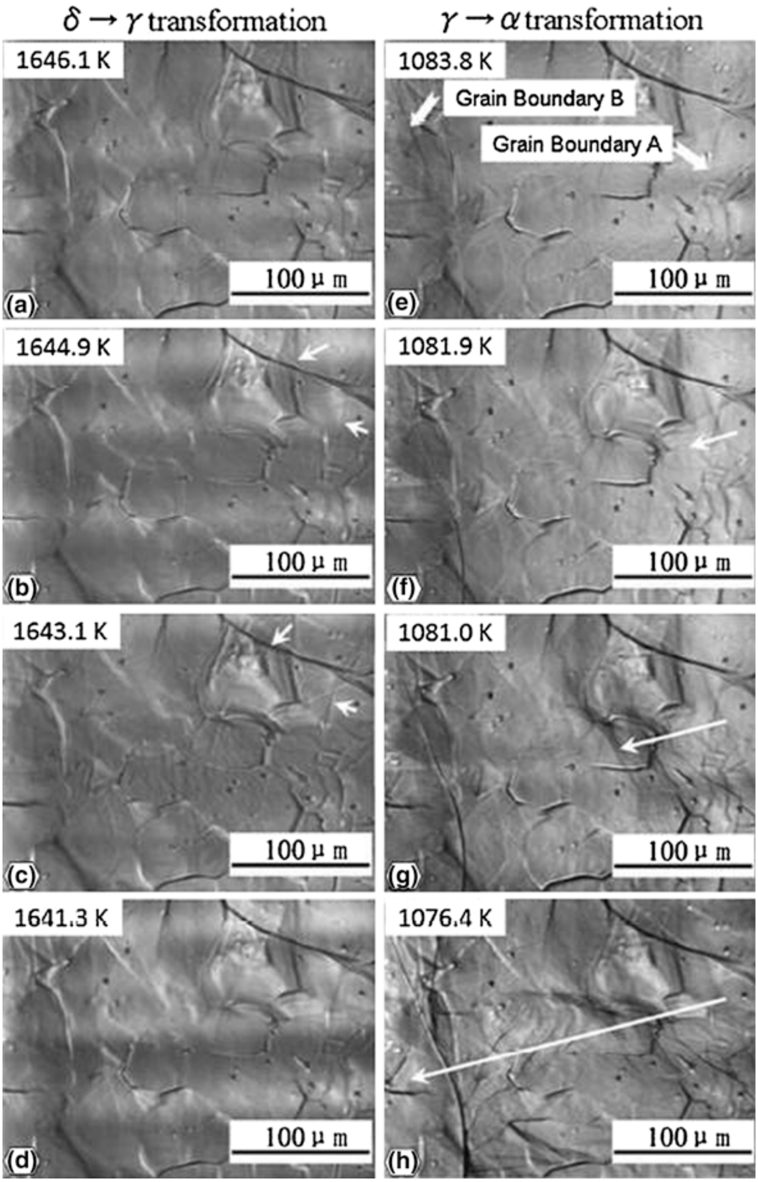

Fig. 5 The microstructural evolution of iron during the cooling process, **a**–**d** the snapshots of the LSCM mages for $\delta \rightarrow \gamma$ transformation, and **e**–**h** the snapshots for $\gamma \rightarrow \alpha$ transformation [34]

spread, as designated by the arrow. In other words, the ferrite can cross the austenite grain boundaries and grow rapidly into the adjacent grains. Similarly, the $\gamma \rightarrow \alpha$ transformation is completed within 1 s based on the in situ observations.

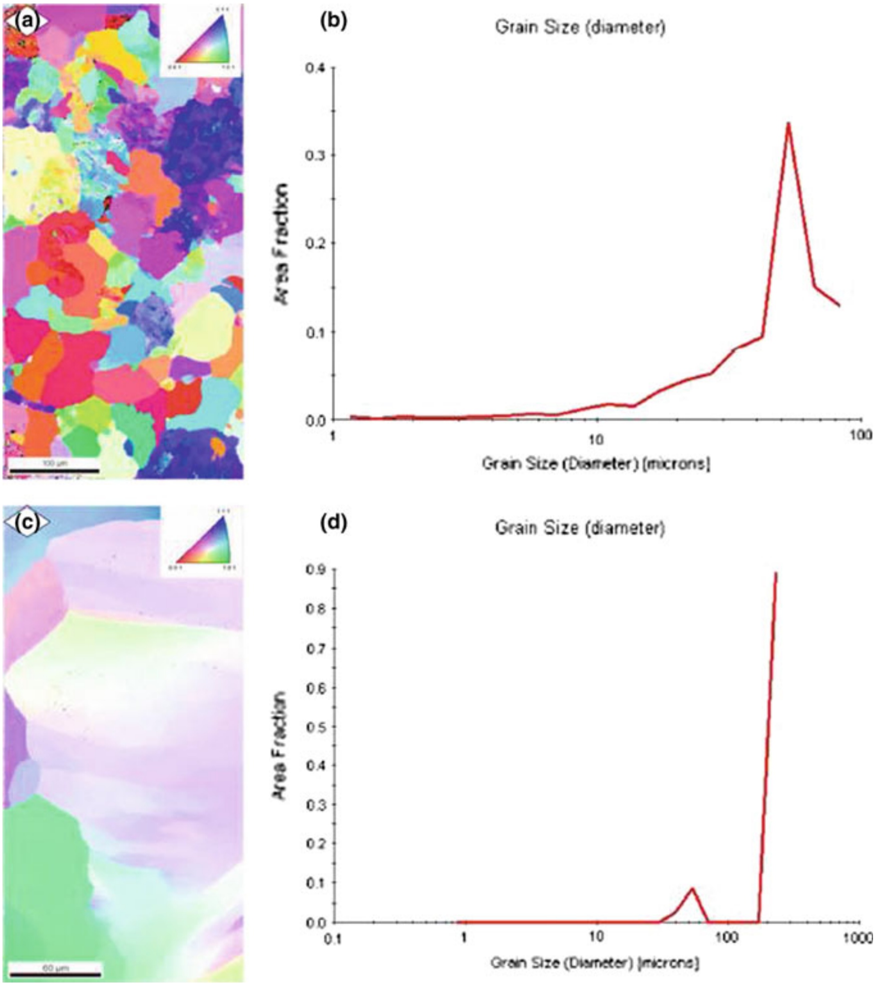

Fig. 6 The results of the EBSD analysis of iron before and after transformation; **a** and **c** the original distribution of α-ferrite before and after transformation, respectively; **b** and **d** the ferrite grain sizes before and after transformation, respectively [34]

3.3 Ex-situ Observations of the Crystallographic Relationships During the Allotropic Transformation Using EBSD

To examine the crystallography and the orientation relationship during the allotropic transformation, the iron samples before and after the transformation are selected for further EBSD analysis [34]. The results of the EBSD analysis are shown in Fig. 6. Figure 6a exhibits the original distribution of the α-ferrite before

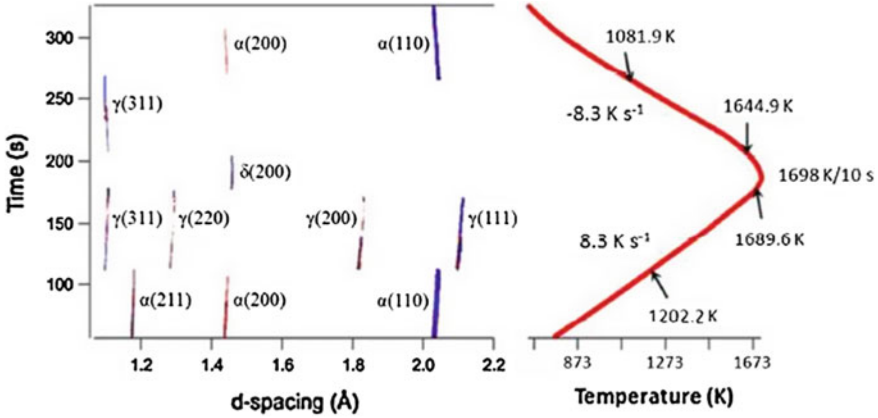

Fig. 7 The d-spacing, time, temperature, and intensity diagram of the iron during phase transformation. The peak temperature is 1,698 K [34]

the transformation, while the distribution of the α-ferrite after the thermal cycle of heating to 1,700 K and cooling is displayed in Fig. 6c. It seems the transformation product phase (α-ferrite) that possessed no crystallographic relationship with respect to the parent phase (austenite). As a good example to determine the orientation relationship, Zhang et al. [35] have observed the ferrite/cementite orientation relationships in near-eutectoid steel using SEM-FEG/EBSD.

It is also to be noted that the α-ferrite grain sizes before and after the transformation have created a great difference, as displayed in Fig. 6b, d. The grain size of the α-ferrite after the transformation is beyond 115 μm (Fig. 6d), while that of the α-ferrite before the transformation is about 51 μm (Fig. 6b). It suggests that the grain size of the re-transformed α-ferrite from the γ-austenite becomes much larger than that before α to γ transformation. Takasaki et al. [36] also observed the similar experimental results during the allotropic transformation.

3.4 In Situ Observation of the Allotropic Transformation in Iron Using TRXRD

To further probe the characteristics of this rapid transformation, synchrotron radiation technology has been used in this study. This investigation is interesting from a fundamental as well as a technological viewpoint. The dynamics of phase transformations can be well monitored using this method. Figure 7 presents the d-spacing, time, temperature, and intensity diagram of the iron during heating and cooling. The diffraction data are analyzed using the method and programming described in the Ref. [37]. A series of thousands of diffraction rings from ferrite (110), (200), (211), and austenite (111), (200), (220), (311) are integrated into an image format, as summarized in Fig. 7. Before the $\alpha \rightarrow \gamma$ transformation, the clear diffraction peaks, marked as $\alpha(110)$, $\alpha(200)$, and $\alpha(211)$, can be observed. When the temperature reaches 1,202.2 K, the transformation from ferrite to austenite occurs. After fully austenitizing, the diffraction peaks, marked as $\gamma(111)$, $\gamma(200)$, $\gamma(220)$, and $\gamma(311)$, can be observed clearly. However, only $\delta(200)$ diffraction peak can be captured after $\gamma \rightarrow \delta$ transformation. The start transformation temperature from austenite to δ-ferrite is about 1,689.6 K. Under this condition, the signal/noise ratio decreases with the increase of temperature because the larger grain size in the δ-phase implies a smaller number of crystals to satisfy Bragg's conditions. Thus, the diffraction peaks, such as $\delta(110)$ and $\delta(211)$, cannot collected by the pixel detector.

For the cooling process, the $\delta \rightarrow \gamma$ transformation occurs at 1,644.9 K, and only $\gamma(311)$ can be detected due to the increased austenite grain size. It can be found that the austenite grain size is huge after the $\delta \rightarrow \gamma$ transformation, as shown in Fig. 5e. For the $\gamma \rightarrow \alpha$ transformation (occurs at 1,081.9 K), the $\alpha(110)$ and $\alpha(200)$ can be observed, but the $\alpha(211)$ disappears. This indicates that the grain size of α-ferrite gets large after the transformation, and then a smaller number of crystals are to satisfy Bragg's conditions. In fact, EBSD results of Fig. 6 have indicated that the grain size of the α-ferrite becomes extremely large after the transformation. Since the final microstructure is mainly determined by the $\gamma \rightarrow \alpha$ transformation, direct tracking of austenite lattice parameter changes before onset of the transformation can provide more kinetics information about the transformation, especially for the elemental partitioning behaviors during the transformation [32, 34, 37]. As mentioned above, the austenite grain size gets large after the $\delta \rightarrow \gamma$ transformation, and it continues to grow with the increasing of annealing time. Accordingly, the signal/noise ratio decreases with the increase of austenite grain size because the larger grain size in the austenite phase implies a smaller number of crystals to satisfy Bragg's conditions. Under these situations, alternative thermal cycle for tracking lattice expansion during the $\gamma \rightarrow \alpha$ transformation should be performed. Figure 8a displays the d-spacing, time, temperature, and intensity diagram of the iron by lowering the peak temperature to 1,473 K. Based on the TRXRD analysis, the start transformation temperature from austenite to α-ferrite is 1,087.7 K. Figure 8b presents the progression of the measured $\gamma(200)$ d-spacing value as a function of temperature. The d-spacing value displays a steady decrease, which generally corresponds to lattice contraction due to decreasing temperature. In other words, the lattice expansion shows a linear change along thermal cycle during the $\gamma \rightarrow \alpha$ transformation. The result of the linear change is verified by other repeated experiments. In general, the LSCM images are compatible with the diffraction pattern during the allotropic transformation. Hence, the developed system could follow the phase transformation in both real and reciprocal space.

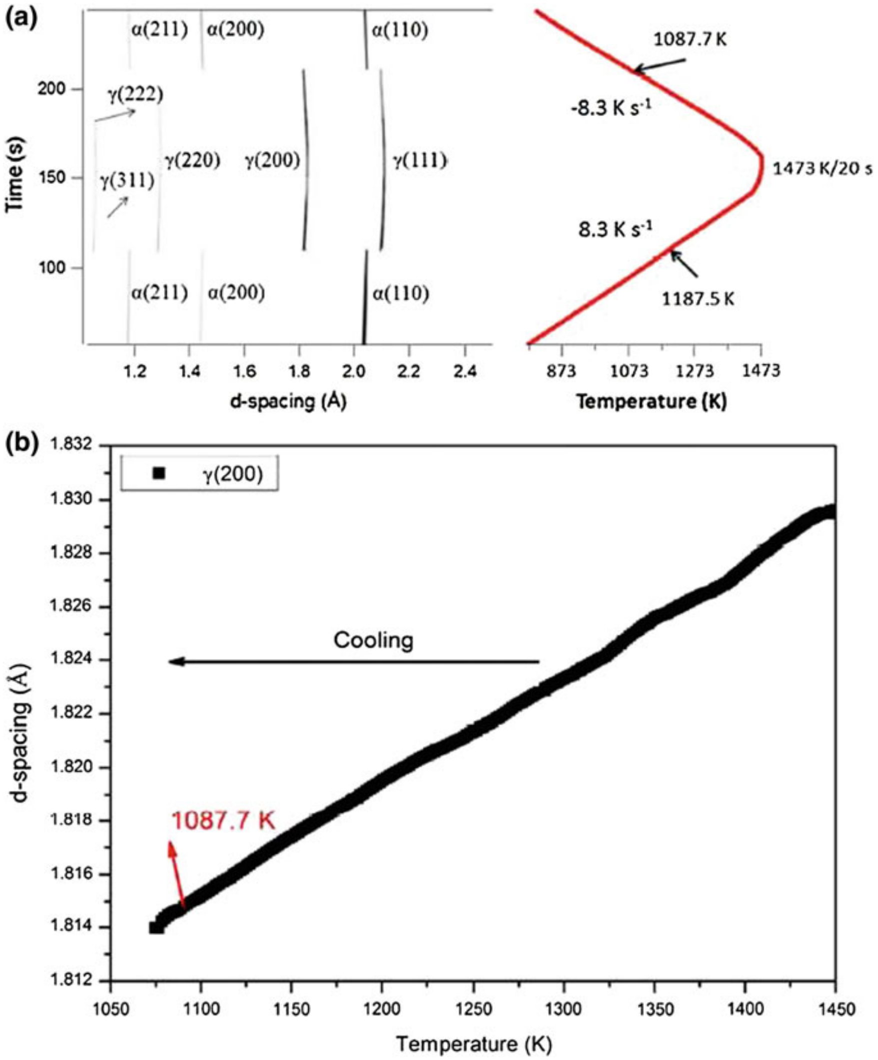

Fig. 8 **a** The d-spacing, time, temperature, and intensity diagram of the iron by lowering the peak temperature to 1,473 K; **b** the progression of the measured $\gamma(200)$ d-spacing value as a function of temperature during the $\gamma \rightarrow \alpha$ transformation [34]

3.5 Characteristic of the Morphology in the Allotropic Transformation

Figure 9a displays the morphology of the martensitic product phase in the studied steel based on EBSD observations. When the temperature is decreased to 651 K, the martensitic laths generates quickly with the needle-like appearance. The

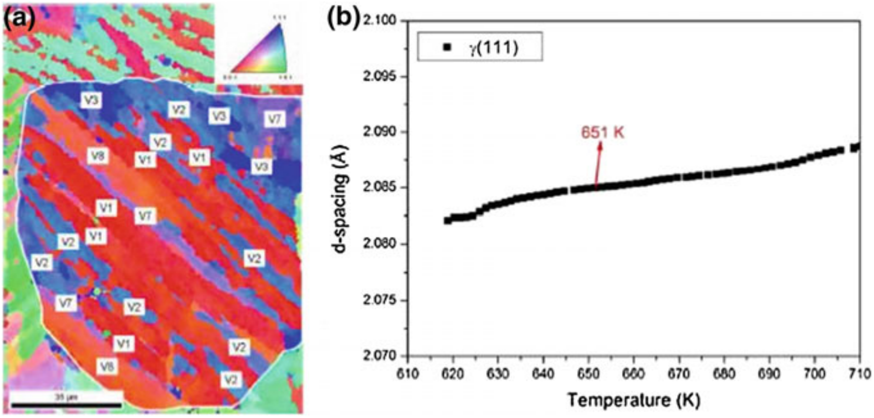

Fig. 9 **a** An inverse pole figure (IPF) color map of the lath martensite structure showing the K–S orientation relationship, and the *white lines* indicate the prior austenite grain boundaries; **b** a linear change of d-spacing value with temperature during martensitic transformation [34]

martensitic transformation is completed within 4 s in a cooling rate of 8.3 K s^{-1}. As shown in Fig. 9a, a lenticular or needle-like appearance is the most typical characteristic of a martensitic phase produced in a polycrystalline material. However, the phases in the allotropic transformation display irregular appearances, as displayed in Figs. 4, 5 and 6. Accordingly, the morphological differences in the allotropic and the martensitic transformations can be distinguished by in situ observations and ex-situ EBSD analysis. Furthermore, for the $\gamma \rightarrow \alpha$ transformation, the α-ferrite phase grows rapidly into the adjacent grains (Fig. 5f–h), that is, the allotropic product can cross the grain boundaries. The heterogeneous nucleation of ferrite may take place at austenite grain boundary by forming a low energy interface with at least one of the two grains, while the ferrite nuclei meet difficulty in growing in the same grain due to a highly coherent character of the interface and tend to purse their growth into the opposite grain.

3.6 *Characteristic of the Crystallographic Relationships in the Allotropic Transformation*

Figure 9a shows an inverse pole figure (IPF) color map of the lath martensite structure for a limited area. The white lines in Fig. 9a indicate the prior austenite grain boundaries. Based on the report of Morito et al. [38] and Kitahara et al. [39], variant analysis of the lath martensite in the present study is conducted. By analysis, the martensite under investigation maintains the Kurdjumov–Sachs (K–S) orientation relationship with respect to retained austenite. For example, the variants of V1, V2, V3, V7, and V8 appear in the selected region (the white arrow). In other words, austenite grains appear by the martensitic transformation as cooling proceeds leading to an interconnected austenite-ferrite structure. Both phases are related by near K–S crystallographic relationships. However, the allotropic transformation possesses no strict crystallographic relationship with respect to the parent phase based on the analysis of Fig. 6. On the other hand, the phase appearance of the allotropic transformation is irregular compared to the needle-like lath during the martensitic transformation. Therefore, the K–S relationship between parent phase and the product cannot be observed due to its irregular transformation.

3.7 Characteristic of Short Range Diffusion in the Allotropic Transformation

In light of the present observations, it is useful to study the kinetics of phase transformations by this hybrid in situ observations system. Figure 9b exhibits a linear change of d-spacing value with temperature during the martensitic transformation. It can therefore be concluded that there is no partitioning of carbon before onset of austenite to α-ferrite transformation. The shear-type diffusionless mechanism during the martensitic transformation can be drawn. This is consistent with the previous reports [32].

Similar result has also been observed during the allotropic transformation (Fig. 8b). According to the early reports [40–42], the growth of the allotropic product may be achieved by thermally activated short range jumps of atoms across an incoherent interface. This mechanism leads to the curved interfaces between the two phases. This has been confirmed as mentioned above, that is, the curved interfaces between the two phases have been observed during the transformation (Figs. 4, 5, 6). On the other hand, Banerjee [43] argues that only a few atomic jumps are required for an atom to cross-over the transformation front during the allotropic transformation. The transformation front can be treated as a thin film of certain thickness. The diffusivity within this thin film is much higher than that in the bulk of parent and product crystals. Accordingly, only a few Fe atoms might gather on the transformation front under the atom-vacancy interchange process. However, this does not lead to the lattice expansion in the parent phase during allotropic transformation, which is consistent with the linear change of d-spacing in Fig. 8b.

As described in the Introduction, the tracking of lattice parameter changes can provide information about the element partitioning behaviors during the phase transformation. But for the case of the allotropic transformation, knowledge of lattice parameter change is still lacking. In this study, the d-spacing value of the austenite displays a steady decrease along thermal cycle during the $\gamma \rightarrow \alpha$ transformation. This information will be helpful to understand the kinetic information about the phase transformation.

Table 2 Chemical compositions of the studied steel (in mass %) with balance of Fe

/	C	Si	Mn	Cr	Ni	Nb	N	Co	Mo	V	W	B
Austenitic	0.06	0.4	1.2	20	20	2	0.25	/	/	/	/	/
Ferritic	0.12	0.15	0.5	10	0.5	0.16	0.03	2.5	0.5	0.2	2	0.005

4 Thermal Stability of Carbides and Carbonitrides During Thermal Cycle

Precipitation reactions of heat-resistant steel occurring during welding, both growth and coarsening of existing phases and the formation of new phases, can be detrimental for creep strength. However, understanding of the thermal stability of precipitates during the heat cycle of welding is insufficient. In this study, an attempt has been made to investigate the possibility of analyzing carbides/carbonitrides stability occurring in the heat affected zone based on in situ time-resolved X-ray diffraction using a synchrotron.

In this study, two types of heat-resistant steels were selected for study, ferritic steel and austenitic steel. The chemical compositions of the steels ware listed in Table 2. Then the in situ observation was carried out using the hybrid observation system.

Figure 10a [44] displays both the TRXRD and the corresponding temperature data obtained during the continuous heating and cooling of the investigated austenitic heat-resistant steel at heating and cooling rates of 8.3 °C s^{-1}. The temperatures and times at which certain phases are present during the heat treatment can be obtained from these plots. Figure 10b shows selected X-ray diffractograms of experimental steel corresponding to Fig. 10a. In the case of the heating process, the diffraction patterns do not exhibit significant changes in the range of temperate from 24 to 1,365.5 °C. However, the diffraction intensity of the ε-Nb(C,N) decreased sharply at 1,365.5 °C, indicating that dissolution in the precipitates is occurring under the thermodynamic driving force. The diffraction intensity of the ε-Nb(C,N) continued to decrease until it had completely disappeared at 1,372.5 °C. At the same temperature, the δ-Nb(C,N) just begins to dissolve, corresponding to the reduction of its diffraction intensity. This indicates that the dissolution of the δ-Nb(C,N) begins at a higher temperature (1,372.5 °C) than the 1,365.5 °C of the ε-Nb(C,N). Finally, only weak δ-Nb(C,N) diffraction peaks could be detected when the temperature dropped to 1,148.3 °C. This indicates that the δ-Nb(C,N) is just starting to re-precipitate in the austenite. The re-precipitation was completed at 1,115.5 °C. Moreover, according to the weak diffraction intensity, there should only be a small amount of reprecipitation in the austenite.

Figure 11 [44] shows the progression of the measured δ-Nb(C,N) (111) and ε-Nb(C,N) (102) d-spacing values of austenitic steel as a function of temperature. In the initial stages of the experiment, the d-spacing values of δ-Nb(C,N) and ε-Nb(C,N) display the steady increase which generally corresponds to lattice expansion due to increasing temperature. After the temperature of 1,274 °C, which

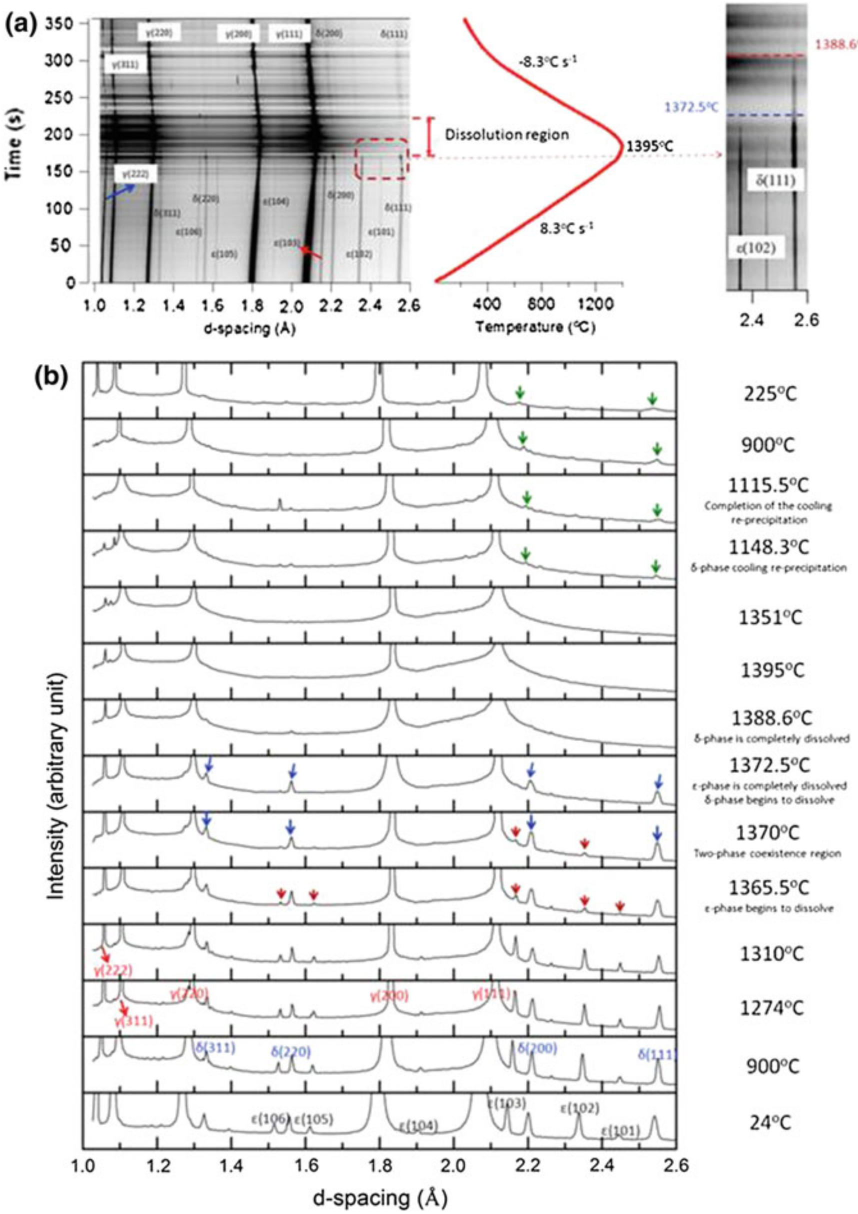

Fig. 10 **a** Changes in diffraction patterns and lattice parameter of austenitic heat-resistance steel during the heating and cooling process. **b** Selected X-ray diffractograms of experimental steel corresponding to (**a**) [44]

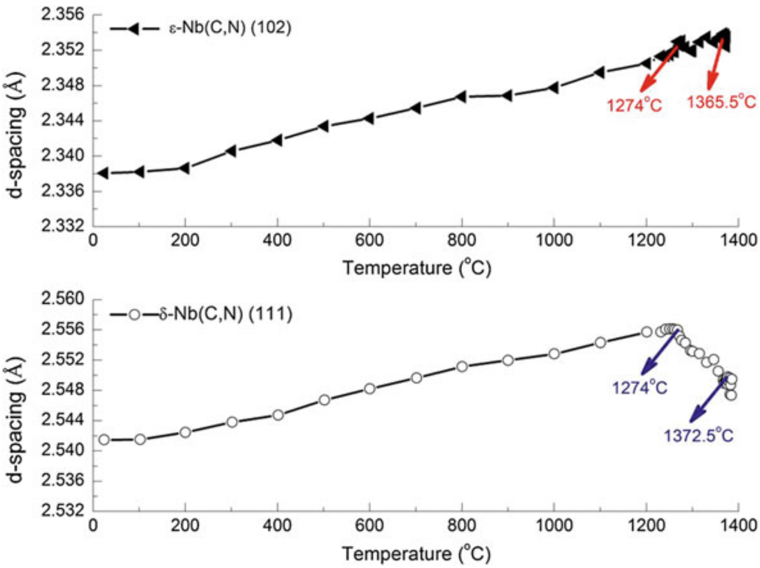

Fig. 11 Changes of d-spacing of ε-NbN (102) and δ-NbN (111) in austenitic heat-resistance steel for heating rate 8.3 °C s^{-1} as function of temperature. *Arrows on plot* indicate the initiation of the niobium carbonitrides coarsening and dissolution, respectively [44]

are indicated on the plot by the arrows, the d-spacing of δ-Nb(C,N) exhibits a sharp decrease during continuous heating when an expansion is expected, indicating that changes in the δ-Nb(C,N) precipitates are occurring before the dissolution. The contraction of δ-Nb(C,N) carbonitrides might be related with covalent bonding energy. According to electronic structure of niobium carbonitrides, the covalent bonds Nb–N and Nb–C are formed by p–d hybridization, which determines its thermodynamic stability. Once the Nb–N or Nb–C covalent bonds have been destroyed by heat prior to the dissolution, N and C atoms dissolve from the interstitial sites of niobium carbonitrides. Thus, the contraction of δ-Nb(C,N) will be manifested in the form of a decrease in d-spacing. With the further increase of temperature, more and more Nb–N and Nb–C covalent bonds will be broken, which leads to a further contraction of the lattice. This seems to indicate that δ-Nb(C,N) particles are not thermodynamically stable during the coarsening process. Until the Nb–N and Nb–C covalent bonds are totally destroyed, δ-phase particles will be completely dissolved into austenite. But the d-spacing of the ε-Nb(C,N) exhibits the continued increase along with the increasing temperature. It is likely that the hexagonal ε-phases possess a larger covalent contribution to the chemical bonding than the cubic one, which may give rise to higher thermodynamic stability as discussed above.

Figure 12 [45] exhibits the progression of the measured $M_{23}C_6$ (420) d-spacings of ferritic steel as a function of temperature. Below 800 °C, the crystal lattice expands as a result of the thermal expansion during heating. The thermal expansion

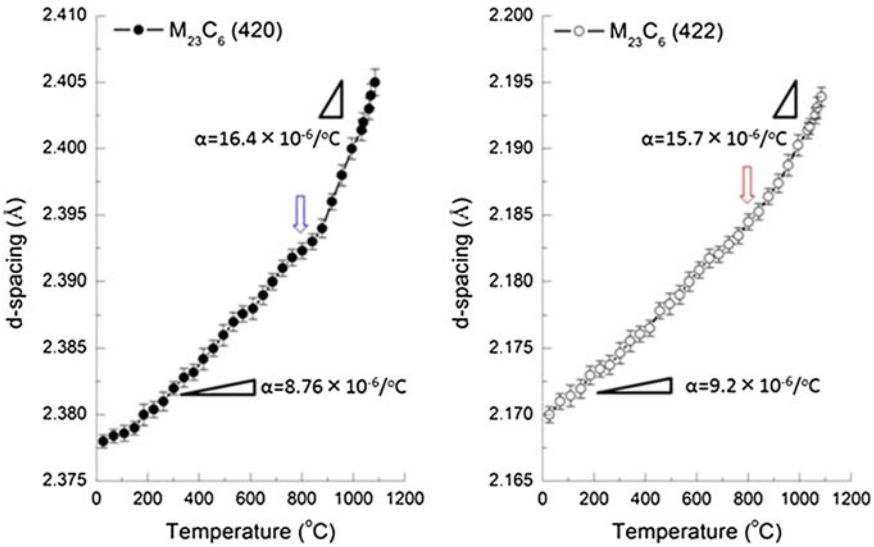

Fig. 12 Tracing the d-spacing changes of 420 and 422 diffraction peaks of $M_{23}C_6$ carbides in ferritic heat-resistance steel [45]

coefficient (CTE) for $M_{23}C_6$ is reported to be 7.9 × 10^{-6}/°C near room temperature. This value corresponds very well with the experimentally measured CTE value (8.76 × 10^{-6}/°C). The result displays a rapid increase in CTE to a value of 16.4 × 10^{-6}/°C above 800 °C, which is approximately 1.8 times that observed at lower temperatures. Similarly, the measured CTE value of the $M_{23}C_6$ (422) is approximately 1.7 times that observed at lower temperatures.

To understand this difference in lattice expansion, the mean crystallite size of $M_{23}C_6$ carbides is considered as a function of temperature. Figure 13 [45] shows the calculated mean particle size using the integral breadth method. Above 800 °C, coarsening of $M_{23}C_6$ carbide particles occurred. The different behaviors before and after 800 °C are most likely explained by the diffusion of alloying elements. $M_{23}C_6$ carbides, though generally Cr rich, can accommodate varying amounts of Fe, Mo, and W, depending on the temperature and time of formation [46, 47]. It is clear that dislocations are energetically stable for the $M_{23}C_6$ precipitates, since Cr-rich $M_{23}C_6$ particles mainly precipitate on prior austenite grain boundaries, ferrite subgrain boundaries and on dislocations inside subgrains. The coarsening of $M_{23}C_6$ precipitates could possibly be caused by a solute drag effect where substitutional atoms are carried by migrating dislocations. Calculations made by Hald on 9–12 % Cr steels show that solubility and diffusion of Mo control the coarsening of $M_{23}C_6$ carbides. Therefore an increased mobility of Mo and W atoms could contribute to the coarsening of carbides. Although it is generally accepted that Cr and Fe are the main elements in $M_{23}C_6$ carbides, Mo and W will also play a role in the coarsening of $M_{23}C_6$ precipitates. The atomic radii of Mo and W are

Fig. 13 Calculated crystallite size of $M_{23}C_6$ versus temperature [45]

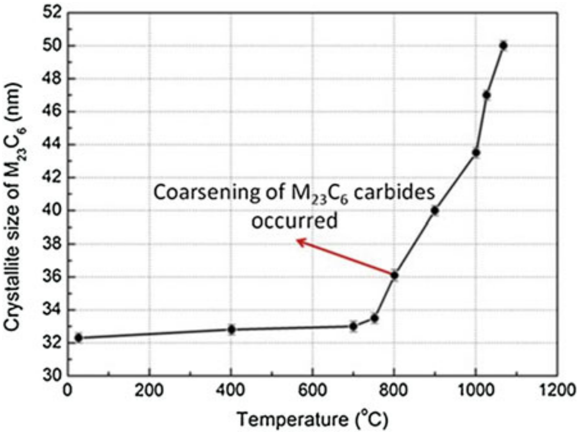

1.90 Å and 1.93 Å, which are larger than the radii of 1.66 Å and 1.56 Å for Cr and Fe respectively. Thus, lattice expansion increases markedly during the coarsening of $M_{23}C_6$ carbides.

5 Diffusional and Displacive Transformation Behavior in Low Carbon Low Alloy Steels

As an observational example for hybrid system, the phase transformation behaviour of diffusional (mild steel (MS)) and displacive (low-temperature transformation steel (LTT)) transformations were compared with this system. The origin and morphology of the microstructural change were analysed in real space. The d-spacing change was also analysed to assess the carbon partitioning behaviour in the reciprocal lattice space. An LTT specimen was prepared in order to observe the displacive transformation. The LTT material should reduce the residual stress by using transformation strain in the welding field [48]. The chemical composition of the LTT was 0.03 C, 0.07 Si, 0.09 Mn and 9.88 Ni (wt.%). The chemical composition of the MS was 0.06 C, 0.4 Si, 1.01 Mn, 0.01 P and 0.008 S (wt.%). The specimen was 5.0 mm in diameter and 2.0 mm in height, and it was inserted into a boron nitride crucible. Both specimens were subjected to the same thermal cycle, heated up to 1,000 °C and cooled down to room temperature. The time resolution of XRD detection was 0.2 s. The diffraction data were analysed using the method and programming described in Ref. [37]. On the other hand, the LSCM images were recorded in the time resolution of 0.03 s throughout the thermal cycle. Figure 14 [32] shows snapshots of the LSCM images for the LTT and MS specimens during the cooling cycle. In the case of the LTT, austenite was supercooled to 300 °C, as shown in Fig. 14 LTT-(i). Further cooling caused a martensitic transformation, as shown in Fig. 14 LTT-(ii) and (iii). The image contrast of the precipitate was very clear because of the surface relief of the martensite. The yield

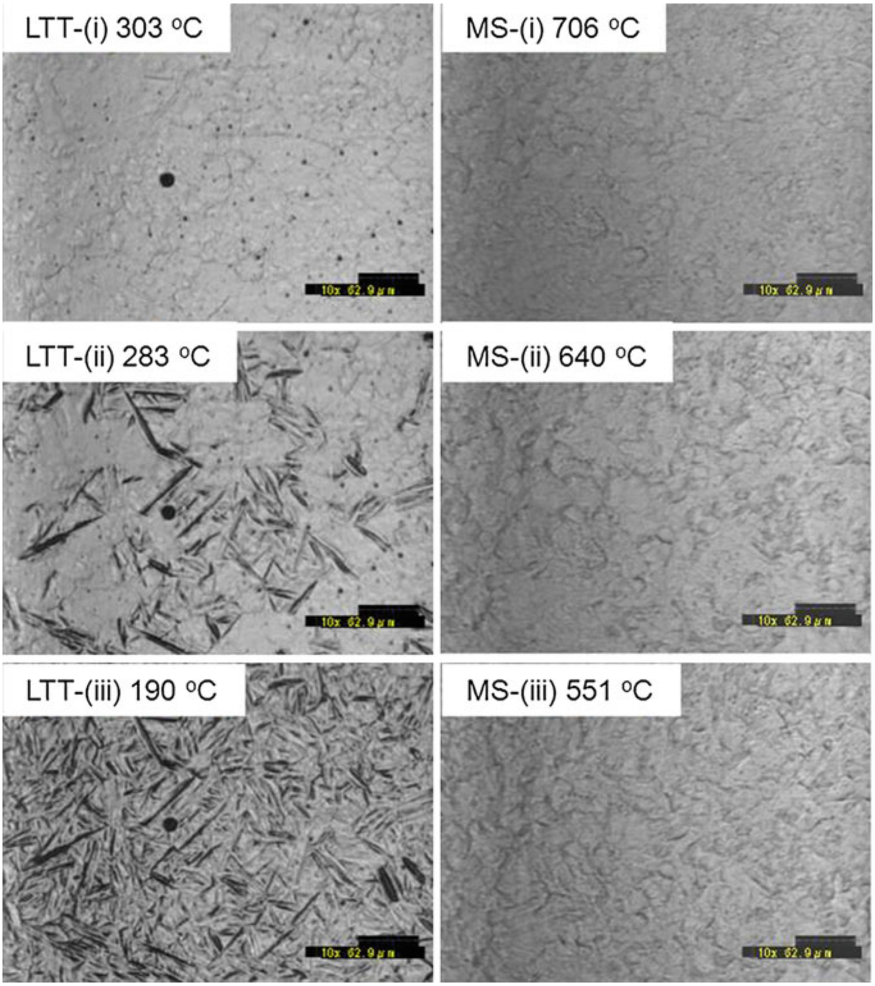

Fig. 14 Snapshots of solid-state transformation during the cooling cycle in LTT [LTT-(i), (ii), (iii)] and MS [MS-(i), (ii), (iii)] [32]

stress increased linearly as the temperature decreased. Then the elastic strain balanced the transformation strain and it was effective in reducing the residual stress in the restricted weld. In the case of the MS, at 640 °C, a very weak contrast was observed on the grain boundary of the austenite and spread throughout the images at 550 °C, as shown in Fig. 14 MS-(ii) and (iii). The nucleation site and the morphology of the precipitate were of the nature of a ferrite allotriomorph. The nucleation temperature should be higher than 640 °C because the magnification of LSCM images is 100. The image contrast of the ferrite allotriomorph was very weak because there was no relief on the surface of the specimen. The contrast in the LSCM image is affected by two factors: the formation of relief and a difference

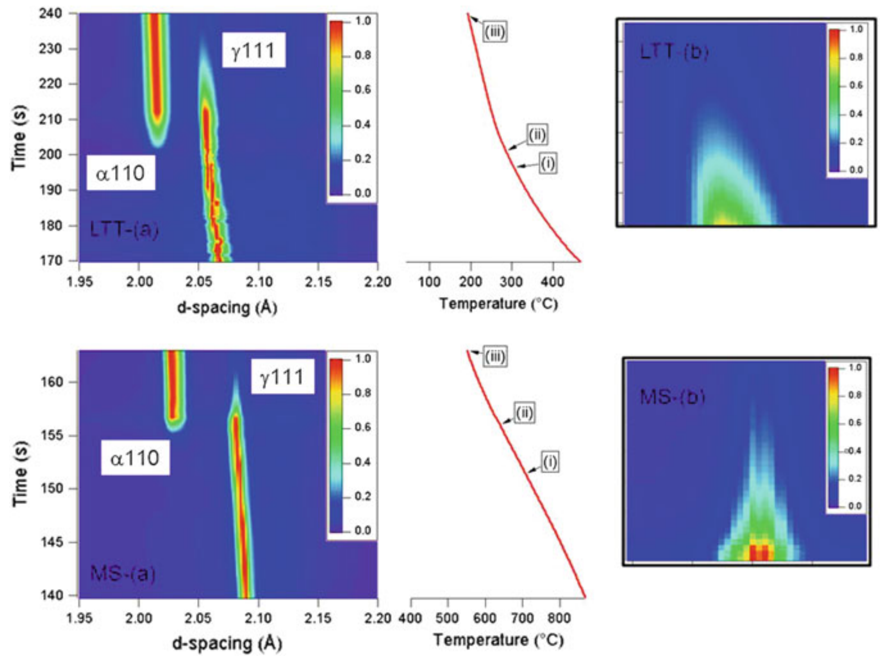

Fig. 15 The d-spacing, time and temperature—intensity diagram during the cooling cycle in LTT [LTT-(a)] and MS [MS-(a)] [32]

in reflectivity. In the case of relief formation, such as displacive transformation and thermal grooving at the grain boundary, the difference in the reflection direction of the laser light is responsible for the clear contrast in the LSCM image. On the other hand, in diffusional transformation, the contrast is very weak, as shown in Fig. 14. This means that there is no surface relief, and the contrast is due to the differences of reflectivity between the ferrite and austenite. The light reflectivity is governed by the electrical conductivity. The difference of electrical conductivity between the ferrite and austenite should be small in the current chemical composition, and this difference causes a very weak contrast in the case of diffusional transformation. Figure 15 [32] shows the d-spacing, time, temperature and intensity diagram [LTT-(a) and MS-(a)] during the phase transformations in the cooling cycle. The displayed reflection is that of austenite (111) and ferrite (110). The intensity was normalized. In the macro-view, the d-spacing of the austenite and ferrite decreased because of thermal shrinkage in the LTT and MS. When the phase transformation occurred, the intensity of the austenite decreased, as shown in Fig. 15. The marks (i), (ii) and (iii) in the temperature profile correspond to the number in Fig. 14 for each steel sample. There was a discrepancy of approximately 20 °C between the surface temperature of the specimen and the thermocouple set behind the platinum plate stage. This discrepancy suggests that the LSCM images were compatible with the diffraction pattern. Hence, the developed system could follow the phase

Fig. 16 Tracing of the d-spacing change during phase transformations in LTT and MS, derived from the fitting of Gaussian peaks [32]

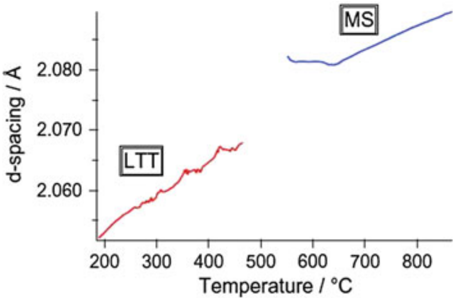

transformations in both real and reciprocal space. Figure 15 LTT-(b) and MS-(b) show enlarged views of the austenite (111) diffraction peaks when the austenite decreased because of the phase transformations. The d-spacing continuously decreased along the trends in the macro-view in the LTT, whereas it increased against the trends in the MS. In order to analyse this phenomenon, a fit of Gaussian peaks [37] to the austenite reflection (111) was performed.

Figure 16 shows the result of d-spacing that was derived using a fit of Gaussian peaks in the LTT and MS (shown in the low-temperature and high temperature region, respectively, in Fig. 10). As expected, in the case of the LTT, the d-spacing continuously decreased along the cooling cycle. On the other hand, in the case of the MS, d-spacing continuously decreased until 643 °C and then suddenly increased at the point shown in Fig. 15 MS-(b). There is a possibility that the inhomogeneous carbon distribution occurred because of the insufficient austenitization and affected the d-spacing change. However, the continuous decreasing of d-spacing prior to phase transformation (as shown in Fig. 16, marked “MS”) means the discontinuous change around 643 °C was due to the phenomena during phase transformation. The d-spacing change in an austenite phase in the diffusional transformation was found to be discontinuous to than in the displacive transformation. This difference reflected the carbon partitioning behaviour. Furthermore, there was no splitting behaviour [49] in the austenite peaks. Thus, it could be concluded that the carbon partitioning expanded the lattice parameter as observed in the ferrite allotriomorph formation. In the case of the displacive transformation, there was no partitioning of carbon, and the expansion was not observed in the TRXRD data. A large-area detector, Pilatus 2M [9], was installed in the experimental system. Then the austenite reflections of (111), (200), (220) and (311) were recorded over time. All the reflections had the same tendency (i.e., increasing d-spacing because of carbon partitioning in MS), and the results were verified statistically. As is clearly observed in Fig. 16, the d-spacing change in the MS looks very smooth, whereas that in the LTT looks uneven. Note that the uneven form appeared before phase transformation and was smooth after phase transformation, as shown in the low-temperature region of Fig. 16. The major difference in the phase transformation of each austenite is the degree of supercooling. The supercooling may affect crystal stability. Further statistical research is needed to assess the effect from this perspective.

The phase transformation behaviour of mild steel and low-temperature-transformation steel was observed in situ with a developed hybrid TRXRD/LSCM system. When the ferrite allotriomorph was formed in the mild steel, carbon partitioning occurred, and the d-spacing of the austenite reflection increased even when thermal shrinkage occurred during the cooling thermal cycle. Our system should also help to analyse other transformation mechanisms of steel, such as bainite and massive transformations.

6 Summary

A new technique, based on the combination of time-resolved X-ray diffraction (TRXRD) and laser scanning confocal microscopy (LSCM), was developed for direct observation of morphological evolution and simultaneous identification of the phases. TRXRD data and LSCM images under the desired thermal cycles were measured simultaneously. As described above, the combination of LSCM and TRXRD is effective in investigating the phase transformation kinetics during thermal cycles of rapid heating and cooling. The system can be applied to the analysis of microstructural changes for improved control of properties in welds.

7 Future Works

Synchrotron based X-ray diffraction techniques combined with high-temperature laser scanning confocal microscopy; provide new and powerful tools for the study of phase transformations and microstructural evolution during welding.

Detecting a wider area of the Debye circle is very important. Mounting several detectors on the arm of the diffractometer increases the detection range for the part of the Debye circle. Continual improvements in synchrotron based methods can only increase the ability to monitor these transformations at higher spatial and temporal resolutions during welding. When combined with additional experiments and modelling, these techniques enable a deeper understanding of the kinetics of phase transformations.

Acknowledgments The synchrotron radiation experiments were performed at the SPring-8 with the approval of the Japan Synchrotron Radiation Research Institute (JASRI) (Proposal No. 2009B2086 and 2011B1968). The authors are grateful to Dr. Sato and Dr. Toyokawa, JASRI, for profitable discussion.

This study was conducted as a part of research activities of ‘Fundamental Studies on Technologies for Steel Materials with Enhanced Strength and Functions’ by the Consortium of The Japan Research and Development Center of Metals (JRCM). Financial support from New Energy and Industrial Technology Development Organization (NEDO) is gratefully acknowledged.

References

1. Elmer JW, Wong J, Ressler T (1998) Spatially resolved X-ray diffraction phase mapping and alpha → beta → alpha transformation kinetics in the heat-affected zone of commercially pure titanium arc welds. Metall Mater Trans A 29:2761–2773
2. Elmer JW, Wong J, Ressler T (2001) Spatially resolved X-ray diffraction mapping of phase transformations in the heat-affected zone of carbon-manganese steel arc welds. Metall Mater Trans A 32:1175–1187
3. Elmer JW, Palmer TA, Wong J (2003) In situ observations of phase transitions in Ti-6Al-4V alloy welds using spatially resolved x-ray diffraction. J Appl Phys 93:1941–1947
4. Elmer JW, Palmer TA (2006) In-situ phase mapping and direct observations of phase transformations during arc welding of 1045 steel. Metall Mater Trans A 37A:2171–2182
5. Elmer JW, Palmer TA, Zhang W, Wood B, DebRoy T (2003) Kinetic modeling of phase transformations occurring in the HAZ of C-Mn steel welds based on direct observations. Acta Mater 51:3333–3349
6. Zhang W, Elmer JW, DebRoy T (2005) Integrated modelling of thermal cycles, austenite formation, grain growth and decomposition in the heat affected zone of carbon steel. Sci Technol Weld Joining 10:574–582
7. Elmer JW, Wong J, Ressler T (2000) In-situ observations of phase transformations during solidification and cooling of austenitic stainless steel welds using time-resolved X-ray diffraction. Scripta Mater 43:751–757
8. Elmer JW, Palmer TA, Babu SS, Zhang W, DebRoy T (2004) Direct observations of austenite, bainite, and martensite formation during arc welding of 1045 steel using time-resolved X-ray diffraction. Weld J 83:244S–253S
9. Elmer JW, Palmer TA, Babu SS, Zhang W, DebRoy T (2004) Phase transformation dynamics during welding of Ti-6Al-4V. J Appl Phys 95:8327–8339
10. Babu SS, Elmer JW, Vitek JM, David SA (2002) Time-resolved X-ray diffraction investigation of primary weld solidification in Fe-C-Al-Mn steel welds. Acta Mater 50:4763–4781
11. Palmer TA, Elmer JW, Babu SS (2004) Observations of ferrite/austenite transformations in the heat affected zone of 2205 duplex stainless steel spot welds using time resolved X-ray diffraction. Mater Sci Eng, A 374:307–321
12. Wong J, Ressler T, Elmer JW (2003) Dynamics of phase transformations and microstructure evolution in carbon-manganese steel arc welds using time-resolved synchrotron X-ray diffraction. J Synchrotron Radiat 10:154–167
13. Komizo Y, Osuki T, Yonemura M, Terasaki H (2004) Analysis of primary weld solidification in stainless steel using X-ray diffraction with synchrotron radiation (materials, metallurgy & weldability). Trans JWRI 33:143–146
14. Osuki T, Yonemura M, Ogawa K, Komizo Y, Terasaki H (2006) Verification of numerical model to predict microstructure of austenitic stainless steel weld metal using synchrotron radiation and trans varestraint testing. Sci Technol Weld Joining 11:33–42
15. Komizo Y, Terasaki H, Yonemura M, Osuki T (2005) In-situ observation of steel weld solidification and phase evolution using synchrotron radiation. Trans JWRI 34:51–55
16. Yonemura M, Osuki T, Terasaki H, Komizo Y, Sato M, Kitano A (2006) In-situ observation for weld solidification in stainless steels using time-resolved X-ray diffraction. Mater Trans 47:310–316
17. Terasaki H, Komizo Y, Yonemura M, Osuki T (2006) Time-resolved in-situ analysis of phase evolution for the directional solidification of carbon steel weld metal. Metall Mater Trans A 37A:1261–1266
18. Yonemura M, Komizo Y, Toyokawa H (2006) SPring 8 Res Front 129–130
19. Yonemura M, Osuki T, Terasaki H, Komizo Y, Sato M, Toyokawa H (2006) Two-dimensional time-resolved X-ray diffraction study of directional solidification in steels. Mater Trans 47:2292–2298

20. Komizo Y, Terasaki H (2008) In-situ observation of weld solidification and transformation using synchrotron radiation. Tetsu To Hagane—J Iron Steel Inst Jpn 94:1–5 (in Japanese)
21. Komizo Y (2008) In-situ microstructure observation techniques in welding. J Jpn Weld Soc 77:26–31 (in Japanese)
22. Komizo Y, Terasaki H, Yonemura M, Osuki T (2008) Development of in-situ microstructure observation techniques in welding. Weld world-Lond 52:56–63
23. Hashimoto T, Terasaki H, Komizo Y (2008) Effect of solidification velocity on weld solidification process of alloy tool steel. Sci Technol Weld Joining 13:409–414
24. Terasaki H, Yamada T, Komizo Y (2008) Analysis of inclusion core under the weld pool of high strength and lowalloy steel. ISIJ Int 48:1752–1757
25. Terasaki H, Yanagita K, Komizo Y, Sato M, Toyokawa H (2009) In-situ observation of solidification behavior of 14Cr-Ni steel weld. Q J Jpn Weld Soc 27:118s–121s
26. Zhang D, Terasaki H, Komizo Y (2009) In situ observation of morphological development for acicular ferrite in weld metal. J Alloy Compd 484:929–933
27. Terasaki H, Komizo Y (2006) In situ observation of morphological development for acicular ferrite in weld metal. Sci Technol Weld Joining 11:561–566
28. Yamada T, Terasaki H, Komizo Y (2008) Microscopic observation of inclusions contributing to formation of acicular ferrite in steel weld metal. Sci Technol Weld Joining 13:118–125
29. Komizo Y, Terasaki H (2011) Optical observation of real materials using laser scanning confocal microscopy Part 1-techniques and observed examples of microstructural changes. Sci Technol Weld Joining 16:56–60
30. Komizo Y, Terasaki H (2011) Optical observation of real materials using laser scanning confocal microscopy Part 2-direct observation of ferrite nucleation sites in weld metal and heat affected zone. Sci Technol Weld Joining 16:61–67
31. Komizo Y, Terasaki H (2011) In situ time resolved X-ray diffraction using synchrotron. Sci Technol Weld Joining 16:79–86
32. Terasaki H, Komizo Y (2011) Diffusional and displacive transformation behaviour in low carbon-low alloy steels studied by a hybrid in situ observation system. Scripta Mater 64:29–32
33. Warren BE (1990) X-ray diffraction. Courier Dover Publications
34. Zhang XF, Komizo Y (2013) In Situ Investigation of the Allotropic Transformation in Iron. Steel Res Int 84:751–760
35. Zhang YD, Esling C, Calcagnotto M, Zhao X, Zuo L (2007) New insights into crystallographic correlations between ferrite and cementite in lamellar eutectoid structures, obtained by SEM-FEG/EBSD and an indirect two-trace method. J Appl Crystallogr 40:849–856
36. Takasaki A, Ojima K, Taneda Y (1995) In-situ transmission electron microscopy of the $\alpha \leftrightarrow \gamma$ allotropic transformation in thin foil of iron. Phys Status Solidi A 148:159–165
37. Babu SS, Specht ED, David SA, Karapetrova E, Zschack P, Peet M, Bhadeshia H (2005) In-situ observations of lattice parameter fluctuations in austenite and transformation to bainite. Metall Mater Trans A 36A:3281–3289
38. Morito S, Tanaka H, Konishi R, Furuhara T, Maki T (2003) The morphology and crystallography of lath martensite in Fe-C alloys. Acta Mater 51:1789–1799
39. Kitahara H, Ueji R, Tsuji N, Minamino Y (2006) Crystallographic features of lath martensite in low-carbon steel. Acta Mater 54:1279–1288
40. Perepezko JH (1984) Nucleation in undercooled liquids. Metall Trans A 15:437–447
41. Massalski TB (1984) Distinguishing features of massive transformations. Metall Trans A 15:421–425
42. Kinsman KR, Richman RH, Verhoeven JD (1976) Geometric surface relief and the allotropic transformation in iron. J Mater Sci 11:1487–1493
43. Banerjee S (1984) Solubility of organic mixtures in water. Mater Sci Forum 1:239–255
44. Zhang XF, Terasaki H, Komizo Y (2012) In situ investigation of structure and stability of niobium carbonitrides in an austenitic heat-resistant steel. Scripta Mater 67:201–204

45. Zhang XF, Komizo Y (2013) Direct observation of thermal stability of M23C6 carbides during reheating using in situ synchrotron X-ray diffraction. Philos Mag Lett 93:9–17
46. Hald J (2008) Microstructure and long-term creep properties of 9–12% Cr steels. Int J Press Vessels Pip 85:30–37
47. Mythili R, Paul VT, Saroja S, Vijayalakshmi A, Raghunathan VS (2003) Microstructural modification due to reheating in multipass manual metal arc welds of 9Cr–1Mo steel. J Nucl Mater 312:199–206
48. Zenitani S, Hayakawa N, Yamamoto J, Hiraoka K, Morikage Y, Kubo T, Yasuda K, Amano K (2007) Development of new low transformation temperature welding consumable to prevent cold cracking in high strength steel welds. Sci Technol Weld Joining 12:516–522
49. Palmer TA, Elmer JW (2005) Direct observations of the formation and growth of austenite from pearlite and allotriomorphic ferrite in a C–Mn steel arc weld. Scripta Mater 53:535–540

In Situ Phase Transformation Study in Fine Grained Heat Affected Zone of Grade 91 Steels

X. Yu, M. L. Santella, Y. Yamamoto, H. Terasaki, Y. Komizo and S. S. Babu

Abstract Creep strength-enhanced ferritic (CSEF) steels such as the 9 Cr steel [ASTM A387 Grade 91] are widely used as tubing and piping in the new generation of fossil fired power plants. Microstructures in the fine-grained heat affected zone (FGHAZ) may significantly reduce creep strength leading to Type IV failures. Current research suggests that reducing pre-weld tempering temperature from 760 °C (high temperature temper, HTT) to 650 °C (low temperature temper, LTT) has the potential to double the creep life of these welds. To understand this improvement, time-resolved X-ray diffraction (TRXRD) measurement with synchrotron radiation was used to characterize the microstructure evolution during fine grained heat-affected zone (HAZ) thermal cycling of Grade 91 steel. The measurements showed both $M_{23}C_6$ (M = Fe, Cr) and MX (M = Nb, V; X = C, N) are present in the sample after the HTT condition. Near equilibrium fraction of $M_{23}C_6$ was measured in high temperature tempering condition (HTT, 760 °C). However, the amount of $M_{23}C_6$ in LTT condition was very low since the diffraction peaks are close to the background. During simulated FGHAZ thermal cycling, the $M_{23}C_6$ partially dissolved in HTT sample. Interestingly, MX did not dissolve in both LTT and HTT samples. Hypothesis for correlation of $M_{23}C_6$ carbide distribution and pre-mature creep failure in FGHAZ will be made.

Keywords Phase transformation · Welding · Creep behavior · Creep strength-enhanced ferritic steels (CSEF) · Low transformation temperature material (LTT) · Time-resolved high energy X-ray diffraction (TRXRD)

X. Yu
The Ohio State University, 1248 Arthur E. Adams Drive, Columbus, OH 43221, USA

X. Yu · M. L. Santella · Y. Yamamoto
Oak Ridge National Laboratory, Oak Ridge, TN 37831, USA

H. Terasaki · Y. Komizo
Osaka University, JWRI, Osaka University, Osaka, Japan

S. S. Babu
Department of Mechanical, Aerospace and Biomedical Engineering, 407 Dougherty
Engineering Building, Knoxville, TN 37996-2210, USA

T. Kannengiesser et al. (eds.), *In-situ Studies with Photons, Neutrons and Electrons Scattering II*, DOI: 10.1007/978-3-319-06145-0_2,

1 Introduction

Due to the heavy use of fossil fuels, the worldwide annual emission of CO_2 from fossil fuel combustion was nearly billion tons in 2007 [1]. A reduction of CO_2 emission is possible by improving power plant efficiency through an increase steam temperature and pressure. The pressure and temperature combination are referred to as steam parameters. For example, an increase in steam parameters from typical 538 °C and 24.1 MPa to 650 °C and 34.3 MPa can reduce the energy required by 6.5 %, resulting in a commensurate decrease in coal use, and hence a reduction of CO_2 emission [2]. Due to its excellent high temperature creep resistance, creep strength-enhanced ferritic (CSEF) steels (such as the ASTM A387 Grade 91) are widely used as tubing and piping in fossil fired power plants to accomplish increased efficiency.

The performance of CSEF steels, however, does not always meet expectations, and there have been reports of numerous failures in the HAZ of CSEF steels after only a few years in service [3–6]. These failure locations are often traced back to the fine-grained heat affected zone (FGHAZ) of a weld, which experiences a weld thermal cycle with a peak temperature just above the A_{c3} temperature. It is a well-established fact that non-equilibrium microstructures and their gradients in FGHAZ regions will significantly reduce creep strength [7–10]. Moreover, the grain size and orientation of the FGHAZ can lead to high tri-axial stress states that may contribute to accelerated creep damage [11, 12]. This combination of circumstances leading to premature failure of welded components is discussed in the literature as "Type-IV failures in CSEF steels." Published literature also show that the creep strength reduction of such joints can be on the order of 40 % compared to base metal [13] for the same service life. The implications of such failures include disruptions of electrical supply, increased cost of electricity, and the potential for failure, endangering the safety of power plant personnel. There is an urgent need to improve the creep strength or decrease the steady state creep rate of the weldments. Possible routes to address this critical issue include modifications of steel composition (e.g. boron addition), welding procedures (e.g. reduce the width of FGHAZ), structural design (e.g. reduce the stress) and operating conditions.

Grade 91 steels are strengthened by $M_{23}C_6$ ($M = Cr, Fe$) and MX ($M = Nb, V$; $X = C, N$) precipitates in a tempered martensite matrix. These precipitates (e.g. size, number density, and composition) play an important role in the creep strengthening of the HAZ after welding. The current work pertains to fundamental understanding of carbide evolution in Grade 91 steel under simulated HAZ thermal cycles by X-ray diffraction.

Extensive characterization of the HAZ microstructure in 9–12Cr power plant steels has been done using optical microscopy [7, 8, 11], scanning electron microscopy (SEM) [6, 9, 14] and transmission electron microscopy [6, 11, 14]. However, to develop a comprehensive understanding of the HAZ, there is a need to measure the microstructural kinetics during continuous heating and cooling typical of welding. One of the in situ methods to measure phase transformation is time-resolved X-ray diffraction (TRXRD). TRXRD is capable of characterizing volume fraction of phases and the lattice parameter as a function of imposed thermal cycles. In the past decade, synchrotron-based in situ TRXRD systems were used extensively, to investigate phase transformations in steels [15–23]. Microstructure evolution and quantitative analysis of $M_{23}C_6$ and MX in stainless steel [24–30] and 2.25Cr-1Mo steels [31, 32] has been extensively studied using XRD, however, simultaneous measurements of carbide evolution with α-γ-α transformations in 9–12 Cr steels are limited when using laboratory X-ray sources, due to the small volume fraction of carbides. Therefore, current research uses a suite of ex-situ and in situ characterization tools to understand the precipitate evolution.

Synchrotron TRXRD and Laser Scanning Confocal Microscopy (LSCM) hybrid in situ system developed by Komizo and Terasaki [21] was used to study phase transformation in Grade 91 steels. A TRXRD technique with high-flux synchrotron radiation was adopted to characterize the samples undergoing typical HAZ thermal cycles. Study of phase transformations by the high-speed X-ray diffraction technique using synchrotron radiation allows one to obtain the crystal structure information of all the phases presented in the sample, as well as their phase fractions (~ 0.002) in situ. The transformation kinetics of $M_{23}C_6$, stability of MX precipitates and α-γ-α are derived from the technique. LSCM was used to characterize martensite substructure during martensitic transformation. Based on these measurements, a hypothesis of carbides evolution is proposed during every stage of the manufacturing path to explain the improved creep resistance of the family of Grade 91 steels. Finally, some of the current challenges and future directions related to this hybrid technique are discussed.

2 Experimental

2.1 Steels and Welding

The chemical composition of ASTM Grade 91 (heat number 30176) is shown in Table 1. After initial thermo-mechanical processing, the steels were normalized at a temperature of 1,080 °C for 2.5 h. Four tempering temperatures were investigated in the current study: 800, 760, 700, and 650 °C. The samples were tempered in a furnace for 1.5 h, followed by air cooling to room temperature. Based on the creep performance, two tempering conditions (760 and 650 °C) were selected for further microstructural study. These conditions are designated as HTT (higher pre-weld tempering temperature: 760 °C) and LTT (lower pre-weld tempering temperature: 650 °C) throughout the text. These two base materials were used for welding and simulated weld thermal cycling experiments.

Two 12.7 mm plates, in the HTT and LTT conditions, were machined on the edge with an angle of 37.5° to make a single-V groove. The grooved plates were pre-heated in a furnace that was set 120 °C. Gas tungsten arc welding (GTAW)

Table 1 Chemical composition (wt%) of heat 30176 Grade 91 steel

C	Mn	P	S	Si	Cr	Mo	Fe
0.081	0.37	0.01	0.003	0.11	8.61	0.89	Balanced
Ni	V	Nb	N	Al	Ti	Zr	
0.09	0.2	0.072	0.055	0.007	0.002	0.001	

with argon shielding gas was performed on the plates with one root pass and six fill passes. Inter-pass temperature was kept under 350 °C, which agrees with ASTM recommendations. Welding current, voltage and speed were 260 A, 8 V and 2.5 mm/s respectively. A 9Cr-1Mo filler wire with 1.6 mm in diameter was used. The welded plates were post-weld heat treated (PWHT) in a furnace at 760 °C for 4 h, followed by air cooling to room temperature. The treated plates were sectioned and machined for creep tests.

2.2 Creep Test

Tensile creep-rupture tests of the weld cross-sections were performed according to ASTM E139-06 [33]. Lever-arm creep machines were calibrated to a load accuracy of ±0.5 %. The temperature was measured by three Chromel/Alumel type K thermocouples (±0.4 % accuracy) wired to the gage section. The temperature variation among the thermocouples was less than 1.0 °C, and the highest temperature was recorded as the test temperature. Constant loading creep-rupture tests were at performed 650 °C with an initial stress of 70 MPa (10 ksi). A proportioning temperature controller was used to control within ±1.0 °C. Length change was measured by an averaging extensometer attached by set screws to a small groove in the specimen shoulder. The displacement reading was converted to true strains by dividing by the reduced section length. The dial gage used in measuring the extension had a resolution of 2.5 μm. The strain was recorded every 36 s in the first 37 min, then every 360 s thereafter.

2.3 Hybrid In Situ Characterization

An in situ characterization system was used to observe phase transformation in these steels. The system has been discussed elsewhere [21, 22]. Disk-shaped samples were prepared 2 mm in height and 5 mm in diameter. The in situ observation system was situated within a 46XU beamline at Spring-8 in Hyogo, Japan. An infrared furnace was set on the theta-axis of the goniometer. Samples were placed inside a boron nitride (BN) crucible, which was held by a platinum holder. A thermocouple was attached to the platinum holder to measure the temperature. The measured temperature was used to control the heat flux generated by the halogen lamps. The disk

Table 2 Experiments summary of HAZ simulation characterization by TRXRD [38]

ID	HTT-Tp1050	LTT-Tp1050	HTT-Tp950	LTT-Tp950
Tempering temperature (°C)	760	650	760	650
Heating rate (°C/s)	20	20	10	10
Peak temperature (°C)	1,050	1,050	950	950
Cooling rate (°C/s)	10	10	10	10
Time resolution (s)	0.2	0.2	0.5	1

sample was placed at the focal point of the halogen lamp and mirror systems. During the experiments, the furnace chamber was evacuated and backfilled with argon to prevent oxidation. The current work showed a small temperature gradient from the top to bottom of the sample, under rapid heating/cooling conditions. A correction factor of 50 °C was used to account for these gradients. A large-area pixel detector, Pilatus 2M [34] was placed on the 2-theta axis. The incident beam (30 keV) shone on the sample surface placed in the furnace and the resulting diffraction rings were recorded by the pixel detector. The X-ray with a wavelength was set at 0.413 Å. The glancing angle of the beam on the sample surface was chosen at 5° and which leads to a total irradiated area on the sample surface of 2.07 mm^2. The depth of X-ray interaction was estimated to be $\sim 16\ \mu m$ [22].

Four thermal cycles, which are detailed in Table 2, were selected to simulate weld similar microstructure of FGHAZ. Two peak temperatures (1,050 and 950 °C) were chosen. The first two experiments (designated as HTT-Tp1050 and LTT-Tp1050) used a heating rate of 20 °C/s and time resolution of 0.2 s. It is realized the heating rate is much slower than real weld condition. However, for microstructure simulation purpose, the heating rate effect can be ignored. Initial screening results found the signal to noise ratio for carbides ($M_{23}C_6$ and MX) to be very low. In the subsequent experiments (designated as HTT-Tp950 and LTT-Tp950) the heating rate was reduced to 10 °C/s and the time resolution was increased to 0.5 and 1 s. The diffraction rings on each image were integrated to give one-dimensional scans of intensity versus interplanar spacing [35, 36]. The diffraction data was then synchronized with measured thermal cycles. The scans were analyzed by using an automatic peak fitting algorithms. The methodologies for these are described in the published literature [21, 22].

3 Results and Discussion

3.1 Creep Rates and Microstructures

The strain-to-fracture curves are shown in Fig. 1. According to the ASTM 387 specification [37], the pre-weld tempering temperature range is defined to be 730–790 °C. The pre-weld temper of 760 °C (HTT) in the current experiments represented the conditions of industrial practice. The creep curves demonstrate that the 650 °C pre-welding tempered sample had the highest creep resistance. As a

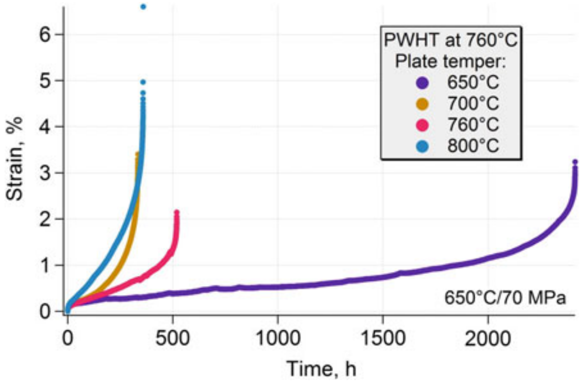

Fig. 1 Creep curves for welded samples with different pre-weld tempering temperature

result, only the 650 °C tempering (LTT) and 760 °C tempering conditions (HTT) were studied in the following experiments. Post-failure examination shows both samples failed in the FGHAZ, approximately 2.1 mm away from fusion line [38]. The HTT sample showed extensive necking compared to the LTT sample, at failure. Microstructures of both samples show equiaxed ferrite grains with creep voids on grain boundaries. Since both LTT and HTT contain this equiaxed ferrite, the role of matrix microstructure on the observed creep resistance change was ruled out in our further analyses. Emphasis was given to transients of carbide distribution in the steel samples as they are subjected to different thermal cycles during pre-weld tempering, welding and post-weld heat treatment.

3.2 Microstructure After Pre-weld Tempering

In order to understand the improvement mechanism of the creep properties in the LTT sample, microstructures of the pre-weld conditions were investigated in the previous study [38]. Figure 2 shows microstructure of two samples which were examined by optical microscopy and SEM. In the LTT sample, two types of carbides (Fig. 2), $M_{23}C_6$ and MX, can be observed [38]. The type of carbide is confirmed by energy dispersive spectroscopy (EDS) [39].

The volume fraction of $M_{23}C_6$ was calculated from SEM images, which were then compared with predicted equilibrium phase fractions using ThermoCalc® software with the TCFE5 database. The volume percentage of $M_{23}C_6$ in the HTT sample was 1.80 vol%, compared to the ThermoCalc® prediction of 1.59 vol%. The result suggests that $M_{23}C_6$ is in a near equilibrium condition after HTT (i.e. 760 °C for 1.5 h). On the other hand, the $M_{23}C_6$ volume fraction in the LTT is measured at 0.5 vol%, much lower than ThermoCalc's prediction (i.e. 1.59 vol%). This result suggests that the tempering of the martensite in the LTT condition is

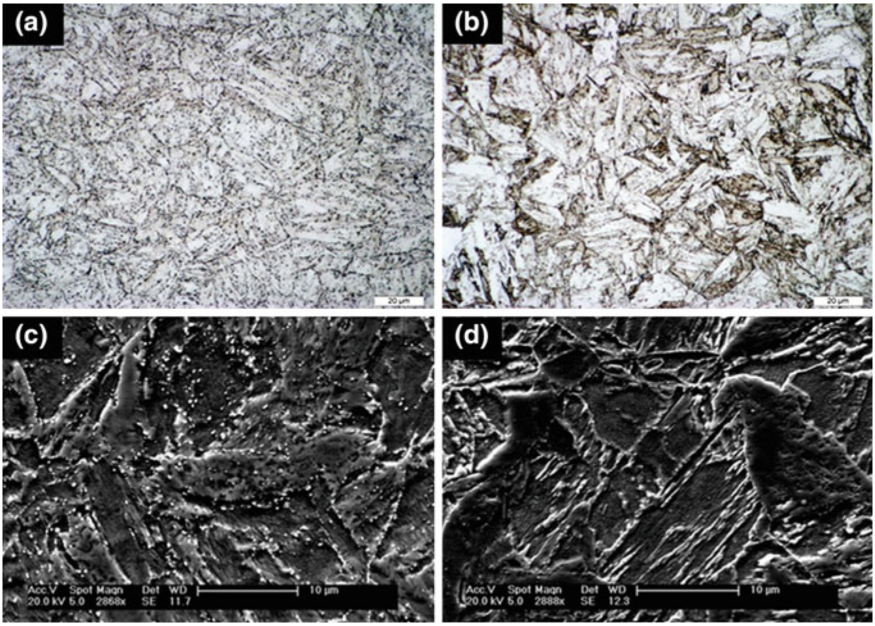

Fig. 2 **a** Optical micrograph of as-tempered HTT sample showing tempered martensitic microstructure. **b** Optical micrograph of as-tempered LTT sample showing a mixture of tempered and untempered martensitic microstructure. **c** SEM images at high magnification of as-tempered HTT sample. **d** SEM images at high magnification of as-tempered LTT sample

not complete and may be still supersaturated with carbon. Although the size of MX is similar in the HTT and LTT conditions, the average size of the $M_{23}C_6$ in HTT is twice as large that of the LTT condition. The difference in the $M_{23}C_6$ size and distribution may affect the final creep properties, even without welding.

3.3 Time Resolved X-ray Diffraction

Since the creep failure occurred in FGHAZ, it was decided to characterize the transients in precipitate ($M_{23}C_6$ and MX) distributions from the pre-weld tempered to welded condition, before PWHT. We were limited in simulating weld microstructures due to the steep temperature gradients of real welds. But the optical micrographs revealed a good correlation of real weld FGHAZ and simulated one. Therefore, we created large-scale LTT and HTT samples that could be subjected to FGHAZ weld thermal cycles in either an in situ characterization system or Gleeble® thermomechanical simulator. The results from the in situ TRXRD experiments performed with two peak temperatures are presented first.

3.4 FGHAZ Microstructure Evolution with 1,050 °C Peak Temperature

Figure 3 presents the comparison of carbide evolution for HTT and LTT samples for the thermal cycle of simulated FGHAZ, whose peak temperature is 1,050 °C. The current study focuses on ferrite (011), austenite (111), $M_{23}C_6$ (422) and MX (200) peaks since they have relatively high signal to noise ratios and are not affected by martensite or austenite peaks. In the HTT sample, the intensities at $M_{23}C_6$ peaks do not change until temperatures reaches about 900 °C, at which the dissolution of $M_{23}C_6$ starts. Intensities of $M_{23}C_6$ peaks become very weak and near the background level at the peak temperature, 1,050 °C. MX peaks are weak and remain unchanged during the heat treatment (Fig. 3a). The increase in d-spacing during heating is due to thermal expansion. Since the intensities at MX peaks are only slightly above the background, it is impossible to fit MX peaks. MX in the current study is not quantified. On the other hand, $M_{23}C_6$ peak intensity in the LTT sample is very weak and close to the background, before the HAZ heat treatment, which implies that only a small amount of $M_{23}C_6$ exists in as tempered condition. When the temperature reaches 1,050 °C, $M_{23}C_6$ peaks cannot be seen any more. The intensities at MX peaks are the same in the LTT as they are in the HTT and remain unchanged (Fig. 3b). The data shown in Fig. 3a, b were analyzed further by fitting a Gaussian peak to austenite (111), ferrite (011) and $M_{23}C_6$ (422) diffraction peaks [16]. After peak fitting, the area under each peak was integrated. The phase volume fraction was derived by using the direct comparison method considering structure factor, multiplicity factor, Lorentz polarization, and temperature factor [40]. The details of data analysis can be found in [16].

Figure 4 shows the $M_{23}C_6$ fraction in the HTT sample and austenite fractions as a function of temperature. There is 1.53 ± 0.22 vol% $M_{23}C_6$ in the HTT sample after pre-weld tempering. This value is very close to the equilibrium volume fraction of $M_{23}C_6$ (1.59 vol%) at 760 °C predicted by ThermoCalc using the TCFE5 database. When the sample is heated to the A_{c1} (998 °C), martensite transforms to austenite. Due to the high C solubility in austenite, $M_{23}C_6$ begins to dissolve. Volume fraction of the $M_{23}C_6$ gradually decreases to 0.2 vol%. When $M_{23}C_6$ is below 0.2 vol%, $M_{23}C_6$ (422) diffraction intensities are close to the background and volume fraction cannot be obtained.

It is of interest to evaluate the stability of these carbides formed after thermal cycling during post weld heat treatment (PWHT). Simulated HAZ samples were further subjected to PWHT at 760 °C for 4 h. Carbides in the simulated HAZ samples, before and after PWHT, are characterized by TEM of carbon replicas (Fig. 5). Identification of $M_{23}C_6$ and MX precipitates is made using SAD and EDS analyses. Even though TRXRD did not show any evidence of $M_{23}C_6$ in HTT-Tp1050 experiments, $M_{23}C_6$ still can be observed by TEM (Fig. 5a). Small amount of MX can also be observed. In the LTT-Tp1050 sample, only MX is present indicating that all the $M_{23}C_6$ carbides have been dissolved in the HAZ with peak temperature of 1,050 °C (Fig. 5b). However, the size of the MX precipitate is

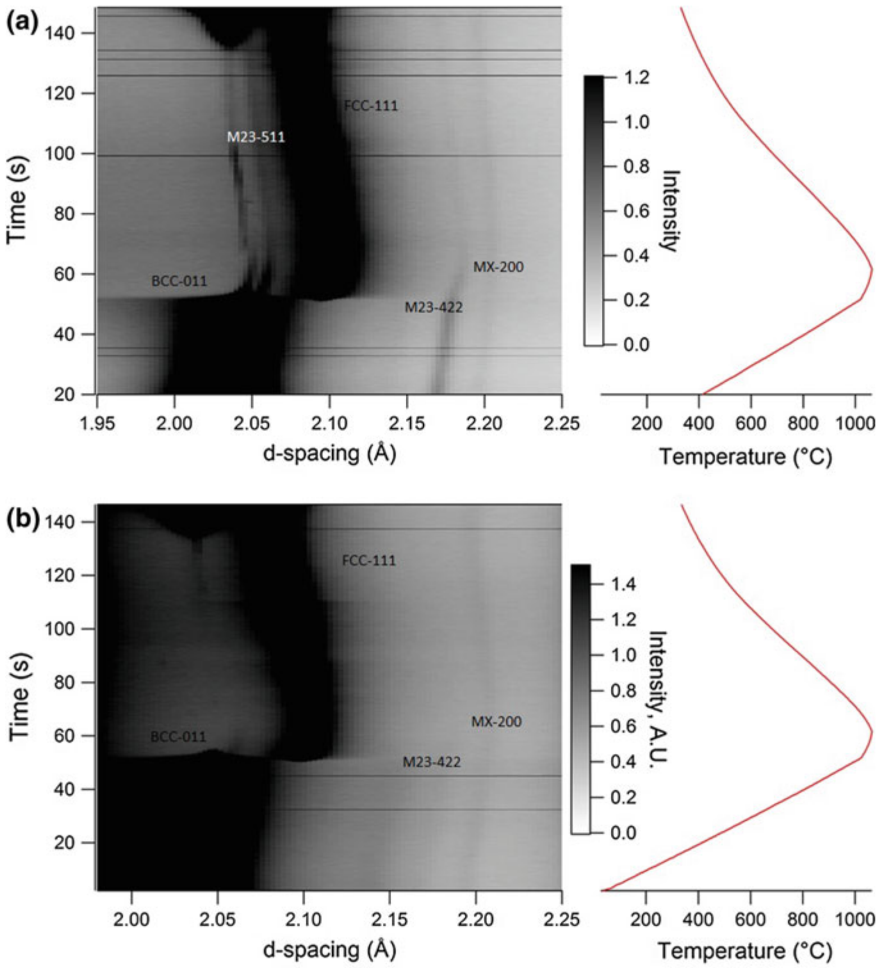

Fig. 3 Carbide peaks intensity with A.U. as a function of time and temperature in HAZ (Tp = 950 °C) for **a** HTT and **b** LTT

smaller than the pre-weld temper condition. Carbide precipitate distributions in simulated PWHT samples of HTT-Tp1050 and LTT-Tp1050 are shown in Fig. 5c, d. Small MX dissolution is also observed in the HTT and LTT conditions, since the reduction is very close to our instrument limits, we neglected this effect. In simulated PWHT samples, size of $M_{23}C_6$ in the HTT condition is slightly larger that of LTT condition, which may be due to coarsening of undissolved $M_{23}C_6$ (Fig. 5c). For both conditions, volume percentage of $M_{23}C_6$ is close to the equilibrium condition. Compared with the HAZ simulated condition, the increment of MX volume percentage after PWHT is again negligible.

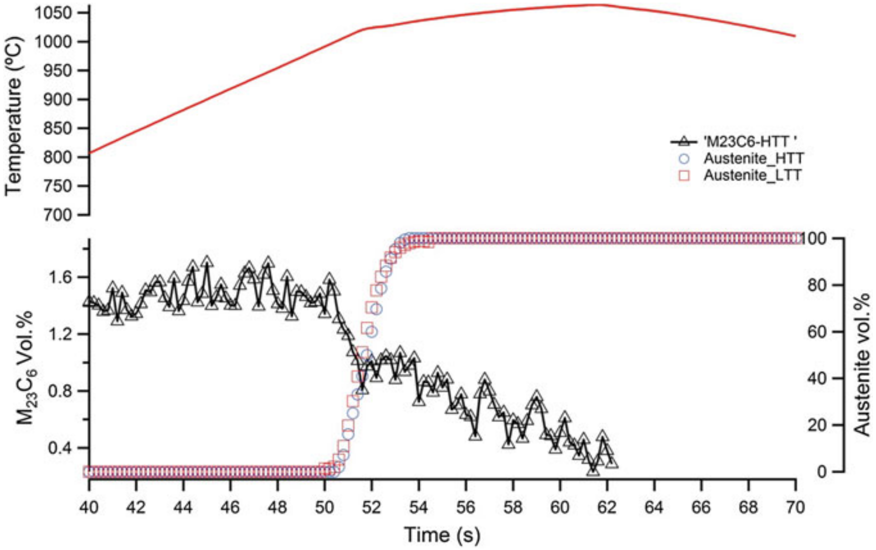

Fig. 4 $M_{23}C_6$ and austenite fraction as a function of time and temperature

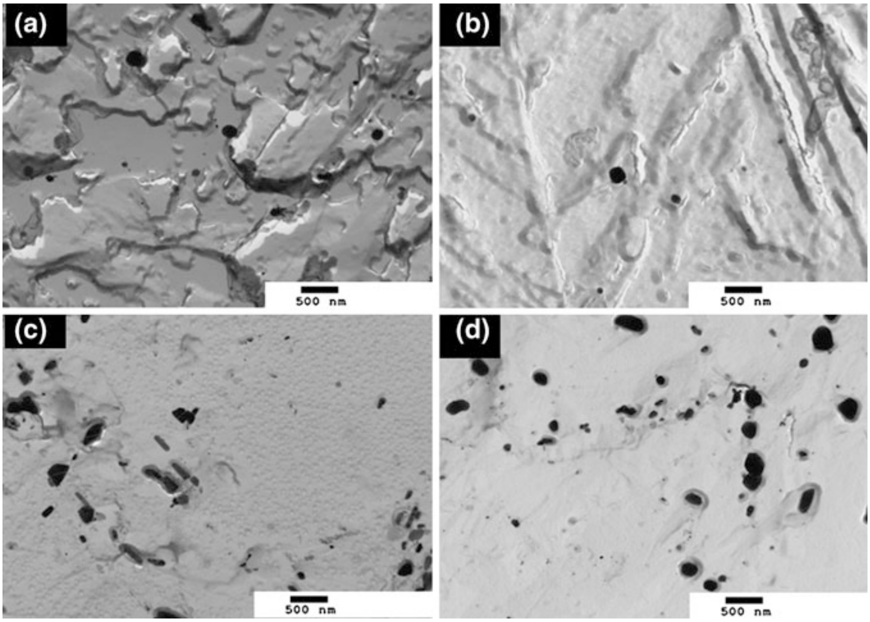

Fig. 5 TEM images on extraction replica of FGHAZ without PWHT **a** HTT **b** LTT; for FGHAZ with PWHT **c** HTT **d** LTT

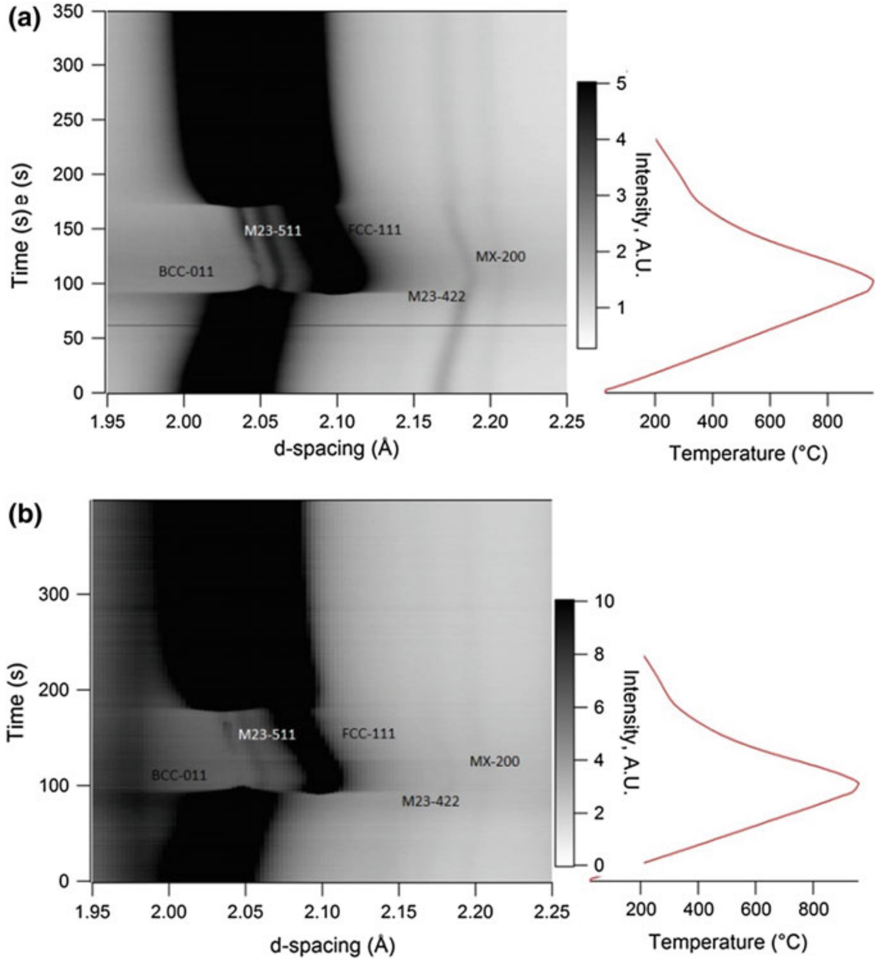

Fig. 6 Carbide peaks intensity as a function of time and temperature in HAZ (Tp = 950 °C) for **a** HTT and **b** LTT

3.5 *FGHAZ Microstructure Evolution with 950 °C Peak Temperature*

Since the Type IV cracking is associated with the FGHAZ region with different peak temperatures, it is of interest to compare the precipitate evolution with a lower peak temperature. Diffraction results for weld thermal cycling with a peak temperature of 950 °C for the HTT and LTT samples are summarized in Fig. 6. Similar to the 1,050 °C peak temperature data, in the HTT samples (Fig. 6a), the $M_{23}C_6$ diffraction peak intensity decreased with the onset of austenite formation at 920 °C. However, the peak intensities of $M_{23}C_6$ were present during the thermal

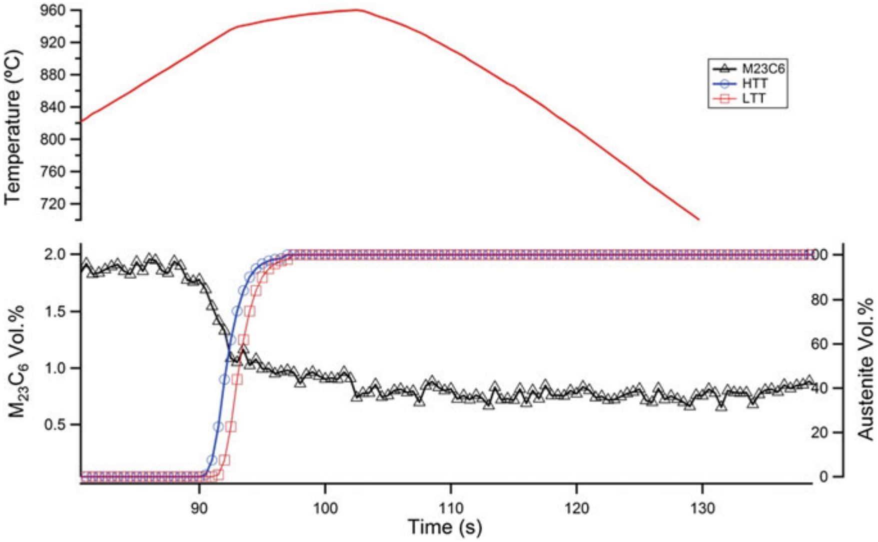

Fig. 7 $M_{23}C_6$ and austenite fraction as a function of time and temperature [38]

cycle even after cooling. Intensity of MX did not change during heat treatment. Both $M_{23}C_6$ and MX peak intensities in the LTT sample were close to the background (Fig. 6b). Quantitative analysis (Fig. 7) shows about 1.8 vol% of $M_{23}C_6$ in the HTT sample before thermal cycling. The amount of $M_{23}C_6$ decreased to 1 vol% after thermal cycling.

TEM images of extracted carbides from the above simulated HAZ samples, before and after PWHT are shown in Fig. 8. Both $M_{23}C_6$ and MX are found in simulated HAZ samples of the HTT and LTT conditions. Significant amounts of carbide exist in the simulated HAZ in HTT-Tp950. On the other hand, very small amounts of carbides are present in LTT-Tp950. TEM results show significant amounts of undissolved carbides in the HTT-Tp950 sample and small amounts of undissolved carbides in LTT-Tp950. Simulated PWHT sample for the HTT condition (Fig. 8c) shows large carbides sizes compared to that of LTT condition (Fig. 8d). Interestingly, the HTT-Tp950 samples even after PWHT contain many coarse carbides compared to the LTT-Tp950 samples after PWHT. This suggests that continued growth and coarsening of undissolved carbides in HTT-Tp950 during PWHT.

3.6 LSCM Observation

Figure 9 shows LSCM images during the austenite to martensite transformation during cooling in the HTT-Tp950 sample. The austenite grain boundaries are imaged due to the surface grooving (Fig. 9a). At 370 °C, the onset of the martensite

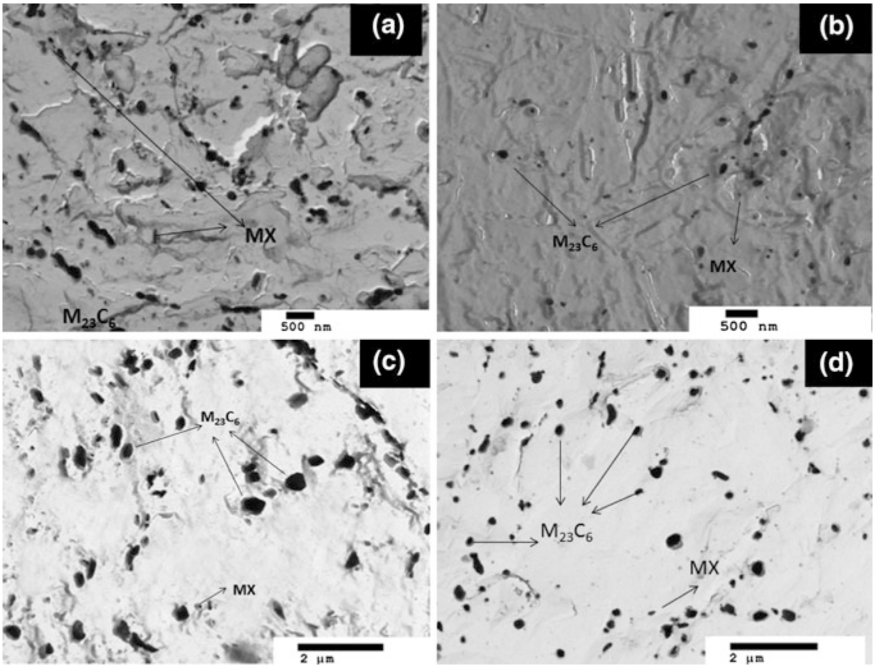

Fig. 8 TEM images on extraction replicas of **a** HTT-Tp950 **b** LTT-Tp950 **c** HTT-Tp950 after PWHT **d** LTT-Tp950 after PWHT [38]

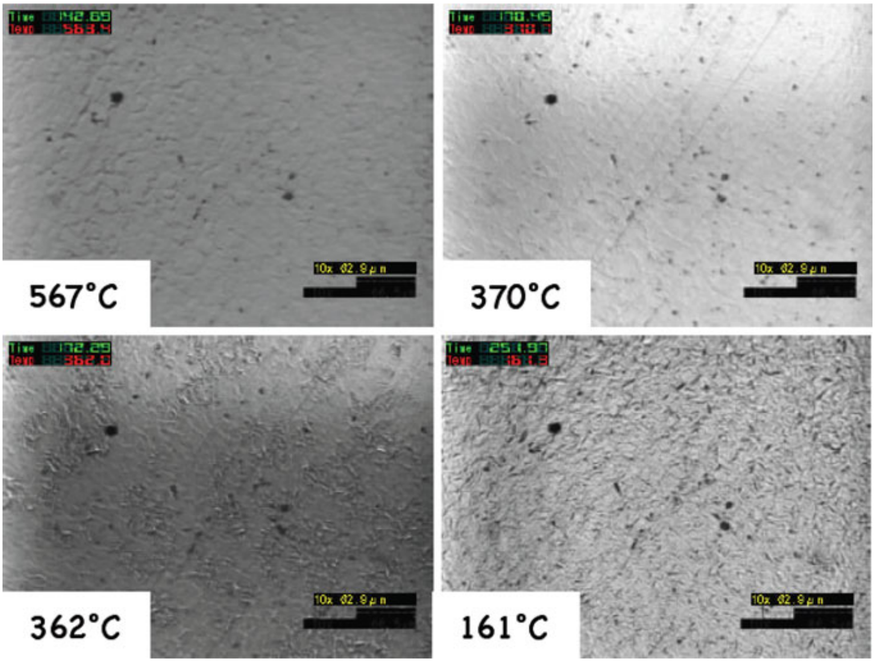

Fig. 9 LSCM images obtained during HTT-Tp950 experiment during cooling

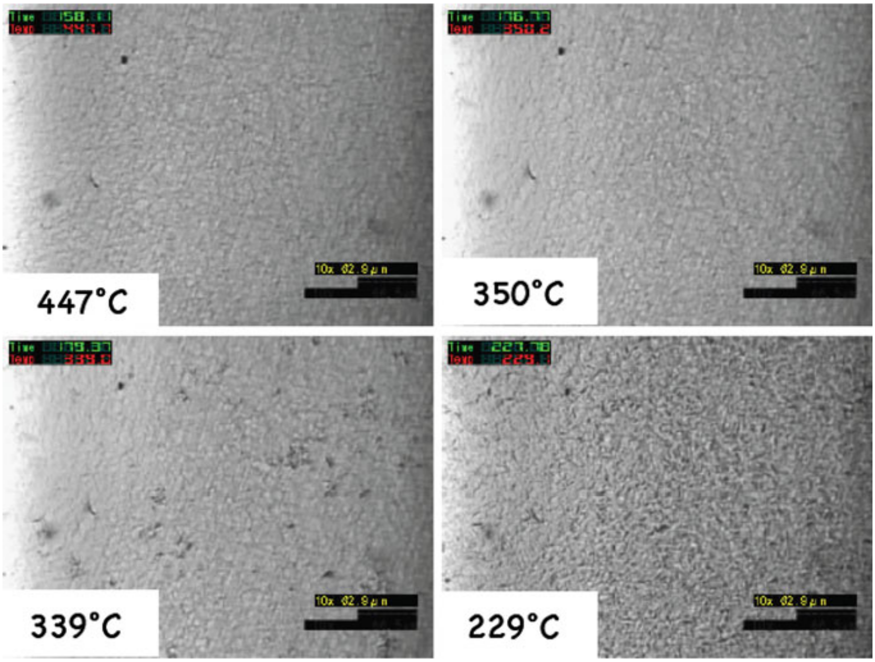

Fig. 10 LSCM images obtained during LTT-Tp950 experiment during cooling

transformation is seen near austenite/austenite grain boundaries. Initially, the transformation occurs very fast. From 370 to 362 °C (about 0.8 s), almost more than 50% austenite transforms to martensite. Figure 10 shows LSCM images during austenite to martensite transformation during cooling in the LTT-Tp950 sample. The observed martensite start temperature (M_s) for this condition is about 350 °C (Fig. 10b), approximately 20 °C lower than the LTT condition. From 350 to 339 °C, approximately 20 % transformation occurs (Fig. 10c). The initial transformation rate of LTT sample is also lower than HTT sample. Figure 11 shows LSCM images during the austenite to martensite transformation during cooling in the HTT-Tp1050 sample. At 412 °C, martensite is seen to form beneath the surface. When martensite forms beneath the surface, there is a contrast change in the image. The change is difficult to observe in the photos presented here, but it is obvious in the images taken during the experiment. Figure 12 shows LSCM images from the austenite to martensite transformation during cooling in the LTT-Tp1050 sample. Subsurface martensite formation is also observed at 404 °C.

LSCM experiments shows samples with peak temperatures of 950 °C yield a lower M_s. The lower M_s may be due to the smaller austenite grain size in Tp950. Yang and Bhadeshia studied the relationship between prior austenite grain size (PAGs) with M_s [41]. As the PAG increase, the M_s increases. Small PAGs sizes give large increases in the M_s. Since the PAGs of the Tp1050 conditions are larger than that of the Tp950 conditions, Tp1050 conditions are expected to have higher M_s.

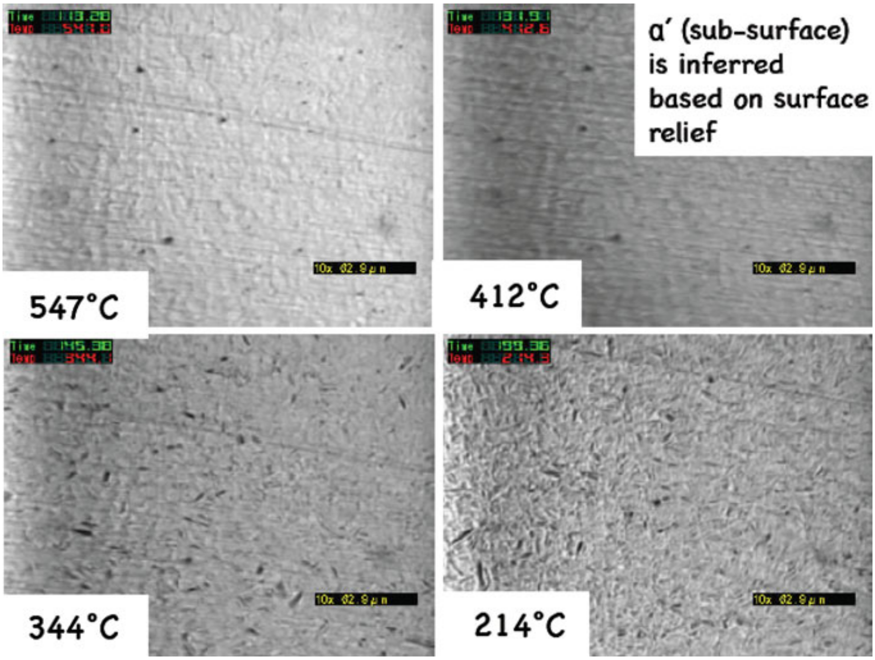

Fig. 11 LSCM images obtained during HTT-Tp1050 experiment during cooling

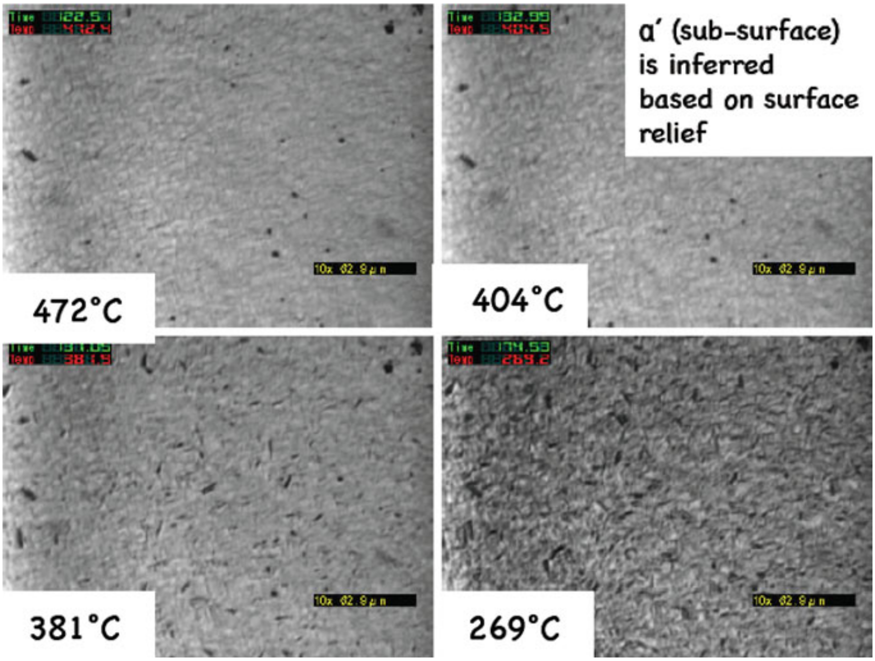

Fig. 12 LSCM images obtained during LTT-Tp1050 experiment during cooling

For the 1,050 °C peak temperature, martensite transformations beneath the surface can be seen before surface transformations are visible, which is not observed in the Tp950 condition. This may be caused by larger martensite sub-structure formation. Since the Tp1050 samples have a larger PAGs size, they also form larger sub-structures during transformation. Larger sub-structure beneath the surface is more observable.

3.7 Decomposition of Austenite in FGHAZ

It is quite conceivable that the changing in precipitate evolution may change the local compositions in the austenite close to the precipitate. For example, local Cr and C enrichment near the carbide-austenite interfaces may trigger the decomposition of austenite at a different temperature in comparison to the bulk austenite. The austenite to martensite transformation kinetics was extracted from TRXRD data. In order to get a comprehensive understanding of transformation kinetics, results from TRXRD are also compared with dilatometry measurement (Fig. 13). With the 1,050 °C peak temperature experiments (Fig. 13a), differences in martensite transformation kinetics between the HTT and LTT samples were minimal. For dilatometry measurements, small amounts of ferrite are observed in HTT sample before the martensite formation (as indicated by the arrow). The ferrite formation in the HTT sample could be, as mentioned earlier, due to dissolution of $M_{23}C_6$ resulting in enrichment of Cr at the carbide interface [42]. In TRXRD measurements, martensite forms at very high rates in the HTT samples at initial stage. This may also be due to the presence of precursor ferrite within the austenite matrix at the carbide interface on which the martensite may nucleate and grow [38]. Evidence of ferrite formation during cooling in the HTT condition has been published [38], however, it is not conclusive. Further characterization (such as TEM and atom probe tomography) is need for supporting this hypothesis. With a peak temperature of 950 °C (Fig. 13b), TRXRD and dilatometry data do not agree with each other. Nevertheless, both measurements confirm that the HTT has a higher M_s than that of the LTT samples. According to previous analysis, there are still about 0.9 vol% $M_{23}C_6$ in HTT condition while $M_{23}C_6$ in LTT is less than 0.2 vol%. As a result, austenite matrix in HTT sample may have less carbon than LTT austenite. This may rise the M_s temperature for HTT sample.

3.8 Overview of Microstructure Evolution and Implications

Figure 14 provides the schematic illustration of carbide evolution based on the above analyses for both the HTT and LTT conditions.

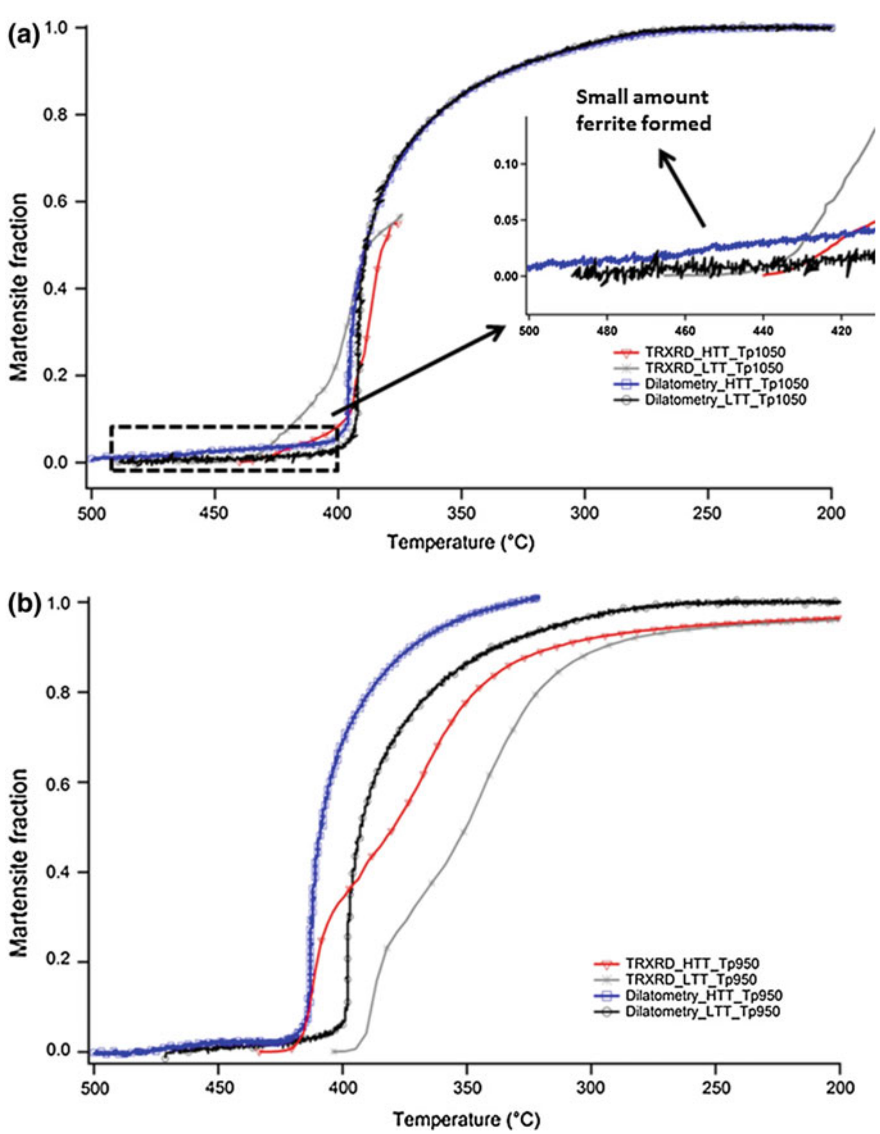

Fig. 13 Martensitic transformation kinetics measured by dilatometry and TRXRD **a** for simulated FGHAZ with peak temperature of 1,050 °C **b** for simulated FGHAZ with peak temperature of 950 °C; cooling rate is 10 °C/s for all experiments [38]

1. *Pre-weld Temper Condition*: In the HTT condition, $M_{23}C_6$ is in near equilibrium condition. $M_{23}C_6$ carbides are located along PAGBs, martensite block and packet boundaries. MX carbides are also present at martensite block boundaries and inside martensite blocks. In the LTT condition, the tempering is not complete; as a result, small $M_{23}C_6$ and MX are observed.

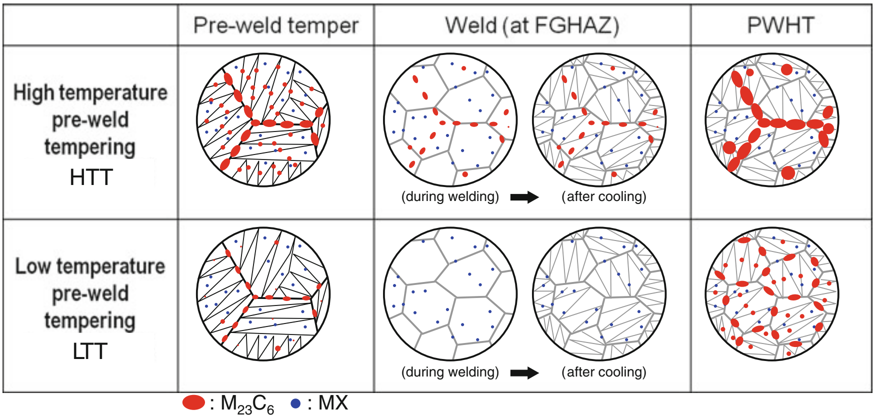

Fig. 14 Schematic showing microstructure evolutions during welding and PWHT for LTT and HTT conditions [38]

2. *During Welding in FGHAZ region*: On heating, austenite grains nucleate and grow. Since the peak temperature is low, the size of the austenite grains is expected to be small. Small $M_{23}C_6$ carbides completely dissolve into the austenite, while large $M_{23}C_6$ carbides are partially dissolved; MX precipitates remain the same. Undissolved $M_{23}C_6$ carbides are present in the martensite matrix after welding. In the LTT samples, on heating $M_{23}C_6$ are completely dissolved. Depending upon the extent of carbide dissolution, the fresh martensite that forms in the FGHAZ will be supersaturated with carbon with the source of the carbon coming from $M_{23}C_6$ dissolution. Based on the current data showing dissolution of carbides in the LTT condition, the carbon supersaturation is expect be higher in these samples compared to the HTT condition.
3. *Post-weld heat treatment*: When the HTT samples are subject to PWHT, the carbon in the martensite matrix will support the growth of undissolved $M_{23}C_6$ instead of forming new $M_{23}C_6$. For the same reason, the number of newly formed and MX will be lower. However, in the LTT samples, since there is no pre-existing $M_{23}C_6$, there will be competition between nucleation and growth of fresh $M_{23}C_6$ and MX phase. We assume that this small (but important) difference change in precipitate distribution leads to improving creep properties. Since the creep mechanism is not fully understood, the assumption cannot be proved completely.

Dudova et al. [42] showed $M_{23}C_6$ plays an important role in the stabilization of the martensite sub-structure. The pinning pressure of $M_{23}C_6$ carbides on the martensite sub-structure boundaries is four times larger than of MX carbides. As a result, it is crucial to have $M_{23}C_6$ on the boundaries to prevent boundary movement. In the FGHAZ of the LTT samples, almost all of the $M_{23}C_6$ were dissolved during welding. $M_{23}C_6$ would re-precipitate on PAGBs and martensite block boundaries when the sample was subjected to PWHT. Those $M_{23}C_6$ on the boundaries will pin the boundaries and prevent recrystallization. However, in the FGHAZ of the HTT samples, since $M_{23}C_6$ is partially dissolved and new austenite forms during welding, most undissolved $M_{23}C_6$ are not at new martensite block boundaries and PAGBs but remains in the pre-weld position. During PWHT, due to the growth of existing $M_{23}C_6$, newly formed $M_{23}C_6$ on boundaries will be significantly limited. As a result, creep strength of the HTT weldments is lower than that of the LTT weldments.

4 Conclusion

The current study shows pre-weld tempering temperature has a great impact on creep behavior of Grade 91 Cr-Mo steel welded structure. Since creep failure was observed in the FGHAZ, the microstructure evolution in this region was characterized using ex-situ and in situ techniques.

1. Creep life of low temperature pre-weld tempering (LTT) welded plate is 5 times higher than that of high temperature tempering (HTT) welded plate in stress to rupture test up to 2,500 h. These differences in creep properties are studied and correlated to precipitate distribution within the martensitic matrix and along prior austenite grain boundaries.
2. Dissolution kinetics of very small amount of carbides (as small as 0.2 vol%) during heat-affected zone thermal simulation were successfully tracked by using time-resolved high energy X-ray diffraction (TRXRD) employing synchrotron radiation.
3. TRXRD experiments show full dissolution of $M_{23}C_6$ in both the LTT and the HTT condition with a peak temperature of 1,050 °C. In contrast, with a peak temperature of 950 °C, partial ($\sim$50 %) dissolution of $M_{23}C_6$ was observed in the HTT condition and full dissolution of $M_{23}C_6$ in the LTT conditions.
4. During post-weld heat treatment, the undissolved $M_{23}C_6$ in the HTT condition continues to coarsen and inhibit the nucleation of new $M_{23}C_6$ precipitates. On the other hand, new $M_{23}C_6$ nucleates and grows in the LTT condition, which yields small $M_{23}C_6$. These differences in $M_{23}C_6$ size contributes to different creep life.

Acknowledgements This research was conducted as part of the Fossil Energy Advanced Research Materials Program, which is sponsored by Office of Fossil Energy, U.S. Department of Energy, National Energy Technology Laboratory. The synchrotron radiation experiments were performed at the BL46XU of SPring-8 as the Priority Research Proposal (priority filed: Industrial Application) with the approval of the Japan Synchrotron Radiation Research Institute (JASRI) (Proposal No. 2011B1968). The authors also greatly thank Thomas Muth for technically reviewing this manuscript.

References

1. http://www.sciencedaily.com/releases/2007/11/071114163448.htm
2. Abe F (2008) Sci Technol Adv Mater 9:013002
3. Shibli IA (2002) OMMI 1:1
4. Henry JF (2005) Combined Cycle Journal. First Quarter 8
5. www.ommi.co.uk/etd/ETD-EPRI-%20P91%20Failures.pdf
6. Berte FJ (2007) Combined Cycle Journal. Second Quarter 52
7. Francis JA, Mazur W, Bhadeshia HKDH (2006) Mater Sci Technol 22:1387
8. Abe F, Tabuchi M (2004) Mater Sci Technol 9:22
9. Hirata H, Ogawa K (2005) Weld Int 19:37
10. Hirata H, Ogawa K (2005) Weld Int 19:118
11. Albert SK, Matsui M, Watanabe T, Hongo H, Kubo K, Tabuchi M (2003) Int J Press Vessel Pipe 80:405
12. Li D, Shinozaki K, Kuroki H (2003) Mater Sci Technol 19:1253
13. Otoguro Y, Matsubara M, Itoh I, Nakazawa T (2000) Nucl Eng Des 196:51
14. Laha K, Chandravathi KS, Parameswaran P, Bhanu Sankara Rao K (2009) Metall Mater Trans A 40:386
15. Elmer JW, Wong J, Ressler T (2000) Scripta Mater 43:751
16. Babu SS, Elmer JW, Vitek JM, David SA (2002) Acta Mater 50:4763
17. Wong J, Ressler T, Elmer JW (2003) J Synchrotron Radiat 10:154
18. Babu SS, Specht ED, David SA, Karapetrova E, Zschack P, Peet M, Bhadeshia HKDH (2005) Metall Mater Trans A 36:3281
19. Stone HJ, Peet MJ, Bhadeshia HKDH, Withers PJ, Babu SS, Specht ED (2008) Proc R Soc A Math Phys Eng Sci 464:1009
20. Offerman SE, van Dijk NH, Sietsma J, Grigull S, Lauridsen EM, Margulies L, Poulsen HF, Rekveldt MT, van der Zwaag S (2002) Science 298:1003
21. Terasaki H, Komizo Y (2011) Scripta Mater 64:29
22. Yu X, Babu SS, Lippold J, Terasaki H, Komizo Y (2012) Metall Mater Trans A 43:1538
23. Yu X, Caron J, Babu SS, Lippold J, Isheim D, Seidma DN (2010) Acta Mater 58:5596
24. Rozenak P, Eliezer D (1986) J Mater Sci 21:3065
25. Lai JKL, Galbraith IF (1980) J Mater Sci 15:1297
26. Terao N, Sasmal B (1980) Metallography 13:117
27. Parish C, Watkins T, Rios O, Mackiewicz-Ludtka G, Ludtka G, Cavin O (2011) Microsc Microanal 17:410
28. Bénéteau A, Weisbecker P, Geandier G, Aeby-Gautier E, Appolaire B (2005) Mater Sci Eng A 393:63
29. Yonemura M, Osuki T, Hirata H, Ogawa K (2008) Metall Mater Trans A 39:113
30. Zhang XF, Terasaki H, Komizo Y (2012). Scripta Mater 67:201
31. Stevens RA, Lonsdale D (1985) J Mater Sci 20:3631
32. Mitchell DRG, Ball CJ (2001) Mater Charact 47:17
33. ASTM Specification A139-06 (2008). ASTM International, West Conshohocken
34. Broennimann C, Eikenberry EF, Henrich B, Horisberger R, Huelsen G, Pohl E, Schmitt B, Schulze-Briese C, Suzuki M, Tomizaki T, Toyokawa H, Wagner A (2006) J Synchrotron Radiat 13:120
35. Hammersley AP, Svensson SO, Hanfland M, Fitch AN, Hausermann D (1996) High Press Res 14:235
36. Hammersley AP (1997) Fit2D: an introduction and overview. ESRF, Grenoble
37. ASTM Specification A387 (2008). ASTM International, West Conshohocken
38. Yu X, Babu SS, Terasaki H, Komizo Y, Yamamoto Y, Santella ML (2013) Acta Mater 61:2194

39. Yu X (2012) Doctor of Philosophy dissertation. The Ohio State University, Columbus, Ohio
40. Cullity BD (1978) Elements of X-ray diffraction. Addison-Wesley Publishing Inc., Reading
41. Yong HS, Bhadeshia HKDH (2009) Scripta Mater 60:493
42. Dudova N, Plotnikova A, Molodov D, Belyakov A, Kaibyshev R (2012) Mater Sci Eng A 534:632

In Situ Synchrotron Diffraction Studies on Peak Broadening During Bainitic Transformation in a High Strength Quenched and Tempered Steel

R. K. Dutta, R. M. Huizenga, M. Amirthalingam, M. J. M. Hermans, H. Gao, A. King and I. M. Richardson

Abstract In situ synchrotron diffraction studies were carried out on a high strength (830 MPa yield stress) quench and tempered S690QL1 structural steel during continuous cooling under different mechanical loading conditions. The volume fraction and lattice parameters of co-existing phases were calculated from the time resolved 2D diffraction patterns. The effect of applied stress on the kinetics of austenite to bainite phase transformation and the transformation plasticity were analysed from the diffraction analysis. The results show that small tensile stresses applied at the transformation temperature do not change the kinetics of the phase. The absence of peak broadening in the bainitic ferrite reflections during phase transformation demonstrated that the plasticity was accommodated in austenite grains.

Keywords In situ synchrotron diffraction · Phase transformation kinetics · Thermo mechanical loading · Steel · Bainite · Transformation plasticity

---

R. K. Dutta · M. Amirthalingam · H. Gao
Materials Innovation Institute M2i, Mekelweg 2, 2628 CD Delft, The Netherlands

R. K. Dutta · R. M. Huizenga · M. Amirthalingam · M. J. M. Hermans ·
H. Gao · I. M. Richardson
Department of Materials Science and Engineering, Delft University of Technology,
Mekelweg 2, 2628 CD Delft, The Netherlands

A. King
Formerly with EuropeanEuropean Synchrotron Radiation Facility, 6 Rue Jules Horowitz,
BP 220, 38043 Grenoble Cedex, France

M. Amirthalingam (✉)
Metals Processing, Microstructure and Properties (MPMP), Department of Materials
Engineering, Delft University of Technology, 2628 CD Delft, The Netherlands
e-mail: m.amirthalingam@tudelft.nl

T. Kannengiesser et al. (eds.), *In-situ Studies with Photons, Neutrons and Electrons Scattering II*, DOI: 10.1007/978-3-319-06145-0_3,

1 Introduction

S690QL1 is a high strength quenched and tempered structural steel, with a minimum yield strength of 690 MPa and a notch toughness of at least 30 J at −60 °C [1]. These steels are increasingly used in welded constructions, such as machines for structural engineering, cranes and bridges. The microstructure of this steel typically consists of tempered martensite in a ferritic matrix, but upon welding, solid state phase transformations occur, accompanied by changes in specific volume. Details of the phase transformation kinetics can be derived from in situ synchrotron diffraction measurements [2–6].

During welding or while applying heat-treatments to steel, the transformations generate thermal and metallurgical stresses in the material [7]. Moreover, if the transformation is assisted by an externally applied stress, lower than the yield stress of the weaker phase [7], transformation plasticity occurs. For commercial exploitation and modelling purposes, it is necessary to thoroughly understand the phase transformation behaviour under mechanical loading. For precise modelling of the residual stress distribution during welding of such steels, it is essential to fully characterise the transformation temperatures and the nature and magnitude of the transformation strains. The nature and magnitude of transformation strains that manifest when austenite decomposes on cooling will depend strongly on the mechanism of transformation. It is known that when austenite transforms on cooling to bainite or martensite, the transformation is described as displacive [8], which involves the formation of plate-like microstructures through the coordinated movement of atoms. At the crystallographic level, both of these displacive transformations have an associated strain that comprises a large shear component (~ 0.22) as well as a smaller dilatational component (~ 0.03) [9]. Upon transformation, each austenite grain will produce some combination of the 24 possible crystallographic variants that may occur in the product phase. In the absence of macroscopic stresses, the crystallographic variants may form in an unbiased manner so that the large shear strains that occur at the crystallographic level can cancel each other when viewed on a macroscopic scale. If, however, the transformation takes place under the influence of macroscopic stresses (such as residual stresses), then the crystallographic variants that occur in the product phase may form in a manner that is influenced by the applied stresses, and this can lead to corresponding anisotropy in transformation strains [10–14]. Such transformation strains during bainitic transformations under tensile loading in S690QL1 steel was previously studied by Dutta et al. [15–17].

In the present study, in situ X-ray diffraction measurements were performed to study the transformation strains during the formation of bainite from austenite during cooling in S690QL1 steel on a microscopic scale. A modified transformation plasticity test was used within this work [15]. Time-temperature-load-dependent diffraction patterns were collected to study the transformation kinetics during heating and cooling cycles. The lattice parameters of bainitic ferrite during cooling were calculated under different loading conditions to study the thermal

Table 1 Chemical composition in wt% of S690QL1 steel

Elements	Wt%	Elements	Wt%
C	0.16	Mo	0.21
Si	0.20	N	0.0035
Mn	0.87	Nb	0.027
Ni	0.11	Ti	0.005
P	0.012	Cu	0.02
S	0.001	B	0.0021
Cr	0.33	Fe	Bal.

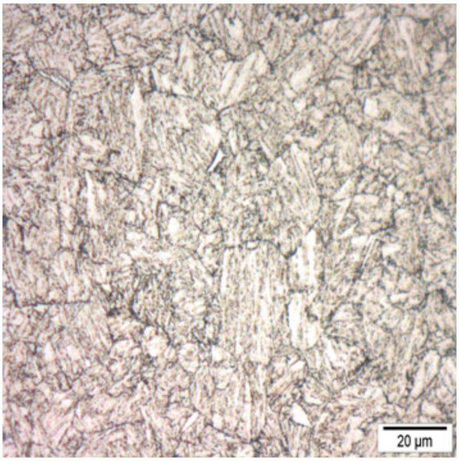

Fig. 1 Microstructure of S690QL1 base metal showing tempered martensite in a ferritic matrix

expansion behaviour. The transformation strains and the plastic accommodation between the co-existing phases during the phase transformation while cooling was calculated from the peak broadening of the planar reflections.

2 Experimental Procedure

Table 1 shows the chemical composition of the high strength quenched and tempered S690QL1 steel used in this study. The steel has a typical grain size of around 40 μm and the microstructure is shown in Fig. 1.

2.1 Sample Preparation

Small cuboidal blocks were cut from the as-received S690 steel plate which were homogenised at 950 °C for 48 h in a vacuum chamber. The blocks were then

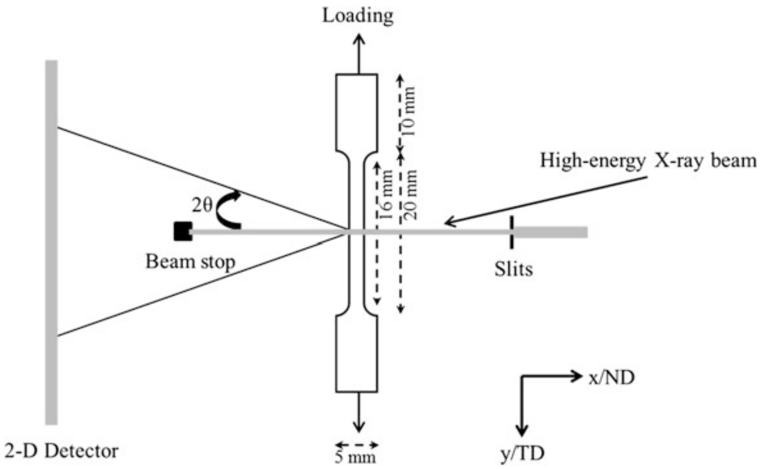

Fig. 2 Sketch of the experimental setup of in situ thermo-mechanical studies by synchrotron based high energy X-ray diffraction with sample dimensions. TD and ND correspond to the transverse and normal direction of the rolled sheet

annealed in a salt bath at 890 °C for 15 min in order to obtain a completely austenitic microstructure and quenched in cold water. This was followed by tempering in another salt bath at 635 °C for 20 min followed by air cooling. This heat treatment was given to achieve a tempered martensite microstructure for the tensile specimens, similar to the base metal microstructure of S690QL1 steels. Tensile specimens (Fig. 2) having a $1 \times 1\ \text{mm}^2$ square cross section and a gauge length of 16 mm were electro-discharge machined from the heat treated blocks. The loading axis was chosen parallel to the transverse direction (TD).

2.2 *In Situ Synchrotron Diffraction*

In situ synchrotron diffraction experiments were carried out at the ID11 beamline of the European Synchrotron Radiation Facility (ESRF) in Grenoble, France. To evaluate the transformation plasticity phenomenon, several tests were performed using an Instron/NPL electrothermal mechanical testing (ETMT, Fig. 3) machine. This comprised a 3 kN screw driven mechanical testing stage, with thermal cycles being achieved by Ohmic heating due to a direct current applied through the sample. Control was achieved by means of feedback from a type-R thermocouple discharge welded to the centre of the sample. Heating and cooling rates of up to 100 °C s^{-1} may be readily achieved, with superimposed mechanical loads using the ETMT.

The experimental arrangement is shown in Fig. 2. To limit the effects of temperature gradients due to the parabolic temperature distribution generated along the gauge length of the samples, slits positioned in the incident beam path were used to

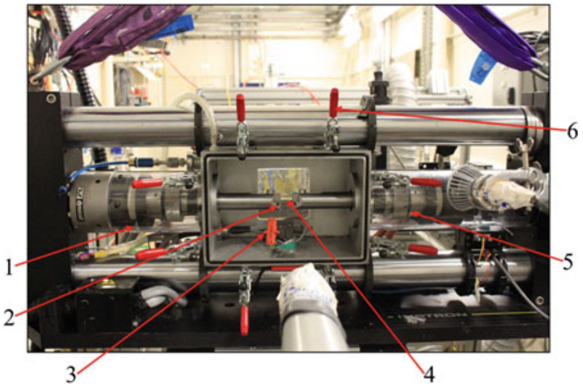

Fig. 3 Photograph of the ETMT machine on the ID11 beam line at the ESRF facility in Grenoble, France. The sample environmental chamber is photon transparent, so that X-rays can pass through the back of the chamber (from behind the machine *on the left*), and then pass through the sample gauge volume before reaching the detector which lies on the other side of the ETMT. (*1*) Load cell (*2*) Sample clamps (*3*) Thermocouple (*4*) Sample (*5*) Motor (*6*) Clamping system for the photon transparent lid

define a 677 (vertical) × 761 (horizontal) × 1,000 (normal) μm^3 diffraction gauge volume at the centre of the sample. A variation of no more than 3 °C is anticipated over such a volume at a temperature of 1,000 °C. To ensure correspondence between the temperature measured by the thermocouple and that of the gauge volume, the test machine was translated across the beam until the centre of the thermocouple bead could be identified from the observed diffraction patterns. The sample was then translated vertically such that the diffraction gauge volume was fully immersed in the sample, directly below the centre of the thermocouple bead, at a point at which no further diffraction signal was detected from the thermocouple bead. To prevent decarburisation during the thermal cycles, the ETMT chamber was continuously flushed with helium gas (flow rate of 1 l $\min^{-1}$).

A photon energy of 78.7 keV ($\lambda = 0.157649$ Å) was selected using a double Si {111} monochromator. Diffraction data were acquired with a 2-D CCD detector (FReLoN—fast readout low noise) camera system [18] having 2,048 × 2,048 pixels, each corresponding to 46.8 × 48.0 μm^2, mounted approximately 273 mm downstream of the sample with its centre aligned with the transmitted beam. The 2-D diffraction patterns were continuously recorded using an exposure time of 0.08 s. Including data recording time, a time resolution of 0.24 s was achieved and powder diffraction rings were therefore recorded at 0.24 s intervals. The instrument parameters (sample-detector distance, position of the straight-through beam and the tilt of the detector) of the 3-D X-ray diffraction microscope were determined using a CeO_2 calibrant (NIST SRM 674b), which was placed on each sample prior to the tests. Additionally, to eliminate the contribution from the background signal, dark exposures in the absence of the beam were subtracted from the acquired diffraction images.

Fig. 4 Thermal-mechanical histories applied during the transformation plasticity tests with a load of 0, 20, 30 and 40 N

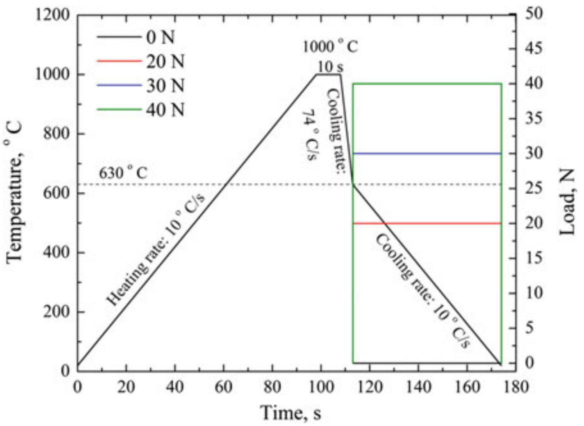

2.3 Thermal Mechanical Cycles

All the specimens were heated at a rate of 10 °C s^{-1} maintained at a temperature of 1,000 °C for 10 s, and then cooled to 630 °C at a constant rate of 74 °C s^{-1} followed by cooling to room temperature at a constant rate of 10 °C s^{-1}. Considering an exposure time of 0.08 s, such cooling rates lead to smearing of data over 5.92 °C (during cooling rate of 74 °C s^{-1}) and 0.8 °C (during cooling rate of 10 °C s^{-1}). In the transformation plasticity cycles, an axial force of 20, 30 and 40 N was applied to the test specimen during the cooling stage, at a temperature above B_S and released at the end of the test (Fig. 4). B_S is defined as the start temperature for the bainitic transformation and is the temperature at which 0.01 volume fraction of the bcc phase is formed. The axial force was initiated at 630 °C. This force was maintained during the entire transformation. In all cases, the specimen was subjected to the same thermal cycle, which leads to austenite formation during heating and the transformation of austenite into bainite during cooling.

2.4 Data Analysis

Processing of the raw diffraction images was performed using the Fit2D image processing software from the European Synchrotron Radiation Facility, including corrections for the spatial distortion and detector efficiency along with subtraction of the background signal [19]. Integration over the azimuthal angles at a constant scattering angle was performed to obtain the corresponding one-dimensional (1-D) diffraction patterns (Fig. 5).

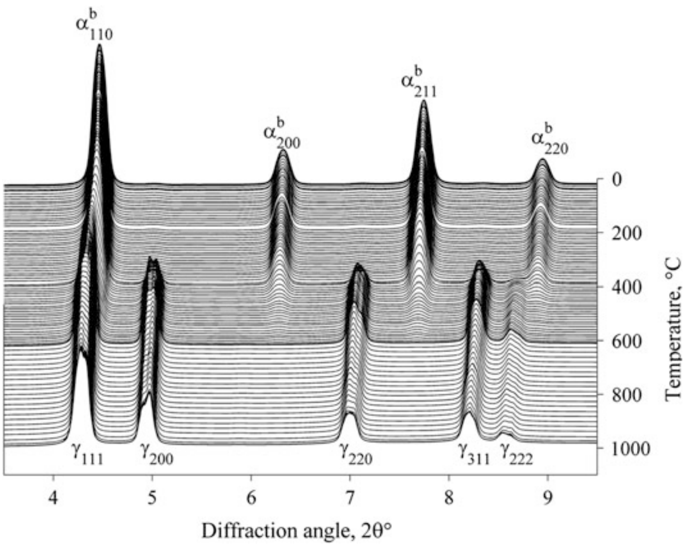

Fig. 5 Diffraction pattern showing the transformation of S690QL1 from austenite to bainitic ferrite during the cooling cycle with 0 N load

The evolution of the phase fractions and the lattice parameters during the applied thermal cycles can be calculated from the diffraction peak intensities and scattering angles [3], which leads to the transformation strains. Additionally, the strain variation during the thermal cycles under different loading will help to characterise the evolution and effect of elastic, plastic and thermal strain fields. Thermal expansion coefficient, transformation kinetics, planar strain development, and diffraction elastic moduli under the applied thermal-mechanical conditions can be further calculated from the lattice parameter and phase fraction evolution.

In order to calculate the above-mentioned material characteristics, the 1-D diffraction images need to be pre-processed in order to determine accurately the peak position and the integrated intensity of the diffraction spots. The global (grain-independent) parameters of the experiment, such as the wavelength of the X-ray beam, the sample-to-detector distance and the tilts of the detector and the centre of the beam on the detector, also need to be determined. The determination of the 1-D diffraction characteristics is described in Sect. "Characterisation of peaks", and the fitting of the global parameters were performed using the Fit2D image processing software.

A fit of individual reflections to a pseudo-Voigt profile function over the integrated azimuthal angles was used to find the peak positions, full width at half maximum, integral breadth and peak intensities from the 1-D diffraction pattern. The volume fraction of austenite was calculated from the integrated intensities and the experimental mean scattering angle ($2\theta_i$) of three austenite ($\gamma_{(200)}$, $\gamma_{(220)}$ and $\gamma_{(311)}$) and 2 ferrite ($\alpha_{(200)}$ and $\alpha_{(211)}$) rings using the following equation [20]:

$$f_\gamma = \frac{\frac{1}{N}\sum_{i=1}^{N}\left(\frac{I_{\gamma,i}}{R_{\gamma,i}}\right)}{\frac{1}{N}\sum_{i=1}^{N}\left(\frac{I_{\gamma,i}}{R_{\gamma,i}}\right) + \frac{1}{M}\sum_{i=1}^{M}\left(\frac{I_{\alpha,i}}{R_{\alpha,i}}\right)} \tag{1}$$

where N and M are the number of considered austenite and ferrite reflections, respectively. The index i refers to the {hkl} reflection of interest. R is the normalisation factor and is a function of incident photon flux, illuminated sample volume, sample transmission factor and theoretical diffraction intensity of the {hkl} diffractions. The mean lattice parameters were calculated from the experimental mean scattering angle ($2\theta_\mathrm{i}$) of three austenite ($\gamma_{(200)}$, $\gamma_{(220)}$ and $\gamma_{(311)}$) and 2 ferrite ($\alpha_{(200)}$ and $\alpha_{(211)}$) rings using the equation [20]:

$$a = \frac{1}{N}\sum_{i=1}^{N}\left(\frac{\lambda}{2}\right)\frac{\sqrt{h_i^2 + k_i^2 + l_i^2}}{\sin(\theta_i)} \tag{2}$$

where a is the lattice parameter, N is the number of {hkl} of austenite and ferrite considered and λ is the wavelength of the beam. The dislocation density in the bcc and fcc phase ρ was calculated from the integral breadth of the {200} and {211} bcc peaks and the {200}, {220} and {311} fcc peaks as proposed by [21, 22] using the following equation:

$$\Gamma_m^* = k^* g^* b^* \sqrt{\rho} \tag{3}$$

where b^* represents the length of the Burgers ($b^* = a\sqrt{3}/2$ for bcc and $b^* = a\sqrt{2}/2$ for fcc). g^* is the length of the reciprocal diffraction vector given by $\left(\sqrt{h_i^2 + k_i^2 + l_i^2}\right)/a$ and k^* is a dimensionless coefficient associated with the dislocation distribution, the orientation of dislocations with respect to the diffraction vector and is taken as 1 during the calculation. Γ_m^* is the integral breadth in the reciprocal space and is calculated from the real space breadth (Γ_m) through $\Gamma_m^* = (\Gamma_m \cos(\theta_i))/\lambda$ where Γ_m is the measured integral breadth in radians. The upper limit of lattice strain (e) is then estimated by:

$$e = \frac{\Gamma_m}{4\tan(\theta_i)} \tag{4}$$

2.5 Characterisation of Peaks

The 1-D diffraction images acquired after integrating over the azimuthal angles usually consist of a large number of pixels of background intensity, interspersed with a considerably smaller number of pixels of signal intensity (i.e. intensity higher than the background) on diffraction rings from the diffracting grains. For diffraction data with peak overlap, the determination of peak characteristics by fitting a diffraction image as a whole with multiple diffraction peaks can be computationally very intensive because (i) a significant number of pixels (background) are not of interest and thus need not be processed; and (ii) depending on the number of peaks in the diffraction image, the number of parameters to be fitted can be very large. In the methodology presented here, these issues are avoided as follows: (i) background pixels in the diffraction image are removed by applying a threshold to the diffraction image; (ii) the 1-D diffraction images are then identified into 'regions' (a smaller set than all the peaks present in the diffraction image); and (iii) estimates of the parameters to be fitted are obtained using information about the peaks in the 'regions'. The procedure for the determination of the characteristics of the peaks is then divided into two parts:

1. A peak-searching algorithm to carry out the thresholding operation, to determine the number of peaks in each set of 1-D diffraction pattern using the number of maxima and to determine the approximate characteristics of the peaks (integrated intensity and centre-of-mass position).
2. A peak-fitting routine to refine the peak characteristics by fitting the peak shape with a symmetric two-dimensional function.

2.5.1 Peak Searching

The diffraction images are first corrected for background (a combination of the dark current of the detector and the background from the sample), the flood of the detector (defined as the heterogeneity in the pixel response to photons) and the beam current. A linear background is subtracted from the whole profile. The peaks are then fitted separately (see Sect. Peak fitting). For this the 2θ range of the peak is determined by finding the local minima on either side of the theoretical peak position, which changes with temperature. A first estimate of the peak height is determined by finding the maximum in this 2θ range. A first estimate of the peak position is calculated from the centre of mass of the peak. The peak is then fitted in Matlab with the lsqnonlin function, using these parameters as initial approximation.

2.5.2 Peak Fitting

The program for fitting requires an input from peak searching. The algorithm works by fitting peaks in the 1-D diffraction image. The output of the program contains the refined parameters of the peaks along with the time, temperature and load information corresponding to each 1-D diffraction image. In the present framework, the results of peak searching are used only as initial values for fitting, and thus the accuracy of the values of the peak characteristics obtained from peak searching is not paramount.

Minimisation: The algorithm is designed to fit peaks using a one-dimensional pseudo-Voigt function, although a Gaussian or a Lorentzian function can also be used. The minimized function in the fitting program is

$$\sum\left(I-\left\{I_0+\sum_n A_n[\mu_n L_n+(1-\mu_n)]G_n\right\}\right) \tag{5}$$

i.e. the sum of the squared differences between the recorded intensity in the diffraction image and the intensity according to the parameters of the peaks obtained using the one dimensional pseudo-Voigt profile. I is the recorded intensity of the x_i^{th} pixel on the detector. L_n and G_n are the Lorentzian and Gaussian contributions per peak, respectively, given by

$$L_n=\frac{1}{1+\left(\frac{x_i-x_c^n}{w^n}\right)^2} \tag{6}$$

and

$$G_n=\exp\left[-0.5\left(\frac{x_i-x_c^n}{w^n}\right)^2\right] \tag{7}$$

The parameters that are refined are the background intensity I_0, the maximum intensity for each peak A_n, the Lorentz fraction μ, the coordinate position of the centre x_c^n and the width of the n^{th} peak w_c^n in each search region.

3 Results

3.1 *Phase Fraction and Lattice Parameter of Bainitic Ferrite During Cooling*

Microstructural examination shows that the specimens cooled at 10 °C s^{-1} under different loading conditions, primarily consists of bainite (see Fig. 6).

Figure 7a shows the evolution of the bainitic ferrite fraction as a function of temperature for the various thermal-mechanical cycles presented in Fig. 4. The change in bainitic ferrite fraction follows a typical reversed S-curve. It is observed that the loading has a significant effect on the fraction of bainitic ferrite formed. B_S for the steel are 620, 588, 555 and 494 °C under 0, 20, 30 and 40 N loads, respectively (Fig. 7a). The kinetics of the bainitic transformation (Fig. 7b) was not affected significantly under small mechanical loading. It can be seen that around B_S, the derivative df_{α^b}/dt starts to increase indicating that the decomposition of austenite has started. It reaches a maximum at 428, 420, 433 and 400 °C under 0, 20, 30 and 40 N loads respectively, confirming a faster decomposition at this

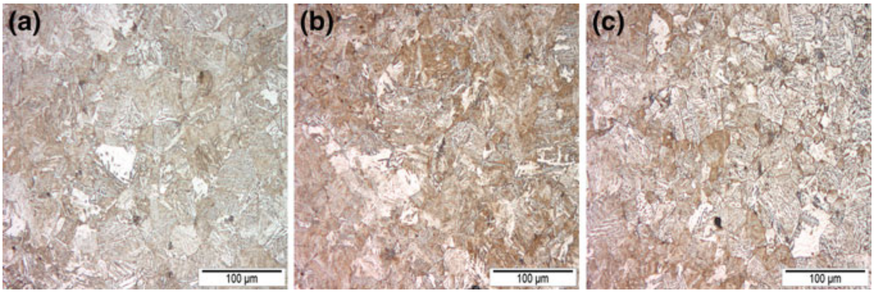

Fig. 6 Microstructure of S690QL1 after cooling under **a** 0 N, **b** 20 N and **c** 40 N loading conditions from Fig. 4 etched with 5 % Nital solution. Bainite appears brown in the microstructure

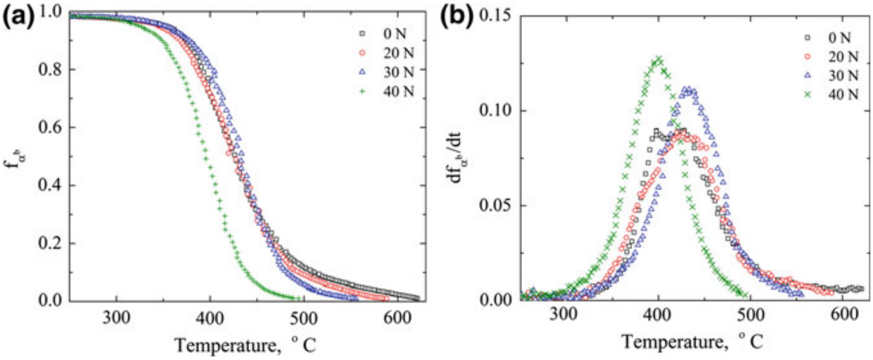

Fig. 7 Variation of the fraction of bainitic ferrite during cooling under different thermal–mechanical conditions. **b** Transformation kinetics of bainitic ferrite during cooling under different thermal–mechanical conditions

temperature. Around 300 °C, the derivative approaches 0 indicating the end of decomposition. It can also be seen that the different loading conditions do not affect the transformation kinetics significantly.

The lattice parameter of bainitic ferrite during cooling under different loading conditions is presented in Fig. 8.

The lattice parameters of bainitic ferrite are fitted to a polynomial of second order (Eq. 8). The resulting parameter values for the steel are given in Table 2 along with the temperature range within which they were fitted. The average linear thermal expansion coefficient of bainitic ferrite (under 0 N load) calculated from the parameter values in Table 2 within a temperature range of 40 and 276 °C is $1.422 \times 10^{-5}\ °\mathrm{C}^{-1}$ with a standard deviation of $0.004 \times 10^{-5}\ °\mathrm{C}^{-1}$.

$$a_i = a_i^0\left(1 + \alpha_i T + \beta_i T^2\right). \tag{8}$$

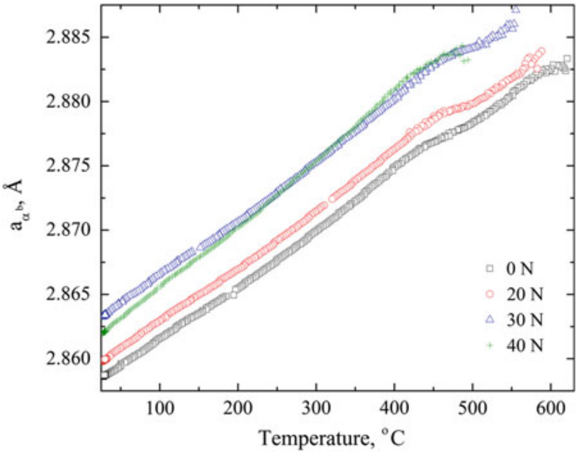

Fig. 8 Variation of the lattice parameter of bainitic ferrite during cooling under different thermal–mechanical conditions

Table 2 The fit results of the lattice parameter of bainitic ferrite as a function of temperature during the cooling cycle under different loading conditions. The lattice parameter of bainitic ferrite is fitted to a second order polynomial (Eq. 8). Data within the given temperature range were used in the fit. The upper limit of the temperature range is defined as the temperature when 98 % of bainitic ferrite is formed. B_S is defined as the temperature when 1 % of bainitic ferrite is formed

Load	B_S	Temperature range	$a_{\alpha^b}^{0,L}$	$\alpha_{\alpha^b}^{0,L}$	$\beta_{\alpha^b}^{0,L}$
N	°C	°C	Å	$\times 10^5$ °C^{-1}	$\times 10^9$ °C^{-2}
0	621	[20, 276]	2.8576 ± 0.0002	1.360 ± 0.003	1.98 ± 0.03
20	588	[20, 285]	2.8589 ± 0.0002	1.384 ± 0.001	2.03 ± 0.05
30	555	[20, 285]	2.8624 ± 0.0002	1.406 ± 0.004	2.65 ± 0.06
40	494	[20, 277]	2.8610 ± 0.0002	1.557 ± 0.003	3.37 ± 0.05

3.2 *Transformation Induced Plasticity*

Figures 9 and 10 shows the variation of the measured integral breadth in reciprocal space Γ_m^* and the full width at half maximum (FWHM) in reciprocal space $\Delta 2\theta^*$ (for the three austenite ($\gamma_{(200)}$, $\gamma_{(220)}$ and $\gamma_{(311)}$) and the two ferrite ($\alpha_{(200)}$ and $\alpha_{(211)}$) reflections under different loading conditions as a function of the transformed bainitic ferrite fraction f_{α^b}, respectively.

Figures 11 and 12 shows the variation of the density of dislocation (ρ) and the upper limit of lattice strain (e) for the three austenite ($\gamma_{(200)}$, $\gamma_{(220)}$ and $\gamma_{(311)}$) and the two ferrite ($\alpha_{(200)}$ and $\alpha_{(211)}$) reflections under different loading conditions as a function of the transformed bainitic ferrite fraction f_{α^b}, respectively, calculated from the analysis of the width of the diffraction peaks (see Sect. Data analysis, Figs. 9 and 10).

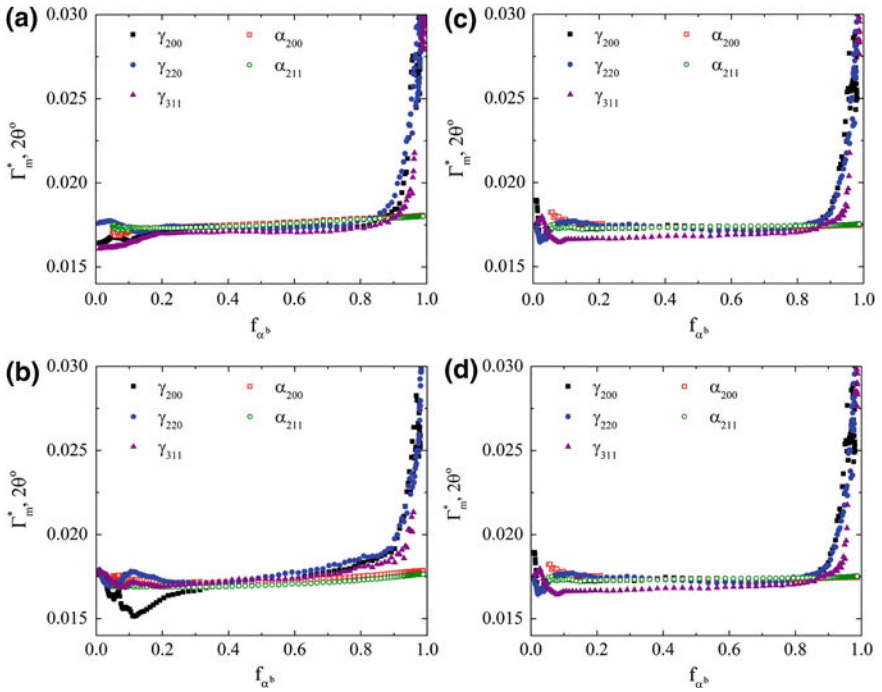

Fig. 9 Γ^*_m for the $\gamma_{(200)}$, $\gamma_{(220)}$, $\gamma_{(311)}$, $\alpha_{(200)}$ and $\alpha_{(211)}$ reflections under **a** 0 N, **b** 20 N, **c** 30 N and **d** 40 N loading conditions

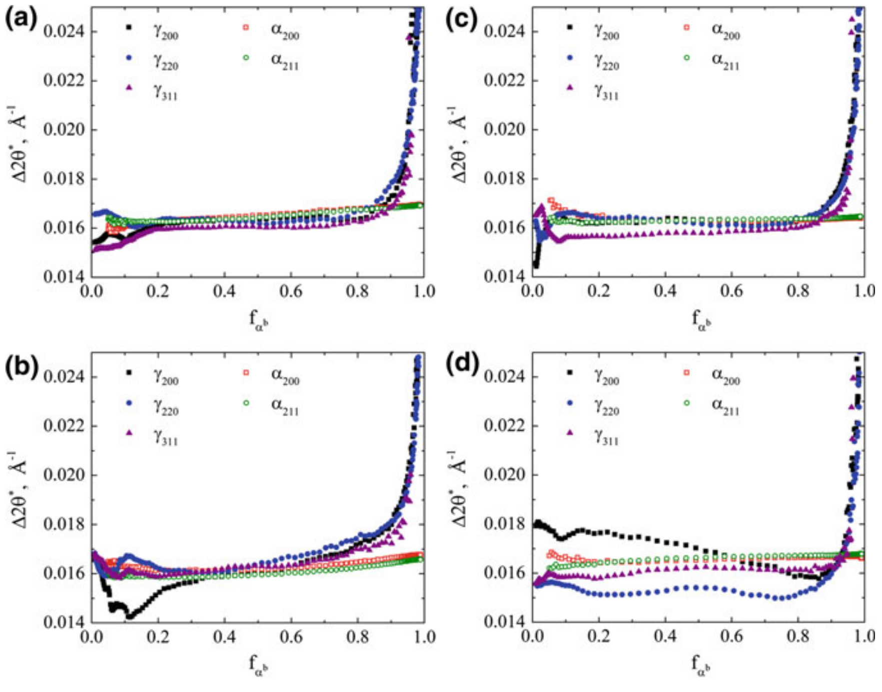

Fig. 10 $\Delta 2\theta^*$ for the $\gamma_{(200)}$, $\gamma_{(220)}$, $\gamma_{(311)}$, $\alpha_{(200)}$ and $\alpha_{(211)}$ reflections under **a** 0 N, **b** 20 N, **c** 30 N and **d** 40 N loading conditions

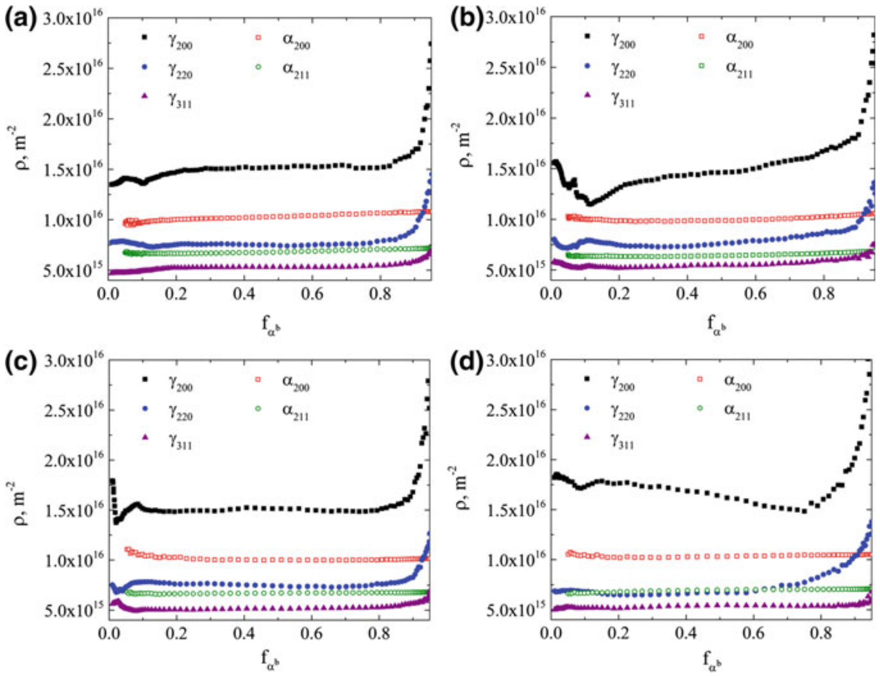

Fig. 11 Density of dislocation ρ for the $\gamma_{(200)}$, $\gamma_{(220)}$, $\gamma_{(311)}$, $\alpha_{(200)}$ and $\alpha_{(211)}$ reflections under **a** 0 N, **b** 20 N, **c** 30 N and **d** 40 N loading conditions

It is observed that the Γ_m and the FWHM of the bainitic ferrite reflections ($\alpha_{(200)}$ and $\alpha_{(211)}$) does not change significantly with the fraction of bainitic ferrite transformed (*i.e.* decreasing temperature) and/or increasing load. The absence of peak broadening in the bainitic ferrite reflections demonstrates the absence of the formation of new dislocation networks within the grain during the progress of phase transformation. Bainitic ferrite nucleates with a dislocation density which remains unchanged during the progress of phase transformation.

On the contrary, the peak broadening in the austenite reflections change considerably during cooling. Figure 13 shows the variation of the FWHM of the $\gamma_{(200)}$ reflection under 0 N loading condition. The peak broadening is divided into five zones named (a) to (e). In the absence of a macroscopic load, the $\Delta 2\theta^*$ of the austenite reflections first increases (peak at around 0.05 fraction of f_{α^b} in Fig. 13) marked by zone (a). This may be caused due to (1) coherent and semi-coherent strains arising from the nucleation of bainitic ferrite resulting in generation of defects and/or plasticity in the surrounding austenite matrix and (2) increase in the grain boundary area in austenite due to the nucleation of bainitic ferrite resulting in plasticity in the austenite matrix. Zone (a) is followed by zone (b) where the $\Delta 2\theta^*$ decreases (until 0.1 fraction of f_{α^b}). As the bainitic ferrite grows moderately in size, the grain boundary decreases resulting in stress relaxation in austenite in zone (b).

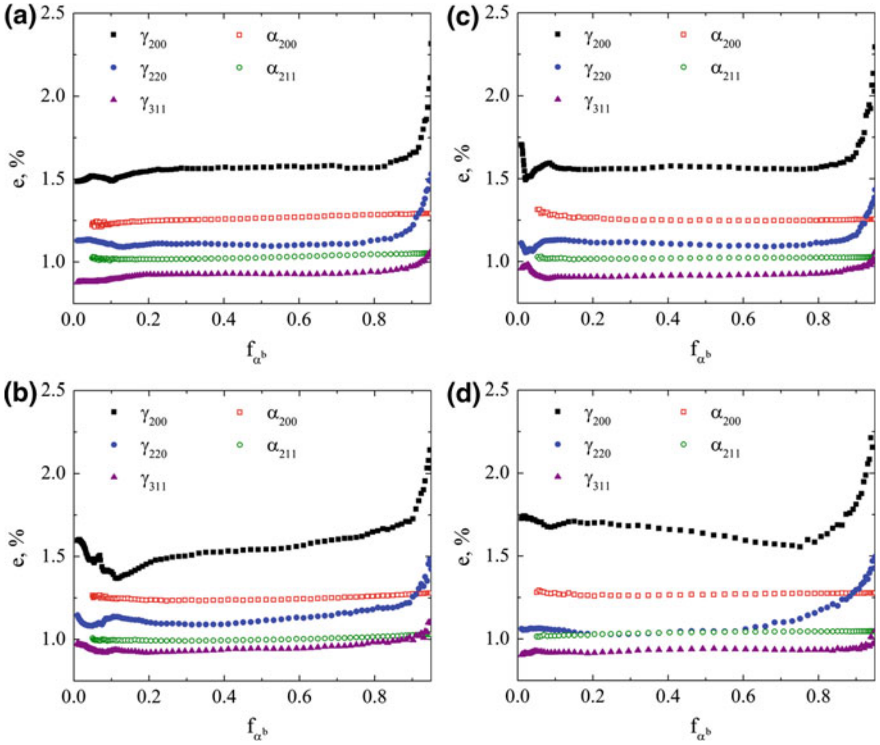

Fig. 12 Upper limit of lattice strain e for the $\gamma_{(200)}$, $\gamma_{(220)}$, $\gamma_{(311)}$, $\alpha_{(200)}$ and $\alpha_{(211)}$ reflections under **a** 0 N, **b** 20 N, **c** 30 N and **d** 40 N loading conditions

Fig. 13 $\Delta 2\theta^*$ for the $\gamma_{(200)}$, reflection under 0 N loading conditions

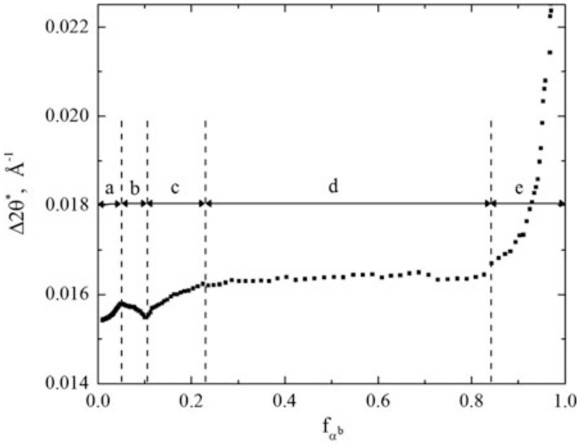

Zone (c) shows the increase in $\Delta 2\theta^*$ until 0.2 fraction of f_{α^b}. At higher undercooling at this stage, bainitic ferrite forms in a displacive manner resulting in increased plasticity in the austenite matrix. Also, during this stage there is rapid growth of bainitic ferrite since it is energetically favourable to grow the existing embryos rather than forming new ones. This stage also involves the coalescence of bainitic ferrite. The rapid growth of bainitic ferrite is a consequence of autocatalytic bainitic transformation [23] where the growth of bainitic ferrite in one grain is transferred to the surrounding austenite grains, causing them to transform. The $\gamma/\alpha^{\mathrm{b}}$ interface is strained extensively, and when the α^{b} grows above a critical size the coherency is lost, generating lattice strain in γ. The coherency loss causes dislocation pile-ups and misfit dislocations within γ grains to either become part of the new interface or escape resulting in an increase in $\varDelta 2\theta^{*}$. With transformation until the formation of 0.8 fraction f_{α^b}, represented by zone (d), the $\varDelta 2\theta^{*}$ remains unchanged demonstrating creation of no new dislocation networks and/or defects in austenite. Upon further transformation ($f_{\alpha^b} > 0.8$ fraction) represented by zone (e), the $\varDelta 2\theta^{*}$ increases, thereby increasing the strain as the plate shape of bainitic ferrite is reached, as more and more austenite is trapped between the bcc phases. Due to the difference in density of the bcc and the fcc phases, the austenite is compressed by the surrounding bainitic ferrite. This results in increased plasticity in austenite. Around 400 °C ($f_{\alpha^b} \approx 0.8$), $\varDelta 2\theta^{*}$ in austenite begins to increase indicating an increase in the plastic deformation in γ. The plastic deformation in austenite leads to the retardation of the kinetics of the displacive transformations. This effect is more pronounced in the presence of an external macroscopic load. For the $\gamma_{(200)}$ reflection, the rate of change of FWHM with respect to fraction of bainitic ferrite transformed decreases with increasing load. A similar trend is observed for the other austenite reflections. With increasing external load, upon nucleation of bainitic ferrite, the extent of plastic deformation in the austenite increases. The increased dislocation density in the austenite grains indicates that the plasticity was accommodated in austenite grains. This effect is most pronounced in the $\gamma_{(200)}$ reflection. With increasing external load, it is observed that the peak broadening in austenite during phase transformation to bainitic ferrite is reversible to some extent, demonstrating annihilation of dislocations in austenite. This continues until 80 % of the bainitic ferrite has formed. Further transformation proceeds with the creation of permanent dislocation networks.

4 Discussion

The lattice parameter of bainitic ferrite during cooling under different loading conditions is shown in Fig. 8. The average linear thermal expansion coefficient of bainitic ferrite (under 0 N load) calculated from the parameter values in Table 2 within a temperature range of 40 °C and 276 °C is 1.422×10^{-5} °C^{-1} with a standard deviation of 0.004×10^{-5} °C^{-1}.

The transformation of austenite during cooling was found to be fast in the initial stages of cooling (1,000–350 °C). Almost 98 % of austenite was transformed after cooling to ~276 °C within a cooling time of 34.7 s from 1,000 °C. The formation of bainite during cooling after the start of the bainitic transformation further enriches the untransformed austenite with carbon, resulting in increased stability of austenite [24, 25]. As a result, the transformation of austenite at lower temperatures was found to be slower. A small amount of austenite was left untransformed (1.8 %) at 50 °C.

It was observed that the kinetics of transformation was not affected significantly under small mechanical loading (see Fig. 7). The results are consistent with the work of Dutta et al. [15], Coret et al. [26] and Gautier et al. [27], who observed no noticeable differences in the case of small applied loads. Upon increasing the tensile stress, the free energy change associated with the transformation of austenite to bainite $\Delta G(\gamma \rightarrow \alpha^b)$ increases, thereby decreasing B_S, the bainite start temperature. However, the mechanical driving force ΔG_{Mech} is very small in comparison to the chemical driving force ΔG_{Chem} at the transformation temperatures [15]. Thus during welding, where similar conditions apply, the effect of small mechanical loads on the kinetics of bainitic transformation can be neglected.

It was observed that the peak broadening in the bainitic ferrite reflections remains unchanged during the entire transformation with/without external applied load. This demonstrates the absence of the formation of new dislocation network within the bainitic ferrite grains during the entire transformation. On the contrary, the peak broadening in the austenite reflections change considerably during cooling. Figure 13 shows the variation of the FWHM of the $\gamma_{(200)}$ reflection under 0 N loading condition. The peak broadening is divided into five zones named (a) to (e) and discussed in the previous section. After almost 80% of the transformation is complete in the absence of external load, the peak broadening in austenite grains increases sharply. This effect is more pronounced in the presence of an external macroscopic load. The transformation induced peak broadening in austenite demonstrates (1) that the plasticity was accommodated in austenite grains (2) that the crystallographic variants that occur in the bainitic ferrite may form in a manner that is influenced by the applied load, and this can lead to corresponding anisotropy in the transformation strain (3) that it leaves additional inhomogeneous strains in the austenite grain interiors upon phase transformation. The rate of change of peak broadening with respect to fraction of bainitic ferrite transformed decreases with increasing load. With increasing external load, it is observed that the peak broadening in austenite during phase transformation to bainitic ferrite is reversible to some extent, demonstrating annihilation of dislocations in austenite, probably due to the absorption of the dislocations in the austenite sub-grain/grain boundaries at lower temperatures. With further decrease in temperature ($f_{\alpha^b} > 80$ %) plasticity increases due to the restrictions in the atomic activity within the surrounding grain/sub-grain boundary. These effects are most pronounced in the $\gamma_{(200)}$ reflection. This is expected since in fcc and bcc Fe, the {200} planes are the planes with large intergranular strains [28].

5 Conclusion

The fast heating and cooling involved in the thermal-mechanical cycles demand characterisation techniques with high time-temperature resolution to study the phase transformation kinetics. The 2-D synchrotron diffraction patterns were recorded in situ every 0.3 s. This resolution was sufficient to calculate the fractions of the co-existing phases and the lattice parameters, in contrast to other conventional techniques [29, 30]. The rate of transformation is almost the same for all applied tensile stresses. The bainite transformation start temperature decreases with increasing applied tensile stress. The peak broadening in the bainitic ferrite reflections remains unchanged during the entire transformation with/without external applied load demonstrating the absence of the formation of new dislocation networks within the bainitic ferrite grains during the entire transformation. The peak broadening in the austenite grains change during the phase transformation and also with the application of external loads demonstrating that the plasticity was accommodated in austenite grains. The rate of change of peak broadening with respect to fraction of bainitic ferrite transformed decreases with increasing load. With increasing external load, it is observed that the peak broadening in austenite during phase transformation to bainitic ferrite is reversible to some extent, demonstrating annihilation of dislocation networks in austenite, probably due to the absorption of the dislocations in the austenite sub-grain/grain boundaries at lower temperatures. With further decrease in temperature (>80%) plasticity increases due to the restrictions in the atomic activity in the within the surrounding grain/sub-grain boundary.

Acknowledgments This research is carried out under Project No. M32.8.09333 in the framework of the Research Program of the Materials innovation institute M2i (www.m2i.nl). The authors thank Allseas Engineering bv for providing the financial support for the project.

References

1. Anonymous (2004) Hot rolled products of structural steels—Part 6: technical delivery conditions for flat products of high yield strength structural steels in the quenched and tempered condition. In: NEN-EN 10025-6
2. Blondé R, Jimenez-Melero E, Van Dijk NH et al (2011) Microstructural control of the austenite stability in low-alloyed TRIP steels. Solid State Phenom 172:196–201
3. Blondé R, Jimenez-Melero E, Zhao L et al (2012) High-energy X-ray diffraction study on the temperature-dependent mechanical stability of retained austenite in low-alloyed TRIP steels. Acta Mater 60:565–577
4. Offerman SE, Van Dijk NH, Sietsma J et al (2002) Grain nucleation and growth during phase transformations. Science 298:1003–1005
5. Offerman SE, Van Dijk NH, Sietsma J et al (2006) Phase transformations in steel studied by 3DXRD microscopy. Nucl Instrum Methods Phys Res, Sect B Beam Interact Mater Atoms 246:194–200

6. Stone HJ, Bhadeshia HKDH, Withers PJ (2008) In situ monitoring of weld transformations to control weld residual stresses, pp 393–398
7. Taleb L, Cavallo N, Waeckel F (2001) Experimental analysis of transformation plasticity. Int J Plast 17:1–20
8. Bhadeshia HKDH (2004) Developments in martensitic and bainitic steels: role of the shape deformation. Mater Sci Eng, A 378:34–39
9. Withers PJ, Bhadeshia HKDH (2001) Residual stress part 2—nature and origins. Mater Sci Technol 17:366–375
10. Babu SS, Bhadeshia HKDH (1992) Stress and the acicular ferrite transformation. Mater Sci Eng, A 156:1–9
11. Bhadeshia HKDH, David SA, Vitek JM et al (1991) Stress induced transformation to bainite in Fe–Cr–Mo–C pressure vessel steel. Mater Sci Technol 7:686–698
12. Matsuzaki A, Bhadeshia HKDH, Harada H (1994) Stress affected bainitic transformation in a FeCSiMn alloy. Acta Metall Mater 42:1081–1090
13. Shipway PH, Bhadeshia HKDH (1995) The effect of small stresses on the kinetics of the bainite transformation. Mater Sci Eng, A 201:143–149
14. Swallow E, Bhadeshia HKDH (1996) High resolution observations of displacements caused by bainitic transformation. Mater Sci Technol 12:121–125
15. Dutta RK, Amirthalingam M, Hermans MJM et al (2013) Kinetics of bainitic transformation and transformation plasticity in a high strength quenched and tempered structural steel. Mater Sci Eng, A 559:86–95
16. Dutta RK, Huizenga RM, Amirthalingam M et al (2013) Transformation-induced diffraction peak broadening during bainitic and martensitic transformations under small external loads in a quenched and tempered high strength steel. Metall Mater Trans A 44(9):4011–4014
17. Dutta RK, Huizenga RM, Amirthalingam M et al. (2013) In situ synchrotron diffraction studies on transformation strain development in a high strength quenched and tempered structural steel—part I. Bainitic transformation. Metallurgical and materials transactions A, doi: 10.1007/s11661-013-1992-4
18. Labiche JC, Mathon O, Pascarelli S et al (2007) Invited article: the fast readout low noise camera as a versatile x-ray detector for time resolved dispersive extended x-ray absorption fine structure and diffraction studies of dynamic problems in materials science, chemistry, and catalysis. Rev Sci Instrum 78:091301
19. Hammersley AP, Svensson SO, Hanfland M et al (1996) Two-dimensional detector software: from real detector to idealised image or two-theta scan. High Pressure Research 14:235–248
20. Vandijk N, Butt A, Zhao L et al (2005) Thermal stability of retained austenite in TRIP steels studied by synchrotron X-ray diffraction during cooling. Acta Mater 53:5439–5447
21. Tirumalasetty GK, Van Huis MA, Kwakernaak C et al (2012) Deformation-induced austenite grain rotation and transformation in TRIP-assisted steel. Acta Mater 60:1311–1321
22. Vermeulen AC, Delhez R, De Keijser TH et al (1995) Changes in the densities of dislocations on distinct slip systems during stress relaxation in thin aluminium layers: the interpretation of x-ray diffraction line broadening and line shift. J Appl Phys 77:5026
23. Van Bohemen SMC, Sietsma J (2008) Modeling of isothermal bainite formation based on the nucleation kinetics. Int J Mater Res 99:739–747
24. De Cooman BC (2004) Structure–properties relationship in TRIP steels containing carbide-free bainite. Curr Opin Solid State Mater Sci 8:285–303
25. Wang J, Van Der Zwaag S (2001) Stabilization mechanisms of retained austenite in transformation-induced plasticity steel. Metall Mater Trans A 32:1527–1539
26. Coret M, Calloch S, Combescure A (2002) Experimental study of the phase transformation plasticity of 16MND5 low carbon steel under multiaxial loading. Int J Plast 18:1707–1727
27. Gautier E, Denis S, Liebaut C et al (1994) Mechanical behaviour of Fe-C alloys during phase transformations. J De Phys. IV: JP 4:279–284
28. Reimers W (2008) Introduction to diffraction methods for internal stress analyses. In: Reimers W, Pyzalla AR, Schreyer A, Clemens H (eds) Neutrons and synchrotron radiation in engineering materials science. Wiley-VCH Verlag, GmbH & Co. KGaA, pp 113–135

29. Amirthalingam M, Hermans MJM, Huizenga RM et al (2010) In situ phase transformation studies on a transformation induced plasticity steel under simulated weld thermal cycles using synchrotron diffraction. In: Kannengiesser T, Babu SS, Komizo Y-i, Ramirez AJ (eds) In situ studies with photons, neutrons and electrons scattering. Springer, Berlin, pp 133–148
30. Amirthalingam M, Hermans MJM, Zhao L et al (2010) Quantitative analysis of microstructural constituents in welded transformation-induced-plasticity steels. Metall and Mat Trans A 41:431–439

In Situ Synchrotron Diffraction Studies on the Formation, Decomposition and Stabilisation of Austenite in TRIP Steels During Simulated Weld Thermal Cycles

Murugaiyan Amirthalingam, M. J. M. Hermans, R. M. Huizenga, S. E. Offerman, J. Sietsma and I. M. Richardson

Abstract In situ phase transformation behaviour of silicon and aluminium containing TRIP steels, while subjecting them to heat affected zone weld thermal cycles, have been studied. Time-temperature resolved 2D synchrotron diffraction patterns were recorded and used to calculate volume fractions and lattice parameters of the co-existing phases. Results show that during heating, the retained austenite starts to decompose once the temperature reaches 290 °C. The variation in the lattice parameters of austenite and ferrite reflect the nature of phase transformations that occur during cooling from austenitisation temperatures. The lattice parameter of austenite increases linearly up to 290 °C, followed by an increase in slope due to the formation of iron carbides. The combined effect of carbon concentration and thermal expansion causes scatter in the lattice parameter of austenite once the temperature reaches the inter-critical ($\alpha + \gamma$) region. It is also observed that a significant amount of austenite (6–7 %) was found to be retained at room temperature despite a high cooling rate (>20 °C s^{-1}). Even after cooling the samples to room temperature, the volume fraction of retained austenite decreased with time at room temperature.

Keywords TRIP steel · Retained austenite · Welding · HAZ · In situ synchrotron diffraction

---

M. Amirthalingam (✉) · M. J. M. Hermans · R. M. Huizenga ·
S. E. Offerman · J. Sietsma · I. M. Richardson
Metals Processing, Microstructure and Properties (MPMP), Department of Material Science and Engineering, Faculty of 3mE, Delft University of Technology, 2628 CD Delft, The Netherlands
e-mail: m.amirthalingam@tudelft.nl

T. Kannengiesser et al. (eds.), *In-situ Studies with Photons, Neutrons and Electrons Scattering II*, DOI: 10.1007/978-3-319-06145-0_4,

1 Introduction

The use of high-strength thinner-gauge TRIP steels in passenger cars leads to the possibility to reduce vehicle weight, resulting in reduced fuel consumption and emissions. Moreover, compared with conventional steels, the higher dynamic energy absorption during crash improves passenger safety and the crash-worthiness of the vehicle. The combination of properties of TRIP steels is mainly achieved by the stress induced transformation of meta-stable retained austenite (RA) in the microstructure. The meta-stable austenite is stabilised due to the addition of alloying elements such as silicon and aluminium, which suppress the formation of iron carbides during the bainitic transformation of austenite, thereby enriching the untransformed austenite with carbon. The enriched austenite is subsequently retained at room temperature.

Unfortunately, the higher alloying content of TRIP steels limits weldability, and the thermal cycle of a welding process destroys the carefully designed austenite-containing microstructure, resulting in inferior mechanical properties of the weld. Studies on the microstructural evolution during gas tungsten arc welding of TRIP steels have shown that complex inclusions form in the fusion zones of silicon- and aluminium-containing TRIP steels, and that stabilisation of ferrite occurs at the fusion boundaries of aluminium containing TRIP steels [1]. Quantitative analysis of retained austenite in the HAZ and fusion zones (FZ) of the welded TRIP steels using a magnetic saturation method revealed that a significant amount of austenite was retained after welding [2].

Babu et al. [3] previously observed fluctuations in the lattice parameter of austenite at high temperatures and studied the kinetics of austenite transformation to bainite using in situ time-resolved synchrotron X-ray diffraction in higher carbon (0.75 wt% C) containing steel samples. Babu et al. [4] also used the synchrotron X-ray diffraction to study the solidification of a Fe-C-Al-Mn steel in situ. During welding, synchrotron X-ray diffraction was also used to study the solidification and the nature of solid state transformation behaviour in steels in situ while applying weld thermal cycles [5, 6]. Synchrotron X-ray diffraction was previously used in TRIP steels to study the decomposition of retained austenite in aluminium containing TRIP steels during cooling to liquid nitrogen temperature [7] and to study the mechanical stability of retained austenite while subjecting the TRIP steels to mechanical loading [8].

During a typical thermal cycle in the heat affected zone (HAZ), in the heating stage the steel reaches peak temperatures close to the liquidus temperature near the fusion boundary and progressively lower temperatures with increasing distance from the boundary. The welded steel is cooled continuously from the peak temperature at various cooling rates. Due to the imposed thermal cycle, the austenite grain size, volume fraction and composition (especially carbon) vary in the HAZ. Moreover, the variation in the thermal expansion behaviour of co-existing phases induce stresses and thus affect the stability of retained austenite in welded TRIP steels.

In this work the decomposition, formation and transformation behaviour of austenite in TRIP steels are described based on the measurements made, while subjecting the steels to heat affected zone (HAZ) thermal cycles applied in situ in a synchrotron beam line using a unique high temperature furnace designed especially for this purpose. Time-temperature dependent diffraction patterns were collected to study the decomposition kinetics of retained austenite during initial heating, the kinetics of formation of austenite upon further heating and the transformation kinetics during subsequent cooling. The lattice parameters of austenite and co-existing phases during the applied thermal cycles were also calculated to study the thermal expansion behaviour of individual phases. This study also explores the stability of retained austenite with time after cooling to room temperature from austenitisation temperatures.

2 Experimental Procedure

In situ synchrotron diffraction studies were carried out on silicon (High-Si) and aluminium containing (High-Al) TRIP steel samples (Table 1) using a specially designed furnace in ID-11 of the European Synchrotron Radiation Facility (ESRF), Grenoble, France.

Cylindrical samples for in situ synchrotron diffraction were electro discharge machined (EDM) from the TRIP heat treated plates (inter-critical annealing at 800 °C for 1,800 s and isothermal bainitic holding at 400 °C for 60 s, see [2] for the heat treatment procedures) with the axis of the samples oriented in the rolling direction. The sample design and dimensions are shown in Fig. 1.

An S-type (Pt− Pt+ 10 wt% Rh) thermocouple was spot welded on the top of the sample and was used to control the temperature using Eurotherm™ temperature controller. A 3D-XRD furnace was used to apply the thermal cycle to the samples. A detailed description of this furnace design, its characteristics and performance is given elsewhere [9]. A monochromatic X-ray beam with an energy of 78.395 keV (wavelength 0.15815 Å), a horizontal beam size of 1.2 mm and a vertical size of 0.55 mm was used to illuminate the steel sample. The furnace was mounted on an x-y-z-ω table. Snap shots of 2D diffraction rings of austenite and ferrite were recorded in transmission geometry using a FreLon™ 2D area detector with an exposure time of 0.1 s. Including data recording time, a time resolution of 0.6 s was achieved and diffraction rings were therefore recorded at 0.6 s intervals. To study the effect of steel composition, both High-Si and High-Al samples were heated to 1,000 °C from room temperature in 60 s and held at that temperature for 70 s (Fig. 2). After holding, the sample was cooled to room temperature over a period of 60 s by simultaneously purging helium through the sample chamber and switching off the power supply. This procedure generated thermal cycle, which resemble the heating and cooling conditions experienced in the gas tungsten arc (GTA) welded TRIP steel [1], where at a point 4.2 mm from the weld centre line, a peak temperature of 1,000 °C was achieved.

Table 1 Composition of the steels under investigation

Elements, wt%	C	Mn	Si	Cr	Al	S	P	O
High-Si	0.19	1.67	1.47	0.21	0.04	0.005	0.080	0.002
High-Al	0.19	1.63	0.35	0.019	1.1	0.005	0.089	0.002

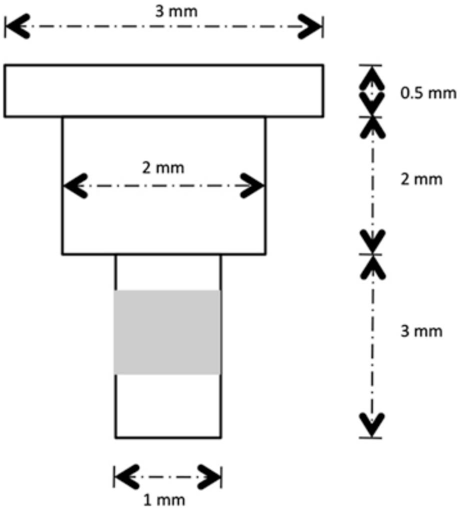

Fig. 1 Schematic illustration of sample geometry used for synchrotron X-ray diffraction. *The grey area* indicates the position of beam

In order to characterise the base metal, cylindrical samples with a diameter of 1 mm and a length of 3 mm were electro-discharge-machined (EDM) from the as heat treated TRIP steel plates with the cylindrical axis oriented in the rolling direction of the plate. These cut samples were then mounted and illuminated with a synchrotron X-ray beam with an energy of 71.64 keV (wavelength–0.1732 Å), but with different horizontal and vertical beam sizes (1.2 and 0.6 mm respectively) as used in the HAZ thermal cycle simulation measurements. During the illumination of the base metal samples, they were continuously rotated around the sample axis, starting from −90° to +90°. Measurements were integrated over successive angles of 10° using an exposure time of 6 s in each step.

The 2D diffraction patterns obtained from the base metal samples and during the thermal cycles were then corrected for detector background and spatial distortion. The sample to detector distance and the position of the beam centre were determined using a standard LaB_6 powder diffraction pattern. The volume fraction of austenite was calculated from the integrated intensities of two austenite $\gamma(200)$, $\gamma(220)$ and two ferrite $\alpha(200)$, $\alpha(211)$ peaks using the procedure explained elsewhere [7]. The lattice parameters of austenite and ferrite were calculated as a function of temperature from the mean scattering angles (2θ) of the austenite [$\gamma(200)$, $\gamma(220)$ and $\gamma(311)$] and ferrite rings [$\alpha(200)$, $\alpha(211)$ and $\alpha(220)$] using equation,

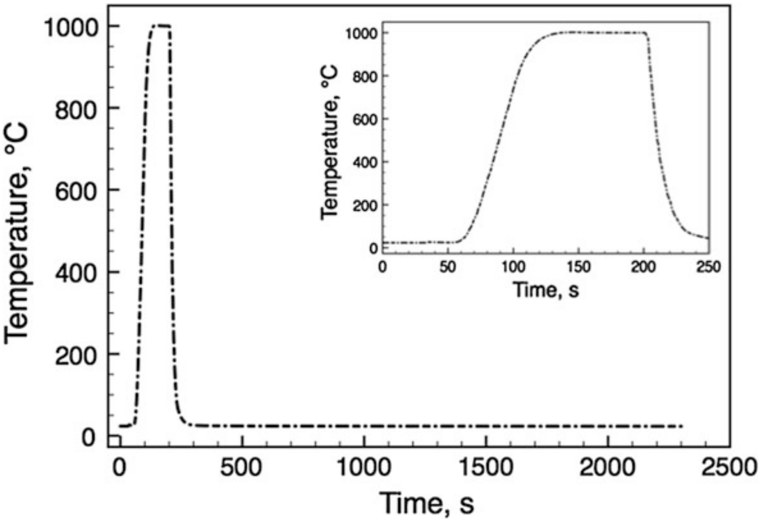

Fig. 2 Thermal cycle used in this study. *Insert* shows the same thermal cycle without room temperature holding part

$$a = \frac{1}{N}\sum_{i=1}^{N}\left(\frac{\lambda}{2}\right)\frac{\sqrt{h_i^2 + k_i^2 + l_i^2}}{\sin(\theta_i)} \tag{1}$$

where a is the lattice parameter, N is the number of {hkl} reflections of austenite and ferrite considered and λ is the wavelength of the X-ray beam.

3 Results

3.1 Characteristics of Base Metal Steel Sample

The phase transformation behaviour of the High-Si and High-Al steels used here differs significantly in terms of their transformation temperatures and the phase fields (Fig. 3). The Ae_3 temperature of the High-Si is about 885 °C, whereas High-Al steel shows a higher Ae3 temperature (1,036 °C).

Figure 4 shows the diffraction patterns of High-Si and High-Al base metal samples after the average radial integration of hkl reflections over 360°. Table 2 shows the lattice parameters of retained austenite and ferrite in the High-Si and High-Al base metal samples, calculated from the mean scattering angles ($2\theta_\mathrm{i}$ from Fig. 4) using Eq. 1. The carbon concentration of retained austenite was then estimated from the calculated lattice parameter a_γ using the relationship [7];

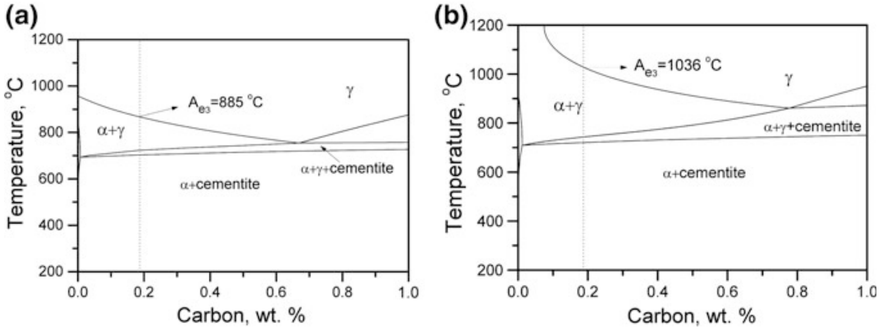

Fig. 3 Pseudo binary phase diagrams of TRIP steels under investigation, **a** High-Si and **b** High-Al, calculated using TCFE5 database of Thermocalc^{TM}

Table 2 Lattice parameters of retained austenite (a_γ) and ferrite (a_α) in Å, retained austenite content (γ_{RA}) and carbon in retained austenite (x_c) in heat treated TRIP steel base metal samples

Steel	a_γ (Å)	a_α (Å)	γ_{RA} %	x_c wt%
High-Si	3.60709	2.86450	10.9	1.2
High-Al	3.61791	2.87002	15.4	1.04

$$a_\gamma = 3.556 + 0.0453x_c + 0.00095x_{Mn} + 0.0056x_{Al} \tag{2}$$

where x_c, x_{Mn} and x_{Al} are carbon, manganese and aluminium in austenite (wt%). Assuming the bulk Mn and Al contents, the retained austenite carbon concentration (γ_c) in the High-Si and High-Al base metal samples was found to be 1.2 and 1.04 wt% respectively. The volume fraction of retained austenite present in the High-Al base metal sample was found to be higher (15.4 %) than in the High-Si steel sample which contained only 10.9 % although both steels underwent the same TRIP heat treatment (inter critical annealing at 800 °C and iso-thermal bainitic holding at 400 °C, Table 2). It can be seen from the pseudo binary phase diagram of High-Al steel (Fig. 3b) that the addition of aluminium in steels increases the equilibrium carbon content of austenite in the inter critical ($\alpha + \gamma$) region and extends the region to higher temperature. The equilibrium carbon content of austenite at 800 °C in High-Al steel is 0.77 wt% which is higher than that of the High-Si steel (0.43 wt%); as a result, the austenite is enriched in carbon to a greater extend during inter-critical holding at 800 °C in High-Al steels, resulting in higher austenite stabilisation during iso-thermal holding at 400 °C and subsequent cooling to room temperature.

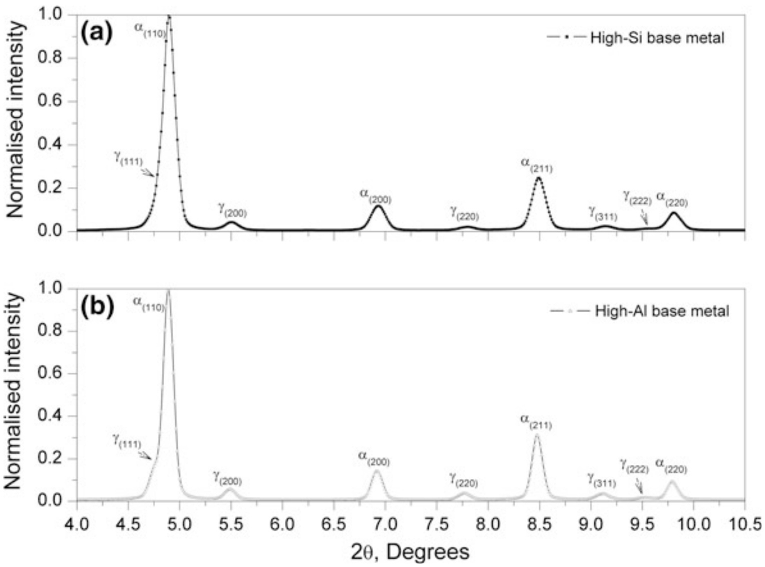

Fig. 4 The integrated diffracted rings of TRIP steel base metal samples showing different austenite and ferrite (hkl) reflections. **a** High-Si base metal and **b** High-Al base metal

3.2 In Situ Synchrotron Diffraction Analysis

The thermal cycle (Fig. 2) is divided into three parts to facilitate the data analysis of the in situ 2D diffraction patterns. The first comprises heating to 1,000 °C from room temperature in 60 s and holding at that temperature for 70 s. The second part of the thermal cycle involves cooling from 1,000 °C to room temperature ($\simeq$24 °C). During the third part of the thermal cycle, the sample is held at room temperature for 2,000 s. The diffraction patterns, which were recorded during this room temperature holding, were then analysed to study the stability of retained austenite upon holding. Figure 5 shows the recorded 2D diffraction patterns at 6 different temperatures while applying the thermal cycle using the furnace on a High-Al TRIP steel sample.

3.3 Transformation Kinetics During Hearting to 1,000 °C

Figure 6 shows the austenite content during heating of High-Al and High-Si base metal samples. The retained austenite present in the High-Si and High-Al base metal samples (15.4 and 10.3 % respectively) is stable up to 290 °C. Upon further heating, the austenite content decreased in the High-Al sample continuously up to 529 °C and reached a minimum level of 7.1 % during heating. In the case of the

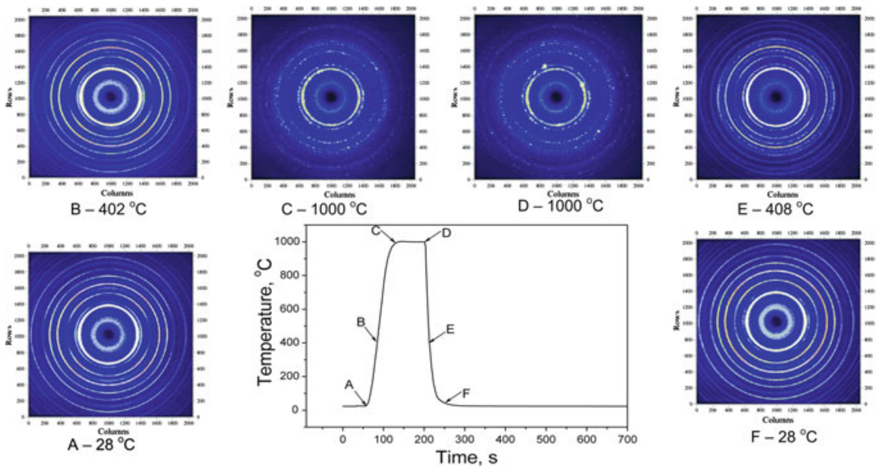

Fig. 5 Examples of the 2D diffraction patterns recorded while applying the thermal cycle on a high-al steel sample. The inner most diffuse ring in "A, B and F" patterns are due to diffuse scattering from the quartz capsule of the furnace. In "A, B and F" from inside towards outside, the patterns show the diffraction rings of $\gamma(111)$, $\alpha(110)$ [merged with $\gamma(111)$], $\gamma(200)$, $\alpha(200)$, $\gamma(220)$, $\alpha(211)$, $\gamma(311)$, $\gamma(222)$ and $\alpha(220)$ respectively. Patterns "C and D" show diffraction rings of austenite only

High-Si steel, decrease in retained austenite content to 3.6 % was evident up to 550 °C. A further increase in temperature resulted in an increase in austenite content, indicating that the samples reached the Ac_1 temperatures (529 and 551 °C for High-Al and High-Si steels respectively) for the current average heating rate (16 $°C\ s^{-1}$). A complete austenisation of the High-Si steel sample is evident when the temperature reached 802 °C. In the case of High-Al steel sample, the austenite fraction exceeds 99 % once the temperature reaches 1,000 °C.

3.4 Lattice Parameter Variation During Heating to 1,000 °C

The variation in the lattice parameters during heating reflected the decomposition and formation kinetics of austenite. Figure 7 shows the variation in the lattice parameter of austenite after subtracting the contribution from thermal expansion (the thermal expansion co-efficient of austenite was found to be 28.819×10^{-6} and $27.859 \times 10^{-6}\ °C^{-1}$ respectively for the High-Si and High-Al steels between 25 and 290 °C, where retained austenite was stable). The thus corrected lattice parameters of austenite in both steels show that upon the onset of decomposition of retained austenite, the lattice parameter increases, indicating enrichment of untransformed austenite with carbon. Upon further heating above the Ac_1 temperature, lattice parameter decreases continuously as the carbon content of the retained austenite decreases as dictated by the phase diagram.

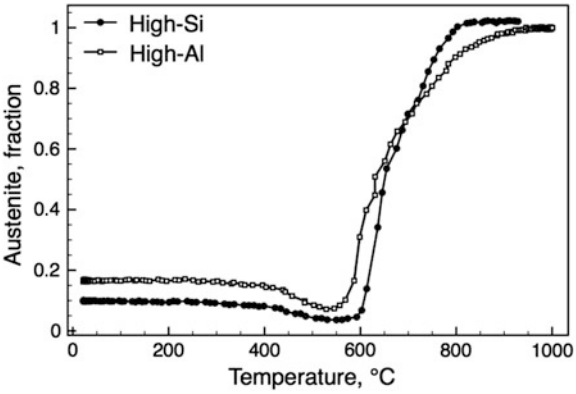

Fig. 6 Austenite fraction during heating to 1,000 °C

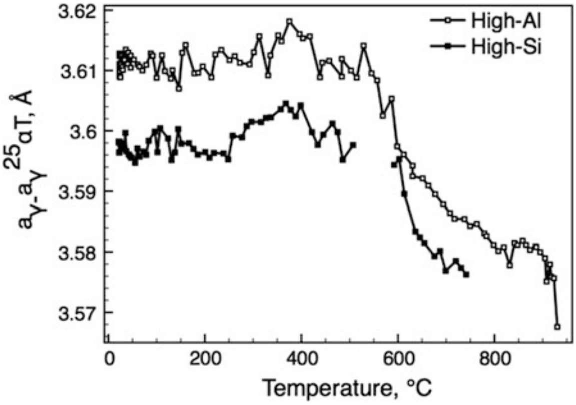

Fig. 7 Variation in the lattice parameter of austenite (a_γ) during heating, where α is linear thermal expansion coefficient of austenite, calculated from 24 to 290 °C

3.5 *Transformation Kinetics During Cooling from 1,000 °C*

In the High-Al steel sample, the transformation of austenite during cooling was observed to start at 974 °C, indicating the Ar_3 temperature of this steel (Fig. 8). In High-Si steel, the appearance of first ferrite rings was observed at 727 °C (Ar3 temperature). It can be seen from Fig. 8 that the transformation of austenite is initially sluggish in High-Si steel and even after reaching about 400 °C, 90 % of austenite is still untransformed, whereas in the High-Al steel, at 400 °C, the amount of austenite left is about 35 %.

3.6 *Lattice Parameter Variation During Cooling from 1,000 °C*

Unlike in heating, the lattice parameters of austenite and ferrite show several deviations from linearity while cooling from 1,000 °C. In High-Al steel samples,

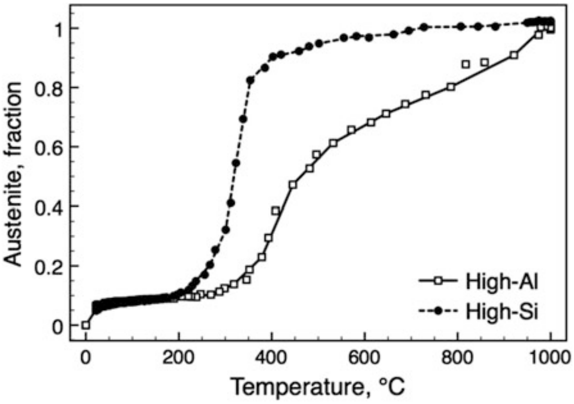

Fig. 8 Austenite fraction during cooling from 1,000 °C

the lattice parameter of austenite (a_γ) decrease linearly down to about 550 °C (Fig. 9a). A further decrease in temperature results in an increase of the (a_γ) while it remains constant from 495 to 405 °C. Upon further decreasing the temperature, the a_γ continues to decrease to 270 °C after which again an increase is observed. The changes in a_γ appear random once the temperature decreases below 200 °C until the sample reached 100 °C. The ferrite lattice parameter a_α showed a similar decrease until about 600 °C and a further decrease in temperature showed an increase in lattice parameter up to 530 °C (Fig. 9b). After this temperature, the a_α decreases linearly to 445 °C. The measured a_α remains constant till the next temperature step where the sample temperature reached to 405 °C. Upon further cooling, the a_α decreases linearly albeit in several steps, indicating a possible thermal non-equilibrium during cooling. The austenite and ferrite lattice parameters of High-Si steel showed a slightly different behaviour compared to the High-Al steel sample (Fig. 10).

Though the general variation pattern remains the same, compared to the High-Al steel, the temperatures at which changes in slopes are observed and the magnitude of the parameter shift differ for this steel. The austenite lattice parameter a_γ in High-Si steel decreases linearly until the temperature reaches about 500 °C. At the next measured temperature step, the sample cooled to 480 °C and an increase in lattice parameter is observed. The a_γ decreases further with cooling temperature and there are no distinctive shifting patterns observed henceforth. The ferrite lattice parameter a_α in this steel also initially decreases until the temperature reached 460 °C. Upon decreasing the temperature further to 400 °C, a steep increase in a_α is observed. a_α remains constant to 320 °C and at the next measured temperature step (310 °C) it starts to decrease. a_α decreases linearly from 310 to 205 °C. Upon further cooling, as in High-Al steel a_α decreases linearly albeit in several steps.

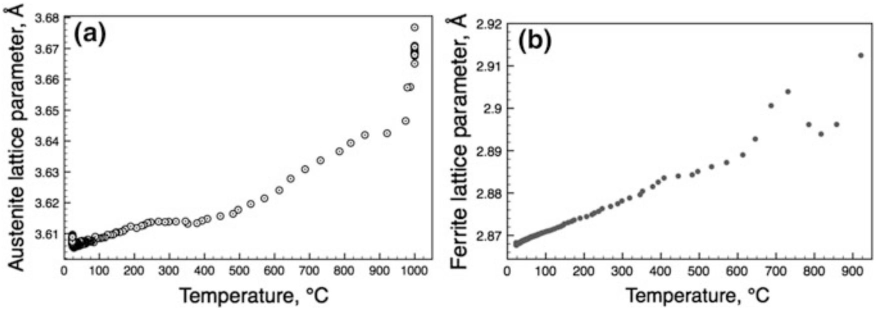

Fig. 9 Lattice parameter of austenite (**a**) and ferrite (**b**), during cooling from 1,000 °C in high-al steel

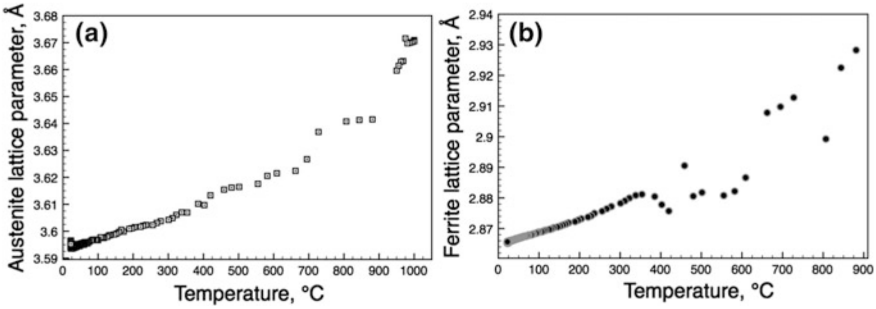

Fig. 10 Lattice parameter of austenite (**a**) and ferrite (**b**), during cooling from 1,000 °C in high-Si steel

3.7 *Transformation of Austenite at Room Temperature Holding*

After cooling from 1,000 °C, during holding at room temperature, the austenite content in both High-Si and High-Al samples was found to decrease continuously. Figure 11 shows the austenite fraction during cooling, in the range of 40 °C to room temperature. In both cases, about 1.5 % of austenite decomposes while holding at room temperature (23 °C) for 2,000 s.

4 Discussions

The fast heating and cooling involved in a typical weld thermal cycle, demands characterisation techniques with high time-temperature resolution to study the phase transformation kinetics, such as synchrotron X-ray diffraction. A previous

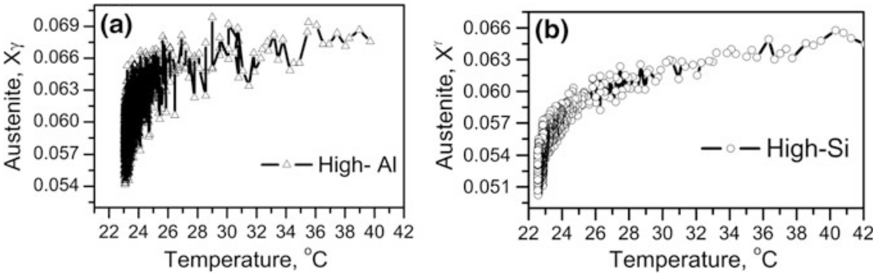

Fig. 11 Variation of austenite in room temperature after cooling from 1,000 °C (with an error in fraction of ±0.005)

synchrotron X-ray diffraction study on the welded TRIP plates indicated a significant amount of austenite retained in the heat affected and fusion zones [10]. The retained austenite fraction in the heat affected zone varied along the welded plate depending on the peak temperatures reached during the weld thermal cycle [10]. The thermal cycle examined in the in situ diffraction studies simulated the heating and cooling cycles of a GTA weld thermal cycle. The peak temperature reached at a point 4.2 mm from weld centre line and 1.1 mm from the fusion boundary was about 1,000 °C [1, 10]. The 2D synchrotron diffraction patterns were recorded in situ every 0.6 s and temperature recordings were carried out at 0.1 s intervals, while applying the thermal cycle. This resolution was found to be sufficient to calculate the fractions of co-existing phases and their lattice parameters with a better time-temperature resolution than conventional X-ray diffraction, dilatometry or magnetic saturation techniques [2]. Apart from the mechanical properties, the generation of residual stresses which determine the buckling and bending distortion of welded plates are greatly influenced by the kinetics of phase transformations [11]. In TRIP steels where transformation plasticity controls the required mechanical properties, it is also important to study the thermal expansion/contraction behaviour of co-existing phases along with the phase transformation kinetics [12, 13]. Moreover, the measurement of lattice parameters and thereby the thermal expansion co-efficients of individual phases and quantification of microstructural phases as a function of temperature yields essential fundamental material data for the physical simulation of material behaviour during a weld thermal cycle [14].

4.1 Effect of Composition

The amount of retained austenite present in the base metal High-Al and High-Si samples is 10.3 and 15.4 % respectively. During heating to 1,000 °C, the retained austenite present in both steels is stable only up to 290 °C. Above this temperature, the retained austenite fraction starts to decrease slowly, but when the temperature reaches 450 °C, the decomposition rate is as high as 2.5 % s^{-1} in High-Al steel. In a typical weld thermal cycle [1], a peak temperature of 290 °C is achieved at about 9 mm from the weld centre line. Thus in comparison to conventional auto-body steels, welded TRIP steels ought to have an extended heat affected zone where the base metal microstructure is altered by the weld thermal cycle. In the conventional auto-body steels, a heat affected zone weld thermal cycle where the peak temperature reaches about 300 °C seldom significantly alters the microstructure. However, in TRIP steels, decomposition of the retained austenite at low temperatures ($\geq$290 °C) eventually leads to inhomogeneous distribution of microstructure in a larger area.

The decomposition of retained austenite during heating of a Fe-0.18C-1.8Si-1.5Mn (wt%) TRIP steel was also observed earlier but that study reported that the decomposition started from 340 °C compared to 290 °C in the present study [15]. In the present study, the High-Si steel contains 0.4 wt% less silicon and 0.01 wt% higher carbon than the steel used in the previous study (Table 1). Silicon is known suppress the precipitation of iron carbides from the austenite and as a result, despite containing slightly higher carbon, the decomposition of austenite is evident at a slightly lower temperature in the present study. Moreover, the ability of aluminium to suppress iron carbide formation is also reported to be lower than that of silicon due to its slightly higher solubility in the iron carbides. The decomposition of retained austenite was also confirmed by the thermo-magnetic measurements carried out on a TRIP steel sample where the formation of ferro-magnetic ferrite and transient carbides were observed while heating above 295 °C [2]. During this synchrotron diffraction study, there were no diffraction spot/patterns of transient carbides observed possibly due to their limited size, volume and distribution. However, the formation of the transient carbides during the decomposition of retained austenite cannot be neglected as thermo-magnetic measurements and previous studies reported the possibilities of their formation [2, 16]. The austenite content in High-Al and High-Si samples reached a minimum when the temperatures reached 528 and 550 °C, respectively. Thus, during welding, when a heat affected zone thermal cycle reaches peak temperatures of about 525 to 550 °C, a minimum of austenite can be expected to be retained in the microstructure for this steels.

The increase in austenite fractions were observed during heating when the temperature reached 529 and 551 °C respectively in High-Al and High-Si samples. These Ac_1 temperatures are far less than the equilibrium Ae_1 temperatures (719 and 702 °C respectively in High-Al and High-Si steels) calculated from a thermodynamic database TCFE5 using Thermocalc^{TM} (Fig. 3). This is possibly due to the existence of untransformed austenite nuclei and no barrier for growth of austenite with an increase in temperature. Moreover, the nucleation of new austenite at low temperatures can also occur due to the chemical heterogeneity and high carbon containing regions (where prior retained austenite grains were present) in the microstructure. The retained austenite contained 1.2 and 1.04 wt% carbon respectively in High-Si and High-Al samples (Table 2). This high carbon containing retained austenite also becomes more enriched with carbon due to the formation of ferrite during its decomposition. The high carbon containing sites are known to facilitate the nucleation of austenite during heating [17]. As a result, nucleation of austenite may start earlier than the equilibrium austenite nucleation temperature. Based on the peak temperature in the heat affected zone, several areas in this zone locally enter into the inter-critical ($\alpha + \gamma$) region at lower temperatures (from 529 and 551 °C respectively, in High-Al and High-Si steels).

The decomposition kinetics of retained austenite during heating is also reflected in its lattice parameter. The lattice parameter of the austenite was found to increase linearly with temperature up to a temperature of 290 °C during heating. The linear thermal expansion co-efficient of austenite (a_γ) during heating was determined to be 27.859×10^{-6} °C^{-1}, which is a more realistic value than the previously reported value of 24.53×10^{-6} °C^{-1}, extrapolated from a high temperature (1,273 °C) [18]. Once the decomposition of retained austenite starts above 290 °C, the lattice parameter increases initially due to the possible enrichment of carbon in the remaining austenite. This deviation in linearity was also reported by Choi et al. [15] while heating a retained austenite containing steel. A further heating above 290 °C, the lattice parameter of austenite in both steels decreases at 430 °C possibly due to the depletion of carbon from the austenite matrix, driven by the formation of iron carbides.

During cooling, the formation of new ferrite rings was observed once the sample temperature decreased below Ar_1 and thereafter the lattice parameter of austenite (Figs. 9a, 10a) was found to be affected by the combined effects of carbon in austenite (given by the lever rule) and thermal contraction. In High-Si steel, the transformation of austenite is sluggish down to 420 °C and upon cooling below this temperature a rapid transformation of austenite is observed (Fig. 8). This kind of transformation behaviour has already been reported for austenite transformation to martensite during continuous cooling from a fully austenitic temperature, as in the present case [19]. However, in High-Al steel, the austenite transformation is continuous from 1,000 to 480 °C, indicating that the transformation is predominantly ferritic and bainitic. The calculated martensitic start (M_s) temperatures for High-Si and High-Al steels are 407 and 409 °C respectively (using the well known Andrews' equation) [20]. The faster transformation rates of austenite were observed during cooling below 420 and 480 °C in High-Si and High-Al steels respectively, which can be due to the onset of martensite transformation. However, the start temperatures do not correlate with the calculated Ms temperature from Andrews' equation because the equation suggested by Andrews does not include the effect of silicon and aluminium. The amount of austenite left untransformed after cooling to 40 °C is 6.5 and 7 % in High-Si and High-Al steel.

Although the kinetics of austenite transformation during cooling showed a possibility for martensite transformation in High-Si steel, in High-Al steel it does not explicitly show the nature of transformation such as formation of bainite or martensite from austenite. However, the variation in the lattice parameter with cooling temperature does show some qualitative information about the possible bainite and martensitic transformations in both steels. During cooling, the ferrite lattice parameter in High-Al steel showed two distinctive shifts in linearity, one at

613 °C and another at around 450 °C (Fig. 9b). The calculated bainitic start (B_s) for the High-Al steel is 630 °C (using Steven and Haynes empirical equation) [21]. This equation however does not include the effect of aluminium and silicon when calculating B_s. The change in the slope of the ferrite parameter at 613 °C most likely correlated to the formation of bainite from austenite during cooling. In the High-Si steel, the ferrite lattice parameter showed a distinctive jump at from 460 to 310 °C, possibly due to the formation of martensite from austenite (Fig. 10b). There are no distinctive changes in the slope of the ferrite lattice parameter at around 600 to 650 °C which can otherwise be correlated to bainite formation from austenite in this High-Si steel.

The results indicate that the variation of lattice parameters of ferrite and austenite with cooling are not linear with temperature and the effect composition and the transformation stresses are reflected when the transformation of austenite proceeds. Thus, while simulating the microstructural evolution during welding and calculating the residual stresses, it is important to incorporate the temperature dependant lattice parameters of individual phases to reflect the effect of composition and transformation stress associated with the phase transformation.

4.2 Transformation of Austenite at Room Temperature

In situ synchrotron diffraction analysis in TRIP steel samples showed that a significant amount of austenite is left untransformed at room temperature after cooling from the austenisation temperatures (Fig. 11a). The High-Al steel contained 6.6 % of retained austenite at 25 °C after cooling from 1,000 °C. After holding at room temperature (23–24 °C) for 2,110 s, the retained austenite content reduced to 5.4 %. Thus about 1.2 % of retained austenite left in the sample transformed at room temperature holding. Similarly, in the High-Si steel, the retained austenite content reduced from 6.3 to 5.1 % after cooling from 1,000 °C (Fig. 11b). This is quite significant in TRIP steels where the mechanical properties are severely affected by the retained austenite content in the microstructure.

It was already reported that the properties of welded TRIP steels are not stable with time after the welding during commercial production [22]. Zhao et al. [23] showed a time dependent strain development under constant stress due to the decomposition of retained austenite to martensite in TRIP steels. It is possible to explain the decomposition of retained austenite at room temperature due to the build up of stored energy from the transformation stresses under fast cooling rates. Further experimental evidence should be sought to consolidate this finding, for example, a detailed analysis on the variation in peak widths during room temperature holding. The mechanism driving room temperature phase transformation is, as yet, unknown. The measured data shows instability in the volume fraction, which is significantly greater than the measurement error. It is likely that the energy driving the transformation is derived from stress relaxation, possibly initiated by hydrogen diffusion, although to date, no experimental evidence is available to support such a speculation.

5 Conclusions

The decomposition, formation and transformation kinetics of austenite in TRIP steel samples was studied by in situ synchrotron X-ray diffraction. Using a purpose built high temperature furnace, with a high time-temperature resolution, phase transformation kinetics were studied under conditions simulating weld thermal cycle at points in the heat affected zone where peak temperature reaches 1,000 °C. From this study, the following specific conclusions can be derived;

1. The retained austenite present in the base metal is stable up to 290 °C during heating. At the onset of retained austenite decomposition, an increase in the lattice parameter of austenite occurs due to the partitioning of carbon from the new ferrite formed from the decomposing austenite. Conversely, the ferrite lattice parameter shows a linear variation during heating up to Ac_1. When the heating temperature reaches the inter-critical region, the combined effect of thermal expansion and carbon partitioning between the co-existing α and γ phases, results in non-linear variation of the lattice parameters.
2. Significant amounts of austenite (5–7 %) are retained in High-Si and High-Al TRIP steel samples after continuous cooling from 1,000 °C to room temperature in a simulated thermal cycle.
3. The rate of transformation of austenite and the variation of lattice parameters during cooling from the austenisation temperatures shows that for similar cooling rates, the High-Si exhibit a nearly complete martensitic transformation whereas in the High-Al steel, both bainitic and martensitic transformations occur.
4. The austenite content was found to decrease with time during holding at room temperature, change of 1.2 % over a period of 2,110 s. The reduction in austenite content may explain the time dependant changes in mechanical properties observed in welded TRIP steels.

Acknowledgements This research was carried out under the project number MC8.04188 in the framework of the Research Program of the Materials innovation institute M2i (www.m2i.nl), the former Netherlands Institute for Metals Research. The authors gratefully acknowledge the welding research group, Research and Development, Corus, IJmuiden for their interest in this project.

References

1. Amirthalingam M, Hermans MJM, Richardson IM (2009) Microstructural evolution during welding of transformation induced plasticity steels—inclusion and elemental partitioning analysis. Metall Mater Trans A 40A:901–909
2. Amirthalingam M, Hermans MJM, Zhao L, Richardson IM (2010) Quantitative analysis of microstructural constituents in welded transformation induced plasticity steels. Metall Mater Trans A 41A:431–439
3. Babu SS, Specht ED, David SA, Karapetrova E, Zschack S, Peet M, Bhadesia HKDH (2005) In-situ observations of lattice parameter fluctuations in austenite and transformation to bainite. Metall Mater Trans A 36A:3281–3289
4. Babu SS, Elmer JW, Vitek JM, David SA (2002) Time-resolved X-ray diffraction investigation of primary weld solidification in Fe-C-Al-Mn steel welds. Acta Mater 50:4763–4781
5. Palmer TA, Elmer JW, Wong J (2002) In situ observation of ferrite—austenite transformation in duplex stainless steel weldments using synchrotron radiation. Sci Technol Weld Joining 7(3):159–171
6. Elmer JW, Palmer TA, Zhang W, DebRoy T (2008) Time resolved X-ray diffraction observations of phase transformations in transient arc welds. Sci Technol Weld Joining 13(3):265–277
7. van Dijk NH, Butt AM, Zhao L, Sietsma J, Offerman SE, Wright JP, van der Zwaag S (2005) Thermal stability of retained austenite in TRIP steels studied by synchrotron X-ray diffraction during cooling. Acta Mater 53:5439–5447
8. Kruijver SO, Zhao L, Sietsma J, Offerman SE, van Dijk NH, Lauridsen EM, Margulies L, Griguli S, Poulsen HF, van der Zwaag S (2003) In situ observations on the mechanical stability of austenite in TRIP-steel. J Phys IV France 104:499–502
9. Sharma H, Wattjes AC, Amirthalingam M, Zuidwijk T, Geerlofs N, Offerman SE (2009) Multipurpose furnace for in situ studies of polycrystalline materials using synchrotron radiation. Rev Scientific Instrum 80:123301-1–123301-7
10. Amirthalingam M, Hermans MJM, Huizenga RM, Offerman SE, Richardson IM, Gundlach C (2012) Synchrotron diffraction analysis of retained austenite in welded transformation induced plasticity (TRIP) steels. Sci Technol Weld Joining 17(2):146–154
11. Withers PJ, Bhadesia HKDH (2001) Overview: residual stress part 2—Nature and origin. Mater Sci Technol 366–375
12. Murakawa H (1997) Theoretical prediction of residual stresses in welded structures. Weld Int 11(8):599–604
13. Ferro P, Porzner H, Tiziani1 A, Bonollo F (2006) The influence of phase transformations on residual stresses induced by the welding process—3D and 2D numerical models. Model Simul Mater Sci Eng 14:117–136
14. van der Aa EM, Thiessen RG, Amirthalingam M, Hermans MJM, Sietsma J, Richardson IM (2007) Influence of a trailing heat sink on the microstructure and stress distribution in DP600 welds. Math Model Weld Phenom 8:387–407
15. Choi SD, Kim HS, Je JH, Park SH (2002) Annealing behaviour of retained austenite in low carbon steel: real time synchrotron X-ray scattering study. J Mater Sci Lett 21:353–355
16. Jha BK, Mishra NS (1999) Microstructural evolution during tempering of a multiphase steel containing retained austenite. Mater Sci Eng A A263:42–55
17. Savran VI, Offerman SE, Sietsma J (2010) Austenite nucleation and growth observed on the level of individual grains by three-dimensional X-ray diffraction microscopy. Metall Mater Trans A 41A:583–591
18. Onink M, Brakrnan CM, Tichelaar FD, Mittemeijer EJ, van der Zwaag S (1993) The lattice parameters of austenite and ferrite in Fe-C alloys as a function of carbon concentration and temperature. Scr Metall Mater 29:1011–1016
19. Reed-Hill RE, Abbaschian R (1994) Physical metallurgy principles, 3rd edn. PWS Publishing company, Boston

20. Andrews KW (1965) Empirical formulas for the calculation of some transformation temperatures. J Iron Steel Inst 203:721–727
21. Steven W, Haynes AJ (1956) The temperature of formation of martensite and bainite in low alloy steels. J Iron steel Inst 183:349–359
22. Corus R&D and T (2005–2009) Ageing in welded TRIP steels. Internal communication
23. Zhao L, Mainfroy B, Janssen M, Bakker A, Sietsma J (2006) Time-dependent strain development under constant stress in TRIP steels. Scripta Mater 55

In situ Observation of Lattice-Strain and Solid State Transformation in Low Temperature Transformation Weld Metal by Synchrotron X-rays

Shuoyuan Zhang and Yu-ichi Komizo

Abstract Martensite is a microconstituent that is indispensable for the strengthening of steels. In recent years, welding residual stresses reduction due to introducing volume expansion of martensitic low temperature transformation (LTT), has received more attention. In the present study, we quantificationally discussed the relationship between the lattice-strain deformation and the martensitic transformation of LTT, by in situ observation technique, using synchrotron X-rays. Martensitic transformation of 14Cr5Ni was observed by hybrid in situ observation technique. Accommodation mechanism of the transformation strain in martensitic transformation process was quantificationally discussed by the diffraction analysis of austenite phase.

Keywords Martensitic transformation · Austenite · Synchrotron X-ray · Lattice-strain · In situ observation

1 Introduction

Martensite is a microconstituent that is indispensable for the strengthening of steels. In recent years, welding residual stresses reduction due to introducing volume expansion of martensitic low temperature transformation (LTT), has received more attention. The interplay between a solid state phase transformation and a strain deformation was analyzed in detail through qualitative study with

---

S. Zhang (✉)
Research Center for Neutron Science and Technology, Comprehensive Research Organization for Science and Society, CROSS TOKAI, Bldg. IQBRC A402,
162-1 Shirakata, Tokai-mura, Ibaraki-ken 319-1106, Japan
e-mail: s_zhang@cross.or.jp

Y. Komizo
Joining and Welding Research Institute, Osaka University, 11-1, Mihogaoka,
Ibaraki, Osaka 567-0047, Japan

T. Kannengiesser et al. (eds.), *In-situ Studies with Photons, Neutrons and Electrons Scattering II*, DOI: 10.1007/978-3-319-06145-0_5,

in situ observation [1, 2]. The martensite transformation strain should be relaxed by plastic deformation of the austenite and/or martensite resulting in plastic accommodation (PA). In the present study, we quantificationally discussed the relationship between the lattice-strain deformation and the martensitic transformation of LTT by in situ observation technique using synchrotron X-rays.

2 Experimental

The chemical composition of the sample (14Cr5Ni) are 0.047C, 0.32Si, 0.86Mn, 0.007P, 0.003S, 14.2Cr, 5.2Ni (wt%), and the balance iron. The sample 14Cr5Ni was austenitized by heating to 1,000 °C for 50 s, and then quenching to room temperature. The martensitic transformation of sample 14Cr5Ni during cooling process was observed by using hybrid in situ observation system [2]. In situ synchrotron diffraction experiments were performed in undulator beam line (BL46XU) at the third generation synchrotron radiation source, Spring-8 (Hyogo, Japan). The undulator beam was mono-chromatized by a double Si (111) crystal, and photon energy was 30 keV. The incident beam size was used to 0.5 (H) × 0.5 (W) mm^2. The incidence angle was chosen to be 5° between the incident beam and the sample surface. With this setting irradiated area was 2.5 mm^2 on the sample surface. The samples were prepared with the dimension of 5 mm in diameter.

The hybrid in situ observation system consists of High-Temperature Laser Scanning Confocal Microscopy (HLSCM) system and Time-Resolved X-ray Diffraction (TRXRD) system [2–4]. In this research, a time resolution was 0.2 s. Diffraction data were acquired with a PILATUS 2M detector [5]. The sample-detector distance was 470 mm, determined with the software Fit2D, using reference powder sample (LaB_6).

3 Results and Discussion

Figure 1 shows the in situ observation of morphological development and the diffraction patterns for sample 14Cr5Ni during continuous cooling process. Figure 1a shows the γ-austenite reflections as a spot pattern, because the austenite grain sizes become larger (>100 μm, measured by HLSCM). As shown in Fig. 1b, α-martensitic reflection appeared at 184 °C, which corresponds to the beginning of transformation from γ-austenite to α-martensite. Subsequently, as the transformation proceeded, γ-austenite reflections disappear, as shown in Fig. 1d. This means the transformation from γ-austenite to α-martensite were fully completed.

From careful analysis of the data, the relationship between the temperature and the full width half maximum (FWHM) of {311}γ spot diffraction in both the radial angles(2θ) and the azimuth(φ) were obtained as shown in Fig. 2. That was derived

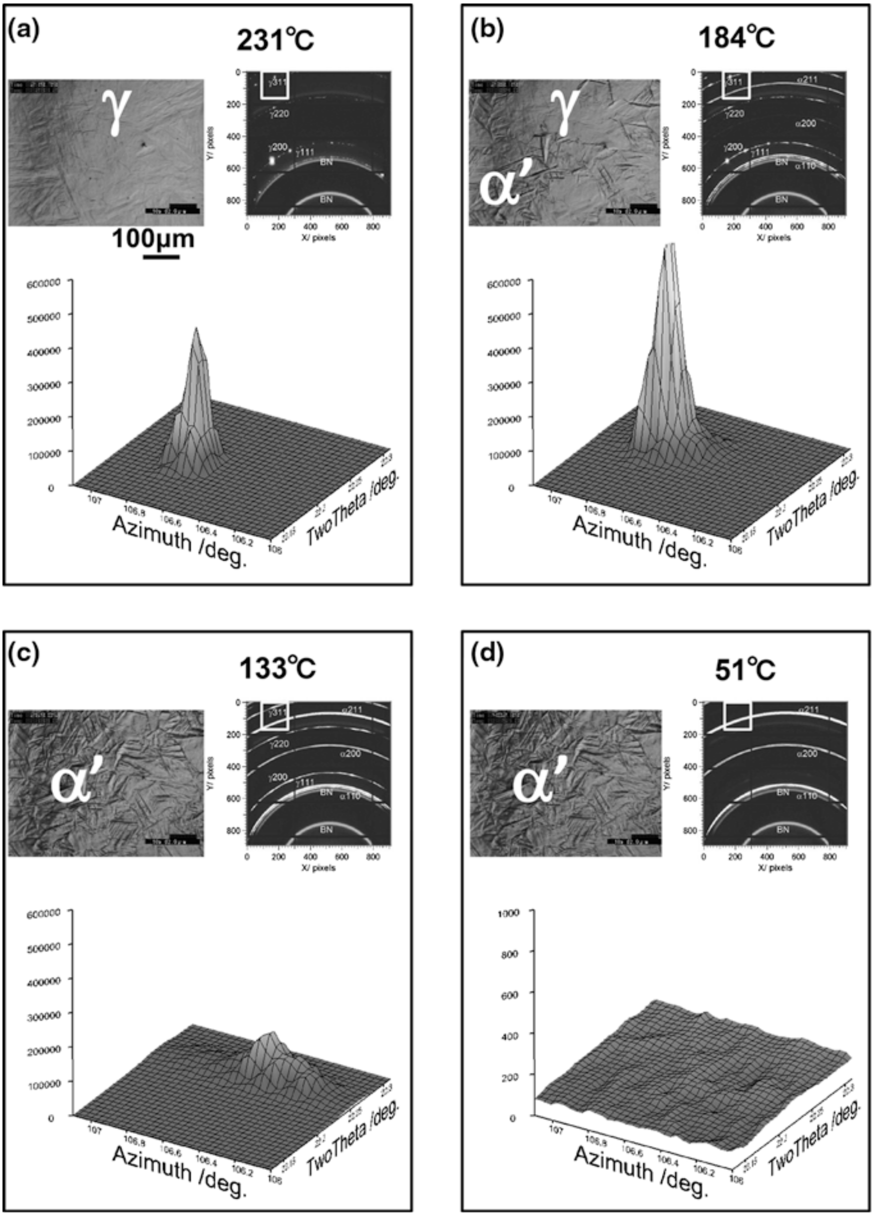

Fig. 1 Overview of the in situ observation results for martensitic transformation

using a fitting function of Gaussian peaks in the {311}γ spot diffraction by integration from 106 to 107.5°, as shown in Fig. 1. It can be found that the FWHM(2θ) was initially 0.02° (see Zone of austenite single phase of Fig. 2a), slowly increased to 0.03° (Zone A of Fig. 2a) and then rapidly increased to 0.13° (Zone B of

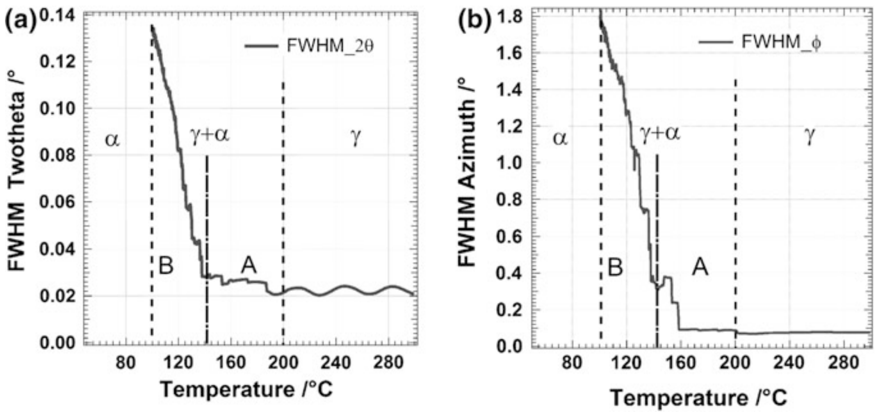

Fig. 2 Relationship between temperature and FWHM in the 2θ and φ directions during continuous cooling process

Fig. 3 Relationship between temperature and lattice constant derived from the diffraction pattern {311}γ

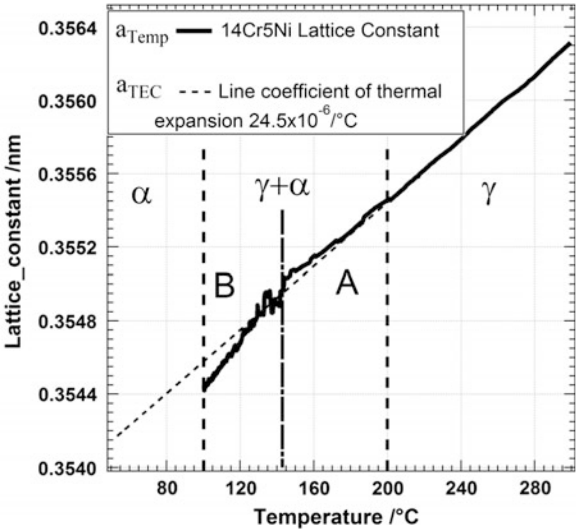

Fig. 2a). FWHM(φ) was initially 0.07° (see Zone of austenite single phase of Fig. 2b), then slowly increased to 0.09° (Zone A of Fig. 2b) and then rapidly increased to 1.8° (Zone B of Fig. 2b). In the case of coarse austenite grains, diffraction spots correspond to individual grains [6].

Figure 3 shows the lattice constant, obtained by spot diffraction of {311}γ. The temperature dependence of lattice constant (a_{TEC}) was calculated by the thermal expansion coefficient (TEC, 24.5×10^{-6}/°C) of the sample in the fully austenite phase. As clearly observed in Fig. 3, the change of the actual lattice constant (a_{Temp}) did not correspond to a_{TEC} in ($\alpha + \gamma$) region.

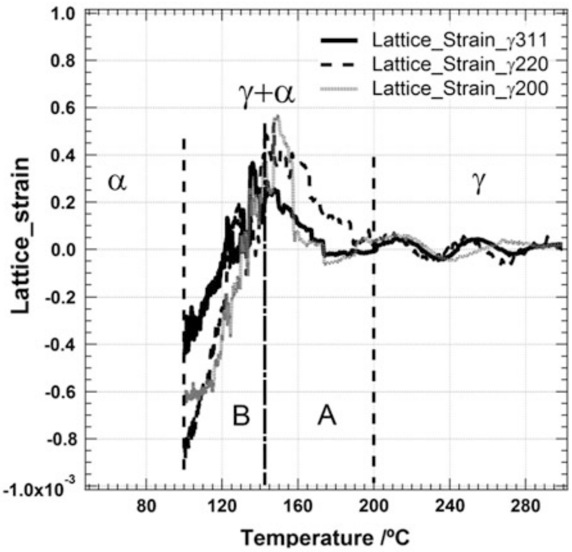

Fig. 4 Relationship between temperature and lattice-strain for out-of-plane, during continuous cooling process

We can suppose that the sample 14Cr5Ni was stress-free state in fully austenite region because the sample was austenitized at 1,000 °C for 50 s. According to the Eq. 1, the lattice-strain of austenitic grain can be calculated.

$$\varepsilon = \frac{a_{\mathrm{Temp}} - a_{\mathrm{TEC}}}{a_{\mathrm{TEC}}} \tag{1}$$

The lattice-strain of austenite reflection can be calculated for out-of-plane direction. Normal stress of the sample is zero, near the free surface. The in-plane strain can be calculated by out-of-plane strain. For example, when out-of-plane strain is a tension, in-plane strain is calculated to be a compression at Zone A. Figure 4 shows the relationship between temperature and lattice-strain for out-of-plane during continuous cooling process. The lattice-strains were calculated from spot diffractions of austenite (311), (220), (200), respectively. They have the same trends: the lattice-strain increased at the beginning of the transformation (Zone A), then decreased during further cooling (Zone B), as shown in Fig. 4.

In the discussion on FWHM and lattice strain of austenite, we also have to take the effect of transformation strain into account. At the beginning of the transformation (Zone A), all reflections from the austenite increased the FWHM and lattice strain, as shown in Figs. 2 and 4. This indicates that the austenite is deformed plastically to accommodate (PA) the transformation strain. The austenite phase may have compressive stress, at in-plane. On the other hand, we observed that the austenite grain size was fine during martensitic transformation, by using high-temperature laser scanning confocal microscopy (Fig. 1c). Therefore, the FWHM rapidly increased (Zone B in Fig. 2) because the grain size of austenite was small. Meanwhile, lattice strain of austenite decrease, and the compressive stress of austenite change into tensile at out-of-plane, because the small grain size is difficult to accommodate the transformation strain.

4 Conclusions

Martensitic transformation of 14Cr5Ni was observed by hybrid in situ observation technique. Accommodation mechanism of the transformation strain in martensitic transformation process was quantificationally discussed by the diffraction analysis of austenite phase. The main conclusions are as follows:

Initially, the plastic accommodation (PA) mechanism of austenite phase can be dominant in the first stage of martensitic transformation. The austenite phase may have compressive stress at this stage. In the next stage, the compressive stress changes to tensile stress, because the small grain size of austenite may be difficult to accommodate the transformation strain.

Acknowledgments This study was carried out as a part of research activities of Grants-in-Aid for Scientific Research A (No. 23246127) and “Fundamental Studies on Technologies for Steel Materials with Enhanced Strength and Functions” by Consortium of JRCM (The Japan Research and Development Center of Metals). Financial support from NEDO (New Energy and Industrial Technology Development Organization) is gratefully acknowledged. The synchrotron radiation experiments were performed at the BL46XU in the Spring-8 with the approval of the Japan Synchrotron Radiation Research Institute (JASRI) (Proposal No. 2009B2086). The authors are grateful to Dr. T. Shobu for the advice of data analysis.

References

1. Zhang S, Morito S, Komizo Y (2012) Variant selection of low carbon high alloy steel in an austenite grain during martensite transformation. ISIJ Int 52(3):510–515
2. Zhang S, Terasaki H, Komizo Y (2010) In-situ observation of martensite transformation and retained austenite in supermartensitic stainless steel (in Japanese). J Iron Steel Inst Japan (Tetsu-To-Hagane) 96(12):691–697
3. Terasaki H, Komizo Y (2006) In-situ observation of morphological development for acicular ferrite in weld metal. Sci Technol Weld Join 11(5):561–566
4. Komizo Y, Terasaki H, Yonemura M, Osuki T (2008) Development of in-situ microstructure observation techniques in welding. Weld World 52(5–6):56–63
5. Henrich B, Bergamaschi A, Broennimann C, Dinapoli R, Eikenberry EF, Johnson I, Kobas M, Kraft P, Mozzanica A, Schmitt B (2009) PILATUS: a single photon counting pixel detector for X-ray applications. Nucl Instrum Methods Phys Res Sect A-Accel Spectrom Dect Assoc Equip 607(1):247–249. doi:10.1016/j.nima.2009.03.200
6. Raghunathan SL, Dashwood RJ, Jackson M, Vogel SC, Dye D (2008) The evolution of microtexture and macrotexture during subtransus forging of Ti–10 V–2Fe–3Al. Mater Sci Eng, A 488(1–2):8–15

Compressive Residual Stress in Welded Joints with Low-Temperature-Transformation Weld Metal in High-Strength Steel

Chiaki Shiga, Hidekazu Murakawa, Yuki Matuo and Kazuo Hiraoka

Abstract The use of low-temperature-transformation (LTT) weld metal is considerably effective in reducing residual stress in welded joints of high-strength steels. The reduction in residual stress is due to the dilatation effect of the martensitic transformation. In this chapter the reduction of residual stress in welded joints of high-strength steels due to LTT weld metal was observed by neutron diffraction analysis. In addition, the relationships between welding conditions and residual stress were examined with FEM simulations for creating the formation mechanism of compressive residual stress. New welding method with LTT weld metal was developed and applied to boxing fillet welded joints. Fatigue measurements of them were carried out to verify the fatigue improvement.

Keywords Residual stress · LTT weld metal · Boxing fillet welding · Martensite transformation · FEM simulation · Neutron diffraction measurement · Fatigue · High-strength steel

1 Introduction

The use of low-temperature-transformation (LTT) weld metal is considerably effective in reducing residual stress in welded joints of high-strength steels [1–5]. The reduction in residual stress is due to the dilatation effect of the martensitic transformation. The residual stress depends not only on the martensite start temperature (Ms) but also on the shape of the weld metal and the restraint force in welded joints. The use of compressive residual stress to improve the fatigue and fracture toughness of steel structures requires the quantitative measurement of the

---

C. Shiga (✉) · H. Murakawa · Y. Matuo · K. Hiraoka
Osaka University, Osaka, Japan
e-mail: ccyshiga@amber.plala.or.jp

T. Kannengiesser et al. (eds.), *In-situ Studies with Photons, Neutrons and Electrons Scattering II*, DOI: 10.1007/978-3-319-06145-0_6,

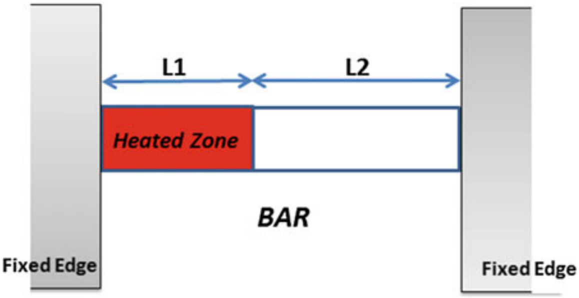

Fig. 1 Schematic drawing of bar model for calculation of stress in bar length direction. The restraint force is varied by a ratio of a heated zone (L1) and a nonheated zone (L2)

residual stress influenced by the abovementioned factors and the development of software simulations that enable the easy estimation of the residual stress at the weld and toe in any weld joint.

In this chapter, we focus on the formation mechanism of compressive residual stress that results from the suitable use of LTT weld metal. We have clarified this mechanism using neutron diffraction measurements [6–8] and finite element method (FEM) computer simulations [9–11]. Finally, we introduce the elongated bead boxing weld [3], which has been developed to improve the fatigue properties of gusset welds [3, 12, 13].

2 Thermal Stress Behavior Under Strong Restraint

Thermal-stress behaviors during cooling after welding were calculated by FEM simulations using the bar model which is shown in Fig 1. The different restraint conditions were obtained by varying a ratio (L2/L1) of heated (L1) to nonheated length (L2) in the bar fixed at both sides.

Figure 2 shows the thermal stress in cooling of conventional (CONV) and LTT weld metals, respectively. Thermal stress behaviors are strongly influenced by the restraint force (L2/L1). Here, the Ms temperature is assumed to be a barometer of the volume of martensite phase which is effective in reducing the residual stress due to the martensitic transformation dilatation. The volume of effective martensite phase increases in case of low Ms having martensitic-finish temperature (Mf) near the room temperature. CONV means the conventional weld metals used for the high-strength steels of 800 MPa grade. In this chapter, CONV represents the weld metal with Ms of 440 °C. LTT represents that with Ms 240 °C in case of no indication of Ms temperature.

In the case of weak restraint force (L1/L2 = 1/10), thermal stress in a low-temperature region is tensile in both LTT and CONV weld metals. However, as the restraint force is increased, the thermal stress in LTT weld metal becomes compressive stress, whereas that in CONV weld metal further increases the tensile stress.

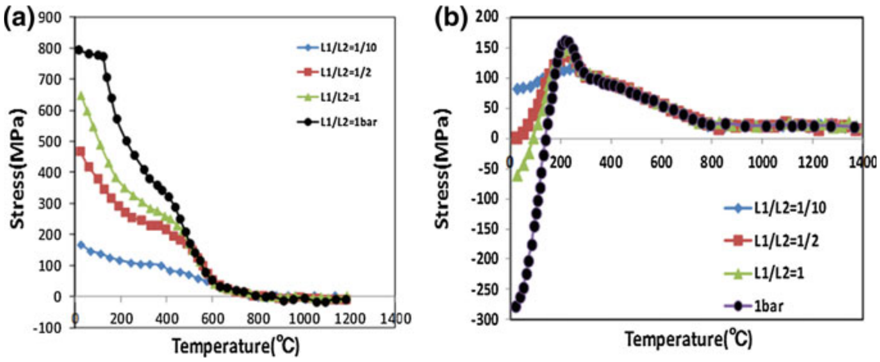

Fig. 2 Effect of restraint force on thermal stress during cooling after welding in **a** CONV, **b** LTT weld metals

Fig. 3 Relationships between residual stress and restraint force in CONV and LTT weld metals

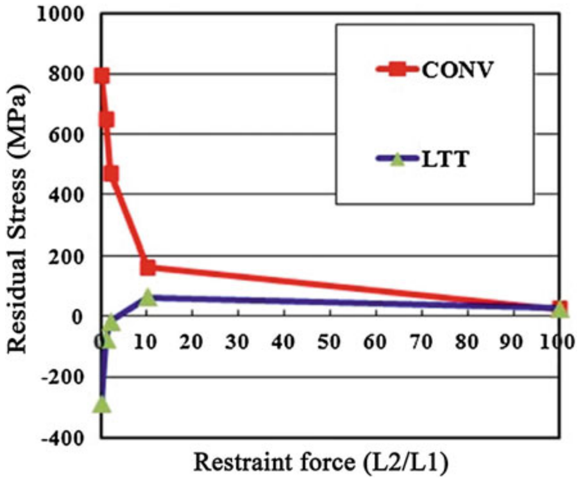

Under the strongest restraint conditions (1 bar), the thermal stress of CONV weld metal during cooling results in an increase in tensile stress to approximately 800 MPa at room temperature. By comparison, the thermal stress of LTT weld metal during cooling results in a compressive stress to approximately −300 MPa at room temperature after beginning to decrease from the Ms temperature of 250 °C. These results demonstrate that a dilatation effect due to the martensitic transformation that started in a low-temperature region such as the region below 250 °C, is so strong that it may result in compressive residual stress in the weld metal and toe.

In Fig. 3, the residual stress, which is corresponding to the thermal stress at room temperature in Fig. 2, is plotted as a function of the restraint force (L2/L1). Under the weak restraint force, the difference in residual stress between both weld

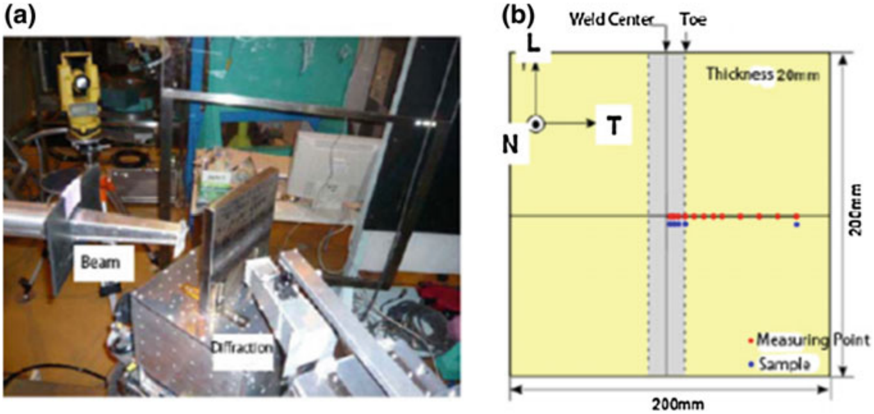

Fig. 4 **a** Neutron diffraction apparatus and **b** test piece of welded joint showing diffraction measurement positions and sampling positions for standard coupons with the dimensions of gauge volume of 2 × 2 × 2 mm^3

metals is small. However, under a narrow range of strong restraint force, the difference in residual stress between them becomes large; that is, the LTT weld metal undergoes an intensification of the compressive residual stress, whereas the CONV weld metal undergoes an intensification of the tensile residual stress.

3 Neutron Diffraction Analysis and FEM Simulations

The distributions of residual stress in large butt-welded joints with LTT and CONV weld metals were determined using a neutron diffraction apparatus and the test piece shown in Figs. 4a, b, respectively, where the measuring points and sampling positions are illustrated for a test piece of a welded joint [6]. Figures 5 and 6 show the residual stress distributions of σ_L and σ_T, which represent residual stress in the welding direction and that transversal to the welding direction, respectively. The residual stresses of σ_L and σ_T showed the compressive stress in the LTT weld metal. In particular, the σ_L of approximately −500 MPa in LTT weld metal exceeded our expectations. For comparison, the σ_L shows tensile stress of approximately 400 MPa in the CONV weld metal. The use of LTT weld metal therefore reduced the residual stress σ_L by approximately 900 MPa.

The weld metal with Ms of 150 °C has the retained austenite of about 5 %, which was measured by Neutron Diffraction Analysis. The Mf of that is below room temperature. The maximum residual stress seems to be a function of Ms if the retained austenite is below about 20 % [7, 8].

A comparison of the residual stress distributions observed with neutron diffraction measurements and those calculated, for the σ_L of butt-welded joints with LTT weld metal is shown in Fig. 7. The calculated values are in good agreement

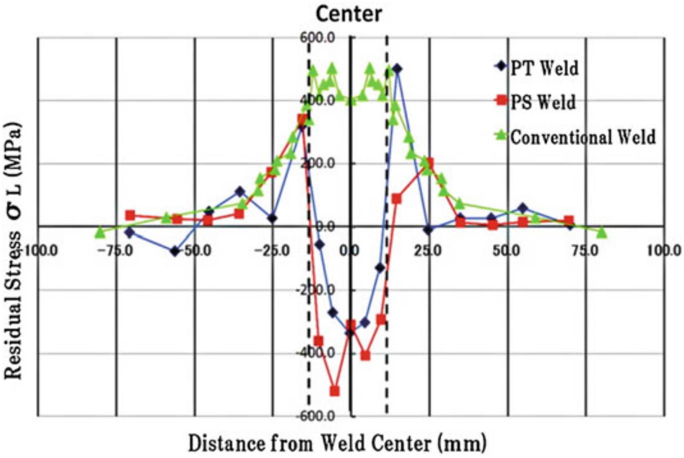

Fig. 5 Comparison of the residual stress distribution between CONV and LTT (PT, PS) weld metals. Residual stress is σ_L on the *red dotted line* transversal to the welding direction in Fig. 4b

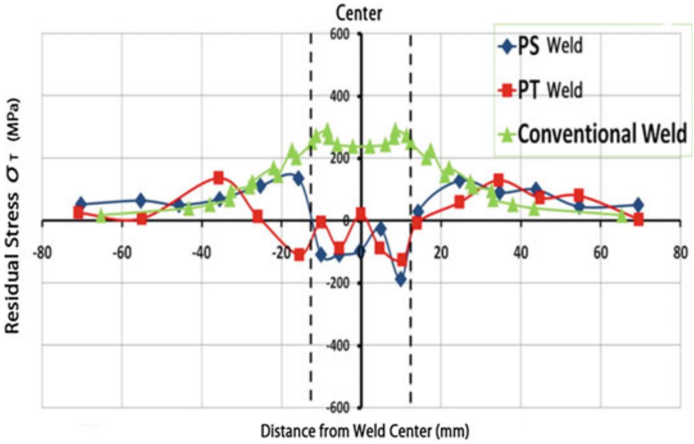

Fig. 6 Comparison of the residual stress distribution between CONV and LTT (PT, PS) weld metals. Residual stress is σ_T on the *red dot line* transversal to the welding direction in Fig. 4b

with the observed values for the weld metal and toe. The reason why σ_T is much smaller than σ_L is that the restraint force in the weld-metal width direction is weaker than that in the weld-metal length direction. Specifically, the reduction in residual stress due to the use of LTT weld metal depends on the restraint force around the weld metal when the Ms temperature of the LTT weld metal is the same. Our FEM simulations are suitable for estimating the residual stress in the weld metal and toes of joints welded under various conditions.

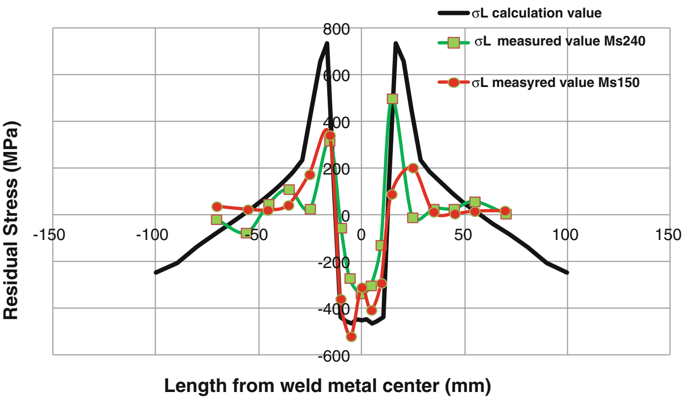

Fig. 7 Comparison of the calculated and observed residual stress distributions for σ_L of LTT weld metal (Ms temperatures of 240 °C and 150 °C)

Figure 8 shows the residual stress distribution in a boxing fillet weld observed with neutron diffraction measurements [7]. The use of an LTT weld metal reduces the tensile residual stress by approximately 300 MPa; however, the residual stress at the toe of a boxing fillet results in a tensile stress of approximately 400 MPa.

The reason why the stress reduction is less in case of the fillet weld compared to the butt weld may be explained by the following interpretation.

The residual stress depends on the restraint force, which is much stronger in welding direction than in one transversal to that. It does not matter that it may be LTT or CONV weld metal. In case of LTT, the stress reduction in the direction transversal to welding one is less than that in welding direction. It is clear in comparison with the experimental results of Figs. 5 and 6. The fillet welding direction in gusset corner front is corresponding to the one transversal to gusset direction. Therefore, the residual compressive stress in gusset direction is less. In other word, the residual stress of gusset direction is much lower because of that transversal to welding direction.

The suitable weld length elongated to gusset direction in gusset corner front is necessary for the increase of residual compressive stress in gusset direction, which is described below.

4 Effect of Weld Length and Weld-Metal Width on Residual Stress

To clarify the effect of the weld-metal length (l), and the weld-metal width (w) in both LTT and CONV weld metals, we performed FEM simulations by using a simple model shown in Fig. 9. Calculations were conducted with the length and width of the heated zone in a plate made of LTT weld metal being varied.

Fig. 8 Effect of the Ms temperature on the residual stress distribution in the longitudinal direction of the base plate (gusset direction) in a gusset-box fillet weld. The Ms temperatures of 200 and 100 °C correspond to LTT weld metal, whereas the Ms temperature of 440 °C corresponds to a conventional weld

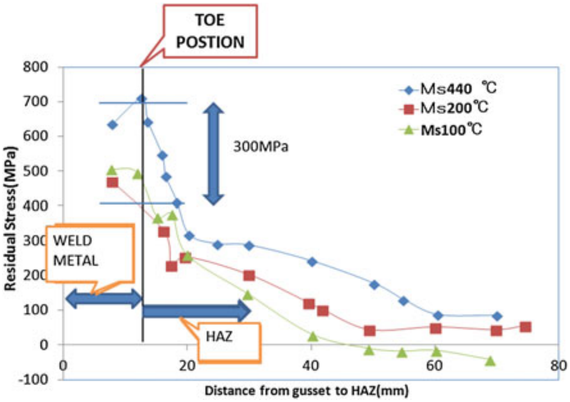

Fig. 9 Schematic weld model used for calculations of effect of the welding length and width on residual stress

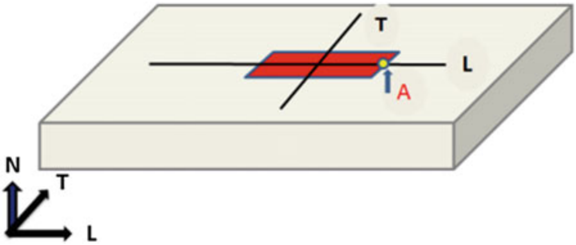

Figure 10 shows the residual stress distribution of σ_L along line L in Fig. 9, which was calculated for a case of length 80 mm, width 20 mm, and depth 20 mm. The residual stress of σ_L in LTT weld metal was lower by approximately 1000 MPa than that in CONV weld metal. The σ_L of LTT weld metal is compressive stress of −400 MPa at the middle of the weld length but is approximately −100 MPa at both ends near the weld toe; that mean, the compressive residual stress at the end position is smaller than that at the middle position because of weak restraint around the end position.

The lower restraint at the end position results from the base plate which is easy to deform. In addition, the restraint there is much weakened because the strength of the base plate is lower than that of weld metal.

Figure 11 shows the residual stress distribution of σ_L along line T in Fig. 9. The σ_L of LTT weld metal is remarkably lower in the region from weld metal to toe compared to the σ_L of CONV weld metal.

To clarify the effect of the width of the LTT weld metal on residual stress, residual stress distributions from the center of the weld metal to the heat-affected zone (HAZ) along line T in Fig. 9 were calculated. Figure 12 shows the results obtained for weld metal widths varied from 2 to 20 mm. The maximum value of compressive residual stress was only slightly affected by the weld-metal width.

To clarify the effect of the weld length of LTT weld metal on the residual stress, residual stresses were calculated by varying the weld lengths from 20 to 300 mm

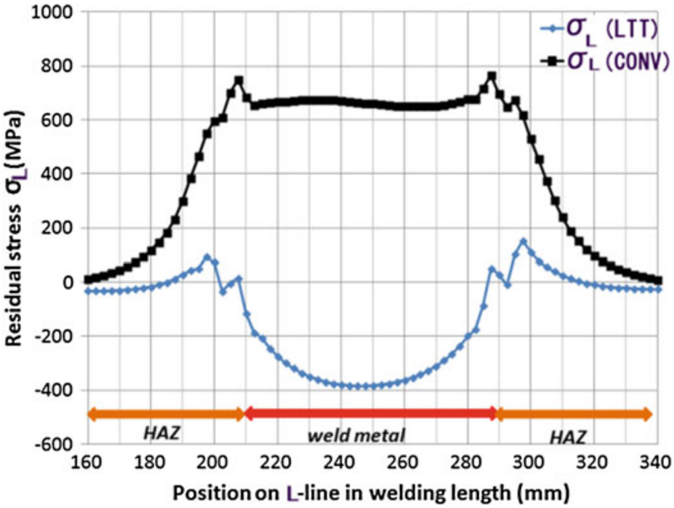

Fig. 10 Comparison of residual stress distributions of σ_L on line L between CONV and LTT weld metals

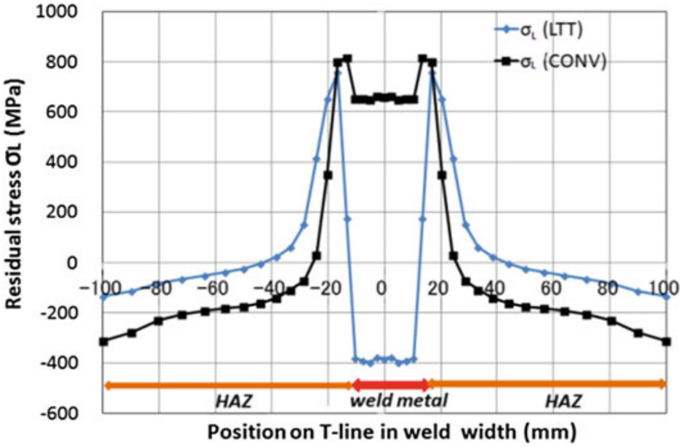

Fig. 11 Comparison of residual stress distributions of σ_L on line T between CONV and LTT weld metal

in Fig. 9. The compressive stress becomes stronger as the weld length is longer. The compressive stress of σ_L rapidly increases in less than about 70 mm, but it much slightly increases in more than that. The compressive stress of σ_L in weld length of 20 and 300 mm is −50 and −450 MPa at the middle of the weld length, respectively [10].

Fig. 12 Effect of weld-metal width on the residual stress distribution of σ_L from the weld metal center to HAZ on line T

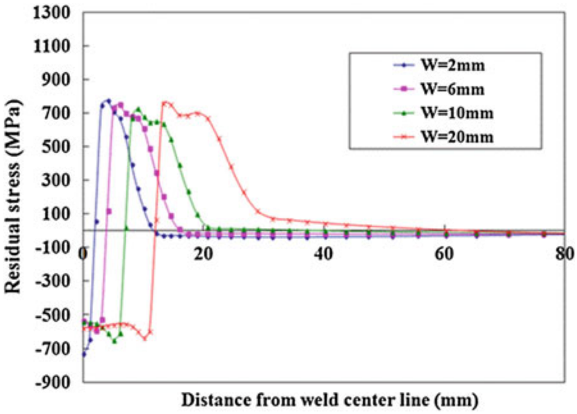

Fig. 13 Finite-element mesh divisions used for calculation of residual stress and concentration stress in conventional weld metal of model 7-5 (i.e., a vertical leg length of 7 mm and a horizontal leg length of 5 mm) and elongated bead-weld metal of model 7-70 (i.e., a vertical leg length of 7 mm and a horizontal leg length of 70 mm)

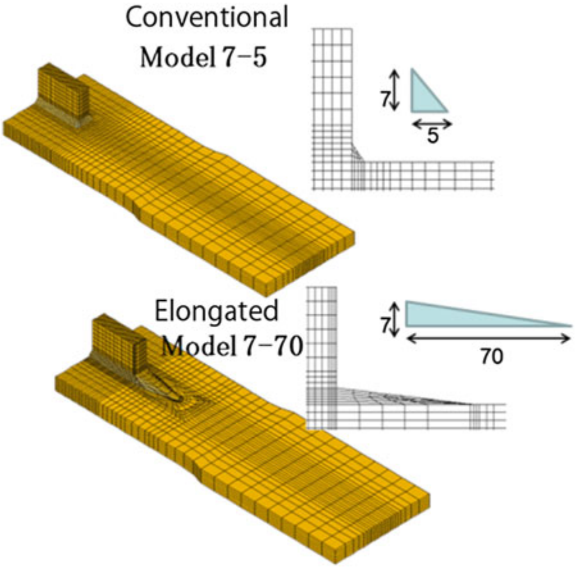

5 Elongated Bead Welding

On the basis of the previously discussed simulations of compressive residual stress, we discovered a new welding method characterized by an elongated bead of LTT weld metal that induces high compressive stress at the metal and toe of a boxing fillet weld. A comparison of the simulated models of an elongated bead (model 7-70) and a conventional fillet weld (model 7-5) is shown in Fig. 13. Residual stress distributions on the red line from the gusset to the HAZ in welded joints with weld metals with various Ms temperatures are shown in Figs. 14 and 15, which were calculated for conventional and elongated bead welds, respectively [3].

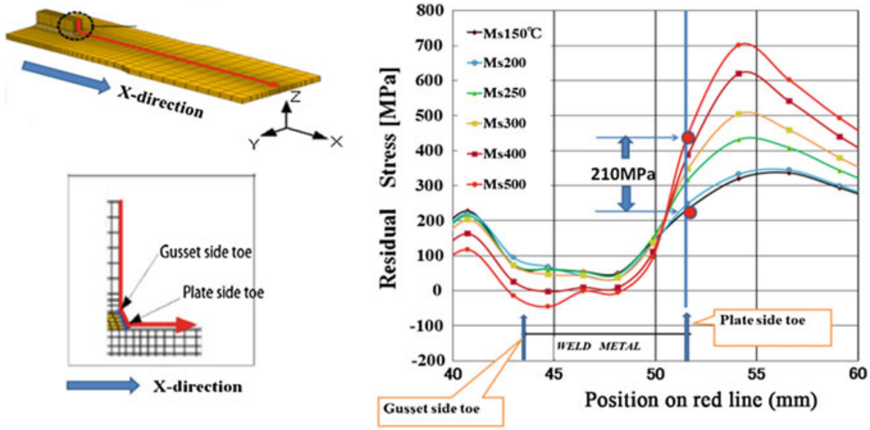

Fig. 14 Effect of the Ms temperature of the weld metal on the residual stress distribution in conventional boxing fillet welded joints. Residual stress in the *x*-direction and each position on the *red line* in the *left* illustration are plotted as the ordinates and abscissae, respectively

In Fig. 14, the residual stress in the plate-side toe controlling the fatigue crack is reduced by approximately 210 MPa in the combination of LTT weld metal and conventional fillet weld, but it is still tensile residual stress. In contrast, in the combination of LTT weld metal and elongated bead weld in Fig. 15, the residual stress of the plate-side toe is reduced to the compressive residual stress level (for example, −500 MPa in case of Ms 150 °C). The X-ray measurements of residual stress demonstrate the effectiveness of the combination of the LTT weld metal and elongated bead weld. Figure 16 shows the residual stress distribution on the surface from toe to the HAZ for the combinations of weld metals and elongated beads in a boxed fillet weld. The LTT welds of B-1 and C-1 substantially reduce residual stress near the toe as compared to that in the conventional weld of A-1. In particular, the combination of LTT wire and an elongated bead results in a compressive residual stress of approximately −100 MPa at the toe and also extends the region of low residual stress in the HAZ.

We observed significant improvements in the fatigue properties in boxing fillet welds through the combination of LTT wire and the elongated bead.

The S–N curves for gusset fillet welded joints with LTT weld metal produced using the new elongated-bead method and those for joints produced using the conventional welding method are shown in Fig. 17 where the previous results for weld joints with conventional weld metal produced using the conventional welding method are plotted to demonstrate the improvement in fatigue [13]. In comparison with welds made using the conventional welding method and conventional weld metal, the new welding method with an elongated bead of LTT extended the lifetime under a stress level of 150 MPa 12-fold and increased the stress level 2.5-fold, i.e., from 60 to 160 MPa, in 2×10^6 fatigue cycles.

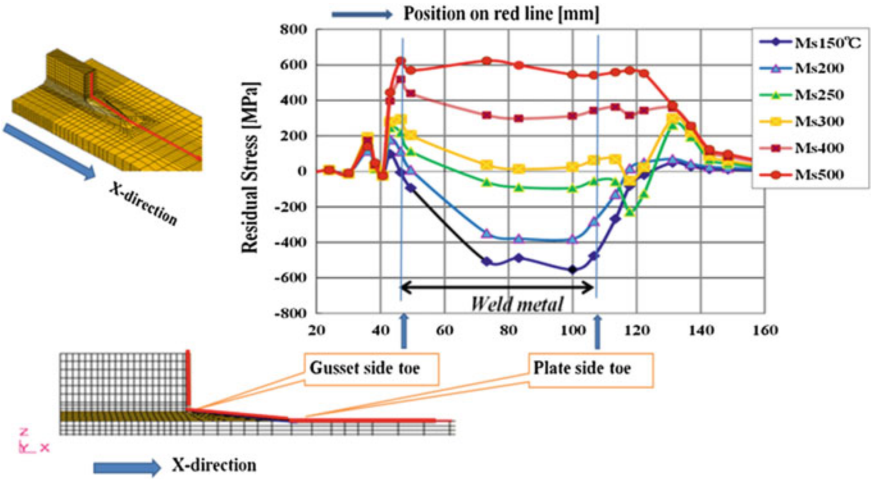

Fig. 15 Effect of the Ms temperature of weld metal on the residual stress distribution in elongated bead boxing fillet welded joints. Residual stress in the *x*-direction and each position on the *red line* in the *left* illustration are plotted as the ordinates and abscissae, respectively

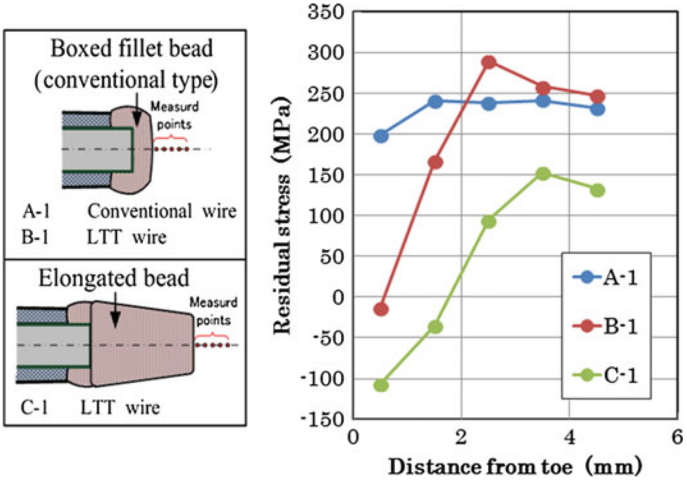

Fig. 16 Comparison of the residual stress distribution in the *x*-direction between A, B, and C welds shown in the *left* illustration, where the *upper diagram* represents a conventional boxing weld, and the *lower diagram* represents an elongated one. A-1 is a combination of conventional boxing and conventional weld metal; B-1 is a combination of conventional boxing and LTT weld metal; C-1 is a combination of an elongated weld and LTT weld metal

We consider that the fatigue improvement is resulting from the twin effects of the compressive residual stress and the reduction of stress concentration at the weld toe position. The reason comes from the experimental facts that the fatigue

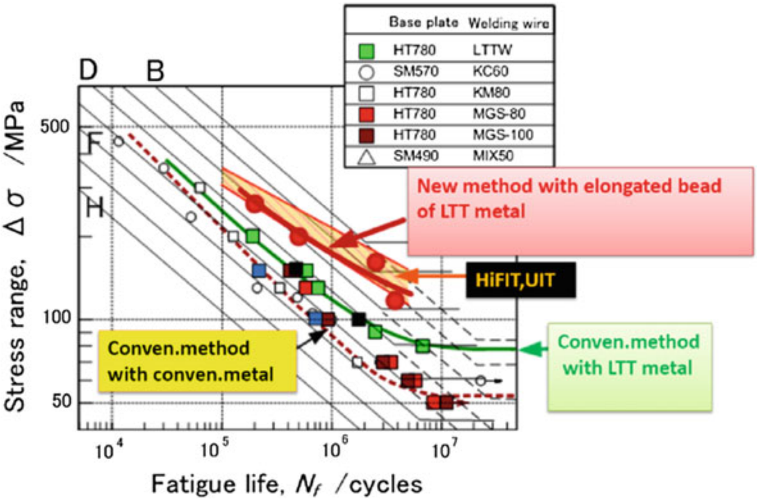

Fig. 17 Fatigue test results of gusset fillet joints welded using different welding methods. The *red circles* show the results of fatigue tests of the new method with an elongated bead of LTT weld metal

improvement of weld joints with the elongated bead of a conventional weld metal is lower than that of the elongated bead of an LTT weld metal.

By application of the elongate bead with an LTT weld metal, the residual stress at the toe position reduces from tensile stress of 200 MPa to compressive stress of −100 MPa (as shown in Fig. 16) and in addition, stress concentration there reduces by 60 %, according to the previous FEM simulation results [3].

It is not really a good idea to have a large bead length only from welding perspective. We knows well that it causes extra work for welding side, but the remarkable improvement in fatigue properties is essential issue for the welded structures of high-strength steels. The new welding method seems to give the excellent properties that other method such as the peening method did not give in the point of view from the safety against fracture, repairs and maintenance which are important for welded structures. In shipbuilding application, the merit and demerit due to the use of the new welding method have being examined as well as welding efficiency has being improved by small bead length.

6 Conclusion

The reduction of residual stress in welded joints of high-strength steels due to LTT weld metal was observed by neutron diffraction analysis. In addition, the relationships between welding conditions and residual stress were examined with FEM simulations for creating the formation mechanism of compressive residual stress.

New welding method with LTT weld metal was developed and applied to boxing fillet welded joints. Fatigue measurements of them were carried out to verify the fatigue improvement. Our conclusions are as follows:

1. In the butt welded joints produced using 800 MPa grade high-strength steel and LTT weld metal, compressive residual stress of −400 MPa was observed in welding direction, but that of the −100 MPa, in transversal direction to that. The compressive residual stress has a strong dependence on welding direction.
2. The strength of compressive residual stress has dependence on the volume of martensite structure transformed in low temperature region in weld metal. The weld metal with lower Ms temperature increases the compressive stress in case of Mf temperature close to room temperature.
3. Compressive residual stresses have dependence on the restraint force around weld metal. In the welded joints with LTT weld metal, the restraint force in welding direction is so strong in comparison with that in transversal direction that the compressive residual stress in welding direction is much larger than that in transversal direction.
4. The compressive residual stress in welding direction has a strong dependence on weld length. It remarkably increases in proportion to the weld length in less than about 70 mm, but it gradually saturates in more than that.
5. The gusset fillet welded joints with LTT weld metal produced using the newly developed elongated-bead method have the excellent fatigue properties in comparison with those produced using the conventional welding method.

References

1. Shiga C (2000) Problems in welded joints and systematic approach to their s solution in STX21 project. Sci Technol Weld Joining 5(6):356–364
2. Ohta A, Watanabe O, Matsuoka K, Shiga C, Nishijima S, Maeda Y, Suzuki N, Kubo T (2000) Fatigue strength improvement of box welded joints by using low transformation temperature welding material. QJ Japan Weld Soc 18(1):141–145 (in Japanese)
3. Shiga C, Murakawa E, Matsuo Y, Ohsuga U, Hiraoka K, Morikage Y, Yasuda K (2013) Fatigue improvement in high-strength steel welded joints with compressive residual stress. Weld World, Sept 2013 (to be published)
4. Nakamura T, Hiraoka K, Hayakawa N, Gunic F (2005) Improvement of welded joint property by new welding technology. In: Proceedings of international ATS steelmaking conference. ATS, Paris, pp 226–227
5. Zenitani S, Hayakawa N, Yamamoto J, Hiraoka K, Morikage Y, Kubo T, Yasuda K, Amano T (2007) Development of new low transformation-temperature welding consumable to prevent cold cracking in high strength steel welds. Sci Technol Weld Joining 12(6):516–522
6. Suzuki H, Holden TM (2006) Neutron diffraction measurements of stress in an austenitic butt weld. J Strain Anal Eng Des 41(8):575–582
7. Shiga C, Mraz L, Bernasovsky P, Hiraoka K, Mikula P, Vrana M (2007) Residual stress distribution of steel welded joints with weld metal of low transformation temperature. J Weld World 51(11/12):11–19 Doc. IIW-1824-07 (ex-doc. IX-2149r1-05)

8. Shiga C, Yasuda H, Hiraoka K, Suzuki H (2010) Effect of Ms temperature on residual stress in welded joints of high strength steels. Weld World 54(3/4):71–79
9. Hiraoka K, Yamamoto J, Shiga C, Mraz L, Mikula P (2009) Numerical simulation of residual stress distribution in welded joints with LTT weld metals, pre-print of IIW international congress in Central and East Europe Region Slovakia, High Tatras, Stara Lesna, 14–16 Oct 2009
10. Shiga C, Murakawa E, Arafune M, Yamamoto J and Hiraoka K (2011) Computer simulation of compressive residual stress in LTT weld joints of high strength steels In: Preprints of the symposium on welded structure of JWS, pp 57–63
11. Shiga C, Murakawa E, Arafune M, Ohsuka Y, Hiraoka K, Morikage Y, Yasuda K (2014) Fatigue improvement in high-strength steel welded joints with compressive residual stress. Weld World 58:55–64
12. Weich I, Ummenhfer T, Nitschke Th, Dilger K, Eslami H (2009) Fatigue behaviour of welded high-strength steels after post-weld treatments. Weld World 53(11/12):322–332
13. Morikage Y, Kubo T, Yasuda K, Amano K, Hiraoka K, Ohta A, Shiga C (2001) Improvement of fatigue strength of welded joints by applying low-temperature transformation welding consumables to high strength steel. In: Preprints of the national meeting of JWS, vol 68 pp 144–145

In Situ Observation of Changing Crystal Orientations During Austenite Grain Coarsening

**Hemant Sharma, Richard M. Huizenga, Aleksei Bytchkov,
Jilt Sietsma and S. Erik Offerman**

Abstract Understanding the underlying mechanisms of grain coarsening is important to control the properties of metals, which strongly depend on the microstructure that forms during the production process or use at high temperature. Grain coarsening of austenite at 1,273 K in a binary Fe-2 wt% Mn alloy was studied using synchrotron radiation. The evolution of volume, average crystallographic orientation and mosaicity of more than 2,000 individual austenite grains was tracked during annealing. It was found that there exists an approximately linear relationship between grain size and mosaicity, which means that orientation gradients are present in the grains. The orientation gradients remain constant during coarsening and consequently the character of grain boundaries changes during coarsening, affecting the coarsening rate. Furthermore, changes in the average orientation of grains during coarsening were observed. The changes could be understood by taking the observed orientation gradients and anisotropic movement of grain boundaries into account. Five basic modes of grain coarsening were deduced from the measurements which include: anisotropic (I) and isotropic (II) growth (or shrinkage); movement of grain boundaries resulting in no change in volume but change in shape (III), movement of grain boundaries resulting in no change in volume and mosaicity, but change in crystallographic orientation (IV); and no movement of grain boundaries (V).

Keywords In situ · Synchrotron radiation · Iron alloys · Coarsening · Annealing

---

H. Sharma · R. M. Huizenga · J. Sietsma · S. E. Offerman (✉)
Department of Materials Science and Engineering, Delft University of Technology,
Mekelweg 2, 2628 CD Delft, The Netherlands
e-mail: S.E.Offerman@tudelft.nl

A. Bytchkov
Institute Laue Langevin, BP 156, 38043 Grenoble Cedex, France

T. Kannengiesser et al. (eds.), *In-situ Studies with Photons, Neutrons and Electrons Scattering II*, DOI: 10.1007/978-3-319-06145-0_7,

1 Introduction

This chapter is based on work that we published earlier [1][1]. At high temperatures, coarsening of grains occurs in order to reduce the total energy of the system [2]. Understanding grain coarsening in three-dimensional (3D) structures is essential for control of microstructures of metals and ceramics, which bears a direct influence on the resulting mechanical and functional properties. For example, control of grain size at high temperatures is very important for maintaining high strength of materials over time during operation in energy conversion systems.

For many decades, extensive effort has been devoted to understanding and prediction of grain coarsening at high temperatures. However, even for very simple systems, knowledge of the process of grain coarsening is still incomplete [3, 4]. A substantial part of the work has focused on the development of models for prediction of grain coarsening [4–9]. These models assume grains as perfect crystals, the character of which does not change during coarsening and attribute coarsening entirely to the reduction of total interface area of the system [10], but cannot yet accurately reproduce the real material behavior [2].

Classically grain coarsening at high temperatures in polycrystalline materials is attributed to reduction of the grain boundary area and consequently of the total energy of the system. A widely used semi-empirical grain coarsening equation to fit the experimental data for average grain sizes is expressed as

$$D^n = D_0^n + kt \tag{1}$$

where D is the average grain size at time t, D_0 is the average grain size at the start of isothermal annealing ($t = 0$) and k and n are empirical fitting parameters [2]. In most studies, values of n are commonly found to be much higher than the ideal value of 2, which is based on proportionality of the local grain curvature driving coarsening and the grain size [2]. A higher value of n means that the rate of grain coarsening decays faster than if n had a lower value. This effect is commonly attributed to solute drag (that is, slowing down of grain boundaries by foreign atoms present in the matrix), to non-regular microstructures or to presence of texture [2], but no underpinning observations for these assumptions have been presented. More recently, a model based on stagnation of grain coarsening induced by grain-boundary smoothening has been proposed [4]. In the present chapter, an additional contribution to the often observed fast decay of the rate of grain coarsening is presented.

Even though significant advances have been made in modeling of coarsening, direct experimental observation of the coarsening process is lacking. Direct experimental observation of grain coarsening at high temperature requires a combination of experimental settings that, until recently, had not been accomplished: in situ observations of *three-dimensional* grain volumes in the bulk of the

---

[1] Reprinted with modification from Acta Materialia, vol. 60, Sharma H, Huizenga RM, Bytchkov A, Sietsma J, Offerman SE, Observation of changing crystal orientations during grain coarsening, pp. 229-237 (2012), with permission from Elsevier.

material during coarsening. Up to date, experimental studies have been limited to ex situ observations on cross-sections of quenched materials [11] or in situ observations on the surface of specimens at high temperature [12]. In the first approach, the time resolution and the accuracy of the observations was limited, especially if the microstructure (e.g. austenite in steel) underwent a phase transformation upon cooling. In the latter case, coarsening at the surface was studied, which can essentially differ from the bulk behavior [13]. In either case, just a 2D analysis of the grain-size distribution was performed.

The recent advances made at 3rd generation synchrotron sources capable of generating high energy X-rays with increased flux have made it possible to observe the bulk of materials [14] and study individual grains in polycrystals [15–19]. In a promising study, Schmidt et al. [20] studied grain coarsening in an aluminum alloy by employing the 3DXRD technique [21]. However, in the case of alloys which undergo a phase transformation upon cooling to room temperature, the technique of interrupted heat treatments as followed by Schmidt et al. [20] cannot be used. In the present chapter, the first in situ three-dimensional observations of bulk grain coarsening at high temperatures in an alloy that undergoes a phase transformation upon cooling are presented. It will be shown that experimental observations at the level of individual grains reveal essential information about the behavior of grains during coarsening.

2 Experimental Details

2.1 Sample

The alloy under investigation was manufactured from electrolytic (99.999 % purity) iron and manganese to get a composition of 2 wt% Mn. The concentration of other impurities was kept very low in order to minimize any influence of other solute particles on the rate of grain coarsening. The composition was chosen in order to slow down the rate of grain coarsening by solute drag as compared to pure iron. This was warranted by time resolution of the 3DXRD technique used. The initial material was homogenized at 1,553 K for 21 days followed by furnace cooling to room temperature. The sample was manufactured using electro discharge machining (EDM) with dimensions shown in Fig. 1 in order to fit in the furnace described in reference [22]. The sample had a change in diameter from 1 to 1.5 mm in the middle which is used to define a reference by scanning with the X-ray beam.

2.2 3DXRD Experiment

The experiment was carried out at beamline ID11 of European Synchrotron Radiation Facility (ESRF), Grenoble, France. Figure 2 shows the experimental setup. The sample was placed in a furnace developed especially for 3DXRD

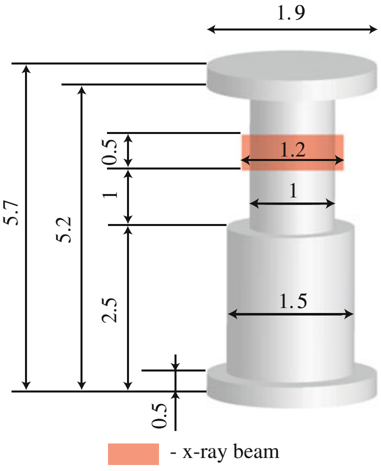

Note: All dimensions are inn mm.

Fig. 1 Schematic geometry of the sample. Location of the X-ray beam is highlighted

measurements, described in reference [22]. An S-type thermocouple was spot-welded to the top of the sample for accurate temperature control. The sample chamber was purged with helium and sealed at a pressure of 0.4 atm. The X-ray beam, 500 μm high and 1,200 μm wide with energy equal to 88.005 keV, calibrated using a Pb-foil, was incident on the sample at the location depicted in Fig. 1. The sample was heated rapidly to a temperature of 873 K in 60 s, followed by isothermal holding for 900 s and heating to a temperature of 1,173 K at a rate of 0.033 K/s, followed by rapid heating in 120 s to 1,273 K. The sample was then held isothermally at 1,273 K for 7,740 s (2.15 h). During the heat treatment, the furnace was rotated repeatedly over a total angle ω equal to 24° (so-called *sweep* equal to one full rotation of 24°). Diffraction patterns were recorded during every 0.3° rotation with an exposure time of 0.2 s. This setup means that every 180 s a diffraction pattern is recorded at the same orientation of the sample with respect to the incident beam. The sample was then cooled to room temperature. Due to the limited number of grains in the illuminated volume which satisfy the Bragg condition for diffraction in a certain orientation of the sample, individual spots from individual grains were observed in the diffraction patterns. An example of a diffraction pattern is shown in Fig. 3. The sample to detector distance was adjusted in such a way that four complete diffraction rings of the austenite phase were recorded. An austenite grain of any crystallographic orientation combined with a rotation of the sample over 24° for the first four families of *hkl*-planes would come into diffraction between 3 and 9 times. Thus, all the grains in the illuminated volume were studied in the present experiment. The small rotation angle of 24° means that spatial characteristics of the grains cannot be determined. However, this angle was chosen in order to get a good time resolution. At the beginning and end of isothermal annealing, the vertical size of the X-ray beam was increased to 600 μm in order to verify the diffraction spots originating from the grains situated partially in the illuminated volume.

3 Data Analysis Method

This section describes the method that we used to analyze the diffraction patterns. A more extensive description of the methodology is given in two papers by Sharma et al. [23, 24].

3.1 Grain Volume

The grain volume is calculated from the diffraction patterns according to the following procedure:

1. The recorded diffraction images are corrected for beam current, electronic noise and detector imperfections.
2. A minimum intensity (threshold) is set in order to identify different peaks originating from grains. In the current case, the threshold is set at 200 counts above the background, which corresponds to a minimum detectable grain volume of around 35 μm^3 (grain radius of ~ 2 μm). The pixels in the diffraction image which have intensity above the threshold and are connected are identified as a single peak and the sum of intensity of all the connected pixels is stored as integrated intensity from that peak.
3. If the diffraction spot is present in multiple diffraction patterns, that is, if the location of some pixels constituting two or more peaks is the same in the images, the total intensity of the diffraction spot is calculated by summing all the individual peaks and is counted as one diffraction spot.
4. By calibrating the distance between the sample and the detector, all the peaks found in the previous step are assigned to families of *hkl* planes. For this purpose, Transformation code is used, which is a part of the Fable package [25].
5. The location of the center of mass of the diffraction spot is calculated in terms of η, 2θ and ω (see Fig. 2 for definitions).
6. The powder intensity (I_p) per diffraction image for a *hkl*-ring is calculated by summing the total intensity of all the peaks recorded during one full rotation of the sample (or furnace) over the angle of 24° lying on the *hkl*-ring and dividing by the number of diffraction images. Such a procedure ensures the most accurate value for I_p, compensating for texture effects.
7. The volume of the grain (V_g) giving rise to the diffraction spot is calculated according to the following expression

$$V_g = \frac{1}{2} m_{hkl} \cos(\theta) V_{gauge} \frac{I_g}{kI_p} \Delta\theta \qquad (2)$$

where m_{hkl} is the multiplicity of the *hkl*-ring, θ is the Bragg diffraction angle, V_{gauge} is the volume of the sample illuminated by the X-ray beam, I_g is the integrated of the diffraction spot, k is the normalization factor for I_g and is

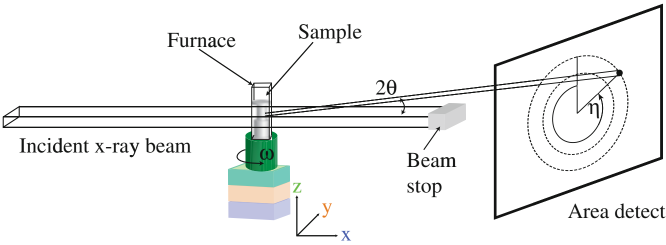

Fig. 2 Schematic showing the experimental setup. The dimensions are not to scale. The angles 2θ, ω and η are defined

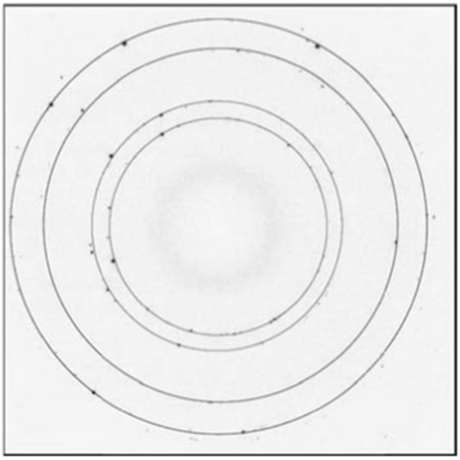

Fig. 3 Example of a diffraction pattern showing austenite reflections at 1,273 K. Dark regions show pixels with positive intensity. The solid rings indicate the expected location of Debye-Scherrer rings for austenite phase at 1,273 K for the following *hkl* planes (radially outwards): {111}, {200}, {220} and {311}. The deviation of diffraction spots from the ideal location at the diffraction rings is due to the effect of positioning of the diffracting grain inside the sample

equal to the number of diffraction patterns in which the diffraction spot is observed, I_p is the powder intensity per diffraction image for the *hkl*-ring and Dθ is the rotation of plane normal over which the diffraction spot is observed or, in other words, Dθ is the change in the scattering angle due to rotation over Dω. Dθ is given by the following expression

$$\Delta\theta = \sin^{-1}(\sin(\theta)\cos(\Delta\omega) + \cos(\theta)\sin|\eta|\sin(\Delta\omega)) - \theta \tag{3}$$

where Dω is the rotation angle of the sample over which the diffraction spot is observed, θ and η are defined in Fig. 2.
For derivation of Eq. (1) and details on Eq. (2), please see the Appendix.

8. The set of volumes obtained during each repeated rotation of the furnace over 24°, from now on called a sweep, are stored as the volumes of austenite grains during that particular sweep in the illuminated volume.

3.1.1 Volume Evolution of Individual Grains

1. The volume grains and location of the center of masses of the corresponding diffraction spots are calculated in the previous step. The location of the center of mass of each diffraction spot in a sweep is then matched with the location of the center of masses of all the diffraction spots in the next sweeps.
2. By using a relatively small tolerance (±3 pixels in the position of the spot on the detector and ±0.3° in ω), the diffraction spots coming from the same grain are identified in different sweeps and the volume of the grain as a function of the time of acquisition of the diffraction pattern is stored.
3. If two or more diffraction spots come from the same austenite grain, the evolution of grain volume must be the same for all of them. By matching the time evolution of grain volumes for all the diffraction spots found with a tolerance of 5 % in volume, a list is generated with the spots belonging to the individual austenite grains. The total volume of the grains found in such a manner is 97.3 % of the illuminated volume, the rest being grains for which the diffraction spots overlap or grains which are too small to be detected.
4. The volume of the grain is taken to be the average of the volumes resulting from all the diffraction spots belonging to the same grain per sweep.
5. The spots which show an increase in intensity more than 5 % of the integrated intensity upon opening of the X-ray beam are rejected as coming from the grains which are partially illuminated by the X-ray beam.
6. The number of grains during each sweep is calculated by counting the total number of grains identified in step 3.
7. The average austenite grain volume of all the austenite grains is calculated by computing the volume weighted average of the grain volumes.

3.1.2 Calculation of Mosaicity of the Grains

Mosaicity, $\Delta\upsilon$, defined per grain as the maximum difference in crystallographic orientation between any two regions in the grain [26], was calculated as the rotation of the diffracting plane normal required to produce a diffraction spot of the observed size in ω and η. In either ω or η, the mosaicity calculated is the maximum difference in orientation in a single direction of the grain. The average mosaicity was calculated as the average mosaicity of all the grains with radius between intervals of

5 μm.[2] The mosaicity per grain was calculated by averaging the mosaicity calculated from all the diffraction spots identified as belonging to the grain.[3]

The following procedure was used to calculate the mosaicity:

1. The mosaicity or the maximum difference in orientation of plane normal between any two regions of the grain can be characterized by analyzing the diffraction spots arising from the grain.
2. In case of an un-deformed grain, the change in orientation of a grain with an isotropic shape is assumed to be isotropic in all directions.
3. In diffraction, the mosaicity of a grain can be described in terms of the size of the diffraction cloud in reciprocal space. The size of a diffraction spot on the detector is the convolution of the beam divergence, the Darwin width of the reflection, the size of the diffracting grain and the mosaicity of the grain. In the current experimental setup, the location of the detector far away from the sample (375 mm) and use of an undulator beamline at a synchrotron mean that the size of the grain and the divergence of the X-ray beam have a negligible effect on the size of the spot as compared to the mosaicity of the grain. Furthermore, the Darwin width of the reflection, which can also cause widening of the spot, has a negligible contribution in the current experimental setup.
4. In terms of the diffraction geometry shown in Fig. 2, the mosaicity of the grain can be calculated either by calculating the size of spot ($\Delta\eta$) along the η-direction (mosaicity by rotation of the diffracting plane normal around the X-ray beam) or the rotation of plane normal, $\Delta\theta$ (mosaicity by rotation around the diffraction plane normal) from Eq. (3), characterizing the diffraction spot. Depending on the number of diffraction patterns that the diffraction spot is present in, the following strategy is used to calculate the mosaicity of the austenite grains:
    (a) If the diffraction spot is present in one or two diffraction patterns, the mosaicity of the grain from the diffraction spot is calculated by calculating the rotation of the plane normal corresponding to the size of the diffraction spot in η-direction corrected for the divergence of the X-ray beam which is known from the setup. In this method, the error in characterizing the mosaicity is equal to the effect of the size of the grain.
    (b) If the diffraction spot is present in three or more diffraction patterns, the mosaicity of the grain is calculated by calculating the spread of the diffraction spot in ω-direction. The amount of rotation in ω for which the grain is in diffraction is calculated as follows:

---

[2] In case of very big grains diffraction spots in first and second diffraction rings are saturated and thus cannot be used for analysis. In such cases, spots from third and fourth rings were used for calculating the mosaicity. However, this has the disadvantage that mosaicity of such grains is underestimated arising from problems with the background. Due to this reason, average mosaicity was calculated only for grains with radiuses up to 130 μm.

[3] In this way, the mosaicity calculated is the average of maximum orientation difference in multiple directions. This was done in order to compare the mosaicity with equivalent grain radius.

$$\Delta\omega = \omega_{step}\left(\frac{I_1}{I_2} + (n-2) + \frac{I_n}{I_{n-1}}\right) \tag{S(iii)}$$

where ω_{step} is the rotation step during acquisition of each diffraction pattern, n is the number of diffraction patterns in which the diffraction spot is present, I_n is the intensity of the diffraction spot in the n-th diffraction pattern.

Equation S(iii) takes into account the fact that the grain is not in diffraction for the whole ω_{step} in the first and the last diffraction pattern. The mosaicity of the grain from the diffraction spot is then equal to the rotation of plane normal, $\Delta\theta$, calculated from Eq. S(ii). In this method, the maximum error in characterizing the mosaicity is equal to the value of $\Delta\theta$ corresponding to half the value of ω_{step}.

5. The value of mosaicity of the grain, calculated by the procedure mentioned above, is always in only one direction in the grain. In reality, however, the mosaicity can be slightly different in different directions. Thus, the average value of mosaicity of the grain is calculated by averaging the mosaicity corresponding to different diffraction spots from the grain.

3.1.3 Calculation of Rotation of Average Plane Normal

The average normal to a diffracting plane was calculated using the centre of mass of the diffraction spots belonging to the grain. The rotation of the average plane normal was then calculated by calculating the angle between the average plane normal of the spots for the first and the successive sweeps.

The following procedure was used to calculate the rotation of the average plane normal:

1. The direction of plane normal of a reflection corresponding to the orientation of the center of mass for an austenite grain is calculated by assuming that the center of mass of the grain is present in the center of the sample and in the center of the beam. This assumption does not give any error for the present calculation if the center of mass of the grain does not move more than 100 μm during coarsening.
2. The center of mass of the diffraction spot is used to calculate the direction of the average plane normal.
3. The rotation of the average plane normal is calculated by calculating the angle between the average plane normal of the grain for the first and the successive sweeps.
4. The value of rotation of the average plane normal is then calculated by averaging the rotations per sweep calculated from different diffraction spots from the same grain.

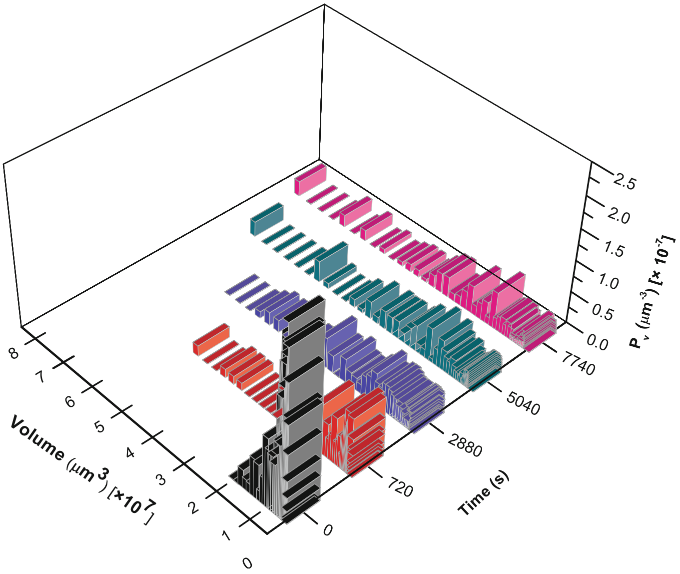

Fig. 4 Evolution of austenite grain size distribution (P_v) during isothermal annealing at 1,273 K

4 Results

Figure 4 shows the evolution of the volume-weighted-grain-size distribution (P_v) in the sample as a function of isothermal annealing time. It can be seen that, consistent with the general idea of grain coarsening, the fraction of the illuminated volume occupied by small grains is high in the beginning of isothermal annealing which gradually decreases as the coarsening progresses. This is reflected in Fig. 5, where the volume-averaged grain volume (red symbols) and the number of grains in the illuminated volume (black symbols) as a function of annealing time are shown. It can be seen that as coarsening progresses, the average grain volume increases and the number of grains in the illuminated volume decreases.

The average volume of austenite grains (Fig. 5, red symbols) increased from 1.24×10^6 μm^3 at $t = 0$ s to 9.08×10^6 μm^3 at $t = 7{,}740$ s. The best fit (Fig. 5, blue curve) of the average austenite grain size data to Eq. (1) gives value of the grain coarsening exponent $n = 8.3$. This value is much higher than the reference value of 2, an observation made more often in literature [2]. During annealing, the number of grains in the illuminated volume decreased from 2,385 at $t = 0$ s to 1,201 at $t = 7{,}740$ s (Fig. 5, black symbols). Out of the 2,385 initial grains, 104 grains increased in volume, 283 had an eventual change in volume less than 5 %, 814 grains decreased in volume by more than 5 % and 1,184 grains disappeared completely.

To highlight the relationship between size and mosaicity of grains, the average mosaicity for all the grains in the illuminated volume is plotted in Fig. 6 as a

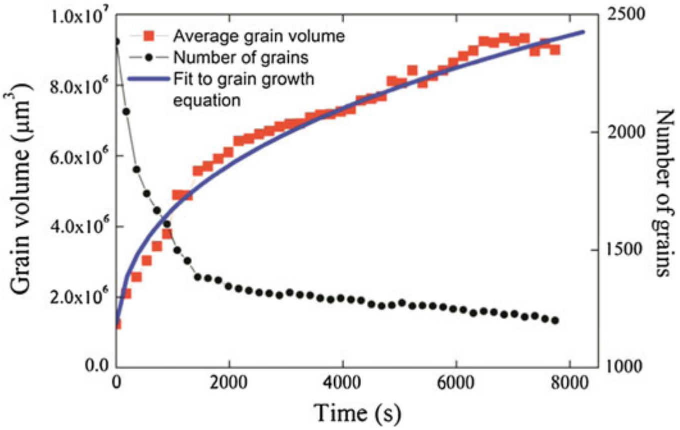

Fig. 5 Grain characteristics during isothermal annealing at 1,273 K. Evolution of number of grains in the illuminated volume as a function of annealing time (*black circles*) and evolution of volume-averaged grain volume as a function of annealing time (*red squares*). The *blue curve* shows the best fit to Eq. (1)

Fig. 6 Plot of the average mosaicity of all the grains during isothermal annealing as a function of grain radius

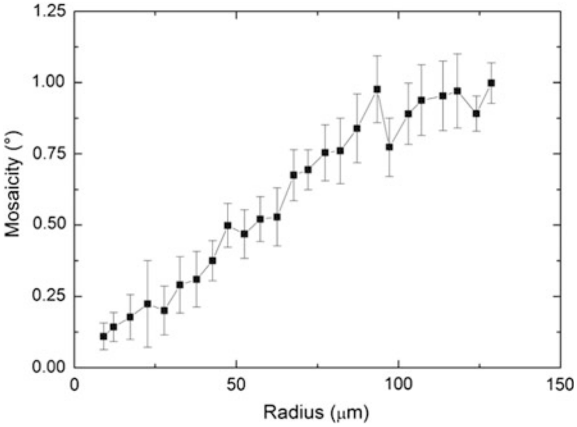

function of the equivalent grain radius (calculated from grain volume by assuming spherical grain shape). The error bars for the average mosaicity give the standard deviation of the observed mosaicity among the observed grains. Figure 6 shows that there exists an approximately linear relationship between mosaicity and grain radius.

For five austenite grains out of the 2,385 observed grains, Fig. 7 shows the evolution of grain volume, mosaicity and rotation of the average plane normal. It can be seen that, in comparison to the average grain coarsening behavior shown in Fig. 5 (red symbols), the volume evolution of individual austenite grains varies considerably. Figure 7a shows an example of an austenite grain that grows continuously over time. The evolution of the grain is similar to the average grain

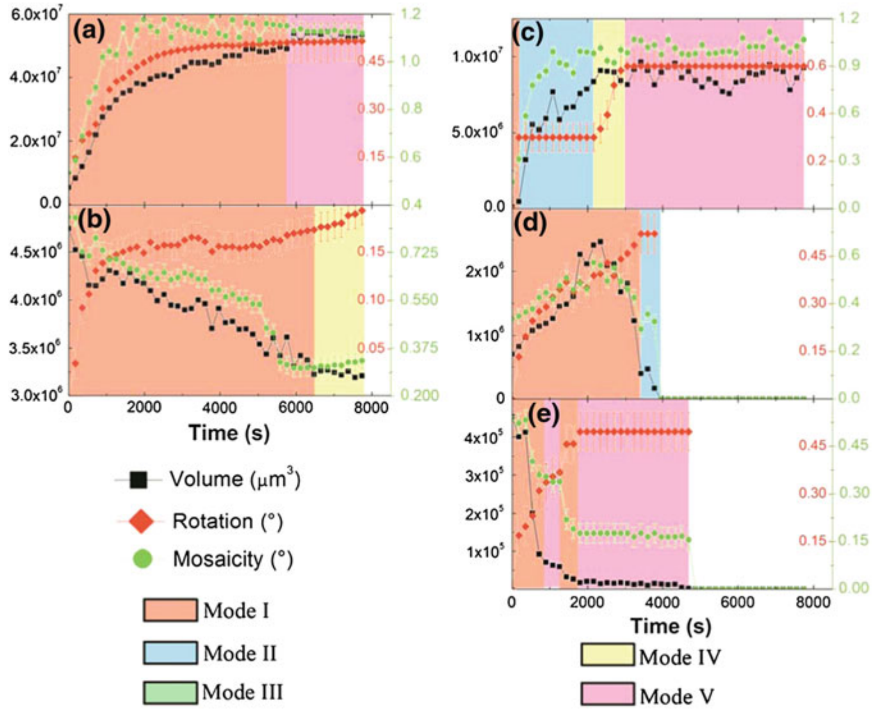

Fig. 7 Evolution of grain volume (*black squares*), cumulative rotation of average plane normal with respect to the original orientation (*red diamonds*) and change in mosaicity (*green circles*) of individual austenite grains during isothermal annealing at 1,273 K. Different shading colors represent regions of different modes shown in Fig. 8. **a** Example of an austenite grain which increases in size. **b** An austenite grain shrinking continuously over time. **c** Example of an austenite grain which grows first and then has constant volume. **d** Example of a grain which initially grows and then shrinks to disappear. **e** Example of a grain which decreases in volume, becomes stable and then shrinks to disappear. The error bars are calculated based on the error in measurement of the quantity

coarsening behavior shown in Fig. 5. However, the grains shown in Fig. 7b–e exhibit a combination of evolution of size of the grains completely different from the evolution of the average grain size in Fig. 5. The grain in Fig. 7b shrinks continuously; the grain in Fig. 7c witnesses rapid growth and then stabilizes in volume; the grain in Fig. 7d first grows, followed by shrinkage, and then disappears; and the grain in Fig. 7e shrinks, stabilizes in volume and then disappears.

A crucial feature of Fig. 7a is the development of mosaicity of the grain, which follows evolution of volume of the growing grain. This is consistent with the results for average mosaicity of all the grains shown in Fig. 6. The grains shown in Fig. 7b–e exhibit the same behavior, that is, the mosaicity of a grain follows the evolution of its volume. This shows that the direct relationship between mosaicity and size of the grains is also maintained during coarsening. Furthermore, Fig. 7a–e show that the average orientation of diffracting plane normal for the grains changes during coarsening. The information shown in Figs. 6 and 7 is unique in terms of the extended insight that can be obtained into the behavior of individual grains during coarsening.

5 Discussion

It is shown in Figs. 6 and 7 that the mosaicity of a grain is directly proportional to its radius and that this relationship holds true during coarsening. The direct relationship between grain mosaicity and radius implies that crystallographic orientation gradients exist in the grains, which persist during coarsening such that during growth of a grain the variations in its orientation increase. The presence of orientation spreads in well-annealed grains has been observed before in literature [27], but the present measurements of constant orientation gradients in grains during coarsening are first of their kind. This is very interesting, since even though, from a theoretical viewpoint, the presence of variations in orientations of crystals is thermodynamically unfavorable [2], the present observations show that not only are crystallographic orientation gradients present in the grains, but also that their magnitude does not reduce during coarsening, but remains constant instead.

Based on the observation of maintenance of constant orientation gradients, a total of five different modes of grain evolution (shown in Fig. 8 and Table 1) can occur:

1. Mode I—anisotropic growth, I(a), or shrinkage, I(b), leads to an increase in the total mosaicity of the grain and a change in the average orientation.
2. Mode II—isotropic growth, II(a), or shrinkage, II(b), leads to increase in total mosaicity but the average orientation remains constant.
3. Mode III—combination of anisotropic growth and shrinkage result in the same volume, however, the mosaicity increases in one direction while it decreases in another direction. The average orientation changes after annealing in mode III(a). Another variant, mode III(b), of this mode is when the average orientation of the grain remains constant while the mosaicity in different direction changes.
4. Mode IV—combination of anisotropic growth and shrinkage results in the same volume and mosaicity of the grain, whereas the average orientation changes after annealing.
5. Mode V—no movement of grain boundaries occurs. Volume, mosaicity and average orientation of the grain remain constant.

The case of shrinkage is analogous to growth and additional features of each mode are explained in Table 1. Different shading colours in Fig. 7 are used to highlight the mode of evolution of the grains in different periods during annealing. An interesting case is the grain shown in Fig. 9, the volume of which remains constant during annealing but the grain exhibits a combination of Mode III (which

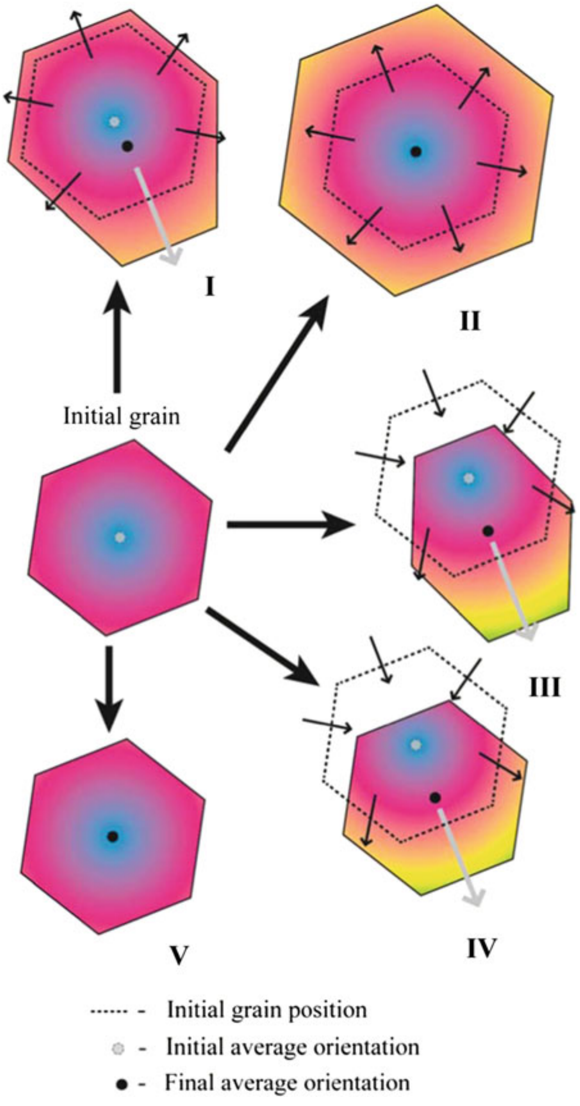

Fig. 8 Schematic illustration of the possible effects of grain evolution on mosaicity and average orientation of the austenite grains for the simplified case of grains having a constant orientation gradient in radial direction. Colors represent orientation. The cases of shrinkage are analogous to growth

indicates changes in shape), Mode IV (which indicates no change in shape but change in centre-of-mass position) and Mode V (which indicates no apparent grain boundary movement). In order to highlight shape effects, mosaicity of the grain in Fig. 9 is calculated using a single diffraction spot such that mosaicity in only one direction is measured. Even though the total volume of the grain remains constant, local grain boundary motion combined with constant orientation gradients can lead to changes in mosaicity and average orientation as seen in Fig. 9.

Table 1 Features of the different modes of evolution of grains shown in Fig. 9

Mode no.	Volume	Rotation of average plane normal	Mosaicity
I(a)	+	Δ	+
I(b)	−	Δ	−
II(a)	+	=	+
II(b)	−	=	−
III(a)	=	Δ	±
III(b)	=	=	±
IV	=	Δ	=
V	=	=	=

The corresponding change in grain volume, rotation of the average plane normal and mosaicity is listed. For rotation of the plane normal, there is no distinction between + or − and change is indicated by Δ. For mosaicity, ± means increase in one direction and decrease in another direction

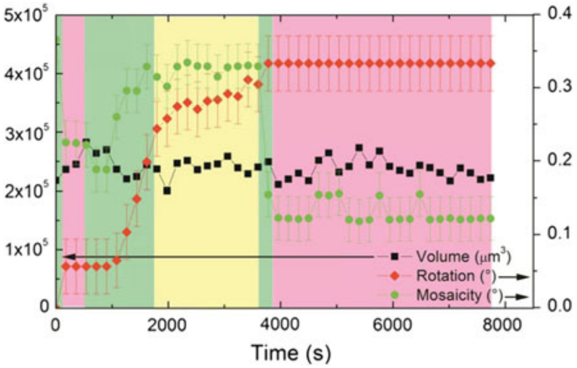

Fig. 9 Example of evolution of grain volume (*black squares*), cumulative rotation of average plane normal with respect to the original orientation (*red diamonds*) and change in total mosaicity (*green circles*) of an austenite grain with constant volume. The axis on *left* is for volume of the grain and the axis on *right* is for the rotation of the diffracting plane normal and the mosaicity of the grain. Different shading colors (legend in Fig. 7) represent regions of different modes shown in Fig. 8

In literature, it has been proposed by the use of simulations that grains in nanocrystalline size range can rotate during coarsening [28, 29], similar to the observed change in orientation of the average diffracting plane normal for the grains in Fig. 7. However, the grains shown in Fig. 6 are of a much bigger size (of the order of tens to hundreds of μm in radius) and rotation of the whole volume of these large grains during coarsening in absence of external stresses is not expected. The constant orientation gradients in grains can be considered to explain the observed changes in average diffracting plane normal. The average orientation of a grain, if the observed constant gradients in orientation are present, is essentially the orientation of centre of mass of the grain. Thus, in case of anisotropic growth (or shrinkage) of grains, when centre of mass of the grains shifts, the average

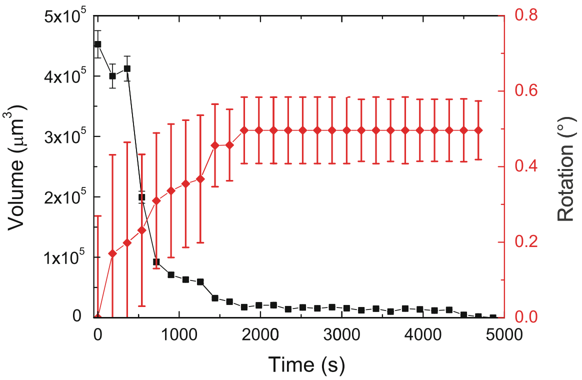

Fig. 10 Example of an austenite grain, same as in Fig. 7e, for which orientation in the beginning of isothermal annealing is completely different from orientation just before disappearing. Evolution of grain volume is shown by *black squares* and cumulative rotation of the average diffracting plane normal with respect to the original orientation is shown by *red diamonds*. The error bars of rotation of the average diffracting plane normal are equal to the mosaicity of the grain

orientation of grains changes as well. An extreme case is for the grain in Fig. 6e shown in Fig. 10, where the error bars of rotation of the average diffracting plane normal are equal to the mosaicity of the grain and thus the limits of the error bars represent the extrema of orientation in the grain. The observed change in average orientation and the reduction in mosaicity mean that no part of the grain remaining at 4,000 s has the same orientation as any part of the grain which was present at the start of isothermal annealing. This is particularly interesting, since, in case of an ex situ study, if the same grain was observed at the beginning of annealing and at 4,000 s into annealing, the different orientations would suggest that a new grain had nucleated.

Having established that grains at high temperatures have orientation gradients which remain constant during coarsening, the possible implications of the results on the process of grain coarsening are now examined. Even though the presence of orientation spreads in grains is well known [2, 3, 27], their influence on the process of coarsening has not been explored before.

Grain coarsening at high temperatures in polycrystalline materials occurs in order to reduce the total interface energy of the system ($\int \gamma \mathrm{d}A$, with γ the specific interfacial energy and the integration running over the grain boundary area in the microstructure). For each grain boundary, its contribution to the total interface energy of the system can be reduced either by reducing the contributing interface area, A, or the specific interface energy, γ. Reduction in A takes place by increase of the radius of curvature of the grain boundaries, so-called capillarity-driven grain coarsening [2]. It has been proposed before by means of simulations that γ can be reduced by changes in the inclination of the grain boundaries [30]. The average interface energy can also be reduced by direct elimination of high energy grain boundaries during grain coarsening [10].

The present observations show that orientation gradients are present in grains and that these gradients remain constant during coarsening. This means that, in the case of neighbouring grains, both having an orientation gradient, the movement of a grain boundary combined with observed constant orientation gradient in all regions of the grains would change the local misorientation (difference in orientation at opposite sides of the grain boundary) across the grain boundary. This can be expected to affect the specific grain-boundary energy (γ), since it is known that γ depends on the misorientation angle (θ) between the grains constituting the grain boundary [3]. In simple terms, the relation between change in interface energy ($\Delta\gamma$) and the change in misorientation ($\Delta\theta$) can be written as:

$$\Delta\gamma = \left(\frac{\partial\gamma}{\partial\theta}\right)\Delta\theta \tag{4}$$

Depending on the sign and magnitude of $(\partial\gamma/\partial\theta)$, Eq. (4) can result in three cases: $\Delta\gamma = 0$, $\Delta\gamma < 0$ and $\Delta\gamma > 0$. In case $\Delta\gamma = 0$, there would be no effect on the driving force for grain coarsening, G, and grain coarsening would be driven only by curvature. In cases when $\Delta\gamma$ is negative, for example in the case of low-angle grain boundaries with decreasing $\Delta\theta$, this would result in a decrease in G, since G is directly proportional to γ. This results, in turn, in additional decay of the rate of grain coarsening during the process. The motion of the grain boundary in this fashion would continue with an ever decreasing rate until the grain boundary reaches a minimum in γ. In cases where $\Delta\gamma$ is positive, the motion of the grain boundary would lead to an increase in γ. Even though γ increases, the total interface energy contribution of the grain boundary, $\int \gamma \mathrm{d}A$, could still continue to decrease as long as the decrease in the interface area, A, can compensate for the increase in γ. A meta-stable condition would be reached when the motion of the grain boundary in any direction leads to an increase in $\int \gamma \mathrm{d}A$, either by increasing A or γ. Thus, for materials with a distribution of grain boundaries of multiple characters, the combined effect of the latter two cases would be a reduction in the overall rate of grain coarsening and increase in the grain coarsening exponent, n. It must be noted here that in situ experimental measurement of γ during coarsening is not possible with the techniques presently available.

The next step is to examine the probability of occurrence of the two cases which affect n. The change in misorientation due to movement of grain boundaries and the added imposition of maintenance of the orientation gradient will be of the order of a degree. This means that the grain boundaries, the energy of which is strongly dependent on the misorientation, for example, low angle tilt boundaries or special $\sum$ boundaries, are affected strongly by the relatively small change in misorientation. It is already known that the fraction of these special low energy grain boundaries in materials is high and increases during annealing [10, 31, 32]. Thus, always a high fraction of grain boundaries in materials would be affected by the change in misorientation resulting from maintenance of a constant orientation gradient.

6 Conclusions

Grain coarsening of austenite in a binary Fe-2 wt% Mn alloy was studied by measuring the evolution of volume, average crystallographic orientation and mosaicity of more than 2,000 individual austenite grains during annealing at 1,273 K. The following conclusions can be drawn from the measurements:

1. For more than 2,000 austenite grains, it was observed that the average mosaicity of all the grains is approximately directly proportional to the average grain size of the grains.
2. For individual grains, it is shown that mosaicity is directly proportional to the grain volume at all times during coarsening at 1,273 K. This means that constant orientation gradients exist in the grains which persist during coarsening.
3. The persistence of orientation gradients coupled with movement of grain boundaries results in changes in the grain boundary character, affecting the coarsening rate.
4. Changes in the average orientation of large (10–200 μm in radius) austenite grains were observed during coarsening.
5. Five modes of grain growth are proposed: anisotropic (I) and isotropic (II) growth (or shrinkage); movement of grain boundaries resulting in no change in volume but change in shape (III) and movement of grain boundaries resulting in no change in volume and mosaicity, but in the average crystallographic orientation (IV); and no movement of grain boundaries (V).

Acknowledgments The authors thank E. G. Dere for assistance during the synchrotron measurements, F. Gersprach for discussions on the generation of defects by moving grain boundaries and C. Kwakernaak for EPMA analysis. This research is financially supported by the Foundation for Technical Sciences (STW) of the Netherlands Organization for Scientific Research (NWO). The authors thank the European Synchrotron Radiation Facility for the provision of beamtime.

A.1 7 Appendix

A.1.1 Equation of Volume of a Grain

The diffracted intensity I_g per unit time from a single grain, rotated through the Bragg condition in order to illuminate the whole grain, is given by the following expression for the kinematic approximation (4, 5):

$$I_{grain} = \frac{I_0}{\Delta\theta}\left(\frac{\mu_0}{4\pi}\right)^2 \frac{e^4}{m^2} \frac{\lambda^3 F_{hkl}^2}{V_c^2} V_g L_g P \exp(-2M) \tag{S(vi)}$$

where I_0 is the incident intensity of photons, F_{hkl} is the structure factor of the *hkl*-reflection, λ is the photon wavelength, V_g is the volume of the grain, $\Delta\theta$ is the change in scattering vector over which the grain is in reflection (Eq. S(ii)), V_c is the volume of the unit cell, $P = (1 + \cos^2 2\theta)/2$ is the polarization factor, and $L_g = 1/\sin 2\theta$ is the Lorentz factor, where 2θ is the scattering angle. The Debye-Waller factor exp(−2 M) accounts for the thermal vibrations of atoms, with

$$M = \frac{6h^2 T}{mk_B \Theta^2}\left[\phi(x) + \frac{x}{4}\right]\left(\frac{\sin\theta}{\lambda}\right)^2 \tag{S(vii)}$$

where h is the Planck constant, m is the mass of the vibrating atom, k_B is the Boltzmann constant, Θ is the Debye temperature, $x = \Theta/T$ is the relative temperature, T is the temperature and

$$\phi(x) = \frac{1}{x}\int_0^x \frac{\xi}{\exp(\xi) - 1} d\xi \tag{S(viii)}$$

The integrated intensity I_p per unit time of a *hkl*-diffraction ring of a polycrystalline material (often termed as powder in diffraction) with randomly oriented grains is given by (4, 5)

$$I_{powder} = \Phi_0 \left(\frac{\mu_0}{4\pi}\right)^2 \frac{e^4}{m^2} \frac{\lambda^3 m_{hkl} F_{hkl}^2}{V_c^2} V_{gauge} L_p P \exp(-2M) \tag{S(ix)}$$

where m_{hkl} is the multiplicity factor of the *hkl*-ring and V_{gauge} is the volume of the diffracting phase. The Lorentz factor for a powder is given by $L_p = 1/(4\sin\theta)$.

The volume of an individual grain is calculated from the measured grain intensity I_g normalized by the powder intensity I_p of the *hkl*-ring in which the reflection from the individual grain appeared. In case the diffraction spot appears in more than one diffraction pattern, the intensity from the grain is divided by a factor k, equal to the number of diffraction patterns in which the spot is present. Combining Eqs. S(vi)) and S(ix) and introducing k gives Eq. S(i)

$$V_g = \frac{1}{2} m_{hkl} \cos(\theta) V_{gauge} \frac{I_g}{kI_p} \Delta\theta \tag{S(i)}$$

Equation S(i) is similar to the equation for volume of a grain used by Lauridsen et al. (6) and Offerman et al. (7). However, the following corrections have been made-

1. In the current analysis, diffraction spots distributed in more than one diffraction pattern were used for the volume calculation. Thus, the additional factor k is used.
2. The expression for $\Delta\theta$ used by Lauridsen et al. and Offerman et al. is $\Delta\theta = \Delta\omega \cdot |\sin(\eta)|$. However, this is an approximation which does not hold for low values of η. In the current analysis, Eq. S(ii) is used which is the exact

form of the expression for $\Delta\theta$. From Fig. S6, the expression for $\Delta\theta$ can be calculated as follows:

The projection along the *x-axis* of the vector (*x, y, z*) of length *r* in the direction of the plane normal before rotation is given as

$$x = -r \sin\theta$$

After rotation, the vector is given as

$$x' = -r \sin(\theta + \Delta\theta) \tag{S(x)}$$

Also, applying the rotation transform on vector r' gives

$$x' = -r \sin\theta \cos\Delta\omega - r \sin\eta \sin\Delta\omega \cos\theta \tag{S(xi)}$$

Combining Eqs. S(x) and S(xi) gives Eq. S(ii)

$$\Delta\theta = \sin^{-1}(\sin(\theta)\cos(\Delta\omega) + \cos(\theta)\sin|\eta|\sin(\Delta\omega)) - \theta \tag{S(ii)}$$

References

1. Sharma H, Huizenga RM, Bytchkov A, Sietsma J, Offerman SE (2012) Observation of changing crystal orientations during grain coarsening. Acta Materialia 60:229–237
2. Humphreys FJ, Hatherly M (2004) Recrystallization and related annealing phenomena. Elsevier, Oxford
3. Gottstein G, Shvindlerman LS (1999) Grain boundary migration in metals: thermodynamics, kinetics, applications. CRC Press, Boca Raton
4. Holm EA, Foiles SM (2010) How grain growth stops: a mechanism for grain-growth stagnation in pure materials. Science 328:1138
5. von Neumann J (1952) Discussion. In: Herring C (ed) Metal interfaces. American Society for Metals, Cleveland, p 108
6. Hillert M (1965) On the theory of normal and abnormal grain growth. Acta Metall 13:227
7. Mullins WW (1989) Estimation of the geometrical rate constant in idealized three dimensional grain growth. Acta Metall 37:2979
8. Glazier JA (1993) Grain growth in three dimensions depends on grain topology. Phys Rev Lett 70:2170
9. MacPherson RD, Srolovitz DJ (2007) The von Neumann relation generalized to coarsening of three-dimensional microstructures. Nature 446:1053
10. Rohrer GS (2005) Influence of interface anisotropy on grain growth and coarsening. Annu Rev Mater Res 35:99
11. Militzer M, Giumelli A, Hawbolt EB, Meadowcroft TR (1996) Austenite grain growth kinetics in Al-killed plain carbon steels. Metall Mater Trans A Phys Metall Mater Sci 27:3399
12. Zhou TH, O'Malley RJ, Zurob HS (2010) Study of grain growth kinetics in delta-ferrite and austenite with application to thin-slab cast direct-rolling microalloyed steels. Metall Mater Trans A Phys Metall Mater Sci 41A:2112

13. Mullins WW (1958) The Effect of Thermal Grooving on Grain Boundary Motion. Acta Metall 6:414
14. Krill CE, Helfen L, Michels D, Natter H, Fitch A, Masson O et al (2001) Size-dependent grain-growth kinetics observed in nanocrystalline Fe. Phys Rev Lett 86:842
15. Margulies L, Winther G, Poulsen HF (2001) In situ measurement of grain rotation during deformation of polycrystals. Science 291:2392
16. Poulsen HF, Nielsen SF, Lauridsen EM, Schmidt S, Suter RM, Lienert U et al (2001) Three-dimensional maps of grain boundaries and the stress state of individual grains in polycrystals and powders. J Appl Crystallogr 34:751
17. Offerman SE, van Dijk NH, Sietsma J, Grigull S, Lauridsen EM, Margulies L et al (2002) Grain nucleation and growth during phase transformations. Science 298:1003
18. Larson BC, Yang W, Ice GE, Budai JD, Tischler JZ (2002) Three-dimensional X-ray structural microscopy with submicrometre resolution. Nature 415:887
19. Schmidt S, Nielsen SF, Gundlach C, Margulies L, Huang X, Jensen DJ (2004) Watching the growth of bulk grains during recrystallization of deformed metals. Science 305:229
20. Schmidt S, Olsen UL, Poulsen HF, Sørensen HO, Lauridsen EM, Margulies L et al (2008) Direct observation of 3-D grain growth in Al–0.1% Mn. Scripta Mater 59:491
21. Poulsen HF (2004) Three-dimensional X-ray diffraction microscopy-mapping polycrystals and their dynamics. Springer, Berlin
22. Sharma H, Wattjes AC, Amirthalingam M, Zuidwijk T, Geerlofs N, Offerman SE (2009) Multipurpose furnace for in situ studies of polycrystalline materials using synchrotron radiation. Rev Sci Instrum 80:7
23. Sharma H, Huizenga RM, Offerman SE (2012) A fast methodology to determine characteristics of large numbers of grains using 3DXRD. I: overlapping diffraction peaks and global parameters. J Appl Crystallogr 45:693–704
24. Sharma H, Huizenga RM, Offerman SE (2012) A fast methodology to determine characteristics of large numbers of grains using 3DXRD. II: volume, centre-of-mass position and crystallographic orientation of grains. J Appl Crystallogr 45:705–718
25. http://sourceforge.net/apps/trac/fable/wiki. Last Accessed 01 Aug 2011
26. Warren BE (1990) X-ray diffraction. Dover Publications, New York
27. Landheer H (2010) Nucleation of ferrite in austenite. PhD thesis. Department of Materials Science and Engineering, Delft University of Technology, Delft
28. Haslam AJ, Phillpot SR, Wolf H, Moldovan D, Gleiter H (2001) Mechanisms of grain growth in nanocrystalline fcc metals by molecular-dynamics simulation. Mater Sci Eng A Str Mater Prop Microstruct Process 318:293
29. Farkas D, Mohanty S, Monk J (2007) Linear Grain Growth Kinetics and Rotation in Nanocrystalline Ni. Phys Rev Lett 98:165502
30. Upmanyu M, Srolovitz DJ, Lobkovsky AE, Warren JA, Carter WC (2006) Simultaneous Grain Boundary Migration and Grain Rotation. Acta Mater 54:1707
31. Watanabe T, Fujii H, Oikawa H, Arai KI (1989) Acta Metall 37:941
32. Holm EA, Hassold GN, Miodownik MA (2001) Acta Mater 49:2981

In Situ Observations of Microstructural Evolution During Annealing or Deformation in an Electro-Deposited Fine-Grained Iron

Yuhua Su, Y. Tomota, S. Harjo, J. Suzuki and Y. Adachi

Abstract Fine grained electro-deposited pure iron shows ultra-high Lankford value larger than 7. Tensile deformation behavior at room temperature was studied using in situ neutron diffraction and semi in situ scanning electron microscopy with electron back scatter diffraction (SEM/EBSD) observation. The characteristic deformation mechanism to bring high R value accompanying grain coalescence is made clear. The sheet was annealed to observe hydrogen behavior and grain growth using thermal desorption spectroscopy, small angle neutron scattering, in situ neutron diffraction and SEM/EBSD. The shape of grain was changed from needle-like shape to polygonal with annealing, leading to a decrease of R value.

Y. Su (✉)
Institute of Applied Beam Science, Graduate School of Science and Engineering,
Ibaraki University, 4-12-1 Nakanarusawa, Hitachi, Ibaraki 316-8511, Japan
e-mail: yuhua.su@j-parc.jp

Y. Su
Neutron Science Section, MLF Division, J-PARC Center, Japan Atomic Energy Agency,
2-4 Shirane Shirakata, Tokai Naka, Ibaraki 319-1195, Japan

Y. Tomota
Institute of Applied Beam Science, Graduate School of Science and Engineering,
Ibaraki University, 4-12-1 Nakanarusawa, Hitachi, Ibaraki 316-8511, Japan

S. Harjo
J-PARC Center, Japan Atomic Energy Agency, 2-4 Shirane Shirakata, Tokai,
Ibaraki 319-1195, Japan

J. Suzuki
Research Center for Neutron Science and Technology, Comprehensive Research
Organization for Science and Society (CROSS), Tokai, Ibaraki 319-1106, Japan

Y. Adachi
Graduate School of Science and Engineering, Kagoshima University,
1-21-24 Korimoto, Kagoshima 890-8580, Japan

T. Kannengiesser et al. (eds.), *In-situ Studies with Photons, Neutrons and Electrons Scattering II*, DOI: 10.1007/978-3-319-06145-0_8,

Keywords In situ neutron diffraction · Small angle neutron scattering (SANS) · In situ scanning electron microscopy · Thermal desorption spectroscopy (TDS) · Hydrogen

1 Introduction

Neutron diffraction is an effective probe to evaluate stress and is widely applied to fundamental studies of materials. Because the crystallographic response can be correlated to bulk properties of the material, neutron diffraction is suitable to investigate lattice (elastic) strain in differently oriented grains and texture evolution during plastic deformation [1–5]. On the other hand, electron backscatter diffraction (EBSD) analysis provides local crystallographic information such as misorientation angles. However, the information is limited to free-surface deformation. An electrodeposited film with a grain size of several hundred nanometers is an appropriate sample to determine deformation behavior by both in situ neutron diffraction and semi in situ EBSD observation [6, 7], which provide comprehensive information, i.e., bulk average and microscopic details. Yoshinaga et al. have reported that it is difficult to explain the reason of ultra-high Lankford (R) value larger than 7.0 in the fine-grained electro-deposited pure iron sheet by employing a conventional slip deformation model [8–10]. Here, R value is usually determined by the plastic strain ratio, i.e., width strain to thickness strain measured by tensile test. Hence, the annealing and plastic deformation behavior of the UFG electrodeposited pure iron sheet was studied by small angle neutron scattering (SANS), in situ neutron diffraction and EBSD observations, with the purpose to investigate how neutron diffraction and EBSD results come together to elucidate the reason of grain coalescence and exceptionally high R value [11–13].

2 Microstructure and Mechanical Properties

Ultra-fine crystalline pure iron sheet used in this study was produced through industrial process by TohoZinc Co.Ltd, with thickness of about 1.5 mm and purity of more than 99.995 wt.%. The definition of specimen directions is presented schematically in Fig. 1. Tensile test specimens were cut from the sheets, with tensile direction shown in the axial direction (AD) of iron sheet. As shown in Fig. 2, the EBSD inverse pole figure maps and transmission electron microscopy (TEM) observation results of the as-deposited specimen. The microstructure consists of columnar or needle-like fine grains. From the top view shown in Fig. 2a and c, the grains appear equiaxed, but they are elongated along ND, as shown in

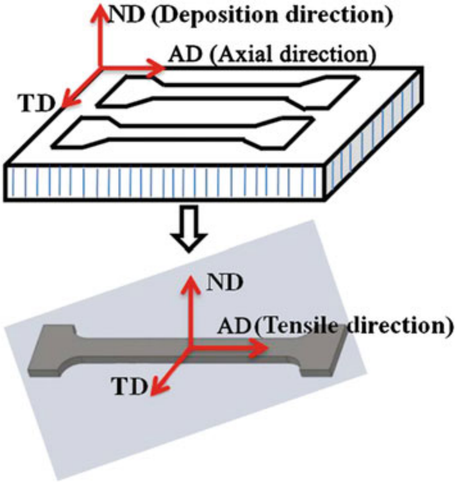

Fig. 1 Schematic diagram of the definition of specimen direction: tensile direction or rolling direction (*AD*), transverse direction (*TD*), and deposition direction, which is defined as the normal direction (*ND*)

Fig. 2b and d. The presence of strong {111} ⟨hkl⟩ fiber texture can also be confirmed from the orientation determination function (ODF) computed from EBSD data as described in Ref. [13]. The mean grain (column) diameter determined from the cross-sectional observation is approximately 800 nm. As was previously reported [14], TEM observations indicated strong strain contrast (residual stress) and small amounts of dislocations, which may be caused by the strain during electro-deposition process.

Such a strong texture was observed by X-ray [14, 15] and neutron diffraction profiles on a macroscopic scale as presented in Fig. 3: for AD, ND and TD of the as-deposited specimen. The neutron diffraction profiles were fitted with Rietveld refinement, as plotted in Fig. 3, and the profiles for different directions could be fitted well. Diffraction peak intensities for ND in Fig. 3 were obviously different from those in the other two directions. There is almost no difference between Fig. 3a and c, showing good reproducibility. The R value increases with increasing of the fraction of ⟨111⟩-oriented grains and decreasing of the amount of ⟨100⟩ -grains parallel to the sheet plane [16, 17]. In Fig. 3b, the ⟨222⟩ peak is dominant, confirming the presence of a strong {111} ⟨hkl⟩ texture. In addition, the ⟨200⟩ peak is invisible in ND. Therefore, the strong texture should be one of the major reasons for the high R value.

The nominal stress-strain curves measured during tensile test for the as-deposited and annealed specimens are shown in Fig. 4. For the as-deposited specimen, similar to many UFG metals, work hardening was quite small. Compared with the as-deposited specimen, the specimen annealed at 700 °C showed lower strength but higher elongation. Here, R value was determined by the strain ratio of the width to that of the thickness at a uniformly elongated region of the tension test specimen and the obtained values were 7.6, 5.2, and 2.2 for the as-deposited pure iron specimen and specimens annealed at 400 and 700 °C, respectively [14].

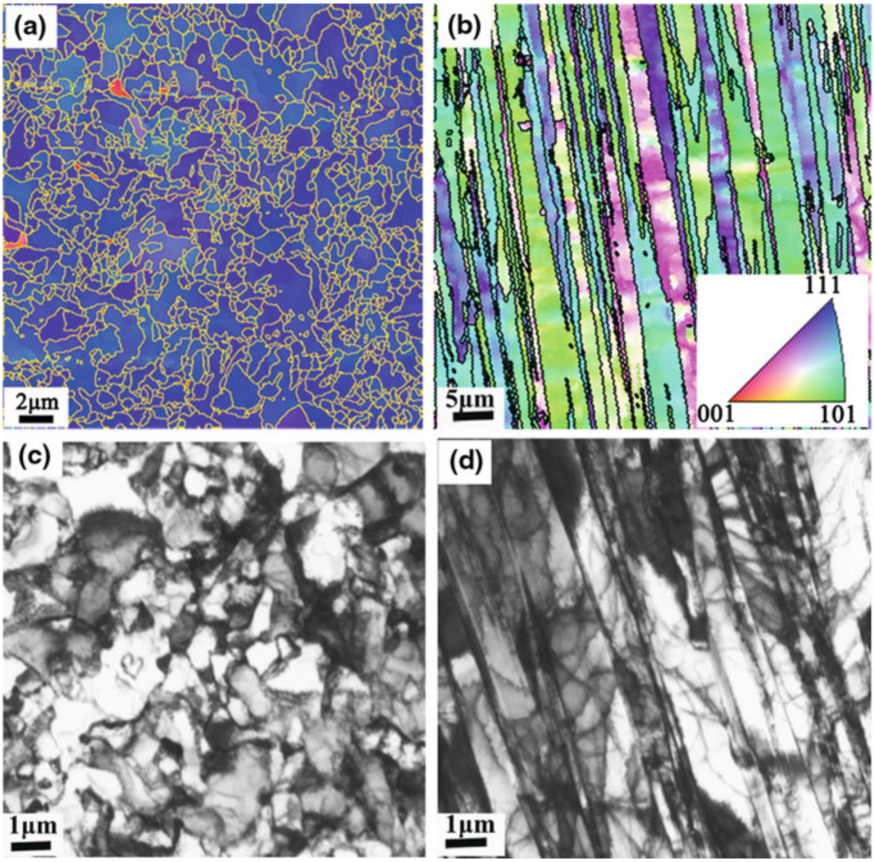

Fig. 2 Microstructures of the as-deposited pure iron sheet: **a** ND IPF map observed on the top surface, **b** TD IPF map observed from the cross-sectional observation, **c** TEM from the top surface and **d** TEM observed on the cross section

3 Annealing Behavior

Motegi et al. examined the influence of annealing on tensile behavior and found that the R-value became lower with increasing of annealing temperature [14]. Small angle neutron scattering (SANS) is an appropriate technique for measuring microstructure in a scale from several nanometers to micrometers for many materials compared with X-ray. Here, SANS and thermal desorption spectroscopy (TDS) were employed to investigate the hydrogen behavior in the electrodeposited pure iron with annealing. In addition, in situ neutron diffraction was performed for the as-deposited specimen during heating process, continuously, at MLF/J-PARC.

Fig. 3 Measured and fitted neutron diffraction profiles obtained in each 300 s of as deposited specimen: **a** AD, **b** ND and **c** TD

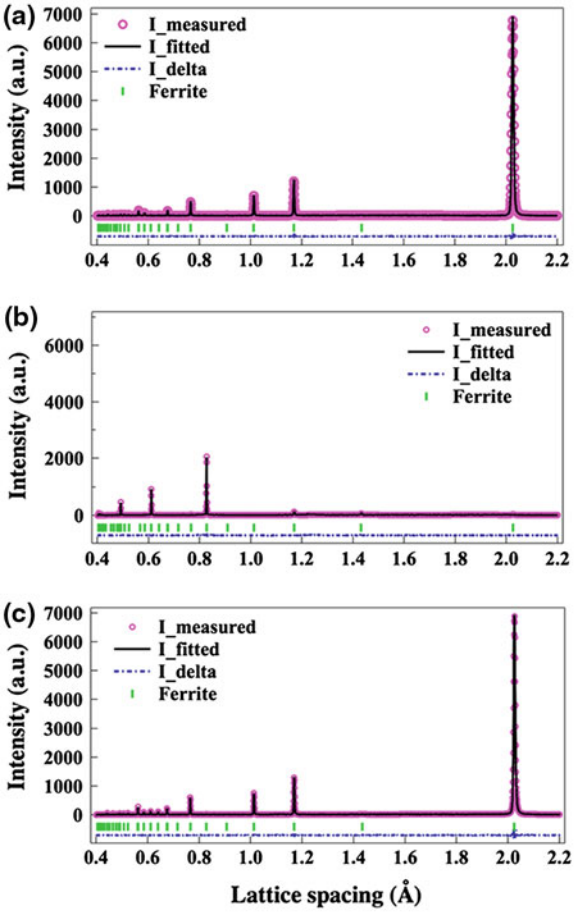

Fig. 4 Nominal stress-strain curves of tensile loading at room temperature for the as-deposited and annealed specimens

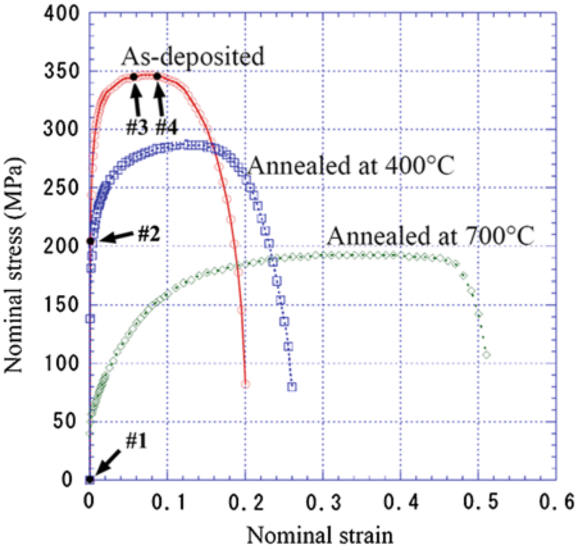

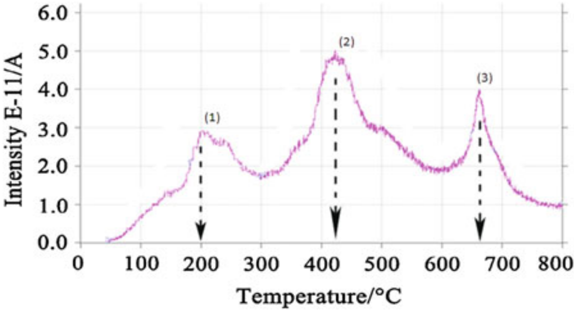

Fig. 5 Hydrogen TDS spectra obtained from the as-deposited specimen

3.1 TDS Measurement

Hydrogen was absorbed in the specimen preparation by electrolytic deposition process. Then, TDS of hydrogen was conducted for the deposited specimen with a heating rate of 8 °C/s in a temperature range from RT to 800 °C in a vacuum chamber, where 10 mm × 10 mm × 1 mm specimens were measured. Figure 5 shows hydrogen desorption profiles obtained from the TDS for the as-deposited specimen. There are three main peaks (1), (2) and (3) on the as-deposited specimen spectra at about 200, 450 and 680 °C, respectively. It is reported that the activation energy for hydrogen evolution from different trapping sites in pure iron increases in the order of grain boundaries, dislocations and microvoid, and that hydrogen is claimed to exist in the microvoids as a molecule.

3.2 SANS Experiments on Annealed Specimens

The as-deposited, 400, 700 °C annealed specimens for SANS measurement with size of 20 mm × 20 mm × 2 mm were prepared. SANS measurements were carried out with a small-angle neutron scattering spectrometer SANS-J-II equipped at the cold neutron source of JRR-3, JAEA. A magnetic field of 1T was applied in order to separate nuclear scattering component from magnetic scattering component. And the scattered intensity was recorded by a two-dimensional detector. The incident wave length was set to be 0.656 nm, which provided the scattering vector q ($q = 4\pi \sin\theta/\lambda$, 2θ is the scattering angle, with neutron wave length of λ) range of $5 \times 10^{-3}\ \mathrm{nm}^{-1} \leq q \leq 1.99\ \mathrm{nm}^{-1}$, corresponding to real structure sizes of the order of 3–1,000 nm).

The SANS intensity in a magnetic field is composed of an isotropic nuclear contribution and an anisotropic magnetic contribution. The nuclear and magnetic components can be separated from each other using the following formula [18–21],

$$I(q) = I_{Nuclear} + \sin^2 \alpha \cdot I_{Magnetic}(q) \tag{1}$$

where α is the angle between the scattering vector q and the magnetic field direction. The nuclear component of the scattering intensity can be determined at $\alpha = 0°$, while the sum of nuclear and magnetic intensity is found at $\alpha = 90°$. Figure 6a shows measured SANS nuclear scattering profiles for the pure iron specimens with a magnetic field of 1T. As seen, scattering intensity decreases with increasing of annealing temperature. So called "Guinier region" caused by the existence of nano-size inhomogeneity which causes SANS scattering contrast, for example, hydrogen bubble, is evidently observed in nuclear scattering profiles for the as-deposited and the 400 °C annealed specimens, while not for the 700 °C specimen. This indicates the disappearance of inhomogeneity by annealing at 700 °C. This is the prediction but very likely to be caused by hydrogen (see the TDS and SANS results). The purity of the present sample was more than 99.995 wt.%. If carbon is concerned, it must segregate at grain boundaries shortly with little contrast to SANS. It is interesting to compare this result with R values reported in [14] (7.6 for the as-deposited, 5.2 for the 400 °C annealed and 2.2 for the 700 °C annealed specimen). The average particle radius determined from the fitting with Guinier approximation [22, 23] was about 15 nm commonly for the as-deposited and 400 °C annealed specimens. A remarkable change in SANS profile for the 700 °C annealed specimen may be ascribed to a few reasons, i.e., defects like void, impurity elements like C and N, and hydrogen. By annealing at 700 °C, the microstructure changes from fine needle-like grains to coarse equiaxed grains as was reported in [12]. This change in grain size and shape is postulated to affect the SANS intensity at a lower q region than in the present measured region. If carbides or nitrides precipitate by annealing, this would increase the SANS intensity. Hence, the drastic decrease in the SANS intensity observed at $q = 0.02$ – 1.00 nm^{-1} in Fig. 6a is believed to be caused mostly by the hydrogen desorption from comparison between Figs. 5 and 6a. Hydrogen pores were not observed by TEM observation. Hence, this is very possible estimation, again by comparing TDS and microstructure observations with SANS.

The following equation can be used for profile fitting to get the particle size distribution assuming spherical inhomogeneity (independent spherical particles mode) [19, 20].

$$I(q) = \Delta\rho^2 N_d \int_0^\infty V^2(R) F^2(q,R) N(R) dR \tag{2}$$

In which, $\Delta\rho$ is the scattering length contrast between the particle and the matrix, $F(q,R)$ is particle shape factor, N_d is number density of the particle, $V(R)$ is the volume of the particle.

The fitted profiles for the deposited and the 400 °C annealed specimens were depicted in Fig. 6b showing good coincidence with the measurements, in which bubble quantity was computed based on the difference of scattering length density contrast $(\Delta\rho)$ between hydrogen bubble assuming 1 atm (0 °C, 101.325 kPa) and the iron matrix. Scattering length density is defined as:

Fig. 6 Effect of annealing on SANS profiles (**a**), and results of SANS profile analysis by sphere particle model fitting (**b**)

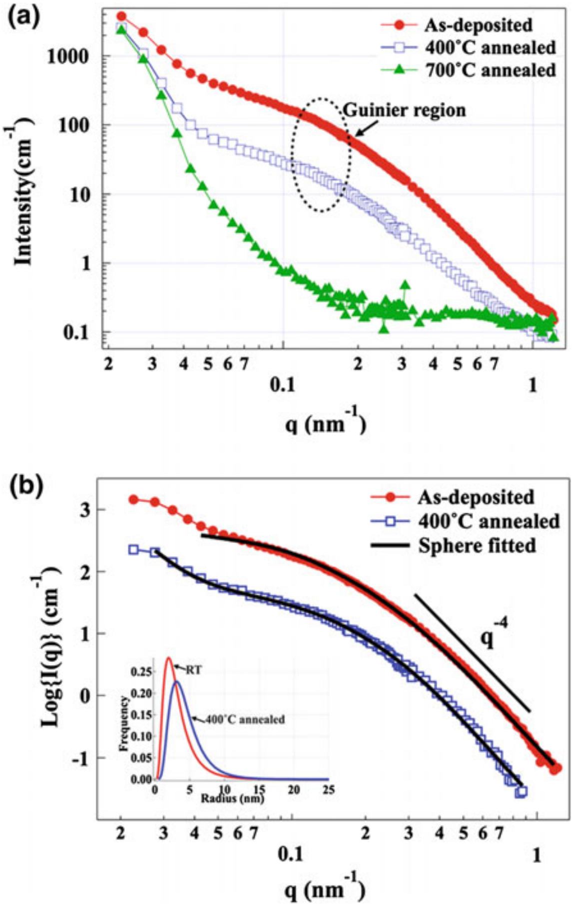

Table 1 Influences of annealing on size, number density and volume fraction of inhomogeniety (hydrogen) measured by SANS and TDS

Specimen	SANS by a sphere fitted method				TDS	
	Rave/nm	Vr/nm^{-3}	Nd/cm^{-3}	Vf/%	Wt./ppm	Vf/%
As-deposited	3.36654	470.694	1.74906e + 16	0.823	0.09	0.788
400 °C annealed	4.49462	806.504	1.49534e + 15	0.121	–	–

$$\Delta\rho = \rho_{H_2} - \rho_{\mathrm{Fe}} \tag{3}$$

As is shown in Table 1, from SANS results, hydrogen bubble size is postulated to become larger after 400 °C annealing. However, bubble number density and volume fraction decreased because of hydrogen desorption. The hydrogen volume fraction in the as-deposited specimen estimated by SANS was in excellent agreement with that measured by TDS. If hydrogen desorbs, the empty bubbles should remain. Such a bubble composed of vacancies must easily be coalescence and disappear by diffusion through grain boundaries. There would need further investigation to find the reason for Fig. 6b result.

3.3 In Situ Neutron Diffraction During Annealing

In situ neutron diffraction during annealing was performed for the as deposited pure iron, using a time-of-flight (TOF) diffractometer for engineering materials research, TAKUMI, at MLF/J-PARC [24, 25]. A specimen used was of rectangle shape with size of 5.5 × 7.5 × 15 mm by stacking 5 pieces of iron sheet. The neutron diffraction profiles were obtained simultaneously from the north and south detector banks for the axial direction (AD) and the normal (deposition) direction (ND) of a specimen, respectively. Step by step heating and holding for 720 s for the neutron diffraction experiments were performed. Neutron diffraction data collected in every 60 or 360 s respectively were used for profile analysis. Since an event mode of data acquisition system has been employed at MLF/J-PARC, the slicing time can be changed after the measurement taking the statistic reliability into consideration. Temperature was measured using a thermocouple attached onto a specimen.

The neutron diffraction profiles were fitted with Rietveld refinement, from which change of the lattice parameter, full width at half maximum (FWHM) and integrated intensity can be compared in the whole annealing process. Figure 7a plots the measured lattice parameter in the function of annealing time. Obviously, the north and south detectors show good agreement. With increase of annealing time, the lattice parameter increased. The heating process, i.e., change of temperature with annealing time was also plotted in Fig. 7a. It is the actual temperature measured by a thermal-couple attached on the specimen.

The degree of expansion $\frac{L_T - L_0}{L_0}$ divided by the change in temperature ΔT is called thermal expansion coefficient, where linear expansion coefficient α_{L} is given as follows,

$$\alpha_L = \frac{1}{L} \cdot \frac{dL}{dT} = \frac{L_T - L_0}{L_0 \cdot \Delta T} \tag{4}$$

Figure 7b shows the relationship between the measured lattice parameter in each 60 s and temperature during the whole annealing process. The lattice parameters show direct proportion with temperature, which increased with increase of temperature and then decreased after cooling, which should be caused by the expansion and contraction of the lattice spacing due to change of temperature. Therefore, the linear expansion coefficients of the pure iron sheet can be calculated and that is about 14.6×10^{-6} °C^{-1} during heating between 20 and 800 °C.

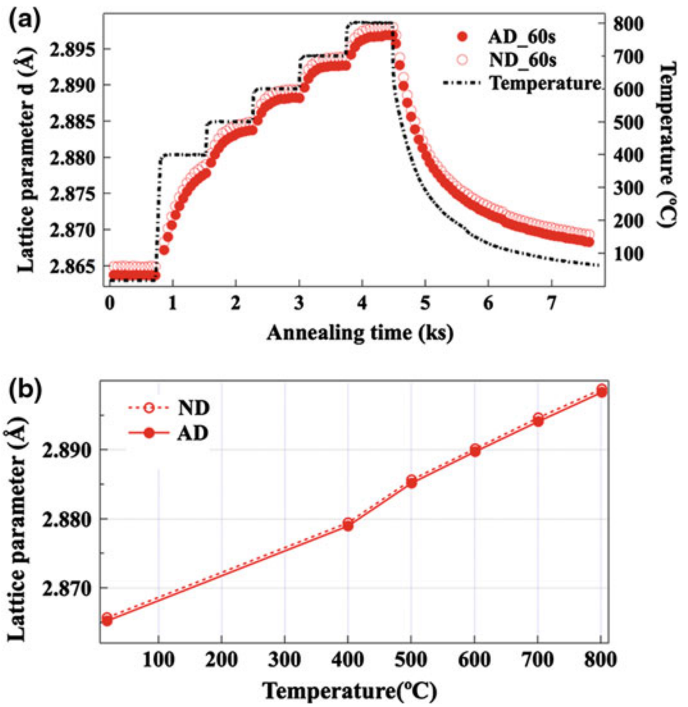

Fig. 7 Lattice parameter obtained during annealing fitted by the Z-Rietveld software

The texture evolution can be monitored by change of integrated intensity of {hkl} diffraction peaks. The change of different peaks in two directions were calculated by the equations as follows,

$$R_{h_ik_il_i} = \frac{\frac{I_{h_ik_il_i}}{V_{h_ik_il_i}}}{\sum_{i=0}^{n} \frac{I_{h_ik_il_i}}{V_{h_ik_il_i}}} \tag{5}$$

$$V_{h_ik_il_i} = \frac{(I_{h_ik_il_i})_0}{\sum_{i=0}^{n} (I_{h_ik_il_i})_0}$$

where $(I_{h_ik_il_i})_0$ integrated intensity of $\langle \mathrm{hkl} \rangle$ peak in texture free pure iron; $I_{h_ik_il_i}$ fitted integrated intensity of $\langle \mathrm{hkl} \rangle$ peak in the measured pure iron specimens.

The $R_{h_ik_il_i}$ can reflect texture transformation in the specimen. As presented in Fig. 8, the texture evolution can be reflected by change of integrated intensity of different peaks. As presented in Fig. 8a, in the ND the largest change occurred at about 500 °C, the integrated intensity in $\langle 211 \rangle$ increased quickly while others decreased in this region. Then that of the $\langle 211 \rangle$ decreased slowly from 600 to 800 °C while increased again after cooling. The absolute integrated intensity of all

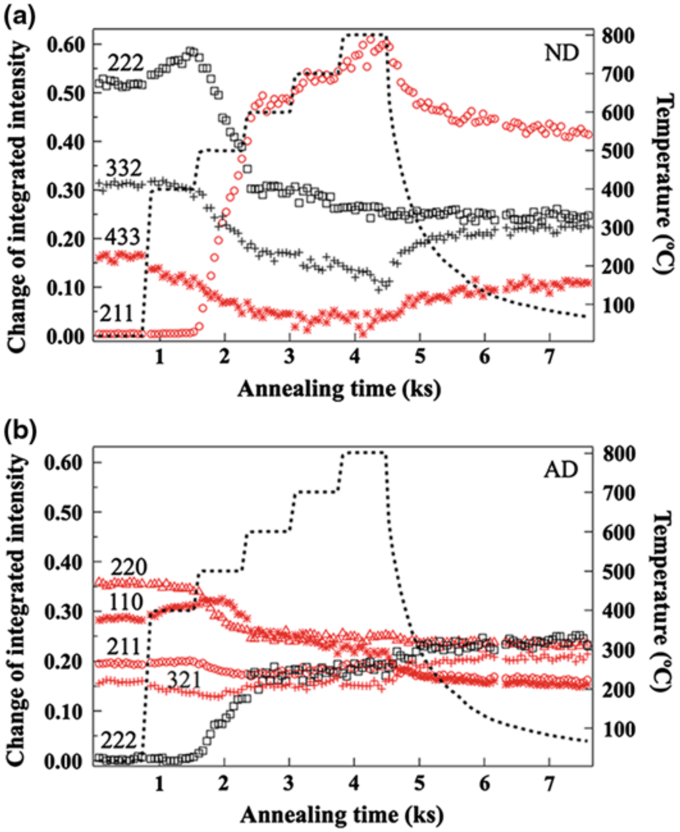

Fig. 8 Change of integrated intensity of the as-deposited specimen: **a** ND and **b** AD

obtained peaks in AD (Fig. 8b) decreased rapidly during holding at 500 °C and then became slowly and finally stable after cooling started. At the same time, the increase of $\langle 222 \rangle$ peak intensity can also be observed.

The increase of FWHM can be caused by the increase of dislocation and/or decrease in grain size. In order to separate the effect of microstrain and crystal size on the FWHM values and to explain the annealing process more easily, the global Rietveld refinement on the diffraction profiles by the Z-Rietveld software was tried, from which the Gaussian FWHM (HG) due to the dislocation and Lorentzian FWHM (HL) affected by grain size, can be determined. As results, the stability of microstructure at lower temperature until 300 °C was confirmed from the stable values of HL. With increase of annealing temperature, the FWHM_L in both directions decreased quickly with temperature until 550 °C, which should be caused by the rapid grain growth. However, there was no obvious change in the HG values during annealing. The details have been reported [11].

3.4 EBSD Observation on Annealed Specimens

EBSD measurements were conducted on specimens annealed at certain temperatures and cooled down to RT to obtain the details of microstructure, with a scanning step size of 0.1 μm for the as-deposited specimen or that of 1.5 μm for the annealed cases.

Abnormal grain growth together with texture change occurred, where most grains of the specimen annealed at 400 °C were similar to that of the as-deposited one. A few excessively large grains with size over than 100 μm appeared from the middle cross section of the sheet subjected to 400 °C for 3,600 s annealing, consuming the surrounding fine-grained matrix. However, the specimen annealed at 700 °C was recrystallized to coarse equiaxed grains after 3,600 s. The crystallographic information of the specimen subjected to in situ neutron diffraction was examined by EBSD and the results are shown in Fig. 9. There are equiaxed grains with size about 100 μm in the top surface IPF maps for the 800 °C annealed specimen, but still elongated in ND.

Grain growth may be divided into two types, normal grain growth and abnormal grain growth (or secondary recrystallization). Normal grain growth, in which the microstructure coarsens uniformly, is classified as a continuous process. While abnormal grain growth is a discontinuous process, during which a few grains in the microstructure grow preferentially and consume the matrix of smaller grains. From neutron diffraction and EBSD results, two main obvious changes took place during annealing on the as-deposited pure iron: (1) an abrupt texture transformation from ⟨111⟩//ND to ⟨211⟩//ND occurred at 500 °C; (2) abnormal grain growth started after holding at 400 °C. The following factors are usually considered to lead the abnormal grain growth, i.e. second-phase particles, texture and surface effects. Abnormal grain growth has been reported predominantly in alloys containing particles. When a specimen containing the considerable amount of dispersed particles is annealed at a temperature above the solidus temperature, discontinuous grain growth occurs due to the dissolution of particles which pinned the grain boundary. Abnormal grain growth may also occur when at least one strong texture component exists. As reported in our previous work [12], three hydrogen desorption peaks appeared at about 200, 400 and 680 °C, respectively, on the TDS profiles for the as-deposited pure iron. The hydrogen bubbles at grain boundary must play a pinning effect for grain growth. At 400 °C, the hydrogen bubbles disappear, that is, pinning is released, so that the abnormal grain growth (secondary recrystallization) would take place. This is, similar to the niobium carbides (NbC) or other nitrides and carbide, dispersion of the second-phase particles (pinning effect) would prevent grain growth. When such a carbide or nitride is dissolved, rapid grain growth takes place.

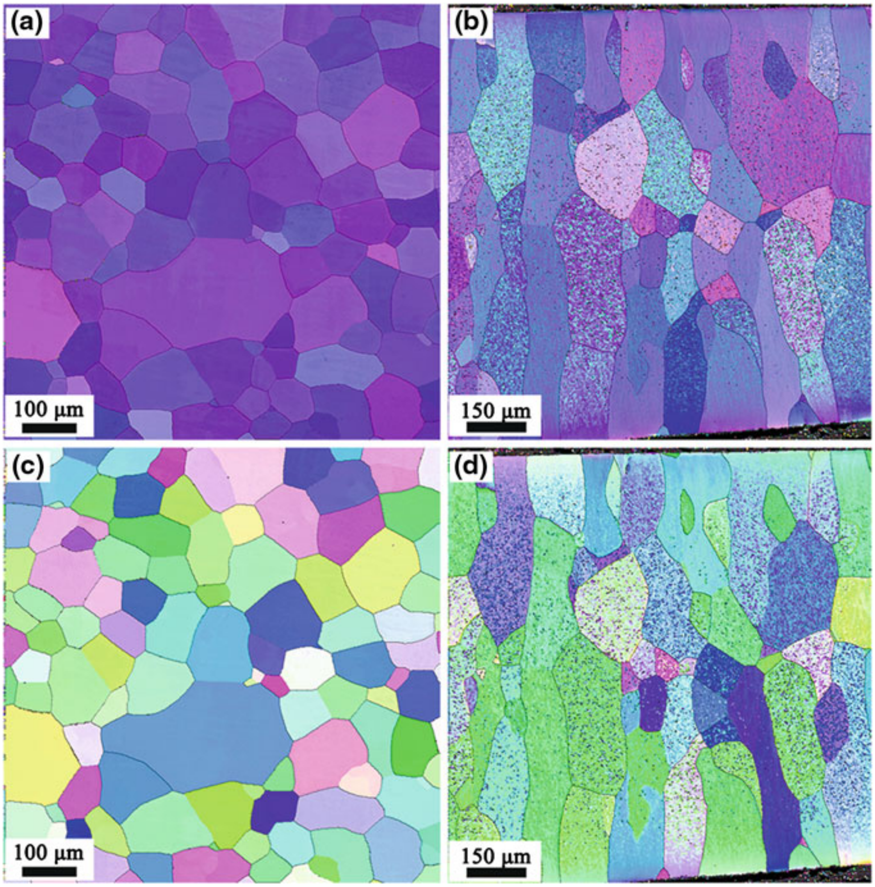

Fig. 9 EBSD IPF maps on the 800 °C annealed specimens subject to neutron diffraction: **a** ND map observed on the top surface, **b** ND map obtained from the cross-section, **c** AD map observed on the top surface and, **d** AD map obtained from cross-sectional observation

4 Room Temperature Tensile Deformation Behavior

The plastic deformation behavior of the UFG electrodeposited pure iron sheet was studied by in situ neutron diffraction and EBSD observations during tension testing at room temperature. The combination of volume-averaged crystallographic orientation changes from neutron diffraction and the local orientation relationship from EBSD effectively reveal the texture change from {111} ⟨hkl⟩ to {111} ⟨110⟩ and the corresponding microstructure changes with tension deformation. Related to such grain rotation, the occurrence of grain coalescence by deformation was evidently found using semi in situ EBSD observations. The results obtained are explained using a characteristic slip model, which also gives the reason of ultrahigh Lankford value in this material.

4.1 In Situ Neutron Diffraction During Tensile Loading

Tensile test specimens were cut from the sheets. The size of the parallel gauge portion was 50 mm × 5 mm × 1 mm for the neutron diffraction experiment. In situ neutron diffraction measurement during tensile loading was conducted with TAKUMI. The angle between the incident neutron beam and the tensile axis is 45°; therefore, diffraction patterns axial and transverse to the loading direction can be measured simultaneously by the south and north detector banks, respectively, with a scattering angle of ±90°. The tensile specimen was set in such a way that either the tensile (or axial) direction (AD) and the transverse direction (TD) data or AD and the deposition (or normal) direction (ND) data could be obtained. The tensile load was increased stepwise with a holding time of 300 s for acquiring a diffraction profile that provides sufficient statistical data for analysis.

The intergranular strain of the ⟨hkl⟩ grain family can be evaluated from the shift of the diffraction profile. The neutron diffraction profiles were then analyzed by single peak fitting with the Gaussian function for individual ⟨hkl⟩ reflections. Lattice strain ε_{hkl} can be evaluated by the following equation:

$$\varepsilon_{hkl} = \frac{d_{hkl} - d_{hkl}^{0}}{d_{hkl}^{0}}, \tag{6}$$

where d_{hkl}^{0} and d_{hkl} denote the lattice plane spacing of the stress-free state (before deformation) and that of loading or unloading after the deformation state, respectively. The changes in diffraction intensity and a full-width at half-maximum (FWHM) can also be obtained from the single peak fitting results.

In electrodeposited materials, possible plastic deformation modes include slip (dislocation motion), grain boundary sliding, and grain boundary migration. If slip is the dominant mode, the amount of plastic flow is different from grain to grain, probably because of the crystalline orientation with respect to AD, resulting in the generation of intergranular stress (strain). The lattice plane spacing increased in AD with increasing applied stress and reverted nearly to the original spacing after unloading. The profiles in TD and ND showed the opposite tendency during loading and unloading, exhibiting the Poisson's effect. The evaluated results are shown in Fig. 10. It has been reported that for a grain family having ⟨hkl⟩ aligned axially in a random-textured material, the resolved stiffness depends on the cubic elastic anisotropy factor A_{hkl}, which is given by [26–28]

$$A_{hkl} = (h^2k^2 + k^2l^2 + l^2h^2)/(h^2 + k^2 + l^2)^2. \tag{7}$$

This parameter varies from a minimum of 0 for the $\langle 100 \rangle$ direction to a maximum of 0.33 for the $\langle 111 \rangle$ crystal direction, indicating that stiffness is the highest in the $\langle 111 \rangle$ direction, while that in the $\langle 100 \rangle$ direction is the lowest. The values of A_{hkl} for $\langle 110 \rangle$ and $\langle 211 \rangle$ are commonly 0.25. In the case of a randomly oriented polycrystalline material, the onset of plastic flow in the $\langle 110 \rangle$-oriented grain family occurs preferentially compared with that in the $\langle 100 \rangle$-oriented one because of higher stress bearing in the elastic deformation stage and a higher Schmid factor for slip deformation, thus resulting in stress partitioning, i.e., generation of intergranular stresses. Lattice plane strain (stress) in plastically softer grains such as $\langle 110 \rangle$-oriented grains stops increasing after yielding, while that in plastically harder grains increases with a higher rate. In contrast, the population of $\langle 200 \rangle$-oriented grains is almost negligible in the material used in this study, as shown in Fig. 3. The $\langle 200 \rangle$ diffraction peak is not visible in AD because of the strong texture. Therefore, stress partitioning among differently oriented family grains is scarcely found. This suggests that all grains are subjected to almost equal stress and appear to have similar resistance to plastic flow, leading to slight stress partitioning in the elastic and elasto-plastic stages. Hence, it is presumed that plastic flow occurs almost equally in all grains in this material. In contrast to the results of AD, transverse strains in ND and TD are different (see Fig. 10a, b), caused by orientation dependence of Poisson's effect. In some nanocrystalline alloys, similar results were observed. For example, the plastic deformation did not introduce any obvious intergranular strains in all the ⟨hkl⟩ grains of a bulk nc Ni–Fe alloy during the uniaxial tensile deformation and it was attributed to lack of dislocation activities [5], which was a little different from the present material.

To track the evolution of texture in the bulk specimen, integrated intensities of the diffraction peaks are fitted with Rietveld refinement [29] for all obtained diffraction spectra. Figure 11 shows the relative changes in integrated intensities of different peaks in the three directions. Apparent changes can be observed in the diffraction peaks of AD and TD, while all peaks in ND almost shows little difference in the whole deformation process (Fig. 11b). In order to compare easily, the relative change in different direction was plotted together in Fig. 11d. After the onset of plastic deformation, the $\langle 110 \rangle$ intensity increased obviously in AD, while it decreased in TD. The change in the $\langle 222 \rangle$ intensity in ND is barely noticeable, suggesting the rotation along the $\langle 111 \rangle$ axis during plastic deformation. Change of texture indicates that dislocation activity is involved in the deformation process.

4.2 Microstructure Observation Results

The local texture and microstructure of the as-deposited specimen before and after tensile deformation at room temperature were analyzed by EBSD, focusing on the

Fig. 10 Stress-strain responses of different crystal lattices in the as-deposited specimens by single peak fitting: **a** AD and ND horizontal set and, **b** AD and TD vertical set

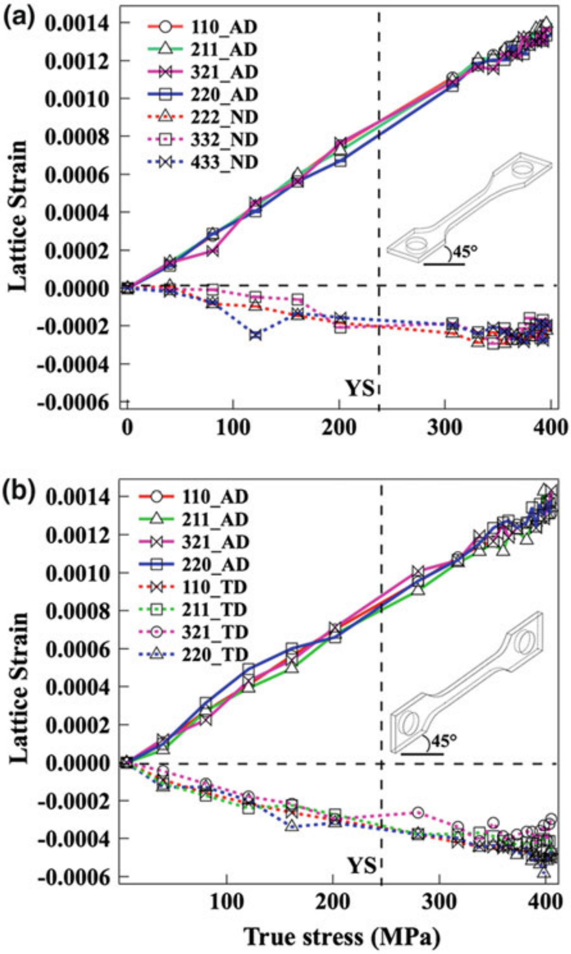

top surface and cross-sectional plane, by using a JSM7000F field-emission scanning electron microscope (FE-SEM, JEOL) equipped with an EBSD system (TSL, TexSEM Laboratory) and analysis software. EBSD measurement was conducted at an accelerating voltage of 15 kV, a tilt angle of 70°, a step size of 0.1–0.2 μm, and a scanning area of 40 μm × 80 μm. A tensile jig was installed in the scanning electron microscope, and in situ EBSD measurement was challenged under external stress by using the as-deposited specimen with a dog-bone shape. The tensile jig installed in the SEM chamber for deformation and specimens used for EBSD observation are shown in Fig. 12a and b. However, the obtained data were not excellent probably because of mechanical vibration. Then, the EBSD data were obtained after unloading and repeatedly subjecting the specimen to tensile deformation in the microscope (Fig. 12c); this method could be called semi in situ observation. To identify the same observation region of the specimen repeatedly,

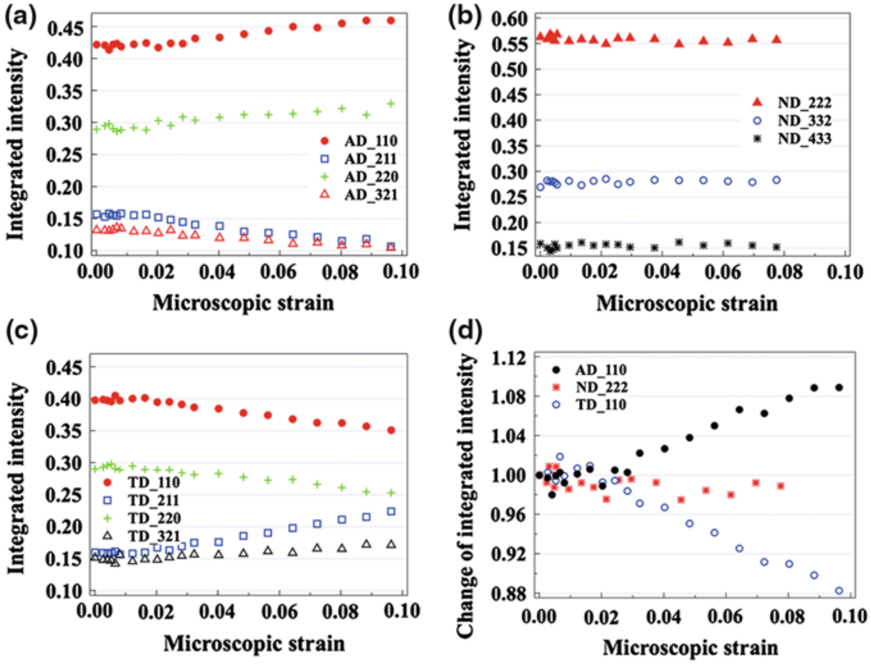

Fig. 11 Changes in the {hkl} integrated intensity of the as-deposited pure iron sheet for different directions as a function of macroscopic strain: **a** AD, **b** ND, **c** TD and **d** comparison on all the directions

small indents were made on it using a microhardness tester. TEM observation was also conducted on the as-deposited specimen after tensile deformation.

The specimens before deformation and after fracture by the tension test were examined by ex-situ EBSD. The results suggest that the initial {111} ⟨hkl⟩ random texture evolves into a {111}⟨110⟩ dominant texture. That is, individual needle-like grains undergo uniaxial rotation around ND. Though grain boundary sliding would not introduce texture, dislocation motion causes texture evolution in the specimen.

To obtain deeper insights into grain size changes, continuous observation at the same place by semi in situ EBSD experiment was performed, where EBSD observation was conducted in 10 steps with increasing tensile strain. From Fig. 13a (before deformation) to b (unloading from a nominal strain of 0.122 after the onset of necking), the transverse length of the grain increased because of tensile elongation. In the elastic region, it is confirmed that the crystal orientation and microstructure show no change until stress exceeds the yield strength. After unloading from a strain of 0.078, crystal rotation apparently occurred. The local lattice rotation is observed particularly in large grains. Figure 13b was obtained after the onset of necking, and a coarse grain is clearly observed. It is found that a high-angle grain boundary converts to a lower angle with progressing plastic

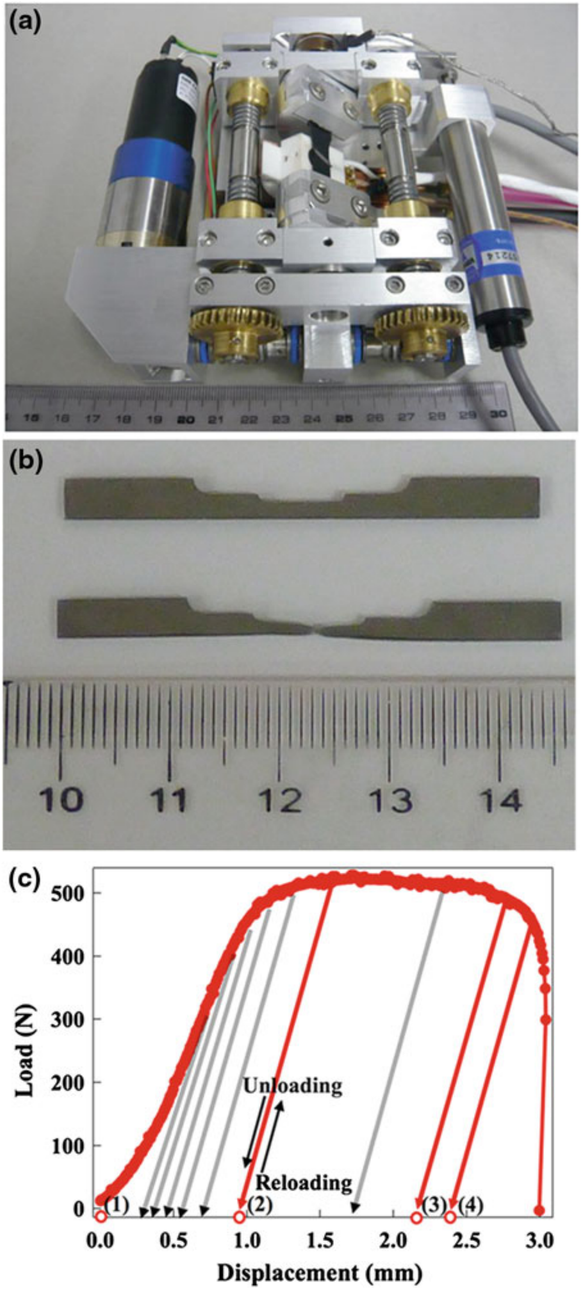

Fig. 12 Schematic diagram of semi in situ EBSD: **a** tensile jig for in situ EBSD, **b** specimen before and after EBSD observation and **c** applied load as a function of displacement during EBSD measurement

deformation from change of the misorientation angle. In addition, a new small-angle grain boundary appears to form. Hence, it is speculated that dislocation motion causes grain rotation and simultaneously decreases the boundary angle.

Fig. 13 Cross-sectional IPF maps by semi in situ EBSD: **a** AD map before deformation, **b** AD map after tensile loading as labeled in point (4) of Fig. 13c and **c**, **d** ND maps for **a**, **b**, respectively

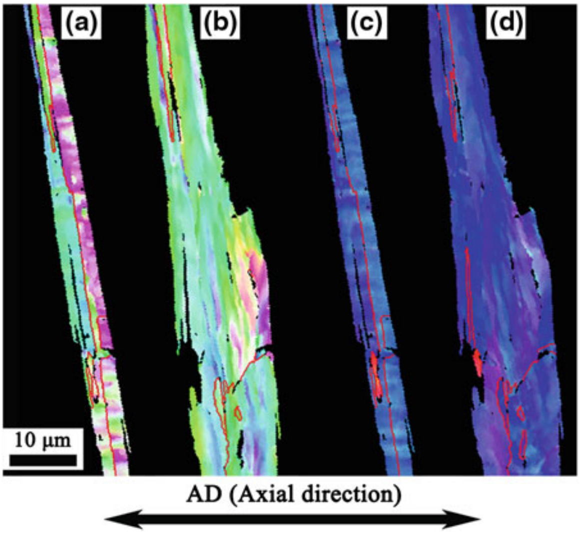

This is one example of in situ tracking of the same area in the specimen during deformation. In conclusion, EBSD observations have revealed that grain coalescence really occurs during tensile plastic deformation. Moreover, from TEM observations on the tensile deformed specimens shown in Fig. 14, dislocations can be observed clearly both from the microstructure of the top surface and the cross section after tensile deformation at room temperature.

All above-mentioned results suggest dislocation motion, i.e., slip is the dominant mode of plastic deformation of this material. In the previous report [14], an as-deposited sample was characterized by surface relief with tensile deformation, while in the specimen annealed at 400 °C wavy slip pattern was observed. From the straight steps observed on the TD plane, the occurrence of grain boundary sliding was suspected. The present results suggest that grain boundary sliding is not the main mechanism. With respect to grain boundary migration, no evidence was obtained for the material used in this study.

4.3 Deformation Mechanism

To discuss the characteristic slip deformation from the perspective of critical resolved shear stress τ, the Schmid factor m was calculated by

$$\tau = \sigma \cdot m, \tag{8}$$

$$m = \cos\varphi \cdot \cos\lambda, \tag{9}$$

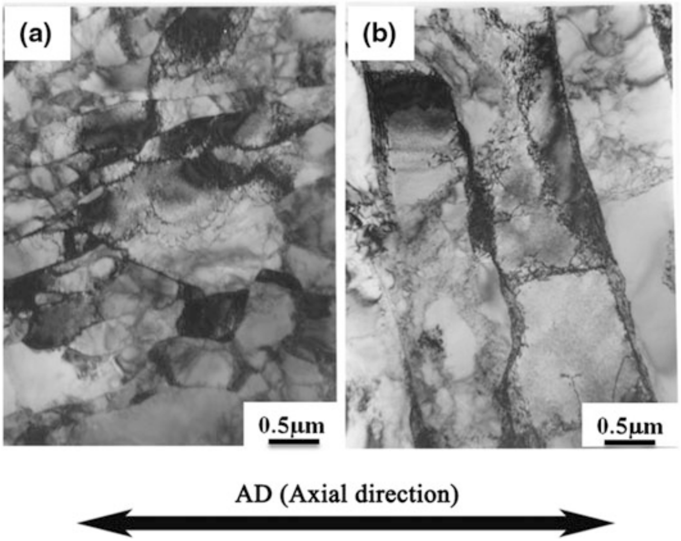

Fig. 14 TEM microstructure after tensile deformation: **a** the equiaxed structure from the top surface and, **b** needle-like structure observed from the cross section

where

φ	the angle between the applied load direction and the slip plane normal
λ	the angle between the applied load direction and the slip direction
σ	the applied stress

For a body-centered cubic structure of α-Fe, there are six slip planes of type $\{110\}$ and two $\langle 111\rangle$ directions in each $\{110\}$ plane. Therefore, 12 slip systems can be activated. In the present textured material, the $\{110\}$ planes can be divided into two groups, as illustrated in Fig. 15a, b. In Group 1 (G1), the angle φ_1 between the direction of the tensile load and the normal of the slip plane satisfies $54.7° \leq \varphi_1 \leq 125.3°$, while in Group 2 (G2), this angle (denoted by φ_2) is less than 30°. AD is always perpendicular to the $\langle 111\rangle$ direction. The Schmid factors for all of the 12 slip systems were calculated. The results showed that the maximum Schmid factor for G2 is always higher than that for G1, which indicates that the preferentially activated slip system always belongs to G2.

MD simulation on nc polycrystal by Haslam et al. [30, 31] demonstrated two mechanisms for grain-growth: curvature-driven grain boundary migration and grain-rotation induced grain coalescence. First, grain rotations driven by the conversion of high-angle into low-angle grain boundaries continuously increase the fraction of low-angle boundaries; second, much higher mobility of high-angle grain boundaries results in their preferential disappearance during grain boundary curvature-driven grain growth. In the rotation-coalescence mechanism, the grain boundary misorientation decreases to zero, eliminating the grain boundary and

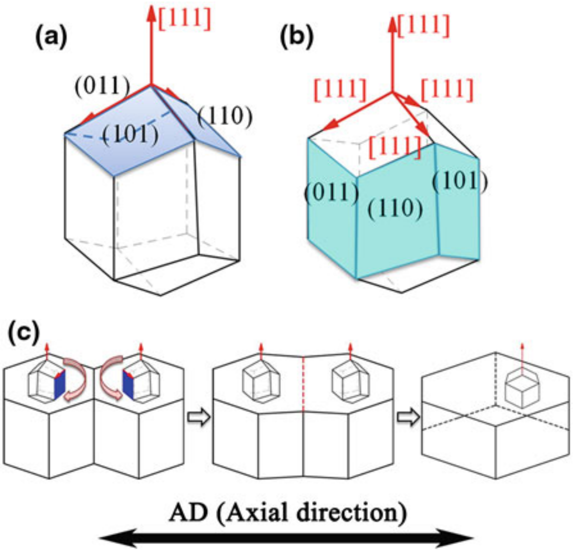

Fig. 15 Schematics of slip systems in the as-deposited specimen: **a**, **b** {110}⟨111⟩ slip systems and **c** illustration of deformation process

thus inducing grain growth. Correspondingly, combining of volume-averaged crystallographic orientation changes from neutron diffraction (intensity changes), the local grain orientation relationship from EBSD and the active slip systems, the deformation model illustrated in Fig. 15c could be proposed. That is, by dislocation motion in the active slip system, a grain rotates to ⟨110⟩ parallel to AD, while the ⟨111⟩//ND is maintained. During deformation, the high-angle grain boundaries continuously convert into lower-angle grain boundary, resulting in grain disappearance, i.e., the two grains finally coalesce to a single grain (see Fig. 13b). When only slip systems of G2 operate dominantly at tensile deformation, the width of a specimen would decrease while the thickness would hardly decrease. This characteristic deformation must cause ultrahigh R value of this material.

5 Summary

The annealing behavior and room temperature tensile behavior of the as-deposited pure iron sheet was investigated by in situ neutron diffraction and EBSD, the obtained results are summarized as follows,

(1) From the SANS results, nano-sized inhomogeneity was found in the as-deposited and 400 °C annealing specimen and it disappeared after 700 °C annealing.
(2) Upon annealing, the needle-like fine grains were stable at lower temperature and abnormal grain growth occurred at about 400 °C, where texture changed

drastically from strong {111} ⟨hkl⟩ to {111} ⟨211⟩ parallel to the normal direction.

(3) Texture change from strong {111} ⟨hkl⟩ to {111} ⟨110⟩ with tensile deformation accompanying little intergranular stresses were found by in situ neutron diffraction. Grain coalescence with plastic deformation was revealed by EBSD results.

(4) The operation of special slip system related to the strong texture in a needle-like grain is believed to bring unusually high R value.

(5) Hydrogen is suspected to play some role for grain coalescence and then high R value.

Acknowledgments This research was financially supported by a Grant-in-Aid for Scientific Research on Innovative Areas "Bulk Nano-structured Metals" through MEXT, Japan (Contract No. 22102006). The authors would like to acknowledge Dr. M. Sugiyama and Dr. E. Oda of Nippon Steel, for their TEM experiment help and Dr. N. Sato for her assistance with the EBSD measurements.

References

1. Daymond MR, Tome CN, Bourke AM (2000) Measured and predicted intergranular strains in textured austenitic steel. Acta Mater 48:553
2. Daymond MR, Priesmeyer HG (2002) Elastoplastic deformation of ferritic steel and cementite studied by neutron diffraction and self-consistent modelling. Acta Mater 50:1613
3. Lorentzen T, Daymond MR, Clausen B, Tome CN (2002) Lattice strain evolution during cyclic loading of stainless steel. Acta Mater 50:1627
4. Xu F, Holt RA, Daymond MR, Rogge RB, Oliver EC (2008) Development of internal strains in textured Zircaloy-2 during uni-axial deformation. Mater Sci Eng A 488:172
5. Fan GJ, Li L, Yang B, Choo H, Liaw PK, Saleh TA, Clausen B, Brown DW (2009) In situ neutron-diffraction study of tensile deformation of a bulk nanocrystalline alloy. Mater Sci Eng, A 506:187
6. Bastos A, Zaefferer S, Raabe D, Schuh C (2006) Characterization of the microstructure and texture of nanostructured electrodeposited NiCo using electron backscatter diffraction EBSD. Acta Mater 54:2451
7. Samet-Meziou A, Etter AL, Baudin T, Penelle R (2008) Relation between the deformation sub-structure after rolling or tension and the recrystallization mechanisms of an IF steel. Mater Sci Eng, A 473:342
8. Yoshinaga N, Hiwatashi S, Ushioda K, Akisue O (1999) Deep-drawability of electro-deposited pure iron. CAMP-ISIJ 12:1277
9. Yoshinaga N, Sugiura N, Hiwatashi S (2008) Deep drawability of electro-deposited pure iron having an extremely sharp <111>//ND texture. ISIJ Int 48:667
10. Sugiura N, Yoshinaga N (2012) Deformation behavior of electro-deposited pure iron with extremely high R-value. Mater Sci Forum 702–703:291
11. Su YH, Tomota Y, Harjo S (2014) Microstructural changes by annealing in ultrafine-grained electrodeposited pure iron. Metall Mater Trans A 45A: 990
12. Su YH, Tomota Y, Suzuki J, Ohnuma M (2011) Hydrogen behavior in an ultrafine-grained electrodeposited pure iron. ISIJ Int 51:1535
13. Su YH, Tomota Y, Harjo S, Adachi Y (2012) Deformation-induced grain coalescence in an electrodeposited pure iron sheet studied by in situ neutron diffraction and electron backscatter diffraction.Acta Mater 60:3393

14. Motegi T, Masuyama M, Iida K, Suzuki T, Sato H, Tomota Y (2002) Plastic anisotropy in an electrodeposited pure iron. Tetsu-to-Hagane 88:801
15. Yoshinaga N, Vanderschueren D, Kestens L, Ushioda K, Dilewjns J (1998) Cold-rolling and recrystallization texture formation in electrodeposited pure iron with a sharp and homogeneous γ-fiber. ISIJ Int 38:610
16. Ray RK, Jonas JJ, Hook RRE (1994) Cold rolling and annealing textures in low carbon and extra low carbon steels. Int Mater Rev 39:129
17. Tomitz A, Kaspar R (2000) Deep-drawable thin-gauge hot strip of steel as a substitution for cold strip. ISIJ Int 40:927
18. Maxelon M, Pundt A, Pyckhout-Hintzen W, Barker J, Kirchheim R (2001) Interaction of hydrogen and deuterium with dislocations in palladium as observed by small angle neutron scattering. Acta Mater 49:2625
19. Ohnuma M, Suzuki J, Ohtsuka S, Kim SW, Kaito T, Inoue M, Kitazawa H (2009) A new method for the quantitative analysis of the scale and composition of nanosized oxide in 9Cr-ODS steel. Acta Mater 57:5571
20. Ojima M, Ohnuma M, Suzuki J, Ueta S, Narita S, Shimizu T, Tomota Y (2008) Origin of the enhanced hardness of a tempered high-nitrogen martensitic steel. Scripta Mater 59:313
21. Przeniosło R, Winter R, Natter H, Schmelzer M, Hempelmann R, Wagner W (2001) Fractal pore distribution and magnetic microstructure of pluse-electrodeposited nanocrystalline Ni and Co. Phys Rev B 63:054408
22. Feigin LA, Svergun DI (1987) Structure analysis by small-angle X-ray and neutron scattering. Plenum Press, New York
23. Michels A , Weissmuller R (2008) Magnetic-field-dependent small-angle neutron scattering on random anisotropy ferro-magnets. Rep Prog Phys 71:066501
24. Ito T, Nagatani T, Harjo S, Arima H, Abe J, Aizawa K, Moriai A (2010) Application software development for the engineering materials diffractometer, TAKUMI. Mater Sci Forum 652:238
25. Harjo S, Ito T, Aizawa K, Arima H, Abe J, Moriai A, Iwahashi T, Kamiyama T (2011) Current status of engineering materials diffractometer at J-PARC. Mater Sci Forum 681:443
26. Daymond MR, Bourke MA, Von Dreele RB, Clausen B, Lorentzen T (1997) Use of Rietveld refinement for macrostrain determination and for the evaluation of plastic strain history from diffraction spectra. Apple Phys 82:1554
27. Korsunsky AM, Daymond MR, James KE (2002) The correlation between plastic strain and anisotropy strain in aluminium alloy polycrystals. Mater Sci Eng, A 334:41
28. Oliver EC, Daymond MR, Withers PJ (2004) Interphase and intergranular stress generation in carbon steels. Acta Mater 52:1937
29. Oishi R, Yonemura M, Nishimaki Y, Torii S, Hoshikawa A, Ishigaki T, Morishima T, Mori K, Kamiyama T (2009) Rietveld analysis software for J-PARC. Nucl Instrum Methods Phys Res A 600:94
30. Haslam AJ, Moldovan D, Yamakov V, Wolf D, Phillpot SR, Gleiter H (2003) Stress-enhanced grain growth in a nanocrystalline material by molecular-dynamic simulation. Acta Mater 51:2097
31. Haslam AJ, Phillpot SR, Wolf D, Moldovan D, Gleiter H (2001) Mechanisms of grain growth in nanocrystalline fcc metals by molecular-dynamics simulation. Mater Sci Eng, A 318:293

In Situ Measurements of Hydrogen Diffusion in Duplex Stainless Steels by Neutron Radiography

Eitan Dabah, Axel Griesche, Katrin Beyer, Eusebio Solórzano and Thomas Kannengiesser

Abstract Hydrogen embrittlement (HE) is a widely known phenomenon and under investigation already for more than a century. This phenomenon, though thoroughly studied, is not yet completely understood, and so far, there are several suggested mechanisms that try to explain the occurrence of HE. One important factor of understanding the HE phenomenon and predicting hydrogen-assisted failure is the descent knowledge about the hydrogen transport behaviour in the material. Neutron radiography is a proven method for tracking hydrogen diffusion and it was applied successfully in various research studies. In the presented study, we examined the hydrogen effusion behaviour in duplex stainless steel by means of neutron radiography and calculated the effective diffusion coefficient from the obtained transmission images.

Keywords Neutron radiography · Hydrogen diffusion · Duplex stainless steels · Hydrogen embrittlement

1 Introduction

Once introduced into metallic materials, hydrogen might cause serious degradation of the mechanical properties [1–3], commonly referred to as Hydrogen Embrittlement (HE). Johnson [4] first reported this phenomenon in 1825 and since then it was subject of thousands of researches. Normally, this degradation of the mechanical properties is accompanied by the appearance of a more or less brittle

---

E. Dabah · A. Griesche (✉) · K. Beyer · T. Kannengiesser
BAM Federal Institute for Materials Research and Testing, Unter den Eichen 87,
Steglitz, 12205 Berlin, Germany
e-mail: axel.griesche@bam.de

E. Solórzano
Condensed Matter Physics Department, Faculty of Sciences, University of Valladolid,
47011 Valladolid, Spain

T. Kannengiesser et al. (eds.), *In-situ Studies with Photons, Neutrons and Electrons Scattering II*, DOI: 10.1007/978-3-319-06145-0_9,

fracture behavior. Since hydrogen is not solely contributing to the cracking process, this phenomenon is called Hydrogen Assisted Cracking (HAC). The metallurgical mechanisms of HAC are not yet completely understood and since the 1940s numerous theories were suggested. More recently, it is assumed that HAC of metallic engineering materials, in particularly steels and stainless steels, is a consequence of mainly two interacting mechanisms between hydrogen and a metal matrix, namely the "Hydrogen Enhanced Decohesion" (HEDE) and the "Hydrogen Enhanced Localized Plasticity" (HELP) [5–7]. However, relevant for these theories and for HAC in general is a decent knowledge about the hydrogen diffusion and trapping behavior in the respective investigated microstructure [8, 9].

Duplex stainless steel is a construction material used mainly in the offshore industry for bridges, rafts etc. In service, the steel components are subject to sour environments and thus require corrosion protection such as cathodic protection or corrosion resistance coatings. An extremely high hydrogen concentration can build up in these alloys during these processes and during welding as well, and though this steel has very good corrosion resistance and mechanical properties, it exhibits a quite high susceptibility to hydrogen embrittlement [10–12].

In order to understand all aspects of the hydrogen embrittlement mechanism and to be able to predict the lifetime of a serving steel component in a sour environment, the hydrogen transport and trapping phenomena are important to be investigated and understood. The hydrogen transport and trapping phenomena play a crucial role in the hydrogen-assisted cracking process because hydrogen can initiate cracks and can foster the crack propagation.

There are several techniques for the investigation of hydrogen transport and trapping behavior in metallic materials, which can be applied in order to determine effective hydrogen diffusion coefficients as characteristic quantity. Examples are the permeation technique and the hot extraction technique [13–15].

Neutron radiography is a non-destructive testing technique in various scientific fields and is an excellent method for observing and measuring hydrogen transport in metallic materials [16–20]. This method has some advantages as e.g. the direct determination of hydrogen compared to the classical methods [21]. Neutrons, which interact mainly with the atom's nucleus, have a strong interaction with hydrogen, as the latter has a relatively large volume ratio of nucleus to atom. Neutrons interact mainly by absorption and scattering depending on their kinetic energy. Scattering means that the neutron is deflected from the nucleus and that it changes velocity and flight direction. Scattering is subdivided into elastic and inelastic scattering. In case of elastic scattering the kinetic energy of the interacting neutron is unchanged, while in inelastic scattering the neutron's momentum changes and the nucleus undergoes an internal rearrangement into an excited state with subsequent emission of radiation [22].

The strong neutron interaction with the hydrogen atoms, which is reflected by a large cross section for interaction (at a certain kinetic energy), allows achieving a good image contrast between hydrogen enriched regions and regions which are depleted of hydrogen. The cross section for interaction of neutrons with hydrogen is 82.02 b, which is significantly larger than the interaction cross section of

Table 1 Chemical comsposition of the duplex stainless steel (1.4462) in wt.% analysed by spark source spectroscopy (balance is Fe)

C	Ni	Cr	Mn	Mo	N	Si
0.023	5.6	21.65	1.8	2.86	0.16	0.35

neutrons with iron (11.62 b) [23]. The non-destructive property of the neutron radiography method allows for in situ measurements of the hydrogen transport, which cannot be performed with conventional methods requiring prepared samples and a post mortem analysis.

In this research, we studied in situ the hydrogen effusion behavior of duplex stainless steel at elevated temperatures by using the neutron radiography technique.

2 Experimental Procedure

For the described study, duplex stainless steel samples with the chemical composition as presented in Table 1, and with the dimensions $45 \times 5 \times 2$ mm^3 were electrochemically charged with hydrogen for 48 h in a 0.1 M H_2SO_4 solution combined with 0.25 g/L of recombination inhibitor $NaAsO_2$. The current density at the cathode (in this case the sample) was 10 mA/cm^2.

The effusion behavior of hydrogen was examined by means of neutron radiography at the neutron imaging facility ANTARES of the research neutron source Heinz Maier-Leibnitz (FRM II) in Garching, Germany. Hydrogen-charged and hydrogen-free samples were each packed in stacks of five in order to obtain a reasonable contrast between the charged sample stack and the uncharged sample stack as reference. An infrared radiation furnace heated both stacks up to 350 °C and then the temperature was kept constant for the rest of the experiment. Hydrogen desorption during heating-up was unavoidable but the heating phase was very short compared to the isothermal phase and thus we neglected the loss of hydrogen during heating. Transmission images were recorded continuously during the isothermal phase. The reference stack and the hydrogenated stack were placed with equal distance from the detector providing the same image distance. An example of a neutron radiography image is presented in Fig. 1. The attenuation characteristic, i.e. the intensity of the transmitted neutron beam, is influenced only from the hydrogen content in the samples if the difference between sample stack and reference stack is monitored. The parameters of the neutron radiography set-up are summarized in Table 2.

Three standard samples made out of different TiH_2 and SiC mixtures were placed below the furnace, as can be seen in Fig. 1. These standards contain a well-defined amount of hydrogen and allow for a quantitative conversion of the grey values (intensities) in the images to hydrogen concentrations C_H in the sample stack.

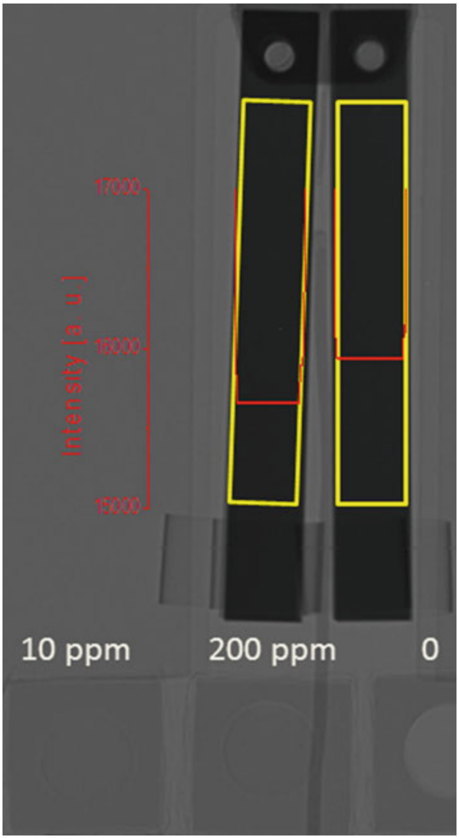

Fig. 1 Transmission image of a neutron radiography experiment. The reference stack is on the *right* side and the hydrogenated sample stack is on the *left* side. The *rectangles* marked in *yellow* are the measurement fields from which the mean *gray* values were taken for analysis. The *red* graph shows the corresponding intensity profile. A lower intensity value corresponds with a higher hydrogen concentration. The standard samples (*circular areas*) with controlled hydrogen concentration in wt.ppm are positioned underneath the furnace

Table 2 Experimental parameters of the neutron radiography set-up

Aperture	(L/D = 400)
Neutron flux	9.4E + 7 cm^{-2} s^{-1}
CCD camera	2,048 pixel × 2,048 pixel
Field of view	87 mm × 87 mm
Effective pixel size	42 µm
Distance sample—detector	39 mm
Exposure time	20 s
Delay (camera read-out time)	12–13 s

The analysis of the transmission images and the conversion of grey values into concentration units were done automatically by a script based on Image J.

Prior analysis and for ensuring the validity of the gray scale values, a series of "open beam" (ob) or "bright field" and "dark field" (di) images were taken. Such corrections are common in microscopy if the images are analyzed quantitatively. Principally, this correction takes into account specific characteristics of both the

Fig. 2 Plot of the intensity difference I_{dif} between sample stack and reference stack versus the frame number

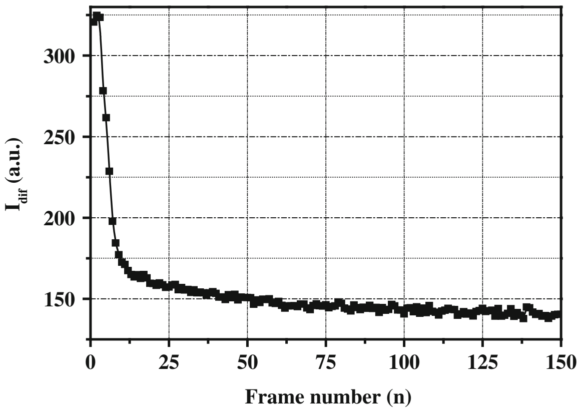

neutron beam (e.g. inhomogeneity of the cross-sectional neutron distribution) and the detector (e.g. changes of the pixel's sensitivity). The correction procedure for every image follows the mathematical operation: Corrected Image = (Original image − di)/(ob − di).

3 Results and Discussion

The difference between the mean intensity values of the hydrogenated stack and the hydrogen-free reference stack are plotted versus the image number in Fig. 2.

Subsequently, the difference of the intensity values I_{dif} is converted to hydrogen concentrations C_H [24]. The conversion from gray scale values to the hydrogen concentration was done by using Eq. (1), which can be applied if at least two standards with known hydrogen concentration exist. Then, the mean grey level values of the sample stack I_{sam}, of the reference stack I_{ref}, and of two different SiC-TiH_2 standards I_{std_A}, and I_{std_B} were taken for all images.

$$C_H = K' \cdot \frac{\ln\left(\frac{I_{ref}}{I_{sam}}\right)}{\ln\left(\frac{I_{ref}}{I_{ref} - \left(I_{std_A} - I_{std_B}\right)}\right)} \tag{1}$$

The constant K' accounts for the different amount of hydrogen in two standards. In order to take into account the different attenuation behaviour of standards (powder) and reference (bulk) the intensity normalization is done by adding the absorption difference $I_{std\_B} - I_{std\_A}$ of both SiC-TiH_2 standards to I_{ref} of the reference stack. The frame sequence was converted to a time scale as each image had 20 s exposure time plus approx. 12 s read-out time of the camera. After conversion of the intensities to hydrogen concentrations and after the conversion of the frame

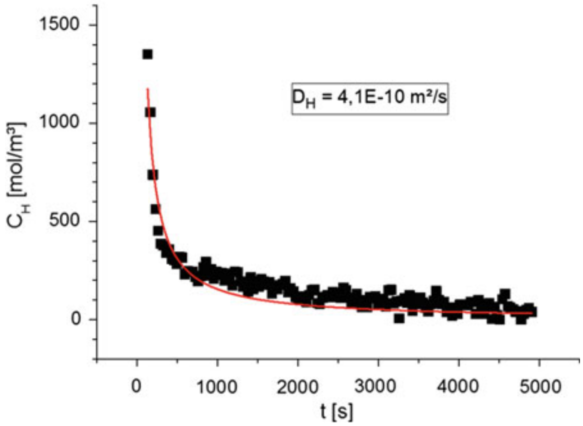

Fig. 3 Plot of the hydrogen concentration versus time during the isothermal effusion process at 350 °C. The effective diffusion coefficient was calculated from the fit (*red line*) of the Fick's equation solution to the hydrogen concentration profile

numbers to a time scale, the hydrogen concentration versus time was used to calculate the effective hydrogen diffusion coefficient. The so called diffusion profile $C_H(t)$ is shown in Fig. 3.

The hydrogen effective diffusion coefficient was calculated by fitting a solution [see Eq. (2)] of Fick's diffusion equation to the obtained curve considering surface evaporation as boundary conditions.

$$M_H = \left(\frac{C_0 - C_1}{h}\right)\left\{\exp\left(h^2 Dt\right) erfc\left(h\sqrt{Dt}\right) - 1 + \frac{2}{\sqrt{\pi}} h\sqrt{Dt}\right\} \tag{2}$$

D is the effective hydrogen diffusion coefficient, t is time, $h = \alpha/D$ a characteristic diffusion length with a constant of proportionality α, C_1 is the initial hydrogen concentration in the sample, C_0 is the hydrogen concentration in the atmosphere ($C_0 = 0$) and M_H is the total amount of effusing hydrogen (Fig. 4).

The result of the effective diffusion coefficient measurement with neutron radiography presented in Fig. 3 is in good agreement with diffusion coefficient data from literature as summarized by Boellinghaus et al. [8]. The diffusion coefficient measured by neutron radiography is located between the data of Sentance 1991 (see Ref. [2] in Fig. 4) and Walker and Gooch 1991 (see Ref. [5] in Fig. 4). The cause of the different diffusion coefficients is probably the different microstructure of the investigated duplex stainless steels. Walker and Gooch conducted the research upon welded steel while Sentence conducted the study upon cold worked tubes. The measurements in this study were done with rolled plates. The chemical composition in all investigated alloys was the same.

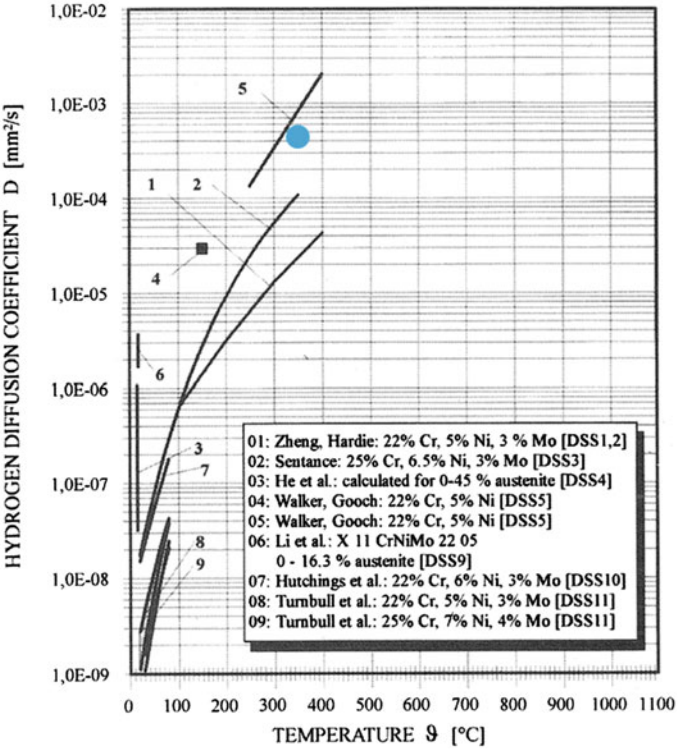

Fig. 4 Semi-logarithmic plot of hydrogen effective diffusion coefficients as function of temperature in duplex stainless steel taken from Boellinghaus et al. [8] the *blue full circle* is the diffusion coefficient measured in this study by means of neutron radiography

4 Concluding Remarks

In this work, the neutron radiography method was applied in order to measure the hydrogen effusion behavior of duplex stainless steel at 350 °C. The following findings can be concluded:

- Neutron radiography is a quantitative technique for studying the hydrogen transport behavior in iron-based alloys and for measuring effective hydrogen diffusion coefficients.
- The effective hydrogen diffusion coefficient in duplex stainless steel measured by neutron radiography is in good agreement with literature data.

References

1. Davis JR (1999) Stainless steels. ASM International, Ohio
2. Herlach D (2000) Hydrogen embrittlement of metals. Physica B 289–290(1–2):443–446
3. Lewis F (1990) Solubility of hydrogen in metals. Pure Appl Chem 22(8):353–358
4. Johnson W (1874) On some remarkable changes produced in iron and steel by the action of hydrogen and acids. Proc Royal Soc London 23:168–179
5. Birnbaum HK, Sofronis P (1994) Hydrogen-enhanced localized plasticity—a mechanism for hydrogen-related fracture. Mater Sci Eng A 176:191–202
6. Pressouyre GM, Bernstein IM (1979) A kinetic trapping model for hydrogen-induced cracking. Acta Metall 27(1):89–100
7. Birnbaum HK, Robertson IM, Sofronis P, Teter D (1997) Mechanisms of hydrogen related fracture—a review. In: Magnin T (ed) 2nd international conference on corrosion deformation interaction. Maney Publishing, Leeds, pp 173–195
8. Boellinghaus T, Hoffmeister H, Middel C (1996) Scatterbands for hydrogen diffusion coefficients in steels having a ferritic or martensitic microstructure and steels having an austenitic microstructure at room temperature. Weld World 37(1):16–23
9. Boellinghaus T, Hoffmeister H, Dangeleit A (1995) A scatter band for hydrogen diffusion coefficients in micro-alloyed and low carbon structural steels. Weld World 35(2):83–96
10. Chou S-L, Tsai W-T (1999) Hydrogen embrittlement of duplex stainless steel in concentrated sodium chloride solution. Mater Chem Phys 60(2):137–142
11. Oltra R, Bouillot C, Magnin T (1996) Localized hydrogen cracking in the austenitic phase of a duplex stainless steel. Scripta Mater 35(9):1101–1105
12. El-Yazgi A, Hardie D (1996) The embrittlement of a duplex stainless steel by hydrogen in a variety of environments. Corros Sci 38(5):735–744
13. Perng T, Altstetter CJ (1984) Hydrogen permeation and diffusion in cryformed aisi 301 stainless steel. Scr Metall 18:67–70
14. Addach H, Berçot P, Rezrazi M, Takadoum J (2009) Study of the electrochemical permeation of hydrogen in iron. Corros Sci 51(2):263–267
15. Ried P, Gaber M, Beyer K, Mueller R, Kipphardt H, Kannengiesser T (2011) Thermo analytic investigation of hydrogen effusion behavior—sensor evaluation and calibration. Steel Res Int 82(1):14–19
16. Beyer K, Kannengiesser T, Griesche A, Schillinger B (2011) Study of hydrogen effusion in austenitic stainless steel by time-resolved in situ measurements using neutron radiography. Nucl Instrum Methods Phys Res Sect A 651(1):211–215
17. Brown DW, Kenkre VM (1987) Neutron scattering lineshapes for hydrogen trapped near impurities in metals. J Phys Chem Solids 48(9):869–876
18. Grosse M, Lehmann E, Vontobel P, Steinbrueck M (2006) Quantitative determination of absorbed hydrogen in oxidised zircaloy by means of neutron radiography. Nucl Instrum Methods Phys Res Sect A 566(2):739–745
19. Lehmann EH, Vontobel P, Kardjilov N (2004) Hydrogen distribution measurements by neutrons. Appl Radiat Isot Incl Data Instrum Methods Use Agric Ind Med 61(4): 503–509
20. Grosse M, van den Berg M, Goulet C, Lehmann E, Schillinger B (2011) In situ neutron radiography investigations of hydrogen diffusion and absorption in zirconium alloys. Nucl Instrum Methods Phys Res Sect A 651(1):253–257
21. Griesche A, Solórzano E, Beyer K, Kannengiesser T (2013) The advantage of using in situ methods for studying hydrogen mass transport: neutron radiography versus carrier gas hot extraction. Int J Hydrogen Energy 38:14725–14729

22. Rinard P (1991) Neutron interactions with matter. In: Reilly D, Ensslin N, Smith H (eds) Passive Nondestructive Assay of Nuclear Materials. National Technical Information Service, Springfield, pp 357–377
23. Sears VF (1992) Neutron scattering lengths and cross sections. Neutons News 3(3):26–37
24. Griesche A, Zhang B, Solórzano E, Garcia-Moreno F (2010) Note: x-ray radiography for measuring chemical diffusion in metallic melts. Rev Sci Instrum 81(5):056104

High-Energy Synchrotron Study of the Stress–Strain Behavior of Hydrogen-Charged High Strength Structural Steel

Arne Kromm, Enrico Steppan and Thomas Kannengiesser

Abstract High strength structural steels are susceptible to hydrogen embrittlement. A critical combination of stress, amount of diffusible hydrogen and microstructure is believed to cause cold cracking. Especially during welding of high strength structural steels high tensile residual stresses may develop. Therefore, a feasibility study was conducted using synchrotron X-ray diffraction in order to analyze the stress–strain behavior during tensile loading. For that purpose two types of steel showing different hardening mechanisms were used. On the one hand a thermomechanically treated S1100MC and on the other hand a quenched and tempered S1300Q were chosen. The samples were electrochemically charged with hydrogen and subsequently stored in liquid nitrogen to prevent effusion. Tensile tests of the samples were conducted in a special load frame allowing for tilting the samples while applying constant loads. High energy synchrotron radiation was used for energy dispersive X-ray diffraction (EDXRD) analysis in transmission geometry. This method offers the possibility for measuring several diffraction lines of all contributing crystalline phases of the material. Strains as well as stresses applying the $\sin^2\psi$-method were determined for varying load situations. This feasibility study shows how the interaction of hydrogen and the stress/strain response may be assessed by diffraction methods. Examples are presented showing that hydrogen alters the load distribution as well as the strain behavior between different lattice planes in high strength steels.

Keywords High energy synchrotron radiation · Energy dispersive X-ray diffraction (EDXRD) · High strength structural steels · Tensile tests · Hydrogen embrittlement

---

A. Kromm (✉) · E. Steppan · T. Kannengiesser
BAM Federal Institute for Materials Research and Testing, Unter den Eichen 87,
Steglitz 12205, Berlin, Germany
e-mail: arne.kromm@bam.de

T. Kannengiesser et al. (eds.), *In-situ Studies with Photons, Neutrons and Electrons Scattering II*, DOI: 10.1007/978-3-319-06145-0_10,

1 Introduction

The ambition for light weight construction with simultaneously increasing the loading capacity is a main aim of many industries such as crane, vehicle, bridge construction, shipbuilding and plant construction. This aim is achieved by application of high strength structural steels with yield strengths above 1,000 MPa. The plate thickness can be reduced and consequently the service load is increased. Application of high strength structural steels has several economic advantages. Material costs are lowered with decreasing plate thickness. Base and filler material can significantly be saved. Lower weld volumes are abbreviating welding time and hence reducing production costs.

High strength structural steels are quenched and tempered and/or even thermomechanically processed. Their superior properties are mainly due to precipitations formed by micro alloying elements finely dispersed in a martensitic matrix. Thus, the strength of quenched and tempered steels is mainly achieved by forming bainitic/martensitic microstructure. The chemical composition (see Table 1) offers the advantage of improved weldability.

The challenge when welding this type of steels is their sensitivity for hydrogen embrittlement [1–4]. The reason is that atomic hydrogen may degrade the mechanical properties. Experimental observations have proven that especially a decrease in ductility up to total embrittlement (yield strength = tensile strength) may occur in high strength structural steels [5]. Nevertheless, up to now the metallurgical mechanisms of hydrogen embrittlement are not fully understood. In the literature it is still discussed contrarily which is the primary mechanism [6–8]. As a result, a single theory seems not capable to completely explain the metallurgical interaction between the metal lattice and hydrogen. Rather the combination of several mechanisms may be a suitable approach to describe this interaction. Theories describing hydrogen embrittlement are on the one hand based on experimental observations and on the other hand on empirical assumptions. However, the latter can only be partially proven experimentally. At the moment, it is supposed that hydrogen embrittlement is the consequence of several interacting mechanisms between atomic hydrogen and the metal lattice. Described i.e. by hydrogen enhanced decohesion (HEDE) theory or hydrogen enhanced localized plasticity (HELP) [6–8].

The higher susceptibility for hydrogen embrittlement of high strength structural steels can be explained as follows. On the one hand the dislocation density is higher due to the production process (hot-/cold working) compared to lower strength steels. Stress fields offer preferred diffusion paths due to the dilatation of the lattice and increase the probability of atomic hydrogen diffusion [9]. In addition, dislocations alter the chemical potential such that the thermodynamic balance is distorted [10]. Stress fields and differences in chemical potential are fostering hydrogen trapping. Dislocations were identified as primary traps, especially in quenched martensitic microstructures [11]. On the other hand, precipitation hardening due to carbides and nitrides is acting as a strong hydrogen trap in

Table 1 Chemical composition of S1100MC and S1300Q (Fe balance)

Material	C	Si	Mn	Cr	Mo	Ni	Cu	Al	Nb	V	Ti	N
S1100MC	<0.18	0.5	1.3	1.5	0.8	2.5	–	0.015	0.09	0.2	<0.01	–
S1300Q	0.12	0.21	0.9	0.48	0.4	1.23	0.01	0.038	0.02	0.02	<0.01	0.06

fine grained micro alloyed steels. Precipitates have high interface energies and build up high distortions in the lattice [12]. Hence, stress fields are generated. In conclusion, the multitude of imperfections present in high strength steels increases the solubility of atomic hydrogen but limits significantly its mobility.

Several studies have been conducted in order to understand the diffusion and trapping behavior of hydrogen, mostly applying methods for the determination of various hydrogen traps, binding energies and diffusion coefficients like thermal desorption spectroscopy and electrochemical permeation technique [13]. Nevertheless, these methods give only little insight into the local interaction of hydrogen and the microstructure. Instead diffraction methods allow for direct observation of the lattice response when hydrogen is present. Strains and stresses may be determined, as recently shown by Dabah et al. [4]. The aim of the present feasibility study was to observe the influence of hydrogen in the microstructure of two types of high strength structural steels with yield strength of 1,100 and 1,300 MPa by using diffraction methods. Energy dispersive X-ray diffraction (EDXRD) available at the EDDI beam line of the HZB in Berlin Germany was utilized to compare the stress–strain behavior of samples exhibiting varying amounts of hydrogen during tensile loading.

2 Experimental

2.1 Sample Preparation

Tensile specimens were produced based on the German standard DIN 50125 showing a length of 80 mm and a diameter of 3 mm. The specimens were electrochemically (cathodically) charged with hydrogen applying a constant current density of 60 mA/cm^2 in a solution of 0.05 M H_2SO_4 with 0.1 M $NaAsO_2$. $NaAsO_2$ affects the recombination conditions at the sample surface. Therefore, it is possible to provide different levels of hydrogen concentrations. The advantage of the electrochemical charging is its excellent repeatability. In principle the loading process is divided into hydrogen formation, adsorption and absorption. The hydrogen formation is carried out due to dissociation of acids or bases in water in case of applied electric potential or current. This potential/current is provided thereby via a reference electrode. The specimen is connected as working electrode. In this case the reference electrode is connected as the anode and the working electrode as the cathode. Figure 1 shows the experimental setup of electrochemical

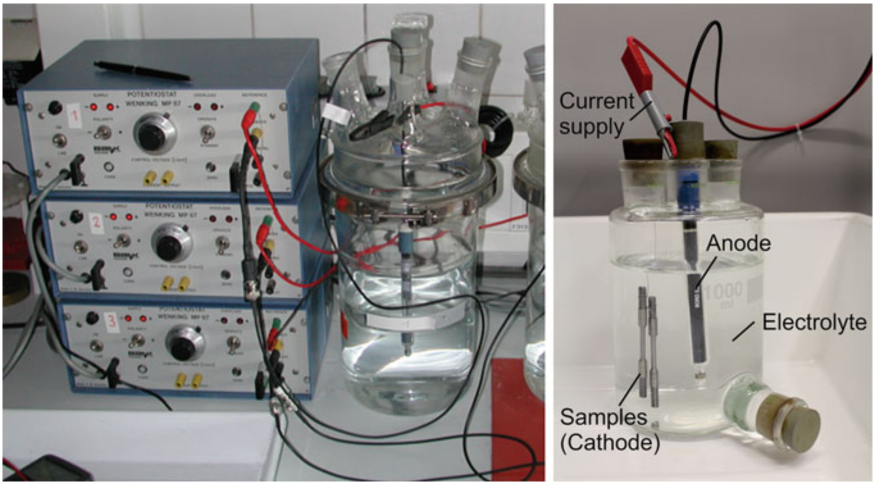

Fig. 1 Experimental setup for cathodic charging of tensile samples

charging. It has been proven by continuous measurements that a period of 24 h is sufficient to completely saturate the samples with hydrogen. This equates to 2.3 ppm for S1100MC and 2.6 ppm for S1300Q. Subsequently after charging, the samples were stored in liquid nitrogen in order to suppress effusion of hydrogen. Before the diffraction experiment the samples were unfreezed using liquid alcohol and immediately fixed to the diffraction setup.

2.2 *Diffraction Setup*

In-situ diffraction during tensile loading was conducted using high-energy, polychromatic synchrotron radiation (white beam) with photon energies between 20 and 150 keV. This allows for evaluation of a multitude of diffraction lines of the material simultaneously within one measurement. Due to EDXRD the lattice spacing d(hkl) can be evaluated as a function of the Energy E(hkl) measured using a fixed diffraction angle. Details are published elsewhere [14]. The lattice plane strains can be assigned to a shift of the diffraction lines ΔE_{hkl} in the spectrum following Eq. (1).

$$\varepsilon^{hkl} = \frac{d^{hkl} - d_0^{hkl}}{d_0^{hkl}} = \frac{E_0^{hkl}}{E^{hkl}} - 1 \qquad (1)$$

High-energy permits experiments in transmission mode to attain information from the interior material. The gauge volume was set by slit systems to approximately 0.018 mm^2 located in the center of the sample (see Fig. 2). The experimental setup consists of a special tensile test rig which can be tilted around the beam axis

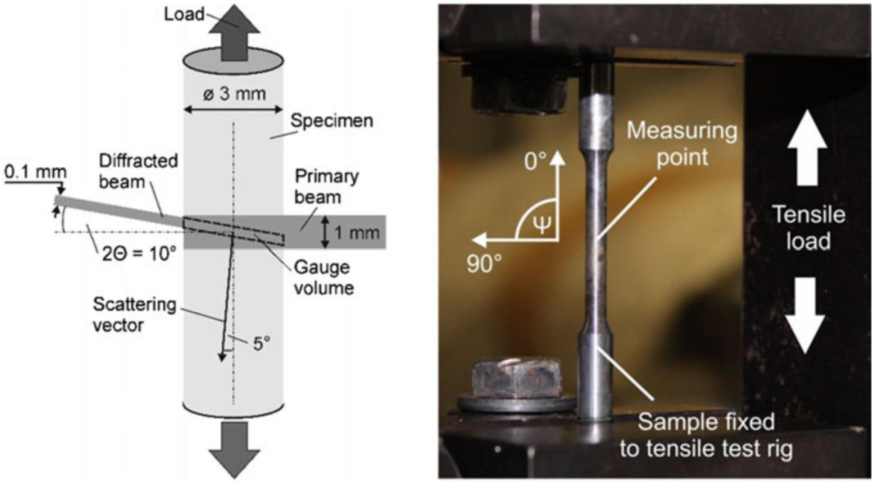

Fig. 2 Schematic of beam path (*left*) and test setup with tensile sample (*right*)

including a ψ range from 0 to 90°, as shown in Fig. 2. For this reason changes of d(hkl) are obtained between longitudinal ($\psi = 0°$) as well as transverse direction ($\psi = 90°$). Owing to this, stresses can be determined applying the $\sin^2\psi$-technique during varying load steps, e.g. [15]. These stresses are always the difference of stresses present in longitudinal ($\psi = 0°$) and stresses present in transverse direction ($\psi = 90°$). This is due to the fact that by using $\sin^2\psi$-technique, usually applied for surface stress evaluation, the out of plane stress component (σ_{33}) is assumed to be zero. In the present series of experiments this is not the case. Thus, based on the justifiable assumption that shear stresses can be neglected in the sample, the $\sin^2\psi$-technique [16] reveals:

$$\frac{d_{\phi=0,\psi} - d_0}{d_0} = \frac{1}{2} s_2^{\{hkl\}} \cdot (\sigma_{11} - \sigma_{33}) \cdot \sin^2\psi + s_1^{\{hkl\}} \cdot (\sigma_{11} + \sigma_{22} + \sigma_{33}) + \frac{1}{2} s_2^{\{hkl\}} \sigma_{33} \tag{2}$$

Therefore, the evaluated stresses which are proportional to the slope of the linear fit of $2\Theta_{\varphi,\psi}$ versus $\sin^2\psi$ always represent the difference of the stress component σ_{11} ($\psi = 0°$) and the apparent stress component σ_{33} ($\psi = 90°$). The stresses shown in this work refer to the average of the evaluated lattice planes weighted by their multiplicity. Measuring and evaluation parameters are shown in Table 2.

Tensile test were conducted at constant loads. For each material a load of 25 % of the yield strength of the respective material was selected. The load of 2.1 kN equals 297 MPa in case of S1100MC and 354 MPa at 2.5 kN for S1300Q. This ensured testing in the elastic range well below any plastic deformation of the samples. During constant loading the lattice response was recorded in time steps of

Table 2 Measuring and evaluation parameters

Primary optics	1×1 mm^2
Secondary optics	0.01×5 mm^2 (equatorial × axial)
Diffraction angle	$2\Theta = 10.3°$
Measuring mode	Transmission
Evaluation	$\sin^2\psi$; $\psi = 0°..90°$ (11 tilts)
Exposure time	120 s/spectrum
Diffraction lines considered	200α, 211α, 220α, 310α, 311α
Diffraction elastic constants (DEC)	$s_1^{\{hkl\}}$ and $\frac{1}{2}s_2^{\{hkl\}}$ calculated from single crystal constants following Eshelby–Kröner

approximately 17 min. This period of time was necessary to completely tilt the samples between 0 and 90° around the beam axis. This way the lattice plane spacing is recorded in loading direction as well as in perpendicular direction.

2.3 Results and Discussion

Tensile tests conducted on hydrogen charged samples of S1100MC (2.3 ppm) revealed embrittlement with a complete loss of ductility, see Fig. 3 (dashed arrow indicate brittle fracture point). The samples of S1100MC failed at 1,175 MPa what equals approximately the yield point. Samples of S1300Q charged with hydrogen to a concentration of 2.6 ppm showed a pronounced embrittlement. During tensile testing brittle fracture with total loss of ductility occurred. Moreover, the yield point of 1,300 MPa was not reached. Instead, the specimen failed at 708 MPa, which equals around 55 % of the nominal yield strength, see Fig. 3 (continuous arrow indicate brittle fracture point).

It is believed that this behavior is related to the different hardening mechanisms in the materials. The thermo-mechanically treated steel S1100MC is characterized by a very fine grained structure showing finely dispersed precipitations. This features are known as strong hydrogen traps [11]. Therefore, the amount of harmful diffusible hydrogen is decreased. In contrast, strength in S1300Q is obtained by tempered martensite characterized by a weaker trapping behavior. It follows that higher amounts of diffusible hydrogen may cause early failure of this material.

The following diagrams (Figs. 4 and 5) show the lattice plane spacing obtained for a number of diffraction lines for S1100MC and S1300Q. The values are converted to the cubic lattice parameter a (100α) (see Eq. 3) to allow for direct comparison. The lattice plane spacing is shown for the loading direction ($\psi = 0°$) as a function of time for samples without and with applied load (25 % yield strength). In some cases single values are missing or are inhomogeneous distributed due to microstructural reasons.

Fig. 3 The curves shows stress strain behavior for S1100MC (*dashed line*) and S1300Q (*continuous line*) without hydrogen. *Arrows* indicate brittle fracture points of hydrogen charged samples (*dashed arrow* indicate the sample of S1100MC and *continuous arrow* the sample of S1300Q)

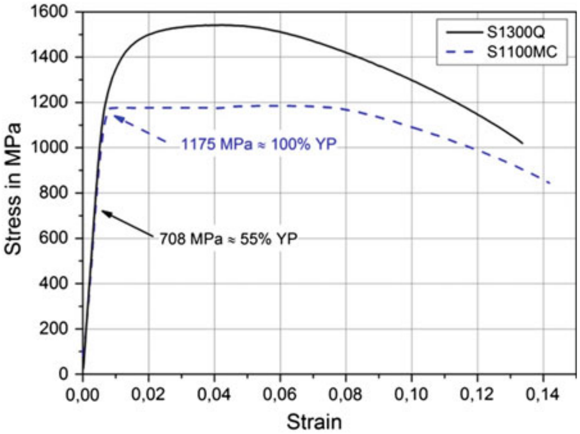

$$a = d_{hkl} \cdot \sqrt{h^2 \cdot k^2 \cdot l^2} \tag{3}$$

During the period of several hours the lattice plane spacing did not change at all for both types of steel investigated here. This is contrary to results from Dabah et al. [4], who observed reversible distortion of the lattice for hydrogen charged supermartensitic stainless steels. However, the amount of hydrogen was more than a hundred times higher in that case. In the present study the lattice spacing is scattered around a mean value during holding time. The fluctuations are barely within the measuring error but may stem from local variations of the hydrogen content due to diffusion.

Comparison of the lattice plane spacing of S1100MC reveals that the lattice is barely distorted without external load (Fig. 4). This indicates that the comparatively low amount of hydrogen alone is not inducing large strains in the material. During elastic loading (25 % yield strength) the lattice spacing is as expected increased in loading direction. Elastic anisotropy is not pronounced. Rather, the lattice planes show uniform deformation. Perpendicular to the loading direction (not shown here) the lattice seems not to be affected besides transverse straining due to loading.

In case of S1300Q the presence of hydrogen alone does not alter the lattice plane spacing as shown in Fig. 5. But contrary to S1100MC the lattice plane spacing is more influenced when external load is applied. Elastic anisotropy of the lattice is most pronounced. The 200α and 310α diffraction lines are affected to a higher degree than 211α, 220α and 321α. The first ones are the lattice planes with the smallest stiffness, while the latter ones are preferred slip planes of α-Fe. This may indicate possible onset of plastic deformation already during loading at only 25 % of the nominal yield strength.

The observation made is conform to HELP theory [1, 2], where hydrogen promotes local dislocation movement causing fracture due to localized plastic

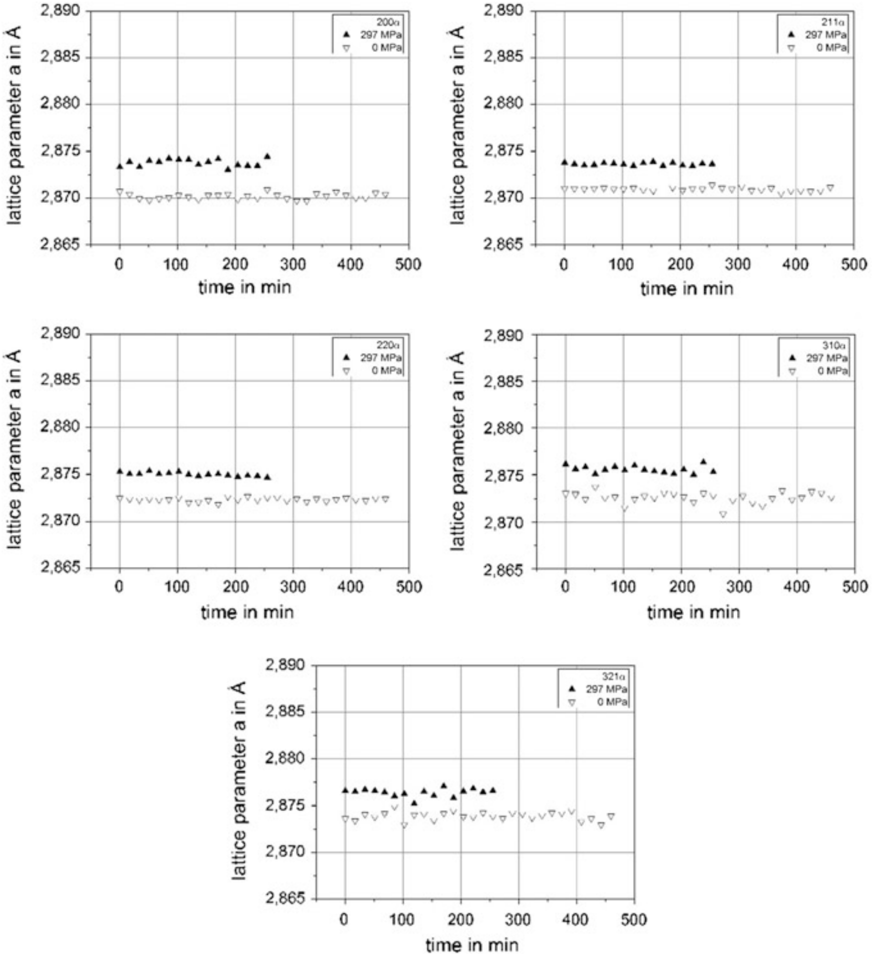

Fig. 4 Lattice spacing normed to cubic lattice parameter a for varying lattice planes of S1100MC obtained from hydrogen charged samples as a function of time and applied load

flow. On the other hand residual stresses already present within the sample may induce early plastic flow, too.

Another indication for beginning plastic flow is given by the integral breadth (IB) of the analyzed diffraction lines. The IB is a measure for stresses located on the microscopic level within the grains and can used as indicator for hardening or beginning plastic deformation. The IB in case of S1100MC does not show any change as a function of time or load, as shown exemplarily for lattice planes 200α and 211α in Fig. 6.

Contrary to that, IB of S1300Q samples is considerably higher (see Fig. 7). The reason may be primarily the presence of inhomogeneous lattice distortions within the grains, e.g. due to thermal processing of S1300Q. Consequently, IB of 200α

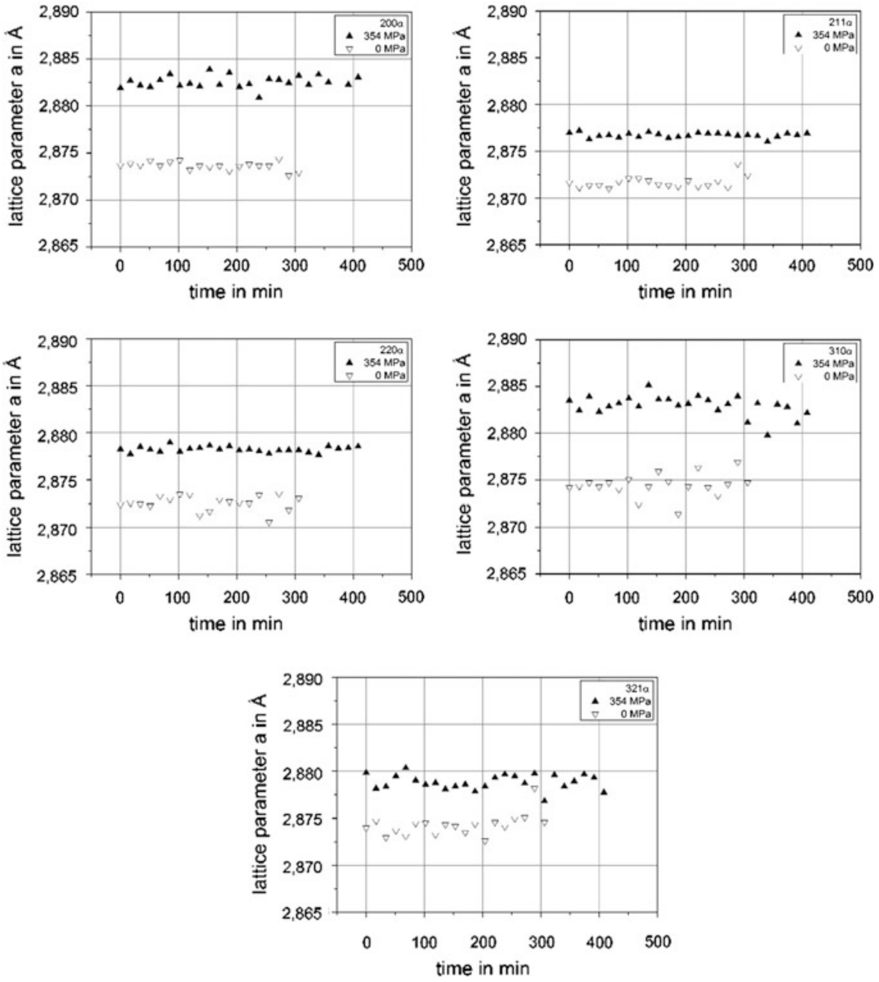

Fig. 5 Lattice spacing normed to cubic lattice parameter a for varying lattice planes of S1300Q obtained from hydrogen charged samples as a function of time and applied load

and 211α is increased. Moreover, the IB is even higher when external load is applied to the sample. This means loading is inducing additional microstresses to the material. The increase in IB is another indication for localized plastic deformation.

The stress difference calculated by using the $\sin^2\psi$ technique are discussed in the following. Figure 8 (left) shows a comparison of these differences obtained for two hydrogen charged samples of S1100MC applying zero load (0 kN) and 297 MPa (2.1 kN). In the load-free case the measured stress difference is quite low. Only 25 MPa indicating low absolute stresses barely influenced by the presence of hydrogen. The reason is that solute hydrogen occupies interstitial sites

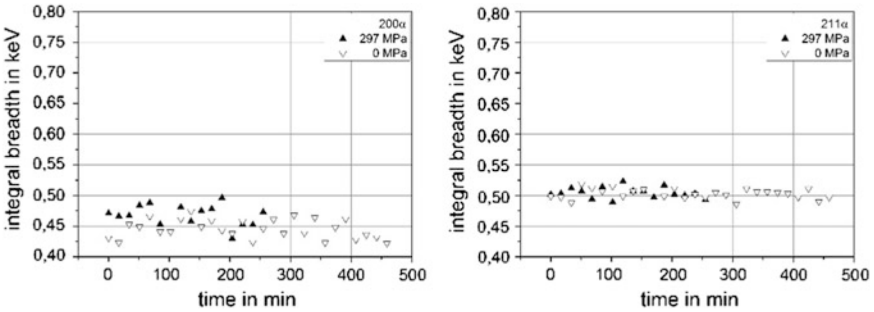

Fig. 6 Integral breadth of 200α (*left*) and 211α (*right*) for S1100MC obtained from hydrogen charged samples as a function of time and load

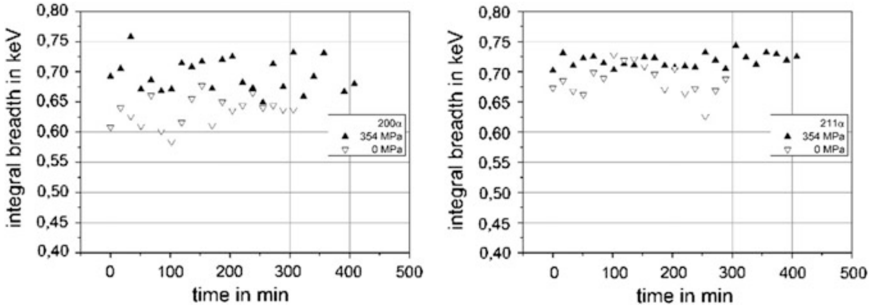

Fig. 7 Integral breadth of 200α (*left*) and 211α (*right*) for S1300Q obtained from hydrogen charged samples as a function of time and load

in the metal lattice producing a solid solution what leads to a low distortion of the lattice. Small fluctuations during increasing holding time may stem from local lattice expansion due to hydrogen diffusion. However, they are within the evaluation method precision (peak fitting).

During loading within the elastic limit the calculated stresses are distributed around 200 MPa, what is around 100 MPa below the applied stress of 297 MPa (2.1 kN). Based on the assumption that the initial sample condition was virtually stress free, the difference of—100 MPa may be related to the presence of hydrogen in the lattice. Investigations by Dabah et al. [4] revealed that hydrogen charging can induce compression to the lattice in high-alloyed martensitic steels.

Figure 8 (right) shows the stresses in comparison for S1300Q between two hydrogen charged samples for loads of 0 MPa (0 kN) and 354 MPa (2.5 kN) as a function of time. It is noticeable, that the stresses show distinct fluctuations in both load situations. The maximum amplitude is approximately 100 MPa. The fluctuations are on the one hand due to measuring uncertainty. On the other hand they may stem from local hydrogen variations due to diffusion.

Without any external load the stress difference ($\sigma_{11} - \sigma_{33}$) shows a mean value of 18 MPa, indicating either a stress free sample or equal stresses in longitudinal

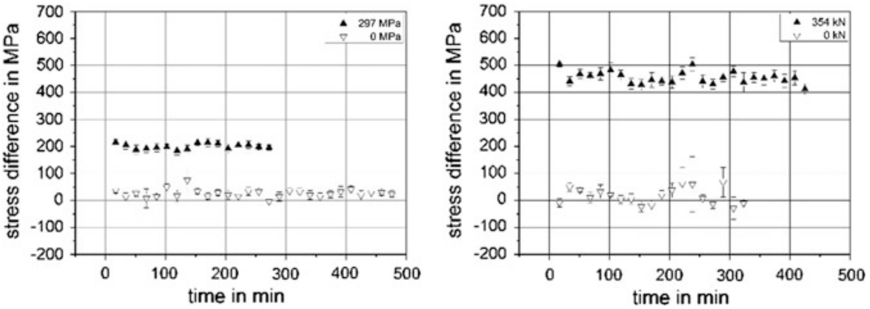

Fig. 8 Stress difference $\sigma_{11} - \sigma_{33}$ obtained from hydrogen charged samples as a function of time S1100MC (*left*) and S1300Q (*right*) without and with applied loads (25 % yield strength)

as well as radial direction. Assuming virtually residual stress free samples before hydrogen charging the presence of hydrogen induces additional tensile stresses only at a moderate level similar to S1100MC.

In case of an additional external load equal to a nominal stress of 354 MPa, the stress difference measured shows a pronounced increase to a mean value of 458 MPa. This is contrary to S1100MC, which has shown lower stresses than applied. As already observed for the individual lattice planes, anisotropic lattice distortion with local plastic flow may responsible for the stresses found. The difference of around 100 MPa might stem from hydrogen which has diffused to local stress concentrations (i.e. lattice defects) promoted by the external load, what leads to additional lattice expansion.

3 Conclusions

In this work a feasibility study was conducted using EDXRD in order to study the lattice response of two types of high strength steels charged with hydrogen. From the experimental observations the following conclusions can be drawn.

Embrittlement with total loss of ductility occurred for thermomechanical treated as well as quenched and tempered steel even at comparatively low amounts of hydrogen. While the thermo mechanically treated steel failed at its nominal yield point the quenched and tempered one failed at approximately 55 %. This can be attributed to varying amounts of diffusible hydrogen present in the steels due to different trapping capacity of the microstructures investigated here.

Determination of the lattice plane spacing revealed no significant changes during hydrogen effusion. No additional strains were induced by the presence of hydrogen alone. This applies also for the stresses determined in the samples.

During external loading of the samples within the elastic range (25 % yield strength) the lattice response of the quenched and tempered steel was more pronounced compared to the thermo mechanically treated one. Pronounced elastic anisotropy was observed for S1300Q which may cause localized plastic deformation well below the nominal yield point responsible for early fail of the material during tensile test. This is accompanied by additional increase of Integral breadth in case of the quenched and tempered variant. Furthermore, stresses found for hydrogen charged samples under load support this findings. Future investigations are necessary to analyze the observed phenomena in detail.

Acknowledgments We sincerely thank Helmholtz-Zentrum Berlin, Germany for granting beamtime. Special acknowledgement goes to C. Genzel and M. Klaus at the EDDI beamline for excellent support before, during and after our experiments.

References

1. Davis JR (1994) Stainless steels. ASM International, Ohio
2. Herlach D (2000) Hydrogen Embrittlement Metals Physica B 289–290:443–446
3. Lewis FA (1990) Solubility of hydrogen in metals. Pure Appl Chem 62:2091–2096
4. Dabah E, Kannengiesser T, Elizier D, Boellinghaus T (2011) In situ analysis of hydrogen behaviour in stainless steels by high energy synchrotron radiation mater. Sci Eng A 528:1608–1614
5. Boellinghaus T, Kannengiesser T, Zimmer P (2004) Effects of hydrogen on weld microstructure mechanical properties of the high strength steels S690Q and S1100QL. IIW-Doc. II-1525-04, Online-document
6. Troiano AR (1960) The role of hydrogen and other interstitials in the mechanical behavior of metals. Trans ASM 52:54–80
7. Oriani RA (1972) Mechanistic theory of hydrogen embrittlement of steels. Berichte der Bunsengesellschaft für Physikalische Chemie 76:848–857
8. Birnbaum HK (1985) Hydrogen related second phase embrittlement of solids. In: Troiano AR, Gibala R, Hehemann R (eds) Hydrogen embrittlement and stress corrosion cracking. ASM International, Ohio, pp 153–177
9. Uhlemann M (1999) Wasserstofftransport und Bindungszustände von Wasserstoff in kubisch-flächenzentrierten Stählen und Nickel-Basislegierungen (in German). Ph.D. thesis, Technische Universität Dresden, Dresden
10. Pressouyre GM (1979) A classification of hydrogen traps in steel. Metall Trans A 10:1571–1573
11. Wei F, Tsuzaki K (2002) Response of hydrogen trapping capability to microstructural change in tempered Fe-0,2C martensite. Scr Mater 52:467–472
12. Michler T, Naumann J (2010) Microstructural aspects upon hydrogen environment embrittlement of various bcc steels. Int J Hydrogen 35:821–832
13. Devanathan MAV, Stachurski Z (1962) Adsorption and diffusion of electrolytic hydrogen in palladium P. R Soc London 270(1962):90–102
14. Genzel C, Denks IA, Gibmeier J, Klaus M, Wagener G (2007) The materials science synchrotron beamline EDDI for energy-dispersive diffraction analysis. Nucl Instrum Meth A 578:23–33
15. Kromm A, Brauser S, Kannengiesser T, Rethmeier M (2011) High-energy synchrotron diffraction study of a transformation induced plasticity steel during tensile deformation. J Strain Anal Eng 46:581–591
16. Macherauch E, Müller P (1961) Das $\sin^2\psi$—Verfahren der röntgenographischen Spannungsmessung Z. angew. Physik 13:305–312

Determination of the Welding Residual Stress Field by Diffraction Methods and Studying Its Behavior Under Uniaxial and Multiaxial Mechanical Loading

Majid Farajian, Thomas Nitschke-Pagel, Robert C. Wimpory and Michael Hofmann

Abstract Weld fatigue strength is currently the bottleneck to designing high performance and lightweight welded structures using advanced materials. In addition to loading conditions, environmental aspects, geometrical features and defects, it has been proven that studying the influence of residual stresses on fatigue performance is indispensable. The extent of the influence is however a matter of discussion. A deeper insight into the source of the welding residual stresses on the basis of sound physical principles would increase the awareness of the extent of their true threat to the structural integrity. In this article the influence of the uniaxial and multiaxial loading on the relaxation of welding residual stresses in small specimens and large components out of different steels namely S235JRG2, S355J2G3, S355J2H, P460NL, 690QL and S1100QL will be presented. X-ray diffraction analysis has been used for the determination of residual stress profiles in surface layers. For residual stress analysis in deeper layers synchrotron and neutron diffraction techniques were applied as complementary methods. A clear recognition of the difference between initial welding residual stresses in small and large scale specimens was observed. Tensile residual stresses as high as the yield strength could appear in large scale welded specimens. That was not the case for small scale welds due to the low grade of restraint. Nevertheless in the flat and tubular butt welds the highest residual stresses were obtained in the weld centerline. At the weld

---

M. Farajian (✉)
Fraunhofer Institute for Mechanics of Materials, Wöhlerstr. 11, 79108 Freiburg, Germany
e-mail: majid.farajian@iwm.fraunhofer.de

T. Nitschke-Pagel
Institute of Joining and Welding, Langer Kamp 8, 38106 Braunschweig, Germany

R. C. Wimpory
Helmholtz Zentrum Berlin für Materialien und Energie GmbH, Hahn-Meitner-Platz 1, 14109 Berlin, Germany

M. Hofmann
Heinz Maier-Leibnitz Zentrum, FRM-II, München, Lichtenbergstr. 1, 85747 Garching, Germany

T. Kannengiesser et al. (eds.), *In-situ Studies with Photons, Neutrons and Electrons Scattering II*, DOI: 10.1007/978-3-319-06145-0_11,

toe which is critical regarding fatigue crack initiation, the magnitude of the residual stresses is lower. Beside that it was observed that in the case of relaxation the first load cycles especially in components out of low strength steels are decisive. The influence of loading conditions and local mechanical properties on the relaxation of welding residual stresses was investigated based on principles of solid mechanics. The von Mises failure criterion was able to describe the relaxation behavior.

Keywords Welding residual stresses · X-ray, synchrotron and neutron diffraction · Fatigue · Multiaxial fatigue

1 Introduction

Experimentally there is no doubt since the fifties that the welding residual stresses influence the fatigue performance and should be regarded in fatigue assessments. According to Gurney [1], the earliest evidence of detrimental effects of welding residual stress on fatigue appeared in 1956 in reports by Kudryavtsev [2] and Trufyakov [3]. However the extent of these detrimental effects on fatigue has been unclear and is still matter of debate.

One reason for this lack of clarity is that the exact determination of the whole residual stress field even at design critical points is time consuming and requires complementary equipment. Another reason is that the interaction between load stress and residual stress fields is complex to estimate. The complexities manifest themselves even more in the case of multiaxial fatigue [4]. There is also in general still lack of insight into the influence of residual stress on fatigue nucleation life (the number of cycles required to initiate fatigue microcracks) and fatigue propagation phase. Residual stresses have been observed to influence the crack initiation phase in [5, 6] and the fatigue crack propagation phase in [7, 8]. Residual stresses may also have remarkable influence on the location of fatigue crack initiation and its propagation rate [9] and the position of the knee point in the Fatigue S-N lines [10].

The developments in the field of characterization of polycrystalline materials and the experimental analysis of residual stresses during the last decades by means of photons and neutrons have contributed to a better understanding of the origins and sources of welding residual stresses. A shortcoming is that quantitative integration of this knowledge in structural health assessments has not kept pace with these advancements. It is obvious that a deeper insight into their source and nature on the basis of sound physical principles could increase the awareness of the extent of their threat to structural safety.

In this chapter it will be presented how photons and neutrons as material characterization tools have contributed to a better understanding of the origins of residual stresses first. Secondly it will be discussed how these tools have been used to study the behavior of the residual stresses under uniaxial and multiaxial cyclic mechanical loadings.

2 Nature and Origin of Welding Residual Stresses

The curiosity to understand the sources of welding residual stresses dates back to the thirties. At this time the classical residual stress measurement techniques based on diffraction were in their infancy and strain gauges were used to validate the diffraction measurements. For a long time, welding residual stresses were treated as purely shrinkage stresses developed during cooling. As a matter of fact it was due to the progressions in the measurement techniques by means of X-ray diffraction that other possible sources of welding residual stresses were discovered. The changes in the material volume due to thermal expansion and contraction are interfered by volume changes due to the solid state phase transformations during heating and cooling phases. The interaction of hindered shrinkage and hindered volume expansion and its role on the welding residual stress field was illustrated with some experiments by Jones and Alberry [11] in 1977. A schematic representation of the stress-temperature curves for the experiments of this type is given by Wohlfahrt [12].

The development of welding residual stresses in steels with phase transformation could be explained qualitatively by means of the already available schematic models [12, 13]. In Fig. 1-left, after solidification and during cooling at relatively high temperatures before the onset of phase transformation, thermal contraction and hindrance of shrinkage cause tensile stresses in austenite.

The introduced tensile stresses can be just as high as the yield strength of austenite at the respective temperature. By decreasing the temperature and beginning of the phase transformation for respective steels the accumulated tensile stress relaxes and approaches zero and even becomes compressive. In this model the magnitude of the compressive stresses is governed based on hindrance of the net expansion due to the phase transformation. In another model [14] it is argued that the transformation plasticity is responsible for this relaxation and transformation strain compensates for any thermal contraction strain during cooling. Regardless of the mechanism of compressive stress accumulation during phase transformation, the continued thermal contraction strains are able to build up stress again after the austenite is exhausted. Theoretically tensile residual stresses as high as the yield strength of the material could be developed after cooling down to room temperature. Depending on the transformation temperature, tensile (curve 1), zero (curve 2) or compressive (curve 3) residual stresses could be developed during cooling.

In the schematic model on the right side of Fig. 1, the development of the residual stress profiles in both transverse and longitudinal direction for the ferritic-pearlitic steel is demonstrated. As seen in the left model for this type of steel (red line) the phase transformation occurs at approximately 700 °C leads to accumulation of compressive stresses. This stress status is illustrated in the right model schematically by the curve A for both transverse and longitudinal direction. In the longitudinal direction two tensile peaks on each side of the weld bead are developed during the phase transformation period because of equilibrium reasons. When the transformation is finished at around 600 °C the hindered-shrinkage-induced

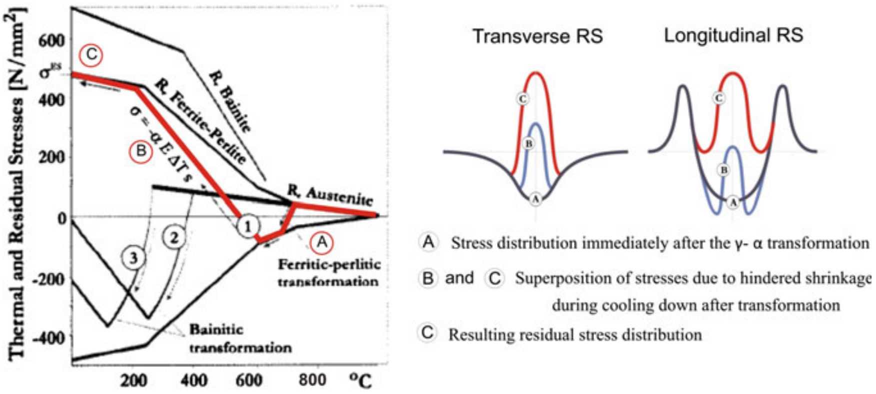

Fig. 1 Residual stress development due to phase transformation and shrinkage [12, 13]

tensile thermal stresses accumulate again and reach the yield strength of the ferritic-pearlitic steel at room temperature. During this period the tensile stresses overcome the compressive stresses (curve B) and continue this way until reaching the final state of residual stresses (curve C).

The validity of this qualitative model for describing the surface residual stresses in flat and tubular butt welds out of different steels with solid phase transformation has been investigated by X-ray diffraction. Here the residual stress measurements were accomplished by using Cr-K_α radiation (35 kV, 30 mA) and studying the interference line from {211} ferrite lattice plane under seven tilt angles (Ψ) 0°, 13°, 18°, 30°, 39°, 42° and 45° for 2θ between 149 and 163. The measurement spots (1–2 mm diameter) were chosen on a line perpendicular to the welding direction. In Fig. 2 the transverse and longitudinal residual stress distribution profiles as the mean values of the measurements on 15 specimens for each base material are presented. For the sake of clarity the scatter bands are not plotted in these diagrams. The profiles show a good symmetry and all have the same common characteristic features.

The position and the order of appearance of the peaks and dips in the profiles are the same. The peaks in the weld seam shifts as expected to higher values by increasing the yield strength of the base metal in both transverse and longitudinal directions. At the same time the gradient of the transverse profile in the transition from weld to base metal increases by increasing the yield strength. In the longitudinal direction a plateau in the weld metal which could be with a slight peak in weld centerline is observed. The two phase transformation induced characteristic peaks in the vicinity of the HAZ are common feature of the longitudinal residual stress profiles. From the fatigue point of view, it is interesting to observe that the regions of maximum stress concentration do not coincide with the regions with maximum tensile residual stresses.

As it is observed in Fig. 3, the residual stress/yield strength ratio is smaller than 1 in the weld bead centerline and does not necessarily increase by increasing the yield strength. The maximum value of the tensile residual stresses available in the

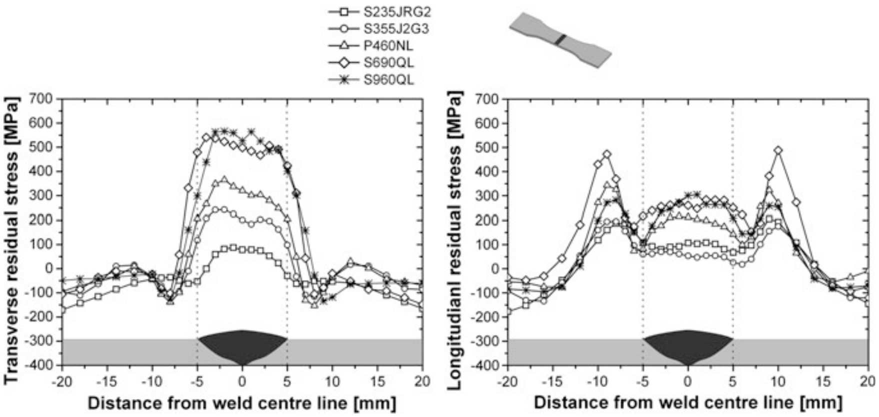

Fig. 2 Residual stress distribution in all the welded specimens in transverse (*left*) and longitudinal (*right*) directions

Fig. 3 Residual stress/yield strength ratio in welded steel specimens with different yield strengths

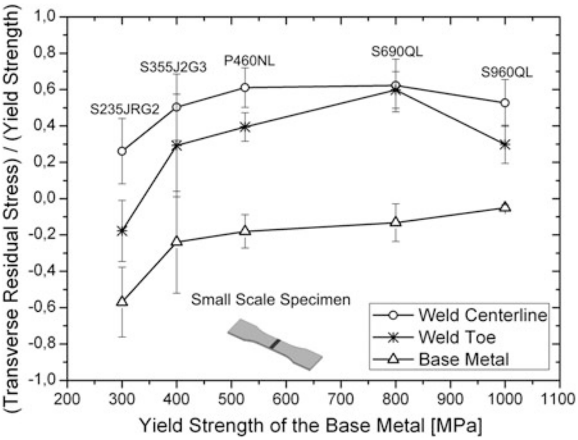

welds in this size is 60 % of the yield strength. After this peak the residual stress/ yield strength ratio decreases for higher strength steels. This could be of importance from the fatigue point of view for high strength steel welds where it is often postulated that weldments out of these steels contain residual stresses of yield strength magnitude.

In the case of tubular joints, the shape of the welding residual stress distribution in the axial and hoop direction could be again described by the qualitative model in Fig. 1. The surface welding residual stresses in the axial and hoop directions of S355J2H samples on four parallel lines which are perpendicular to the weld bead namely Q1, Q2, Q3, and Q4 are presented in Fig. 4. The residual stress profiles in both directions show a good symmetry again on all the Q1 to Q4 lines. The distribution profiles also have the same common characteristic features and

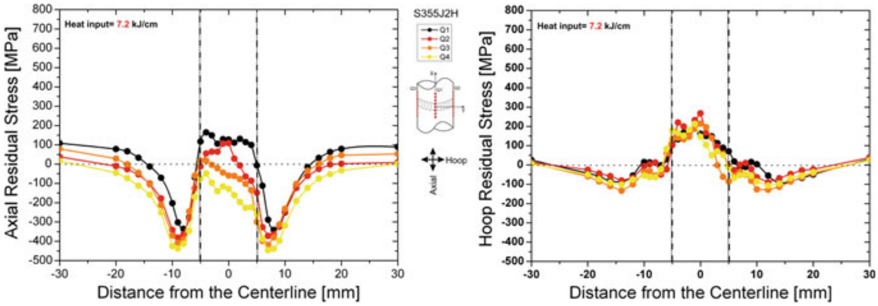

Fig. 4 Welding residual stress profiles in axial and hoop directions with heat input of 7.2 kJ/cm

the position and the order of appearance of the peaks and dips on Q1 to Q4 lines are the same. In the axial direction the residual stress distributions show a W-type profile. The peaks in the weld seam however do not show the same maxima in different quarters. On Q1 where the welding has started and ended, the maximum tensile stress amounts 200 MPa. Although in the hoop direction the phase transformation induced peaks in the vicinity of the weld are not that pronounced, more consistency of the distribution profiles in different quarters is observed. A maximum tensile residual stress of 300 MPa could be found in the weld bead. The residual stresses at the weld toes (marked with dash lines) which could be potentially the fatigue crack initiation sites are negligibly low.

The formation of the characteristic shapes of the welding residual stresses in the tubular joints in S355J2H with phase transformation at relatively high temperature explained by the schematic models (Fig. 1) could be analyzed more in details. For this the thermal history and the continuous cooling transformation diagram of the base material are needed. The temperature measurements (Fig. 5-left) in different quarters of the tube during welding with the heat input of 7.2 kJ/cm showed that the $t_{8/5}$ time would be between 9 to 12 s. For the CCT-diagram, the one for St355 steel (Fig. 5-right) which is similar to S355J2H concerning chemical composition and mechanical properties was selected from literature. The cooling curve representing a $t_{8/5}$ of 10 s is presented in the corresponding welding-CCT diagram with the orange curve.

It is observed that under this cooling condition the transformation of austenite to bainite occurs at approximately 550 °C. At a lower temperature of around 425 °C, 65 % of the austenite is transformed to bainite. Decreasing the temperature the following martensite transformation occurs which is exhausted at 300 °C. The hardness measurement at Q2 and Q4 by means of ultrasonic contact impedance method in Fig. 6 shows that the hardness in the weld agrees well with the hardness range given in the CCT-diagram i.e. 270–324 HV under this welding condition.

The maximum tensile residual stress in the weld (Fig. 4) of 200–300 MPa shows that the temperature at which the martensite transformation ends (around 300 °C) is high enough for further accumulation of tensile stresses during shrinkage. From the fatigue point of view it is favorable to have compressive residual stresses

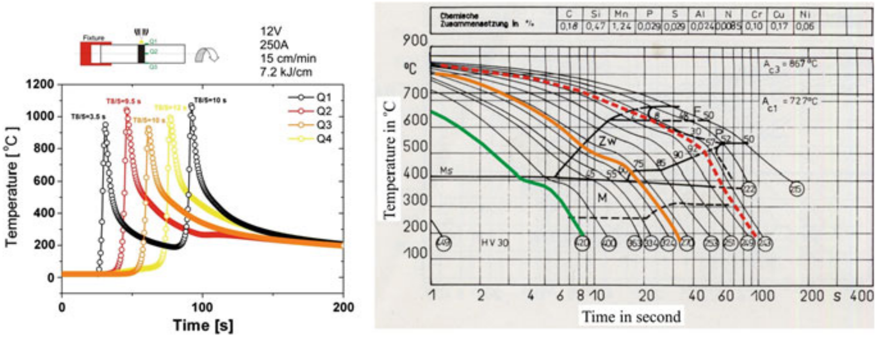

Fig. 5 Temperature measurement at four points of the welding path in every 90° (*left*), CCT-diagram of St35 (*right*)

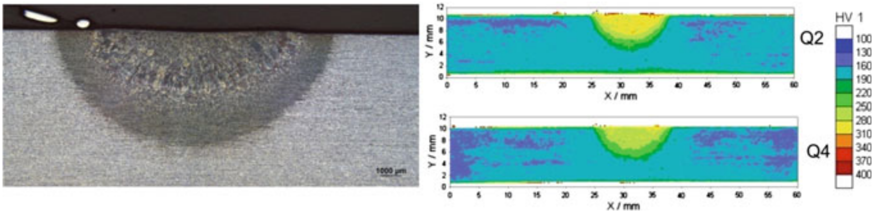

Fig. 6 Cross section of the welded S355J2H (*left*) and hardness field measurements be means of UCI (*right*)

in the vicinity of the welds. In order to obtain compressive residual stresses according to the achieved results, a cooling rate based on the CCT-diagram should be selected which leads to lower temperatures at which the martensite transformation is finished. According to the CCT-diagram by choosing the welding parameters and thus heat input which leads to a cooling curve presented by the green curve, the austenite transforms directly to martensite at 410 °C. The martensite transformation this time is finished at 270 °C leading to a microstructure with a hardness of 420 HV30. As expected from the model in Fig. 1, this time lower tensile or even compressive residual stresses should be present at the weld and its vicinity. Figure 7 shows the axial and hoop residual stresses in the samples being welded by the heat input which was half of the previous case i.e. 3.6 kJ/cm. The $t_{8/5}$ for this case was calculated based on the heat input and the geometry, according to the literature [15].

The axial residual stress shows a w-profile with the maximum in the weld bead at zero level. At the weld toe compressive residual stresses of −400 MPa (Yield strength of this steel is 450 MPa) are present. In the hoop direction the transformation induced peaks reach 100 MPa which are counterbalanced with the compressive residual stresses with their maxima at the distance of 10 mm from the weld centerline.

It could be concluded here that based on the same principle by using the welding parameters which lead to lower cooling rates, the austenite transformation

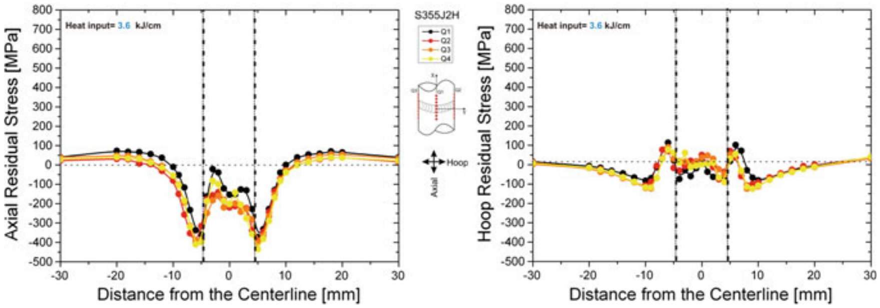

Fig. 7 Residual stress profiles in axial and hoop directions in the case of lower heat input of 3.6 kJ/cm

is shifted to even higher temperatures. This is the case for the red dash cooling curve in the CCT-diagram. As it is observed, the austenite transformation starts at 650 °C and at the temperature of 500 °C, 95 % of the austenite is transformed to bainite where after the shrinkage stresses could continue to accumulate. It could be expected that due to the dominance of the hindered shrinkage mechanism higher tensile residual stresses as the previous two cases could be present in the weld.

Until now the presented investigations included just the surface welding residual stresses, determined by means of X-ray diffraction. As expected in deeper layers in order to satisfy the equilibrium conditions, the residual stress distributions should be different with that of the surface profiles. The tensile residual stresses on the surface should be in balance with compressive residual stresses in deeper layers and vice versa. The in-depth measurement of residual stresses by means of X-ray diffraction and electrochemical removal of thin surfaces is a time consuming process and has its own limitations. Alternatively, the hole drilling method could be used but not without difficulty since the plane surface condition in welds is not fulfilled. In addition to that, the compulsory distance between the rosettes does not allow a uniform measurement of the residual stress profile with appropriate resolution. The synchrotron and neutron diffraction techniques are suitable tools for determination of the residual stresses in a non-destructive way and with sufficient resolution. Investigating the whole welding residual stress field would give a deeper insight into its distribution and development albeit at the cost of time and technical complexity. This topic will be treated in the next section.

3 Determination of Welding Residual Stresses by Means of Synchrotron and Neutron Diffraction

The in depth residual stress determination was done using neutron diffraction method. For this purpose the neutron strain scanner instrument E3 at the Helmholtz Centre Berlin and Stress-Spec at FRM II, München were used. For the samples the {211} ferritic peak was used for all measurements. The gauge

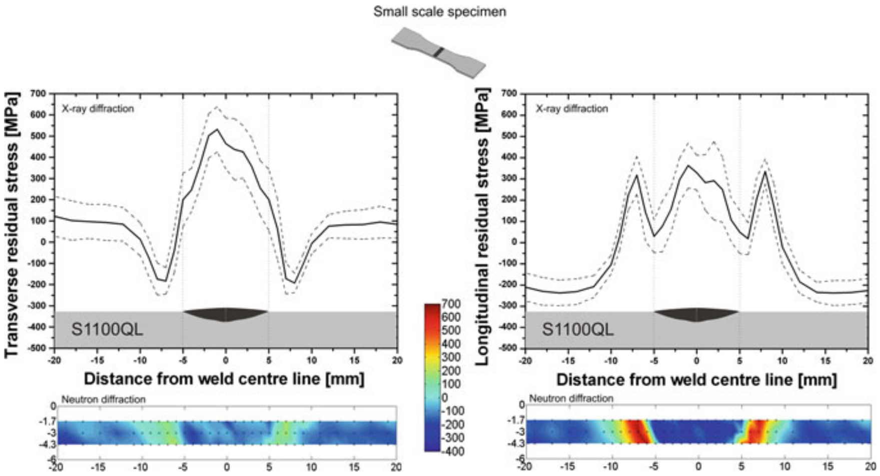

Fig. 8 Residual stress in welded S1100QL determined by X-ray and neutron diffraction methods

volumes of 2 × 2 × 2 mm^3 (E3) and 1 × 1 × 1 and 1 × 10 × 1 mm^3 (FRM II) were used and this was kept as far away as possible from the surface in case of potential surface effects. The specimens were positioned to permit determination of stresses in the three orthogonal directions of the welds. These directions were assumed to be the principal stress directions being coincident with the direction of welding (longitudinal), transverse and normal to the welding. Specimen alignment in all movement directions was done by neutron intensity scanning and alignment with a theodolite. The neutron diffraction measurements were made following the guidelines presented in [16].

For the determination of the strain free lattice spacing (d_o), in different welding zones, comb specimens with teeth 3 mm by 3 mm in section was produced by electrical discharge machining. The dimensions of the teeth allowed for full immersion of the diffraction gauge volume into it. For these reference measurements, the same instrument set-up was used as for the actual stress determinations in the plate, including the size of the gauge volume. For the cases without comb specimens the reference lattice spacing d_o in the base metal and far away (80 mm) from the weld in the main specimen was used.

The surface and in depth residual stresses in the transverse and longitudinal direction of a bead on plate welded sample out of S1100QL are presented in Fig. 8. The presented surface residual stress distribution profile in Fig. 8-top is the mean value of the measurements on 15 specimens for each base material using X-ray diffraction. The scatter band is shown with dashed lines.

In the lower part of the figure the residual stress mapping by means of neutron diffraction is presented. It is known that the near surface strain measurement by neutron diffraction is critical due to the aberration peak shift effect. Because of this technical limitation in the neutron diffraction technique the residual stresses up to a certain depth from the surface cannot be measured. So there is a gap of data between the surface residual stresses which can be measured by X-ray and deeper residual stresses which could be measured by neutron diffraction. In order to fill this gap the synchrotron measurement technique was applied as a complementary method to determine the whole residual stress field. The synchrotron diffraction instrument at BESSY-II in HZB in reflection mode was capable of covering the first 100 μm of the top layer for the residual stress measurement. The measurement results from the X-ray (upper and lower side), neutron (-0.7 mm $< z <-5.1$ mm) and synchrotron ($0 < z <-100$ μm) diffraction could now provide to a better understanding of the residual stress distribution. The transverse residual stresses at the weld centerline, weld toe and base metal (7 mm from centerline) as a function of depth are shown in Fig. 9.

At the weld toe which is of importance from fatigue point of view the tensile residual stress with its maximum at the surface, decreases with a smaller gradient than the weld centerline profile. Within a depth of approximately 2 mm, tensile residual stresses are available at the weld toe. Between 2 and 4 mm from the surface compressive residual stresses contribute to the equilibrium. Below 4 mm, tensile residual stresses appear again. In the lower side compressive residual stress are present. An important conclusion which can be drawn from residual stress field mapping is that high transverse and longitudinal residual stresses which could be of importance concerning fatigue damage initiation are allocated in the very top surface layers.

In the case of tubular welds the surface and in depth residual stresses and their characteristics in welded samples out of S690QL are presented in Fig. 10. The surface residual stresses in axial and hoop directions on 4 parallel lines which divide the tube to four quarters have been already determined by means of X-ray diffraction methods. The distribution profiles could partly describe the mechanisms of the development of welding residual stresses in tubular joints. The neutron strain scanner instrument E3 at the Helmholtz Zentrum Berlin was used for the in depth determination ($Z = 0.336, 0.469, 0.716, 1.117, 1.688, 2.327, 2.828$ mm from the surface) of residual stresses in this sample.

The surface residual stress distributions on the four parallel lines show almost the same profiles. It is interesting to notice that at the weld toes as potential fatigue crack initiation sites low tensile or compressive residual stresses are present. The region in which the welding residual stress peaks are developed is located between -10 and 10 mm from the weld bead centerline. The neutron diffraction measurements in the axial direction show that under the weld bead, compressive residual stresses are in equilibrium with surface tensile residual stresses. In the hoop direction the transformation induced peaks in the vicinity of the weld toe remain compressive through the thickness of the plate.

Again because of the technical limitation of the neutron diffraction method, the residual stresses up to a depth of 336 μm from the surface could not be determined. Although synchrotron diffraction method for determination of the residual stress in the subsurface layers up to a depth of 300 μm is required, X-ray and neutron diffraction could again provide with fruitful information about the whole welding residual stress fields.

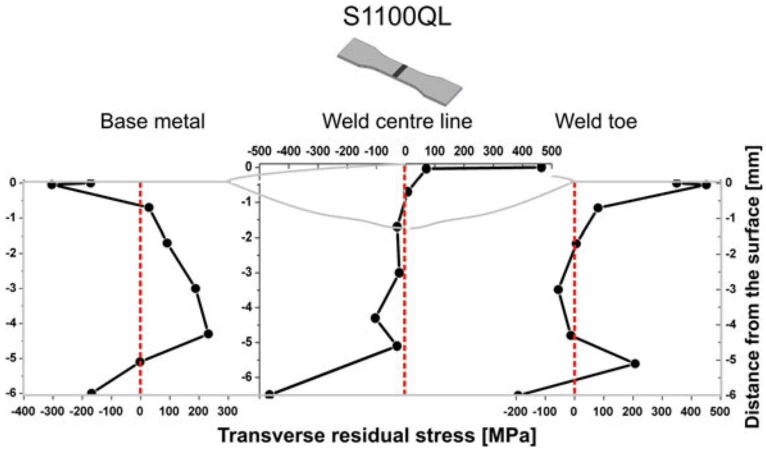

Fig. 9 Welding residual stress depth profiles in the weld centerline at the weld toe and base material in S1100QL specimens by means of X-ray, Synchrotron and neutron diffraction methods

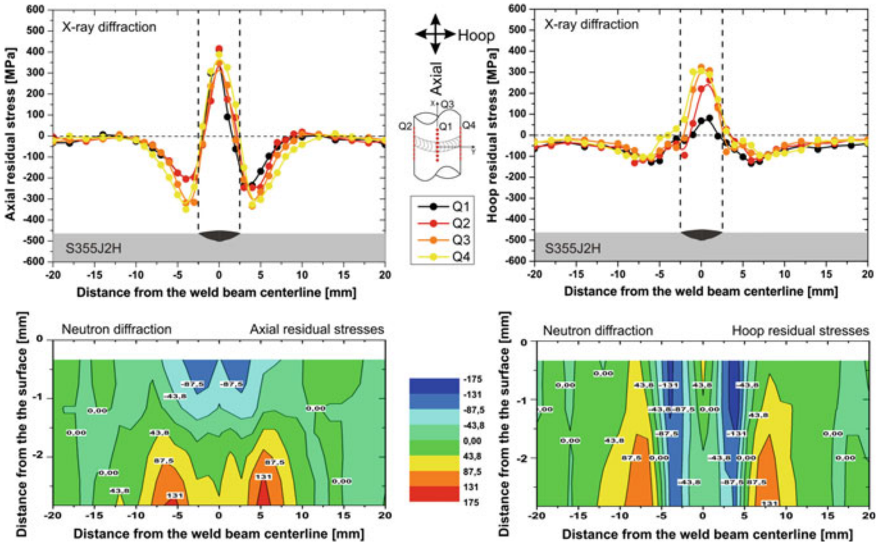

Fig. 10 Determination of the welding residual stress field in tubular S355J2H joints by X-ray (*top*) and neutron diffraction (*bottom*)

4 Influence of Welding Residual Stresses on Fatigue

The lack of clarities in estimating the residual stress threat to the structural integrity has led to conservative assumptions in the current fatigue design of welds. In fatigue design books [17, 18] and codes [19, 20] residual stresses in

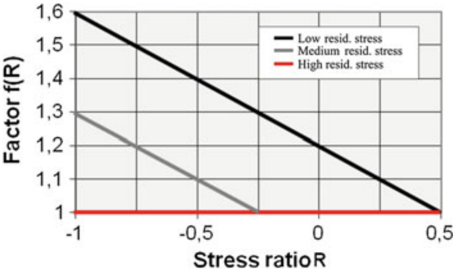

Fig. 11 Enhancement factor as a function of mean and residual stress [19]

welded components are assumed to be of yield strength magnitude. It is also assumed that in general the influences of residual stress and mean stress on fatigue are equal and the distinct differences between these two concerning source, distribution and relaxation under load is not considered. Based on these assumptions a mean stress independency of the fatigue strength is often postulated i.e. regardless of the stress ratio, it is recommended to use the S-N lines which are evaluated under pulsating tension loading with the stress ratio $R = 0.5$. The consequence is that in welds the fatigue loading condition is characterized by the stress range regardless of the stress ratio. In order to integrate the influence of residual stress in the fatigue assessments, Hobbacher [19] suggests, a fatigue enhancement concept based on low, medium and high residual stress levels in IIW-Recommendations (Fig. 11).

In this concept the hazard of high residual stresses is considered by suggesting the FAT (fatigue characteristic strength) values which are obtained in fatigue tests with the stress ratio $R = 0.5$. On the other hand the less hazardous effect of low residual stresses on fatigue performance is taken into account by multiplying the FAT value by the enhancement factor. For example it is suggested to take an enhancement factor of 1.6 in the case of low residual stress and stress ratio $R = -1$. This means that here a mean stress sensitivity $M = [(\sigma_{a(R=-1)}/\sigma_{a(R=0.5)}) - 1]$ of 0.6 has been postulated. This high level of mean stress sensitivity how ever has not been confirmed in the literature. According to the experimental results in [21], it was shown that a mean stress sensitivity of 0.3 could describe the interactive influence of mean and residual stresses on fatigue more consistently.

The concept recommended in [19] is a step towards the rationalizing the fatigue design codes by including the mean stress dependency of fatigue strength and considering the influence of residual stresses in the welds. At the same time it should be also mentioned that categorizing the residual stresses qualitatively into three levels of low, medium and high is not always based on rigorous engineering analysis and could lead to misinterpretations. Despite uncertainties in interpreting the behavior of residual stresses, fatigue design codes and regulations form a well-established basis which serves as useful engineering tools and source of data for designers. However utilizing the material strength reserves without clarifying the uncertainties about the role of the residual stresses seems to be impossible. In another IIW-document [22] an evaluation model is suggested in which for the application of the fatigue design codes [19, 20], the relaxation possibilities of residual stresses could be taken into account. Under the assumption that multiaxiality of the load stress state could influence the effect of residual stress on fatigue in typical welded components, the relaxation of initial residual stresses is approximated. Based on this approximation an appropriate enhancement factor for different levels of remained residual stresses after relaxation is recommended. This evaluation model allows a practical and economical use of the available fatigue design codes. However the experimentally determined residual stresses in the initial status and after the relaxation have not been addressed.

Theoretically, the influence of residual stresses on the service behavior of components depends strongly on whether the effective part of the residual stress field experiences relaxation or stability. It is obvious that if the residual stress relaxes during loading their influence on the fatigue performance decreases. The relaxation is mainly a function of the initial residual stresses, local load stress and local elasto-plastic stress-strain behavior. For an accurate estimation of the fatigue performance of welded joints, not only the initial residual stress field but also its variation under load is decisive. The portion of residual stress which stays stable can shift the load stress range much the same way as the mean stresses do in fatigue loading. The relaxation of residual stresses during fatigue loading however reduces this hazard to the structural health. That is, before considering the influence of residual stresses in fatigue, the effect of fatigue on residual stresses should be understood.

5 Behavior of Welding Residual Stresses Under Axial Loading

As a result of inhomogeneous plastic deformation during welding, the plastically deformed regions do not fit into the space available and residual stresses arise. During loading of the welds, if the sum of the residual stresses and the external load stresses exceeds the local yield strength at the points of misfit, yielding occurs. The material at these points will then “fit” better and the residual stress field changes. Early attempts at modeling variation in welding residual stresses date back to the fifties when the first models to describe the redistribution of the internal stresses under mechanical loadings appeared in literature. Erker 1954 [23] in his model with three connected metallic bars in parallel showed tensile and compressive residual stresses are developed in the middle and side bars respectively if the middle one is welded. The cross section of the middle bar was as big as the other two bars together. This system of bars was then submitted to tensile loading. By increasing the load, the superposition of initial tensile residual stress and load stress in the middle bar exceeds the yield strength. As a result of yielding, the middle bar which cannot carry load anymore becomes longer. At the same time, the side bars containing initial compressive residual stresses carry the load and are stretched with a double strain rate (elastically as long as the yield strength is not exceeded). After unloading, the permanent elongation of the middle bar as a result of plastic deformation compensates the shrinkage of the bar after welding. This in turn leads to the elimination of the inhomogeneous plastic deformation which occurred during welding and thus relaxation of the whole residual stress field. In other words, relaxation takes place as soon as the summation of load stress (σ^{L}) and residual stress (σ^{RS}) exceeds the material yield strength:

$$\sigma^{L} + \sigma^{RS} > R_e \tag{1}$$

In general residual stresses are multiaxial in nature and in the case of relaxation under multiaxial loading the superposition of the stress components in the form showed in relation 1 is not possible. Since yield criteria generally are functions of principal stresses differences, relation 1 in its general form could be written as follows:

$$f((\sigma_1 - \sigma_2), (\sigma_2 - \sigma_3), (\sigma_3 - \sigma_1)) > g(R_e) \tag{2}$$

The critical value g(Re) is a function of yield strength. Assuming von Mises criteria and plane stress condition ($\sigma_2 = 0$), relation 2 could be written as:

$$\sigma_1^2 + \sigma_3^2 - \sigma_1.\sigma_3 > R_e^2 \tag{3}$$

The residual stresses are subjected to the same laws of equilibrium which apply to ordinary stresses produced by external loads. Since relaxation is the local plastic deformation as a consequence of the interaction of external and residual stresses, classical failure criteria used in plasticity should be able to describe this phenomenon. In series of experiments being presented here, the residual stress state was considered to be plane stress and the biaxial residual stress relaxation under axial loading was investigated. Another assumption was that the principal load stresses and the principal residual stresses have the same directions.

The validity of Eq. 3 in describing the welding residual stress relaxation under mechanical loading is shown in Fig. 12 for small specimens out of S355J2G3. It is observed that by increasing the applied load the von Mises stress in the weld and its vicinity approaches and partly exceeds the yield strength and relaxation takes place. The yield strength of the base metal was assumed to be the same for the weld metal and heat affected zone. In the case of a 500 MPa applied nominal load stress the von Mises stress in the whole area of interest exceeds the yield strength and drastic relaxation in weld metal, HAZ and base material occurs.

In the case of cyclic loading, the accumulated microplastic deformation in the deformed volume fraction (surface or interior) can give rise to an altered state of residual stresses and at the same time an altered microstructure of the material containing residual stresses. If during loading the grains harden or soften the resistance against plastic deformation increases or decreases respectively which could lead to an alteration of the relaxation rate. The resistance of the material to

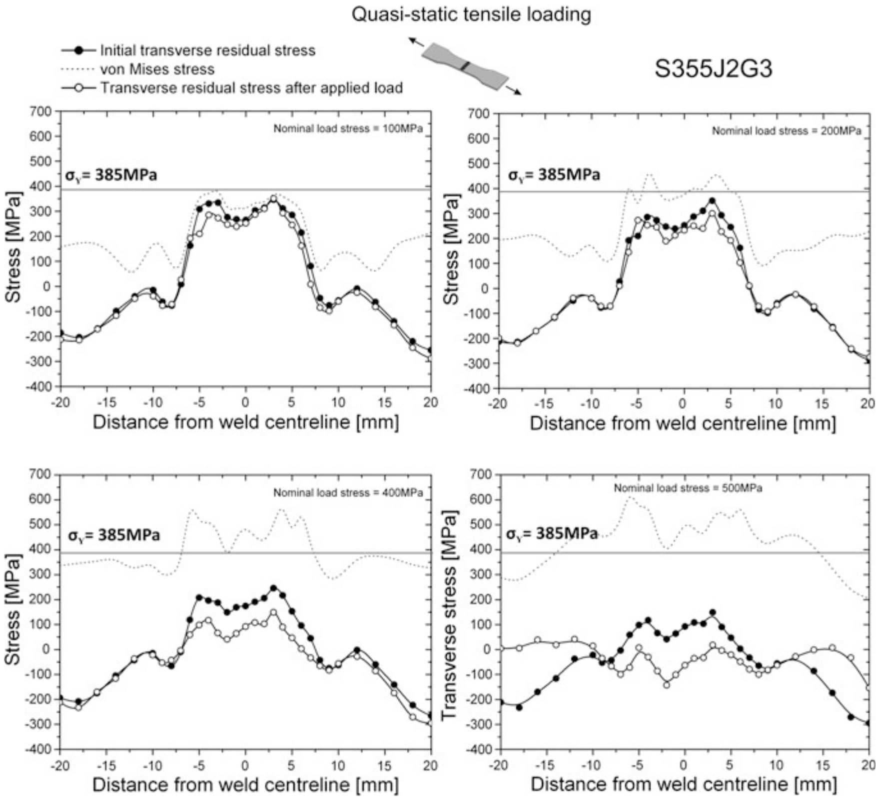

Fig. 12 Transverse residual stress relaxation under quasi-static tensile loading in S355J2G3 welded specimens

residual stress relaxation under cyclic loading is related to its cyclic behavior which is referred as the cyclic yield strength ($R_{e,cycl.}$). It could be expected then that the relaxation takes place if the von Mises stress exceeds the cyclic yield strength.

For the cyclic investigations after the measurement of the initial residual stress profiles, the specimens were loaded by a hydraulic testing machine with constant amplitudes until failure or a maximum of 2×10^6 cycles. The residual stresses in every 10^n ($n = 0, 1, 2, \ldots, 6$) numbers of cycles were determined by X-ray diffraction after removing it from the testing machine. Except the very first relaxation in cases of high initial residual stresses, no further variations could be observed. This was regardless of the position of the investigated points, at the weld centerline (Fig. 13-left) or at the weld toe (Fig. 13-right). By increasing the yield strength the level of initial residual stresses at the weld centerline and toe increases. Thus the remaining residual stresses after the initial relaxation in higher strength materials are higher than that of the lower strength material. This shows

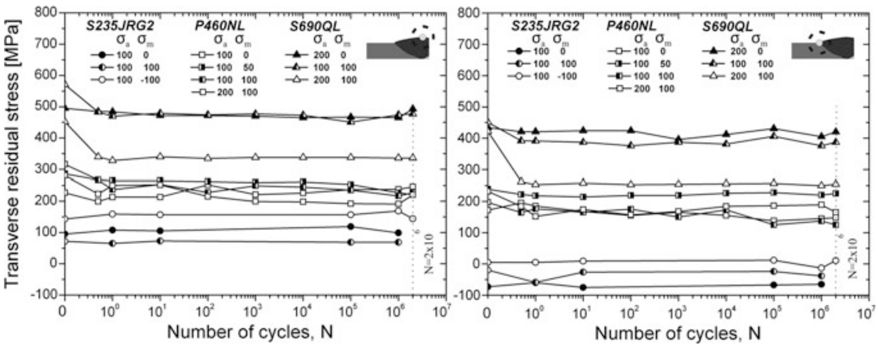

Fig. 13 Transverse residual stress relaxation at the weld centreline (*left*) and at the weld toe (*right*) in high cycle fatigue

the severity of the residual stress threat to structural safety in high strength steels under high cycle fatigue conditions.

In Fig. 14 the relaxation behavior in welded S235JRG2, P460NL and S690QL is again illustrated, this time under higher stress amplitudes. Due to higher load stresses compared with high cycle fatigue condition, the initial relaxation is larger for these cases. After the first relaxation, both stability and variation of the residual stresses is observed. In the case of S235JRG2, with the lowest yield strength, the relaxation under high and low cycle fatigue conditions are at the same negligible level. That is due to the near zero and partly compressive initial residual stresses. The question of to what extent the fatigue crack initiation and propagation influence the variations in the welding residual stresses under low cycle fatigue condition could be only addressed with additional studies.

Studying the relaxation behavior in small scale specimens based on solid mechanics provides the basic understanding of the problems. However in practice in industry larger parts are welded together. The question may arise, if the same relaxation behavior could be expected in larger welded components. Although the welding consumables and the parameters for the small and large samples are the same, the residual stresses in the large scale specimen have considerably higher values. This is due to the increased grade of restraint in large specimens as a consequence of higher stiffness. The differences are more pronounced in the transverse direction in which the whole profile shifts into the tensile regions. In Fig. 15 the transverse and longitudinal residual stresses in a welded large scale component are compared with the corresponding values in small specimens. The base material for both cases is S355J2G3. The course of the profiles in small and large welds is the same and there is only a parallel shift of the residual stress profile in the positive direction for the larger specimen. Consequently the tensile residual stresses at the weld toe are higher in large specimens compared with that of the small specimens.

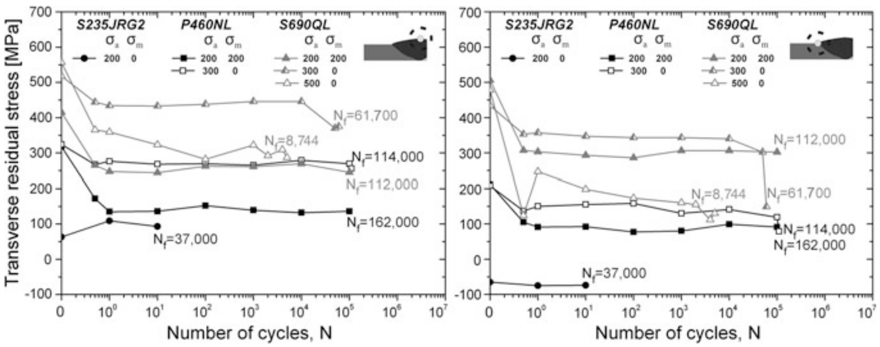

Fig. 14 Transverse residual stress relaxation at the weld centreline (*left*) and at the weld toe (*right*) in low cycle fatigue

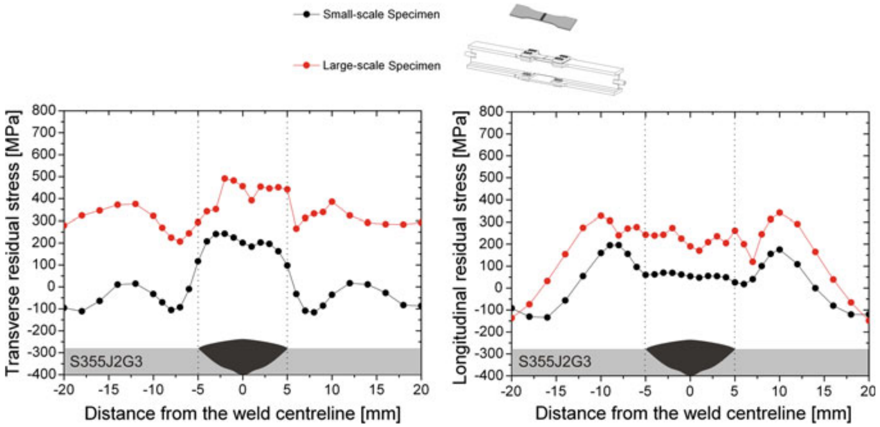

Fig. 15 Transverse (*left*) and longitudinal (*right*) residual stress profiles in small and large scale welds (S355J2G3)

In Fig. 16 the transverse residual stresses at the weld toe in small and large scale specimens are compared. The residual stresses in small specimens increase by increasing the yield strength and reach a maximum value of 60 % of the yield strength in S690QL. In the large components the stresses at the weld toe are as high as almost 80 % of the yield strength already in S355J2G3. The residual stress/yield strength ratio does not necessarily increase in higher strength steel and remains constant throughout.

The behavior of this high residual stresses under cyclic loading could give a realistic picture of their threat to fatigue performance. After the initial residual stress analysis, the I-beam fixtures including the welded parts were loaded by a 630 kN testing machine under four-point bending. Four-point bending with welded parts on the top, would exert compressive load stresses, whilst bending with the

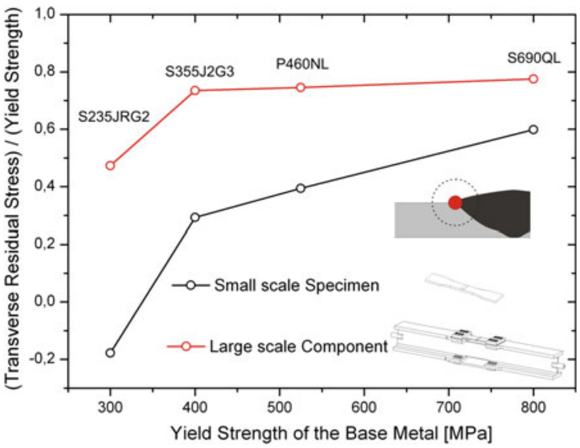

Fig. 16 Comparison of the maximum available transverse residual stress at the weld toe in different steels

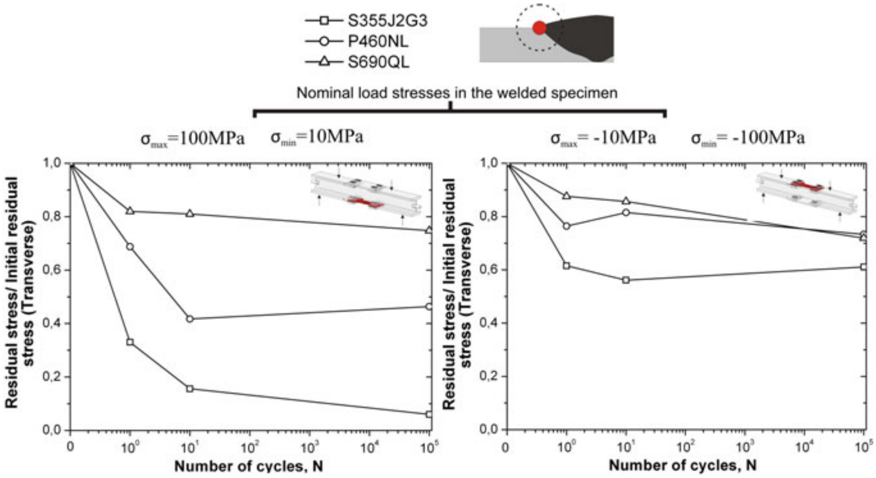

Fig. 17 Relaxation at the weld toe in tension mode (*left*) and compression mode (*right*) in the transverse direction

parts on the lower side of the I-beam, would apply tensile load stresses to the constrained specimen. The loading was stopped after 1, 10 and 10^5 cycles followed by the residual stress measurement in each case. It could be observed that regardless of the tensile or compressive loading the relaxation takes place already during the first 10 cycles under four-point bending of large specimens. However there is a distinct difference between the relaxation behaviors in these two modes of loading. This is presented in Fig. 17 in which the residual stress/initial residual stress ratio at the weld toe as function of number of load cycles is illustrated for the tension mode (Fig. 17-left) and the compression mode (Fig. 17-right). Studying the residual stresses at the weld toe shows that in compression mode the residual stresses are more stable than in tension mode.

Another observation is that in low strength materials after cyclic loading, the transverse residual stress at the weld toe and its vicinity reduce drastically and approaches zero and seems to continue in this manner after 10^5 cycles. Because of the time consuming procedure of loading and residual stress measurement of large scale specimens, this part of the study was limited to a few components and a few loading parameters until 10^5 load cycles the results of which is published in [24]. Nevertheless it was clear again that in spite of distinct differences between the behavior of welding residual stresses in small and large scale welds under load, the relaxation occurs. Depending on the material properties and loading conditions, the initial residual stresses in low strength materials disappear during cyclic loading. This arises in turn the question again that if the welding residual stress influence on the mean stress independency of fatigue strength is not overestimated in general.

6 Behavior of Welding Residual Stresses Under Multiaxial Loading

The complexities concerning the residual stress influence on fatigue manifest themselves even more in the case of multiaxial loading in which the majority of welded components e.g. power generation and transmission, aircraft and marine engines suffer fatigue failure. In multiaxial fatigue investigations of welds, it has been almost always avoided to consider the effect of residual stresses by using stress relieved specimens and components in order not to be disturbed by their influence on fatigue. Thus the investigations in which residual stresses in tubular welds have been determined are not as wide spread as those of the flat welds and the relaxation studies especially under multiaxial loading are scarce. In this section the influence of multiaxial loading on the welding residual stresses will be presented.

The specimens which were used to determine the initial residual stress fields in different investigated steels were used for this part of the work. After initial residual stress determination one specimen was further studied under pure torsion and the other under tension torsion loading by a hydraulic material testing machine (Instron 8850, 100 kN, 1000 Nm). The first specimen subjected to gradually increasing torsion load was unloaded at specific nominal shear stress levels where after the residual stresses were determined before re-loading the samples until the next stress level. In Fig. 18 the variation of welding residual stresses in the axial and longitudinal detections are shown. By increasing the applied nominal shear stress the first considerable variation of the residual stress field is observed when a nominal shear stress of 261 MPa is applied. In this case the axial compressive

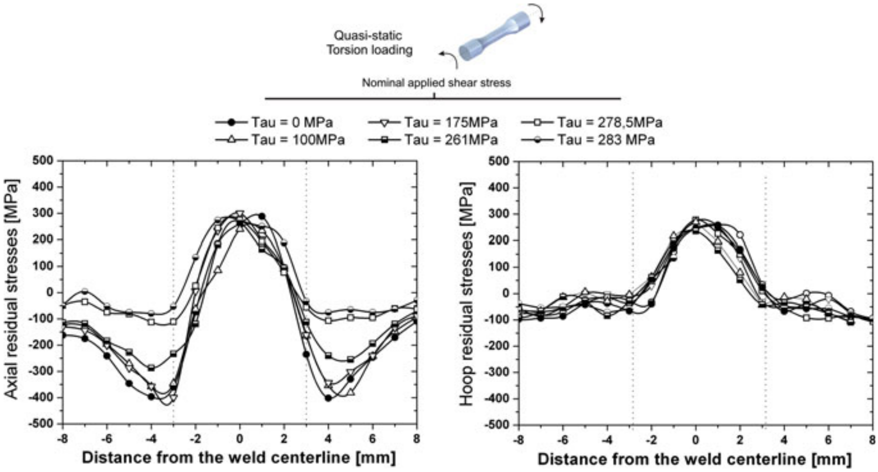

Fig. 18 Welding residual stress relaxation under pure torsion

residual stresses at the weld toe and in the heat affected zone are relaxed. In the weld bead centerline where high tensile residual stresses are present no changes could be observed. By increasing the moment and thus applied nominal shear stress, the relaxation continues at the weld toe and its vicinity in the heat affected zone, while the tensile residual stresses in the weld bead remain unchanged. The test was stopped reaching the nominal shear stress of 283 MPa since the specimens yielded and reached an angle of rotation of 4°. In the hoop direction some variations in the residual stress profiles is observed but these changes are not as pronounced as the relaxation in the axial direction.

For the next step the behavior of the welding residual stresses under multiaxial loading was studied. Since a pure nominal surface shear stress of up to 175 MPa did not lead to relaxation in the previous step, it was aimed here to investigate the influence of the combination of 100 MPa surface shear stress with gradually increasing tensile stresses on the residual stress field (Fig. 19).

It is observed that increasing the applied tensile stress combined with the applied constant torsion stress does not induce a stress state in the weld and its vicinity so that plastic deformation is inevitable. So the residual stresses in both axial and hoop direction show a high level of stability until the applied tensile stress reaches almost the yield strength of the base material i.e. 450 MPa. At this level of applied tensile load stress the compressive residual stresses at the weld toe and heat affected zone are completely eliminated and transform to tensile stresses. In the weld bead again no changes in the axial direction occur although the reduction in the hoop direction is noticeable.

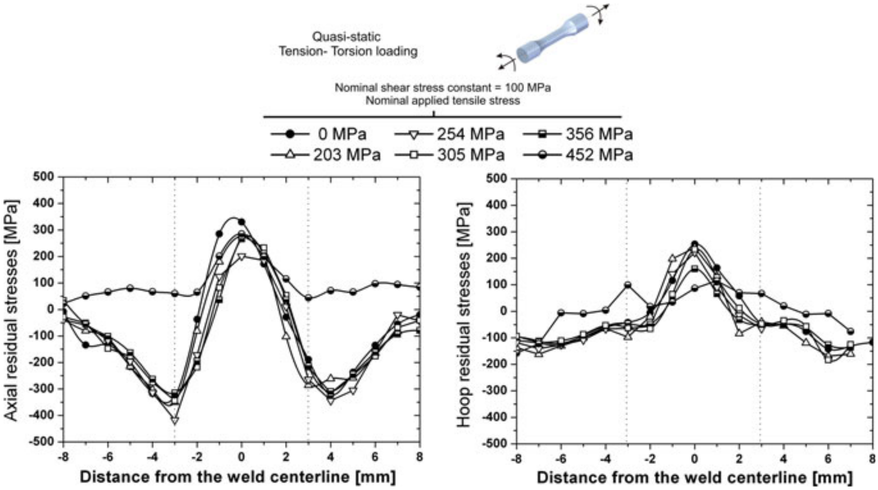

Fig. 19 Welding residual stress relaxation under tension-torsion loading

7 Conclusion

The extensive residual stress determination in S235JRG2, S355J2G3, S355J2H, P460NL, S690QL, S960QL and S1100QL in the form of small large scale and tubular butt welded specimens showed that:

- The maximum values of residual stresses were not as frequently assumed as high as the yield strength in small scale specimens. However in large components with a higher grade of restraint, residual stresses as high as the yield strength of the base metal could be measured in normalised S235JRG2 and S355J2G3 steels.
- The transverse and longitudinal residual stresses are not always highest at the weld toe. In the transverse direction the weld centerlines show the maximum value and in the longitudinal direction the maximum is in the base metal in the vicinity of the heat affected zone.
- From the fatigue point of view, the transverse residual stress at the weld toe of flat specimens was a fraction of maximum available residual stress at the weld centerline. The residual stress/yield strength ratio increases in small scale specimens by increasing the yield strength and reaches a maximum of 0.6. In large components on the other hand, the maximum ratio amounts to 0.8.
- In the tubular welds the welding residual stresses at the weld toe were negligibly small.
- For a complete residual stress field determination a combination of the X-ray, synchrotron and neutron diffraction techniques are required.

- The in depth measurements by means of synchrotron, neutron diffraction revealed that the residual stress peaks in the weld and weld toe appears just on the surface. In deeper layers tensile and compressive residual stresses fulfill the equilibrium conditions.

The relaxation studies on in the form of small and large scale specimens under uniaxial and multiaxial loading showed that:

- The von Mises failure criterion with the local monotonic yield strength as the material limit against local plastic deformation has proven to be capable of describing the residual stress relaxation under quasi-static and cyclic loading.
- In high cycle fatigue loading, with or without mean stresses, except for a small reduction at the beginning, no considerable residual stress relaxation as a function of number of cycles was observed. That is, in the range of high cycle fatigue, high tensile residual stresses in butt welds with low stress concentration at the weld toe, accompany the weld until the failure initiation. Hereafter the relaxation because of the crack initiation and propagation begins.
- In low cycle fatigue and within the finite life, relaxation during the very first loadings takes place. The major portion of the relaxation occurs in the first half of the first loading cycle and could be treated as relaxation under quasi-static loading.
- Residual stresses afterwards either stay stable or relax continuously with a considerably lower rate until failure. To what extent the crack initiation and propagation contribute to residual stress relaxation in low cycle fatigue requires more investigation.
- In large scale specimens which were cyclically loaded under four-point bending, the relaxation of residual stresses occurred not only after the first loading but also during further loading. This was regardless of if the weld was under tension or compression. However the relaxation rate after the first loading was again lower than that of the first relaxation.
- Again in large scale specimens, the first relaxation depended strongly on the yield strength of the base metal. The higher strength steel S690QL showed relatively lower initial relaxation than S355J2G3. The comparatively more stable residual stresses in higher strength steel showed again the severity of the detrimental tensile residual stresses in high strength steels.
- In tubular specimens the welding residual stresses are more stable even under high tensile loads combined with torsion loading. In the case of relaxation, the main changes of the residual stress profile occur at the weld toe and heat affected zone. This is because of the concentration of the plastic deformation in these regions under the applied load combinations and thus residual stress field variation. In the weld bead which has a larger cross section lower amount of shear or tensile stresses lead to lower plastic deformation and the residual stress field in these regions remain unchanged.

It was shown that a more differentiated view into the initial residual stress field and its behavior under loading is required to estimate their hazard to the structural integrity. By increasing the weld quality (concerning weld toe and root) and reduction of geometrical effects on fatigue, the influence of residual stresses on fatigue becomes more important.

Acknwoledgments The chapter was supported by the German Research Foundation (Deutsche Forschungsgemeinschaft—DFG) as part of the project “Residual stress relaxation in welded high-strength steel under multiaxial loading.” The authors would like to thank the DFG for its support.

References

1. Gurney TR (1968) Fatigue of welded structures. Cambridge University Press, Cambridge
2. Kudryavtsev IV (1956) The influence of internal stresses on the fatigue endurance of steel. In: International conference on fatigue I. Mechanical Engineering, pp 317–325
3. Trufyakov VI (1958) Welded joints and residual stresses, Avt. Sv. No. 5, 1956. Br Weld J 5(11):491–498
4. Bäckström M, Marquis G (2001) A review of multiaxial fatigue of weldments: experimental results, design code and critical plane approaches. J Fatigue Fract Eng Mater Struct 24:279–291
5. Lawrence FV, Burk JD, Yun JY (1982) Influence of residual stress on the predicted fatigue life of weldedments. ASTM STP 776:33–43
6. Scholtes B (1990) Residual stresses generated by mechanical surface treatments. DGM Informationsgesellschaft, Oberursel
7. Lieurade HP (1987) In: Niku-Kari A (ed) Advances in surface treatments. Pergamon Press, Oxford, pp 455–482
8. McClung RC (2007) A literature survey on the stability and significance of residual stresses during fatigue. J Fatigue Fract Eng Mater Struct 30:173–205
9. Löhe D, Lange KH, Vöhringer O (2002) Residual stress and fatigue behaviour, Handbook of residual stress and deformation of steel. ASM, pp 27–53
10. Kassner M, Krebs J (2007) Influence of welding residual stresses and notch effect on fatigue data for welded joints and components, XIII-2171r1-07
11. Joens WKC, Alberry PJ (1977) Ferritic steels for fast reactor steam generators. British Nucl Eng Soc 1–4
12. Wohlfahrt H (1986) Die Bedeutung der Austenitumwandlung für die Eigenspannungsentstehung beim Schweißen. Härterei-Technische-Mitteilung 41:248–257
13. Nitschke-Pagel Th, Wohlfahrt H (1991) The generation of residual stresses due to joining process. In: Hauk V, Hougardy H, Macherauch E (eds) Residual stresses-measurement, calculation and evaluation. DGM-Informationsgesellschaft, Verlag, pp 121–134
14. Jones WKC, Alberry PJA (1977) Model for stress accumulation in steels during welding. In: International conference on residual stresses in welded construction and their effects, London, TWI, pp 15–26
15. Seyffarth P, Meyer B, Scharff A (1992) Großer Atlas Schweiß-ZTU-Schaubilder. DVS-Verlag GmbH
16. IS0/TTA3, Polycrystalline materials—Determination of residual stresses by neutron diffraction. In: Technology trends assessment, International standardisation organisation, 2001
17. Radaj D (1995) Ermüdungsfestigkeit, fatigue strength. Springer, Berlin (in German)
18. Haibach E (2002) Betriebsfestigkeit, fatigue strength in service, 2.Aufl. Springer, Berlin (in German)

19. Hobbacher A (2007) Recommendations for fatigue design of welded joints and components, IIW-document, XIII-2151-07/XV-1254-07
20. EN 1993-1-9 (Eurocode 3): Design of steel structures, part 1.9: fatigue strength of steel structures. CEN, Brussels, Belgium, 2005
21. Sonsino CM (2009) A consideration of allowable equivalent stresses for fatigue design of welded joints according to the notch stress concept with the reference radii rref = 1.00 and 0.05 mm. Weld World 53(3/4):R64–R75
22. Krebs J, Kassner M (2006) Influence of welding residual stresses on fatigue design of welded joints and components, IIW-document, XIII-2126-06
23. Erker A (1954) Dehnungsmessungen an geschweißten Bauteilen, Schweißen u. Schneiden, Jahrgang 6, 1954, Heft 2, pp 66–69
24. Farajian M (2011) Stability and relaxation of welding residual stresses. Dissertation, TU Braunschweig

Visualization Technique for Quantitative Evaluation in Laser Welding Processes

Tomonori Yamada, Takahisa Shobu, Susumu Yamashita, Akihiko Nishimura, Toshiharu Muramatsu and Yu-ichi Komizo

Abstract To improve phenomenological understanding of laser welding processes and to control residual stress, we have to characterize the molten pool properties. We succeeded to observe a convection, molten pool shape, and bubbles in situ using an intense X-ray beam and tracer particles during laser spot welding. During the cooling phase, the molten metal was solidified and bubbles were confined in the weld metal. The numerical simulation code has been newly developed to evaluate the effect of molten pool convection to the temperature distribution including phase change, melting and solidification based on the in situ observation results. The numerical code can simulate the laser welding phenomena. We have found that the Marangoni effect on the molten pool surface gives considerable influence to temperature distribution not only on the surface but also in the molten pool. Both the experimental and numerical results provide us useful knowledge about laser welding phenomena for quantitative evaluation.

Keywords X-ray transmission imaging using an intense X-ray beam · Numerical simulation · Laser welding · Flow field · Molten pool

---

T. Yamada · S. Yamashita · A. Nishimura · T. Muramatsu
Japan Atomic Energy Agency, 65-20 Kizaki Tsuruga,
Fukui 914-8585, Japan
e-mail: yamada.tomonori41@jaea.go.jp

Y. Komizo (✉)
Joining and Welding Research Institute, Osaka University,
11-1 Mihogaoka Ibaraki, Osaka 567-0047, Japan
e-mail: komizo@jwri.osaka-u.ac.jp

T. Shobu
Japan Atomic Energy Agency, 1-1-1 Kouto Sayo-cho, Sayo-gun,
Hyougo 679-5148, Japan

T. Kannengiesser et al. (eds.), *In-situ Studies with Photons, Neutrons and Electrons Scattering II*, DOI: 10.1007/978-3-319-06145-0_12,

Nomenclature

C_v	Specific heat capacity at constant volume (J kg/K)
D_{ij}	Velocity strain tensor (s^{-1})
F_i	External force (Pa)
I_{ij}	Identity matrix (-)
Q	Heat source ($\mathrm{W/m^3}$)
Q_S	Amount of latent heat release for solid (liquid) to liquid (solid) phase (J/kg)
R	Reflection rate (-)
T	Temperature (K)
$g_i = (0, 0, -g)$	Acceleration due to gravity ($\mathrm{m/s^2}$)
n_i	A normal unit vector at liquid surface (-)
p	Pressure (Pa)
q_m	Laser power density ($\mathrm{W/m^2}$)
r_0	Radius of the laser irradiation (m)
t	Time (s)
$u_i = (u, v, w)$	Velocity vector (m/s)
$x_i = (x, y, z)$	Located vector (m). The suffix indicates components
α	Absorptivity (m^{-1})
κ	Curvature of liquid surface (-)
λ	Thermal conductivity (W/m/K)
μ	Viscosity (Pa s)
ρ	Density ($\mathrm{kg/m^3}$)
σ	Surface tension coefficient (N/m)
Pe	Peclet number (-)
$Q_{conv.}$	Advective transport rate ($\mathrm{W/m^3}$)
$Q_{diff.}$	Diffusive transport rate ($\mathrm{W/m^3}$)
U	Characteristic velocity (m/s)
l	Characteristic length (m)
Re	Reynolds number (-)

1 Introduction

Laser technologies are widely applied in industrial, medical, and scientific fields because of their advantages such as compact, higher energy density, flexible accessibility, precision and controllability. In terms of the higher energy density and controllability, laser beams have been used in the field of welding. In the laser welding, two types of welds have been performed. One is heat-conduction type welds and the other one is keyhole type welds. These depend heavily on power density. The heat-conduction type welds is characterized by power density of between 10^4 and 10^6 W/cm^2 [1]. As in a cladding by welding, the heat-conduction type dominates because of penetration control. On the other hand, if we use the laser beam of power density of 10^6 W/cm^2 or more [1, 2], we see the keyhole which is formed by evaporation of the materials. In terms of narrow and deep weld penetration, the keyhole type welds dominates. However, despite the widespread use of laser welding, physical processes of the laser welding are not completely understood due to a various complicated phenomena including a heating, melting, solidification and phase transformation processes. The quantitative evaluation for these welding phenomena is not an easy task because the phenomena involve the interaction of thermal, mechanical and metallurgical effects, and is characterized by various scales of time and space. To evaluate the welding phenomena, we need both experimental and numerical studies. For example, interior of a molten pool of sodium nitrate, $NaNO_3$, was directly observed during CO_2 laser irradiation for evaluation of convection flow because $NaNO_3$ is transparent in visible spectral range and the Marangoni number for the simulated $NaNO_3$ molten pool is close to those for steel and aluminum molten pools [3–5]. However, in their experiments, the convection flow of steel and aluminum was observed only on the surface of the molten pool. A real-time observation of interior of molten pool during steel and aluminum welding processes should be necessary to obtain more understanding of the welding phenomena.

To observe the molten pool phenomena during the welding processes, in-situ X-ray transmission imaging technique [2, 6] is a useful tool. For example, a keyhole behavior, bubble formation and molten pool convection during CO_2 laser welding were observed using the X-ray transmission imaging [7]. However, in case of using an X-ray tube, because the spectral intensity was low, defined clear solid–liquid interface was not able to be observed. To evaluate the convective heat transport, we have to observe the molten pool convection as well as solid–liquid interface. To detect a clear boundary between the solid and the liquid phase, we need an intense high energy and monochromatic X-ray beam. Thus, we use an intense X-ray beam which has ultra-bright, highly directional and monochromatic X-ray at SPring-8 (*S*uper *P*hoton *ring-8* GeV). SPring-8 is one of the largest synchrotron radiation facilities which deliver the most powerful synchrotron radiation currently available. For example, X-ray imaging is utilized for the visualization of internal structures of objects in a large number of fields such as material science, condensed matter physics. In welding process, in situ observation of the solidification process and the phases transformation have been carried out using a time-resolved X-ray diffraction system [8, 9]. Toward the understanding of the welding phenomena and controlling the residual stresses, we have been developed an in situ X-ray transmission imaging of interior of molten pool during laser welding using an intense X-ray beam [10–12].

In this chapter, we focus attention on the molten pool of heat-conduction type weld because laser absorption of the keyhole type are more complex than the heat-conduction type. We have carried out in situ X-ray transmission imaging of interior of molten pool during laser welding using an intense X-ray beam and the experimental result compare the numerical result.

2 Experimental Procedures

Figure 1 shows the experimental setup for the real-time observation during laser welding. To clearly observe the convection in molten pool, we use A6061 aluminum alloys which have high transmission of X-ray, good weldability among the many kinds of aluminum, low melting point. The chemical composition of this material is given in Table 1. Tantalum carbides, which have higher melting point and a lower mass density than tungsten, were used as a motion and boundary tracers for the visualization of convection flow and boundary interface between solid and liquid states in a molten pool, respectively.

The in situ X-ray observation was carried out at the bending-magnet beam line (BL19B2) at SPring-8. To clearly visualize the tantalum carbide particles, we used an X-ray energy of 30 keV monochromatized by double Si 111 crystals. The size of the X-ray beam was 5.1 mm (height) × 24 mm (width). A test piece was set on a water-cooling copper plate and it was cooled by water at the temperature of 20 °C. A schematic illustration of the in situ observation during laser spot welding is shown in Fig. 1. When the laser beam was irradiated on the test piece, laser welding processes were successfully observed using the X-ray absorption contrast method. A charge coupled device (CCD) camera made by Hamamatsu Photonics Co., Ltd. was used to obtain images of those processes. The camera was positioned at 120 cm from the test piece. The frame rate of the CCD camera used in this study was about 70 frames s^{-1}.

Additionally, a continuous wave single mode ytterbium fiber laser (IPG YLR-300-AC) was used. The beam quality (M^2) was 1.03, and the emission wavelength was 1,070 nm. The laser beam was focused on the test piece surface with a focal distance of 240 mm for shield of a focus lens against welding fumes and spatters coming from the irradiated surface. To evaluate the molten pool of heat-conduction type, the spot diameter was adjusted about 1 mm and the laser power was setting at 300 W which was almost the maximum power. From the laser power and the surface area, laser intensity on the sample is about 38 kW/cm^2. The laser illuminates for 10 s in N_2 shielding gas (flow rate about 10 l/min) for formation of bigger molten pool.

3 Numerical Procedures

In laser welding simulations, two types of studies have been performed. One is assuming the flat surface of the base material [13, 14] and the other one is considering surface deformations [15]. However, a few studies which take into account the solidification process and the interaction between the gas and the surface of a molten pool have been performed. It is obvious that the solidification processes is very important for controlling the residual stress. The interaction between the gas and the solid surface is assumed to affect the solidification

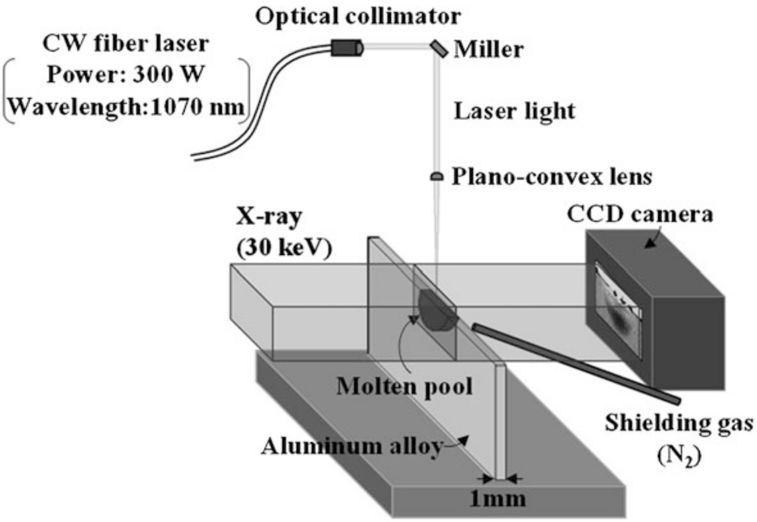

Fig. 1 Schematic of in situ observation during laser welding

Table 1 Chemical composition of A6061 (mass %)

Si	Fe	Cu	Mn	Mg	Cr	Zn	Ti	Al
0.55	0.17	0.27	0.01	0.92	0.10	0.02	0.01	Balance

Table 2 Physical properties of pure aluminum

Physical properties	Solid	Liquid	Air (gas)
Density (kg m^{-3})	2,700	2,377	1.2
Viscosity (Pa s)	–	8.6×10^{-4}	1.8×10^{-5}
Thermal conductivity (W m^{-1} K^{-1})	237	93	0.026
Specific heat capacity (J kg^{-1} K^{-1})	901	1,170	1,000
Melting point (K)	933		
Coefficient of surface tension (Pa)	0.86		
Latent heat (J kg^{-1})	3.94×10^5		

processes. Because the phenomenon has a lot of complex physical processes and wide range of the scale and time of phenomena, we have to construct an accurate, robust and efficient numerical technique. To satisfy such a numerical technique, we have constructed a fully parallelized numerical model for the laser welding processes using advanced numerical models which consists of VSIAM3 (Volume and Surface Integrated Average based Multi Moment Method) numerical model [16, 17] and the accurate surface capturing scheme, THINC/WLIC scheme [18, 19]. In the present study, we employed those models from following reasons;

Firstly, to avoid time-consuming calculation, the mesh stencil of CSLAM3 is simple compared with other multi moment discretization.

Secondly, since the model is based on finite volume method, physical variables, e.g. mass, momentum are completely conserved.

Thirdly, THINC/WLIC method dose not emanate numerical diffusion of the free surface so that the surface re-initialization does not need like a Level-Set method [20].

If an each surface of the gas and liquid phase significantly deform, since surfaces are expressed by orthogonal coordinate, we do not need grid reconstruction due to deformed free surfaces. Therefore, a numerical error and instability can be reduced.

As described, SPLICE (residual *S*tress control using *P*henomenological modeling for *L*aser welding repair process *I*n *C*omputational *E*nvironment) code was developed for phenomenological and mechanistic evaluation of laser processing [12, 21, 22].

3.1 Governing Equations

A shielding gas for welding and melted metal which is induced by the laser irradiation can be treated as a fluid. So that conservation equations of mass, momentum and energy equations can be adopted as governing equations. Assuming the incompressible fluid, these equations are given by

$$\frac{\partial u_i}{\partial x_i} = 0, \tag{1}$$

$$\frac{\partial u_i}{\partial t} + \frac{\partial u_i u_j}{\partial x_j} = -\frac{1}{\rho}\frac{\partial p}{\partial x_i} + \frac{1}{\rho}\frac{\partial}{\partial x_j}\left(2\mu D_{ij}\right) + g_i + F_i, \tag{2}$$

$$\frac{\partial T}{\partial t} + u_i\frac{\partial T}{\partial x_i} = \frac{1}{\rho \mathrm{C}_v}\frac{\partial}{\partial x_i}\left(\lambda\frac{\partial T}{\partial x_i}\right) + \frac{Q}{\rho C_v}, \tag{3}$$

where $u_i, \rho, p, \mu, D_{ij}, g_i = (0, 0, -g)$, F_i, T, C_v, λ and Q represent the velocity vector, density, pressure, viscosity, Velocity strain tensor, acceleration due to gravity, external force, temperature, specific heat, thermal conductivity and heat source, respectively.

In this study, in order to simultaneously express the gas, liquid and solid phase, we use one-fluid model which is often used in multi-phase flow simulation. In the model, effective fluxes on each surface is evaluated by the advection equation of the VOF (volume of fluid) function, ϕ,

$$\frac{\partial \phi}{\partial t} + \frac{\partial (u_i \phi)}{\partial x_i} - \phi\frac{\partial u_i}{\partial x_i} = 0. \tag{4}$$

Based on the local values of ϕ, the appropriate properties and variables are assigned to each control volume within the computational domain. If Y denotes the generic fluid property, e.g. density, viscosity, specific heat, the corresponding value in each cell is given by

$$Y(\phi) = Y_S\phi_S + Y_L\phi_L + Y_G(1 - \phi_S - \phi_L). \tag{5}$$

Suffixes S, L, G indicate a solid, liquid and gas phase, respectively. It is known in fact that the expression for the stress jump F_i, across the interface is given by

$$F_i = \sigma\kappa n_i - \frac{\partial\sigma}{\partial T}\left[\left(I_{ij} - n_i n_j\right)\frac{\partial T}{\partial x_j}\right], \tag{6}$$

where n_i and κ can be written as

$$n_i = \frac{\partial\phi/\partial x_i}{|\partial\phi/\partial x_i|},\ \kappa = -\frac{\partial n_i}{\partial x_i} \tag{7}$$

The second term of the right hand side in the Eq. (6) is the contribution related to surface tension gradients along the interface, Marangoni stress [23, 24].

3.2 Phase Change Model

The solidus and liquidus are determined by the temperature recovering method [25]. The time change of the amount of the phase change can be estimated by this method. In the present study, we directly treat it as a change of the VOF function. The latent heat releases of solid phase to liquid phase is defined as

$$Q_S = \rho\Delta V\Delta gL. \tag{8}$$

The procedure of calculation of the phase change is as follows;

1. Calculate the temperature without phase changes.
2. Calculate the temperature reduction from liquidus temperature T_L $(\Delta T = T_L - T)$ in one time step.
3. If $\Delta T > 0$, materials solidify and the temperature recovers to the liquidus temperature T_L, thus

$$Q_S = \rho C_p\Delta V\Delta T. \tag{9}$$

4. Then we have the material changes, $\Delta g = C_p \Delta T / L$.
5. We suppose that Δg is equals to $\Delta \phi$ and put in the VOF function;

$$\phi = \phi \pm \Delta \phi. \tag{10}$$

3.3 Laser Irradiation Model

The energy input from the laser light was modeled originally as a surface heat flux. Currently, Bouguer-Lambert-Beer law [26],

$$q(x, y, z, t) = (1 - R) q_0(x, y, t) \exp(-\alpha z), \tag{11}$$

was used. Thus the second term of right hand side in Eq. (4) is given by

$$Q = -\frac{\mathrm{d}q}{\mathrm{d}z} = -(1 - R) q_0 \alpha \exp(-\alpha z), \tag{12}$$

where R and α represent the reflection ratio and absorptivity, respectively. The irradiation intensity is described by the product of spatial function $f(x, y)$ (the profile of heat input on the base material) and the time function (t): $q_0 = q_m f(x, y) g(t)$. In the present study, we assume $g(t) = 1$ and $f(x, y)$ are defined as a Gaussian laser-intensity distribution,

$$f(x, y) = \exp\left(-\frac{x^2 + y^2}{r_0^2}\right), \tag{13}$$

where q_m, $f(x, y)$ and r_0 represent the laser power density, laser beam intensity distribution and radius of the laser irradiation, respectively.

The R and α depend on materials, phase, temperature, wave length. It is necessary to consider the complicated interaction processes of the fluid and the solid in the laser welding simulation. In this study, theses parameters are artificially determined so as to fit the experimental result of molten pools dynamics driven by a laser heating which are represent in the following section. Moreover, to handle a complex boundary at the base material, Immersed Boundary Method (IBM) [27] is applied. No-slip boundary condition is applied on the solid surface.

3.4 Algorithm for the Laser Welding Simulation

We use the fractional step method for time proceeding. Firstly, grid, the laser irradiation profile, etc. are set in the initialization phase. After that, in the time proceeding loop, advection equation is solved by fifth order WENO [28, 29]

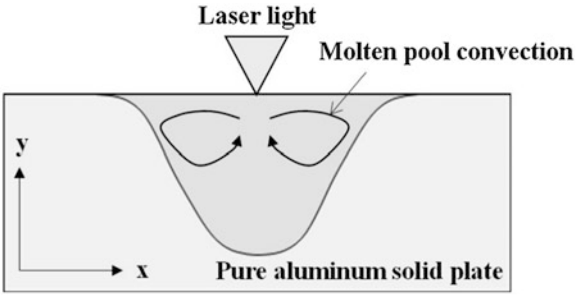

Fig. 2 The schematic diagram of the molten pool convection simulation. The physical properties of each material are shown in Table 2

scheme. After calculating the external forces, e.g. surface tension force, gravity, diffusion equation of the velocity and the space distribution of physical properties are updated as provisional values. The pressure Poisson equation is solved by Krylov subspace method named AMG-BiCGSTAB solver. The solver can solve the Poisson equation which has a large density difference. Then the updated pressure distribution is obtained and the velocity at the next time step is updated using the pressure. Finally, one time step is completed after updating temperature, VOF function and the location of the heat source.

3.5 Numerical Configuration of the Molten Pool Convection

We carry out the laser welding (melting and solidification) simulation. The laser output, irradiation diameter and the material of the base material are, 300 W, 1 mm and pure aluminum, respectively. To simplify the problem, gas phase are neglected, and, liquid and solid phases are considered. As shown in Fig. 2 the length of the computational domain is 10 mm for x direction and 5 mm for y direction and we allocate the grid points, 80 and 40 points, for x and y, respectively. Velocity boundary condition is that the free slip boundary condition for top surface and no-slip boundary condition for right, left and bottom boundary, respectively. Temperature boundary condition for bottom boundary is fixed by the constant temperature of 800 K, to protect all solid phase melted. The other temperature boundary are adiabatic boundary.

4 Results and Discussions

Figure 3 shows successive images of a molten pool as a function of time t. Here, we define the onset of the laser irradiation as $t = 0$ s. We can clearly observe a solid–liquid interface, a flow field, bubbles and porosities using an intense X-ray beam. A molten pool grows up immediately after laser irradiation. Tracer particles (tantalum carbide whose diameter is 45 μm) are injected into the molten pool from

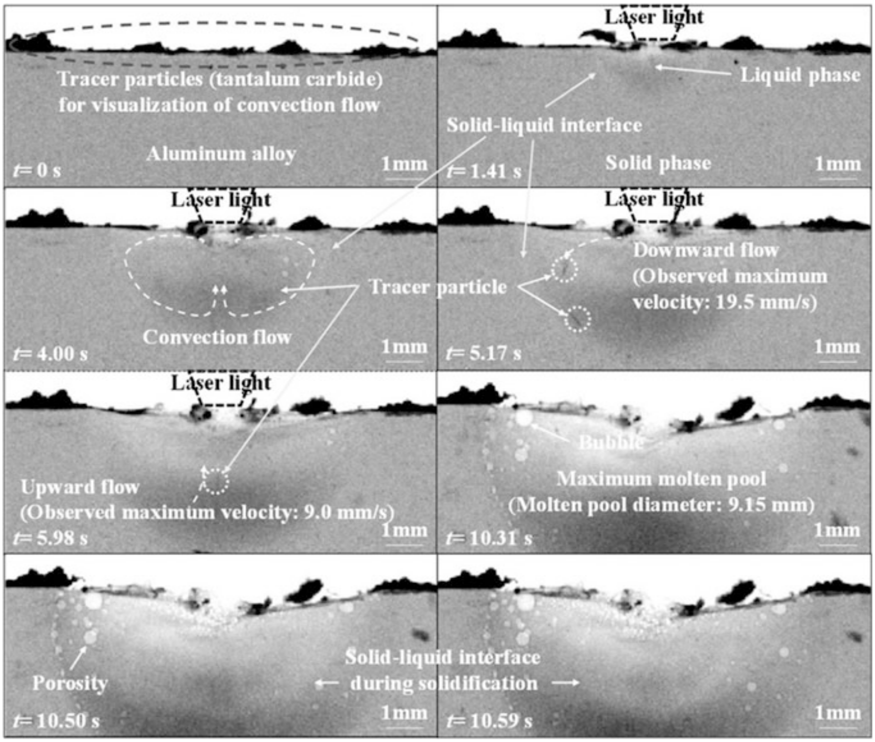

Fig. 3 X-ray transmission images during melting and solidification processes. Time was defined as follows; the onset of the laser irradiation as $t = 0$ s. Solid–liquid interface, flow field, bubbles and porosities were clearly observed using an intense monochromatic X-ray beam

a laser irradiation area at $t = 4.00$ s. Afterward, the tantalum carbide powders transition to the solid–liquid interface and move into the bottom of the molten pool along the solid–liquid interface. Moreover, a part of the tantalum carbides particles move from the bottom to the surface of the molten pool. We think that convection is driven by a surface tension gradient. A maximum downward flow velocity of 19.5 mm/s and upward flow velocity of 9.0 mm/s are observed at $t = 5.17$ s and at $t = 5.98$ s, respectively. The laser irradiation finish at $t = 10$ s. Following the end of the laser irradiation, maximum molten pool is observed. The molten pool diameter is 9.15 mm at $t = 10.31$ s. In solidification process, we cannot observe a convection field, but we can see a rapid solid–liquid interface migration and porosity formation.

The heat conduction and the convective heat transport are equally important for evaluation of temperature distribution in the molten pool. This real-time observation enabled us to evaluate the contribution of convective heat transport quantitatively. These heat transport is characterized by the Peclet number (Pe) which is defined as the ratio of an advective transport and a diffusion transport phenomena.

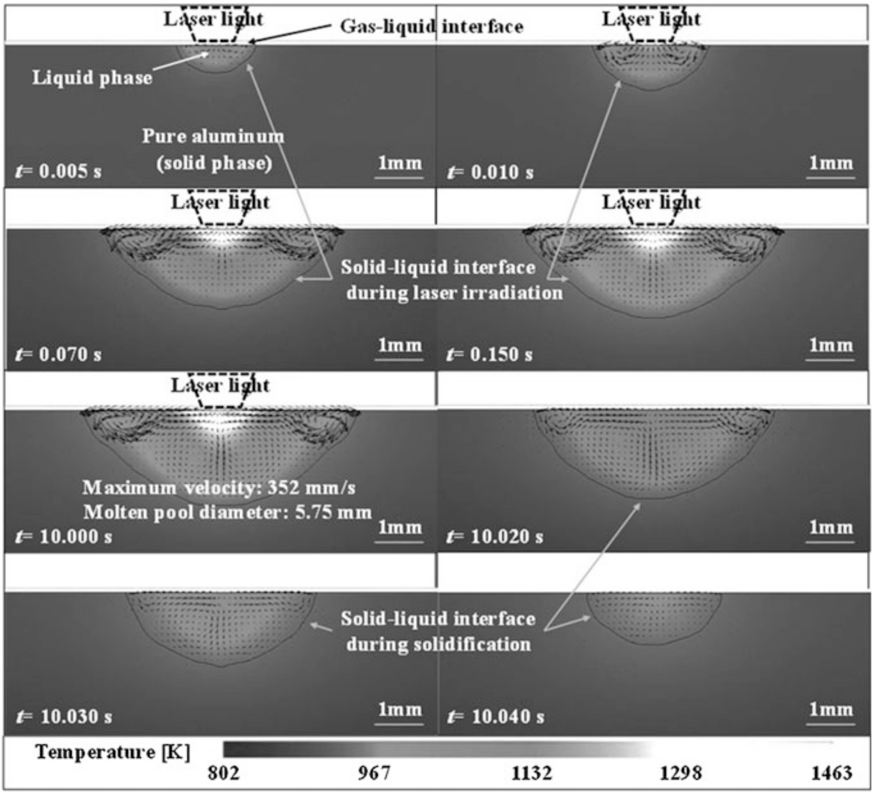

Fig. 4 Numerical results of temperature and velocity vector distribution in a molten pool during laser welding

$$Pe = \frac{Q_{conv.}}{Q_{diff.}} = \frac{\rho C_p UT/l}{\lambda T/l^2}, \tag{14}$$

where, $Q_{conv.}$, $Q_{diff.}$, U and l represent the advective transport rate, the diffusive transport rate, the characteristic velocity and the characteristic length, respectively. From the maximum downward flow velocity and the molten pool diameter, $Q_{conv.}$ and $Q_{diff.}$ were calculated to be 7.6×10^9 and 4.0×10^9, respectively. The estimated quantity of heat caused by convective heat transport is approximately the same as one caused by heat convection. Therefore, to evaluate the temperature distribution, it is necessary to consider both heat conduction and convective heat transport.

In teams of weld quality control, the bubble formation, which cause mechanical strength of the weld metal to deteriorate, is very important. In this real-time observation, the number of bubbles was observed and these bubbles increased after $t = 4.00$ s. The details are beyond the scope of this chapter and we will describe elsewhere.

On the other hand, Fig. 4 shows the numerical results of temperature and velocity vector distribution during laser welding in the pure aluminum using SPLICE code. The numerical result can reproduce the melting processes, convection, and solidification. Laser output, diameter, and other parameters are equal to the experimental values. At the irradiation point of the laser light, the temperature increases and the surface tension increases along a line from the irradiation point to the edge of the molten pool because the temperature coefficient of the surface tension is negative for most materials. Since we took into account the gas phase, the thermal energy in the molten pool was transported to the air phase due to thermal conduction and interface deformation. Here, moving velocity of solid–liquid interface is compared with the experimental results. Although, the velocity in the numerical result is not equal to the experimental result, the molten pool extend isotropically during laser irradiation, and the shape is hemispherical similar to the experimental result. The steady state, which is judged from changes of the convection behavior, is observed at $t = 0.30$ s, and the molten pool diameter is considered to be constant between $t = 0.30$ and $t = 10$ s. The size and flow velocity of the molten pool in the experiment are compared with the numerical results. As shown by X-ray imaging, the molten pool diameter and flow velocity are 9.15 mm and 19.5 mm/s, respectively. On the other hand, the numerical result shows that molten pool diameter is 5.75 mm and the flow velocity is 352 mm/s, which is faster than the experimental result. The comparison of experimental and numerical results contribute to a deeper understanding of hydrodynamic characteristics in the molten pool because we can only see one part of the convection in the experiment.

From the velocity vector distribution, it is evident that the flow propagated from the center of the surface of the molten pool. The molten pool has the heat source for the solid–liquid interface along the top free surface by means of the Marangoni effect which is caused by the temperature difference between a high temperature region and a low temperature region. A strong eddy is induced by the collision of the flow on the free surface with the solid–liquid interface, and the adverse flow is generated beneath the tangential flow on the free surface. Then, a weak eddy is induced at the center of the molten pool. In this state, Reynolds number, Re, was 2,800 where the characteristic length and velocity are the radius of the molten pool and root-mean-square, $= \sqrt{u^2 + v^2}$, therefore, the almost a turbulent flow occurs. The hottest liquid located in the top of the center of the molten pool radially spread. Moreover, the low temperature liquid in the vicinity of the solid–liquid interface is transported to the middle of the molten pool by the strong eddy. Therefore, the convection have considerable effect on the temperature distribution in molten pool. We need quantitative evaluation of the convective heat transport.

Our results indicate that the visualization technique using an intense monochromatic X-ray beam as well as the numerical simulation technique during laser welding was very powerful. When we compared to the previous research results [30], the visualization technique described in this chapter is widely applicable to other industrial processes.

5 Conclusions

We have characterized effects of molten pool convection on the temperature distribution which is one of the key issues of understanding the welding phenomena using both real-time observation technique during laser welding processes and the numerical simulation technique. The main results are listed as follows.

1. We have developed an in situ X-ray transmission imaging using an intense X-ray beam. The imaging technique enabled us to characterize hydrodynamic behavior in the molten pool during laser welding processes.
2. The simultaneous observation of molten pool shape and flow velocity enabled us to clarify the role of the convective heat transport. The convective heat transport was estimated to contribute to the temperature distribution equally to that of heat conduction.
3. We have developed the SPLICE code for phenomenological and mechanistic evaluation of laser processing. The code can appropriately simulate practical laser welding processes.

Toward the understanding of the welding phenomena, we have to further develop the SPLICE code with more sophisticated physical models.

Acknowledgments We thank Dr. K. Kajiwara of the Japan Synchrotron Radiation Research Institute for his assistance. The synchrotron radiation experiments were performed with the approval of the Japan Synchrotron Radiation Research Institute (proposal No. 2010B1833 and No. 2011B1975). A part of this research was supported by Grants-in-Aid for Scientific Research, from Ministry of Education, Culture, Sports, Science, and Technology, Japan (No. 23246127, No. 22860078 and No. 22860079).

References

1. Chmelickova H, Sebestova H (2012) Pulsed laser welding, Nd YAG laser. In: Dan C, Dumitras (ed) ISBN: 978-953-51-0105-5. InTech, http:www.intechopen.com/books/nd-yag-laser/pulsed-laser-welding
2. Fujinaga S, Takenaka H, Narikiyo T, Katayama S, Matsunawa A (2000) Direct observation of keyhole behavior during pulse modulated high-power Nd:YAG laser irradiation. J Phys D Appl Phys 33:492–497
3. Limmaneevichitr C, Kou S (2000) Visualization of Marangoni convection in simulated weld pools, welding research supplement, 126-s–135-s
4. Kou S, Limmaneevichitr C, Wei PS (2012) Oscillatory Marangoni flow: a fundamental study by conduction-mode laser spot welding. Weld J 90:229-s–240-s
5. Kou S (2012) Fluid flow and solidification in welding: three decades of fundamental research at the University of Wisconsin. Weld J, 91:287-s–302-s
6. Arata Y, Abe E, Fujisawa M (1976) A Study on dynamic behaviours of electron beam welding (report I)—the observation by a fluoroscopic method. Trans JWRI 5:1–9
7. Katayama S, Kobayashi Y, Seto N (2001) Effect of vacuum on penetration and defects in laser welding. J Laser Appl 13:187–192

8. Terasaki H, Komizo Y, Yonemura M, Osuki T (2006) Time-resolved in situ analysis of phase evolution for the directional solidification of carbon steel weld metal. Metall Mater Trans A 37A:1261–1266
9. Komizo Y, Terasaki H (2011) In situ time resolved X-ray diffraction using synchrotron. Sci Technol Weld Join 16:56–60
10. Yamada T, Shobu T, Yonemoto Y, Yamashita S, Nishimura A Muramatsu T (2011) Phenomenological evaluation of Laser-irradiated welding processes with a combined use of higher-accuracy experiments and computational science methodologies (3) In situ observations of welded pool using an intense x-ray beam. In: 19th International conference on nuclear engineering, ICONE19-44128
11. Yamada T, Shobu T, Nishimura A, Yonemoto Y, Yamashita S, Muramatsu T (2012) In situ X-ray Observation of molten pool depth during laser micro welding. J Laser Micro/Nanoeng 7:244–248
12. Daido H, Shobu T, Yamada T, Yamashita S, Sugihara K, Nishimura A Muramatsu T (2012) Real-time observation of laser heated metals with high brightness monochromatic X-ray techniques at present and their future prospects, X-Ray Lasers 2012. In: Proceedings of the 13th international conference on X-Ray, pp 69–76
13. Wang H, Shi Y, Gong S (2006) Numerical simulation of laser keyhole welding processes based on control volume methods. J Phys D Appl Phys 39:4722–4730
14. Trivedi A, Bag S, De A (2007) Three-dimensional transient heat conduction and thermomechanical analysis for laser spot welding using adaptive heat source. Sci Technol Weld Join 12:24–31
15. Ha EJ, Kim WS (2005) A study of low-power density laser welding process with evolution of free surface. Int J Heat Fluid Flow 26:613–621
16. Xiao F (2004) Unified formulation for compressible and incompressible flows by using multi-integrated moments I: one-dimensional inviscid compressible flow. J Comput Phys 195:629
17. Xiao F, Akoh R, Ii S (2006) Unified formulation for compressible and incompressible flows by using multi-integrated moments II: Multi-dimensional version for compressible and incompressible flows. J Comput Phys 213:31
18. Xiao F, Honma Y, Kono T (2005) A simple algebraic interface capturing scheme using hyperbolic tangent function. Int J Numer Meth Fluids 48:1023–1040
19. Yokoi K (2007) Efficient implementation of THINC scheme: a simple and practical smoothed VOF algorithm. J Comput Phys 226:1985
20. Sussman M, Smereka P, Osher S (1994) A level set approach for computing solution to incompressible two-phase flow. J Comput Phys 114:146
21. Yamashita S, Yamada T, Yonemoto Y, Kunugi T Muramatsu T (2011) Phenomenological evaluation of Laser-irradiated welding processes with a combined use of higher-accuracy experiments and computational science methodologies (5) Numerical simulation of the welding processes with a multi-dimensional multi-physics analysis code SPLICE. In: 19th international conference on nuclear engineering, ICONE19-43939
22. Yamashita S, Yonemoto Y, Yamada T, Kunugi T, Muramatsu T (2011) Development of laser welding simulation code with advanced numerical models. Quart J Jpn Weld Soc 29:48s–52s
23. Lappa M (2005) Assessment of vof strategies for the analysis of Marangoni migration, collisional coagulation of droplets and thermal wake effects in metal alloys under microgravity conditions. CMC 2:51–64
24. Haj-Hariri H, Shi Q (1997) Thermocapillary motion of deformable drops at finite Reynolds and Marangoni numbers. Phys Fluids 9:845–855
25. Ohnaka I (1985) Heat transmission and solidification analysis using computer. Maruzen 202 (in Japanese)
26. Sobol EN (1995) Phase Transformations and ablation in laser-treated solids. Wiley, New York
27. Kim J, Kim D, Choi H (2001) An immersed boundary finite-volume method for simulations of flow in complex geometries. J Comput Phys 171:132–150

28. Jiang G, Shu CW (1996) Efficient implementation of weighted eno schemes. J Comput Phys 126:202–228
29. Jiang G, Peng D (1996) Weighted eno schemes for Hamilton-Jacobi equations. J Sci Comput 21:2126–2143
30. Seto N, Katayama S, Matsunawa A (2000) Porosity formation mechanism and suppression procedure in laser welding of aluminum alloy. Q J Jpn Weld Soc 18:243–255 (in Japanese)

Investigation of Processes in the Keyhole of Electron-Beam Welding by Monitoring the Secondary Current Signal in the Plasma

D. N. Trushnikov, V. E. Shchavlev, G. M. Mladenov and L. N. Krotov

Abstract An experimental study of the signal patterns of the secondary current in a plasma during electron-beam welding was carried out. The studies show that the spectrum of the secondary emission signal during steel welding has a pronounced periodic component at a frequency of around 15–25 kHz. The signal contains quasiperiodic sharp peaks (impulses). These impulses have a stochastically varying amplitude and follow each other in series, at random intervals between series. The impulses have a considerable current (up to 0.5 A). It was established that during electron-beam welding, the oscillation of the electron beam impulses follow each other almost periodically. It was shown that the probability of occurrence of these high-frequency perturbation increases with the concentration of energy in the interaction zone. This chapter also presents hypotheses for the mechanism of the formation of the high-frequency oscillations in the secondary current signal in the plasma.

Keywords Electron-beam welding · Keyhole · Plasma · Beam deflection oscillation

1 Introduction

Using electron-beam oscillation to prevent defects during electron-beam welding is widely known. However, there are still no universal methods for regulating the form and parameters of oscillation. Recommendations for the choice of parameters

---

D. N. Trushnikov (✉) · V. E. Shchavlev · L. N. Krotov
Perm National Research Polytechnic University, Komsomolsky Avenue 29, Perm,
Russia 614990
e-mail: trdimitr@yandex.ru

G. M. Mladenov
Institute of Electronics, Bulgarian Academy of Sciences, Sofia, Bulgaria

T. Kannengiesser et al. (eds.), *In-situ Studies with Photons, Neutrons and Electrons Scattering II*, DOI: 10.1007/978-3-319-06145-0_13,

Fig. 1 A typical signal spectrum of the secondary current in the plasma during electron-beam welding with beam oscillation (welding power: 2.5 kW, sharp focus regime ($\Delta I_f = 0$), oscillation frequency: 561 Hz, oscillation size −2 A = 0.9 mm)

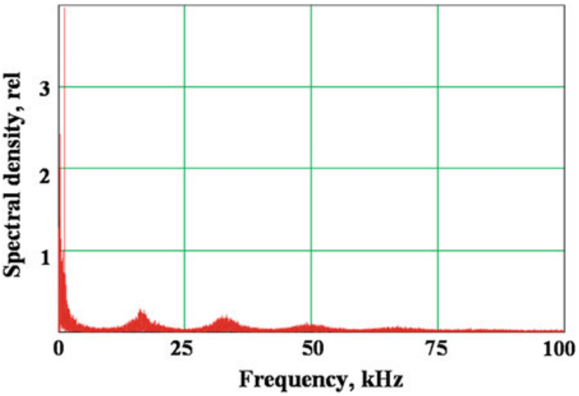

of oscillation are often contradictory. These problems are due to a lack of knowledge. There are no finished dynamic models describing the processes occurring in the keyhole. The complex character and high speed of these processes make numerical modeling very difficult. All of these mean that additional research into electron-beam welding with an oscillating electron beam are necessary.

This research can be conducted with several aims. It is possible to investigate experimentally the influence of various kinds of oscillation on the forms and quality of a weld [1, 2]. Some articles present the results of research into processes in the keyhole for the parameters of the signal from the secondary current in the plasma during electron-beam welding, which have achieved some success [3–8]. Similar research is well underway for laser welding [9–12]. However, many questions are still outstanding. Most studies have considered the low-frequency range of the secondary signals (2–5 kHz) [3, 5, 6]. However, there are studies showing the probability of occurrence of self-oscillating process with a time constant of $t \sim 10^{-4}$ s during keyhole welding [13, 14]. These high-frequency processes in the "electron beam-plasma-keyhole" system will be highlighted in this chapter. The chapter also presents hypotheses for the mechanism of formation of high-frequency oscillations in the secondary current signal in the plasma (Fig. 1).

2 Experimental Procedure

A ring electrode collector was used to measure the secondary current from the plasma. The collector was located over the zone of welding. The collector has a positive potential of 50 V. The loading resistance was 50 Ω. The signal from the collector was registered by a data acquisition system and further processed by a computer. The sampling frequency in the experiments was in a range from 100 kHz to 1 MHz per channel.

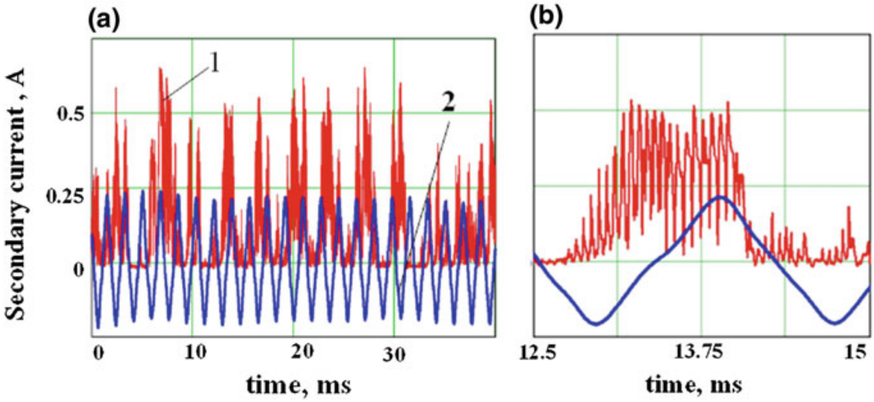

Fig. 2 Waveform of secondary current in the plasma and the signal of the deflection coil current during electron-beam welding with oscillation across the joint. *1*. *Data* (*t*) secondary current. *2*. *Osc*(*t*) signal from the deflection coil current

During the experiments, samples of chrome-molybdenum steel (0.15 % carbon, 5 % chrome and around 1 % of molybdenum) and high-alloy chrome-nickel steel (up to 0.12 % carbon, 18 % chrome and up to 0.8 % titanium) were welded. The accelerating voltage in all experiments was 60 kV. The welding power was in the range from 2 to 4 kW.

During the experiments, the welding power P, focus degree ΔI_f ($\Delta I_f = I_f - I_{f0}$ is the difference between the focus coil current of the welding mode and the focus coil current of sharp focus), the frequency f and amplitude of the oscillations A were varied (Fig. 2).

Beam oscillations across the joint and along the joint were applied. The current in the deflection coils was changed under a linear law. The limits of the beam oscillation frequency were from 90 to 1,500 Hz. The amplitudes of these oscillations were in a range from 0.1 to 1.5 mm for transverse oscillations and from 0.4 to 3.5 mm for oscillations along the joint. Welding speed was 5 mm/s, residual pressure in the vacuum chamber was 10^{-2} Pa. The partial penetration mode took place in experiments.

Transverse metallurgical sections of the weld were made from all the welded samples. The focus regime was determined by the transverse sizes of the penetration depth. The sharp focus regime corresponds to the maximum penetration depth.

In the given work, research into the secondary signal was conducted using coherent accumulation, which is an enhancement of coherent detection, and is widely applied to tracking an electronic beam on a seam, but it has been applied to research processes in the keyhole and welding control only recently. In this research, the high-frequency range 15–20 kHz was studied.

The coherent accumulation method is illustrated in Fig. 3. The small-width square-wave signal is formed from the signal from the current of the deflection coils ($Osc(t)$) less a basic signal $g(t)$. The basic signal $g(t + \tau)$ is shifted relative to the initial signal $Osc(t)$ for a set time τ.

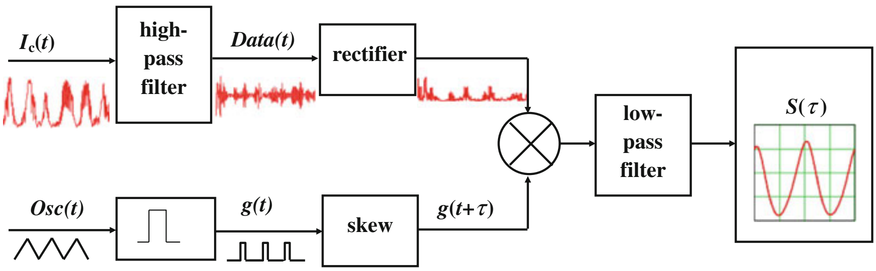

Fig. 3 Coherent accumulation method

3 Results and Discussion

Figure 1 shows a typical spectrum of the secondary current signal in a plasma during welding of steel samples. It can be noted that there is a characteristic maximum in the signal at frequencies close to 15 kHz. Figure 2a shows the secondary signal together with a signal of rejecting deflection coils. The processes in the keyhole become periodic with beam oscillations. Frequency perturbations in the secondary current start to periodically follow at multiples of the oscillation frequency. More detailed consideration (Fig. 2b) shows that each perturbation represents a series of high-frequency quasiperiodic impulses. Their frequency 10–25 kHz is very stable for different materials. The amplitude changes randomly. The spectrums and waveforms of the secondary current in a plasma during electron-beam welding are more fully described in [4, 7, 15, 16]. Further studies are planned on the dependence of the frequency of the pulses from the welded materials.

The signal of the secondary current in the plasma $I_c(t)$ is processed by a digital or analog high-pass filter with a cutoff frequency around 10 kHz. The selected signal of the high-frequency component ($Data(t)$) is rectified and then multiplied by the basic signal, $g(t + \tau)$. The result is integrated over time. As a result, we have the function $S(\tau)$

$$S(\tau) = \int_{0}^{t_0} g(t + \tau) \cdot |Data(t)| dt, \tag{1}$$

where t_0 is the sampling time. This function $S(\tau)$ expresses the average amplitude of the high-frequency secondary signal for each value of the shift τ.

In other words, there is an area of interaction of the beam with the metal on the keyhole wall, which can be described as the area of maximum power allocation. In the oscillation process of the electron beam, this area moves around the walls of the keyhole. In each position, there is an average value of the amplitude of the high-frequency oscillations of the secondary signal.

Figure 4 shows the results of processing the secondary current signal using coherent accumulation with oscillation across a joint. The sharp focus regime was

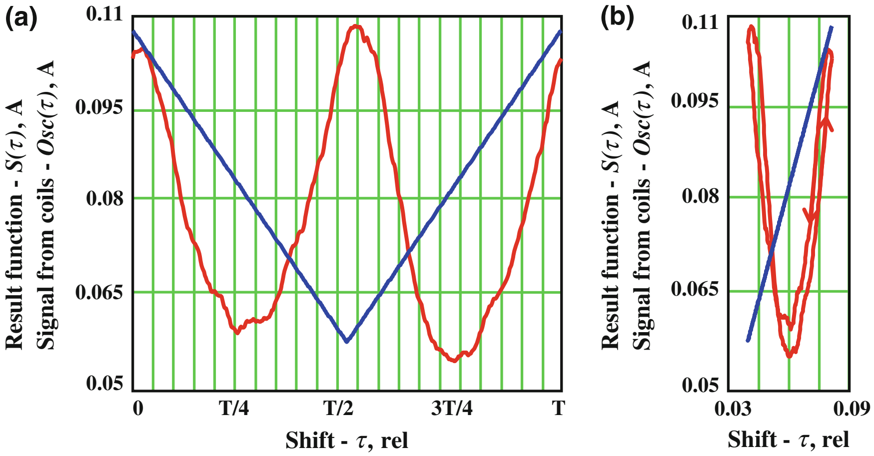

Fig. 4 Function S(τ), obtained using the coherent accumulation method on τ, is the result of secondary processing of the high-frequency component signal. *Osc*(τ) is the record of the deflection coil current ($P = 2.5$ kW, sharp focus ($\Delta I_f = 0$ mA), oscillation frequency $f = 561$ Hz, sweep size 2A = 1 mm)

used. The frequency was 560 Hz and the sweep size was 1 mm. It is noticeable that the function is almost symmetric, as, probably, expected. It is possible to present this function in phase space. For this purpose, on a horizontal axis we postpone the current of the deflection coils or the displacement of the electron beam in the keyhole (Fig. 5b).

Figure 5 shows the results for longitudinal oscillation. The asymmetry of the figure for longitudinal oscillations reflects the asymmetry of the keyhole in the longitudinal direction. In the secondary signal spectrum in this case the first harmonic of the signal will prevail. The characteristic lag of the high-frequency component signal relative to the deflection coil current signal may be noted.

Function $S(\tau)$, which is a result of secondary signal processing using the coherent accumulation method, describes the probability of excitation of high-frequency oscillations of plasma parameters. In addition, the probability of the exit of an electron from the keyhole affects the form of the function S.

4 The Mechanism of Formation of a Secondary Signal in the Plasma

To explain the mechanism of the appearance of high-frequency oscillations in the secondary signal in the plasma we invoke two hypotheses.

The first deals with the assumption of the existence of explosive boiling in the keyhole [13, 14]. The rate of energy input in the interaction of the electron beam with the metal in the keyhole is much higher than the rate of energy output through

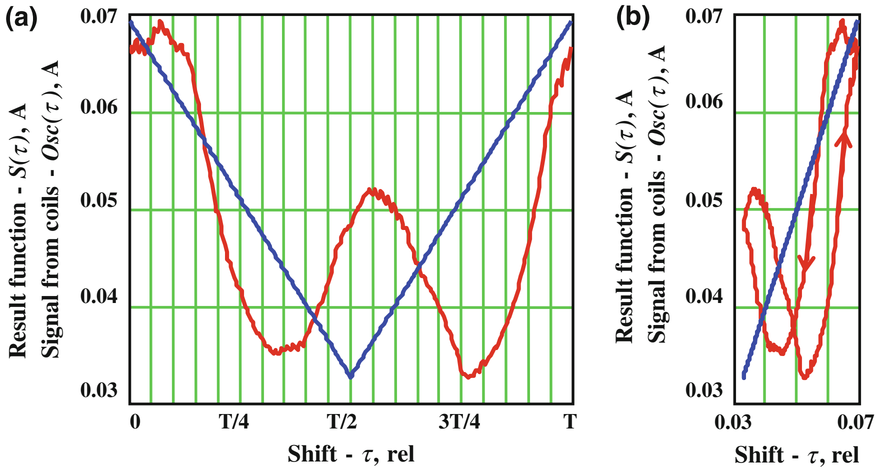

Fig. 5 Function S(τ), obtained using the coherent accumulation method on τ, is the result of secondary processing of the high-frequency component signal. *Osc*(τ) is the record of the deflection coil current ($P = 3$ kW, underfocused regime ($\Delta I_f = -10$ mA), oscillation frequency $f = 556$ Hz, sweep size 2A = 1.5 mm)

conduction. There is local overheating of the metal, followed by explosive boiling. The boiling metal vapor affects beam shielding: the beam is scattered by the metal vapor and the power density is dramatically reduced. After the vapor has been evacuated from the keyhole, the beam's power density again rises above the critical level and the process resumes.

We will estimate the order of the frequencies of the self-oscillating processes that the described hypothesis yields [17].

The process of overheating metal is usually considered first. The primary components of the energy balance look like this

$$q = q_v + q_m + q_c \tag{2}$$

where q is the power added by the beam, q_v is the heat loss due to vaporization, q_m is the heat loss due to melting, and q_c is the heat loss due to thermal conduction.

When moving the beam in the oscillation process into an already melted section the q_m term will not work. The vapor in the keyhole is similar to the saturated [18, 19]; the loss due to vaporization is considered to be no more than 5–10 %. When increasing the power density of the source q, sooner or later the rate of heat input will be much larger than the rate of heat discharge through thermal conduction. Moreover, the maximum energy release takes place at a certain depth below the border of the liquid metal at approximately the depth of the range of the electrons. The estimation is based on the characteristic energy accumulation time τ_0, i.e. the time required to add enough energy for boiling. In the situation described, according to the theory of homogeneous boiling, if the energy accumulation time is comparable to or less than the time of homogeneous nucleation, then overheating followed by explosive boiling are expected [20].

Disregarding the losses due to thermal conduction, the energy accumulation time may be obtained from the condition

$$\tau_0 = \frac{L_V \rho \delta}{q} \tag{3}$$

where Lv is the boiling heat and ρ is the density.

For stainless steel, given welding power $P = 3$ kW and beam diameter $d = 0.5$ mm, the energy accumulation time is $\tau_0 \approx 2 \times 10^{-5}$ s. Moreover, the time will decrease with an increase in the power density, which indicates an increase in the likelihood of the occurrence of explosive boiling as the focus becomes sharp or when, all other things being equal, the welding power is increased.

The process of boiling is a phase transition and is accompanied by an expansion of the matter from an initial density of $\sim 10^4$ kg/m^3 (liquid) to 10^{-1} kg/m^3 (gas). Thus, after the matter boils, a layer of vapor appears in the electron beam's path with a particle concentration that rapidly falls from 10^{26} to $10^{20} - 10^{22}$ m^{-3}.

It is well-known that when an electron beam passes through matter that there is an exponential attenuation in the beam's intensity due to energy being scattered and absorbed as a result of elastic and inelastic collisions. For example, in the case of absorption in a gaseous medium [21], the change in the beam's density is

$$j = j_0 \exp(-n\sigma x) \quad \text{or} \quad j = j_0 \exp(-\alpha\rho n x) \tag{4}$$

where n is the concentration of atoms in the vapor, σ is the interaction cross-section, and α is the absorption factor.

Due to the fact that the vapor's initial density is high, we can expect shielding (scattering, defocusing) of the electron beam as a result of the interaction with the vapor particles. When the beam propagates vapor in the keyhole, the interaction is primarily elastic. Thus, we may suppose that the attenuation of the electron beam's intensity is related to the scattering of electrons outside of the action zone or on the keyhole walls. With a keyhole depth of $H = 1.5$ cm, the energy flow density is attenuated by a factor of e given a concentration of $n = 10^{25}$ m^{-3}. The continuous action of the electron beam is periodically interrupted when the vapor's density exceeds a certain critical level. This self-oscillating process's time balance is the sum of the time for vaporization τ_0 and the vapor dispersion time τ_v.

The simplest way to estimate τ_v is to use sound wave propagation through the keyhole. Given $H = 1.5$ cm and a sonic speed of 700 m/s, we obtain $\tau_v \approx 2 \cdot 10^{-5}$ s.

The frequency of the "quasi-periodic" process becomes $f = 1/\tau$ ($\sim$25 kHz), which agrees well with experimental data (Fig. 1) in terms of the order-of-magnitude. Similar estimates of the frequencies of the described process, which accompanies explosive boiling, have been independently obtained [13, 14, 17, 20, 22].

The conditions of the explosive rupture of metal on the front wall of the keyhole are determined by the pulsed nature of the emission of electrons from the electron beam's action area, which is related to the intense emission of an electron current when the metal transitions from a condensed state to a completely vapor-plasma phase. Estimating the current density of the thermionic emission using Richardson's equation demonstrates that when temperatures in the keyhole are on the order of the boiling temperature at the given pressure, overheating by 100 K leads to a doubling of the thermionic current. This is evidence of the high theoretical values of current emission into the plasma during electron beam welding using a powerfully concentrated electron beam. However, the actual current of a dependent discharge in the plasma during electron beam welding is determined by the current propagation conditions in the plasma and largely depends on the potential distribution in the plasma and external circuit's parameters.

Mladenov and Sabchevski [23] establishes the possibility of a self-oscillating process associated with periodic ionic self-focusing and defocusing. The electron beam's equilibrium radius is extremely dependent on the ion concentration in the keyhole. It causes the oscillatory nature of the electron beam's interaction with the metal. As the power of the electron beam increases above a critical value, the concentration of atoms increases sharply. The metal evaporates from the surface of the weld pool, creating the conditions for the development of noticeable ionic self-focusing of the electron beam. As the beam diameter decreases, the energy concentration increases, which causes a further increase in surface temperature and evaporation. Electron scattering is enhanced. The vapor concentration increases above a certain value and the beam size increases again. The subsequent decrease in temperature and loss of vapor again lead to the predominance of the self-focusing process, etc.

Uglov and Selishev [17] proposes to estimate the frequency of this process by using the electron beam neutralization time

$$\tau_i = (n_0 \sigma_i u)^{-1} \tag{5}$$

where n_0 is the neutral gas's atom density, σ_i is the effective cross-section of the ionization of gas by the beam's electrons, and u is the speed of the beam's electrons. In the case of electron beam welding, $\tau_i < 10^{-4}$ s. The characteristic frequency turns out to be close to the Langmuir ionic frequency and, under the conditions being considered, is greater than 10^2 kHz. Thus, the indicated process cannot be an independent cause of the mentioned oscillations. Furthermore, [24, 25] refute the very proposition of significant "self-compression" of the bean in a keyhole subjected to ionic focusing.

An analysis of all of the factors shows that the occurrence of high-frequency oscillations of the secondary current in the plasma may be related to the occurrence of the phenomenon of anomalous resistance of plasma [26–28]. Anomalous resistance of plasma is resistance that is associated with the development of various kinds of current instabilities and that occurs when the current density in the plasma exceeds a certain critical value. Anomalous resistance of plasma is only related to hybrid electro-ionic instabilities and is substantially larger in magnitude than ordinary classical resistance due to paired electron-ion collisions. The critical current density j at which anomalous resistance occurs is usually expressed through a threshold value of electron drift velocity

$$V_d = j/n_e e. \tag{6}$$

In plasma without a magnetic field, people have spoken of the occurrence of ionic-sonic instability and the minimum value for the velocity V_d at which it occurs, which practically coincides with the velocity of ionic sound in plasma. Ionic-sonic instability is a build-up of longitudinal electrostatic oscillations in plasma with “hot” electrons and “cold” ions [29].

The speed of ionic sound in plasma depends only on the temperature of the electrons and the mass of the ions

$$V_s = \sqrt{\gamma k_b T_e / m_i}, \tag{7}$$

where k_b is Boltzmann’s constant, γ is the adiabatic index, and T_e is the temperature of the electrons. The temperature of the electrons over the zone of electron beam welding is on the order of 4,000 K [3]. In the experiments described, an electron collector with a voltage of $\sim$50 V creates an additional electric field in the plasma in the thin layer close to the cathode (a welding product). This electric field accelerates the electrons and their energy is then converted into thermal energy as a result of collisions with atoms and ions. Suppose that as a result of the described phenomenon the temperature rises to 14,000 K. Then the velocity of ionic-sonic waves is $V_s \approx$ 1,650 m/s.

Let us estimate the conditions under which ionic-sonic instability occurs ($V_d = V_s$). In the experiments described, the strength of the secondary current in the plasma in pulses reaches magnitudes on the order of 1 A, given a collector diameter of 70 mm. Given these assumptions, ionic-sonic instability may occur if the concentration of electrons in the plasma over the welding zone does not exceed

$$n_e = \frac{j}{V_d e} = \frac{4I}{\pi D^2 V_d e} \sim 10^{18}\ \mathrm{m}^{-3}. \tag{8}$$

In the area where the electron collector is located, the concentration is known to be lower, and thus ionic-sonic instabilities are likely to occur.

For ionic-sonic oscillations, in the case of large wavelengths $kr_{De} \ll 1$, the dispersion relation takes the form of a linear dependence $\omega(k) = kV_s$, which is characteristic of sound waves (k is the wave number). If a consistent frequency and arbitrary velocities are typical for Langmuir ionic oscillations, then in ionic-sonic waves the speed is constant, but the frequencies may take on a wide range of values, depending on the wavelength. We will assume a wavelength equal to the typical size of the system (a working distance of 100 mm). In this case, the frequency turns out to be equal to $f = V_s/\lambda \sim$ 16 kHz. Of course, such good

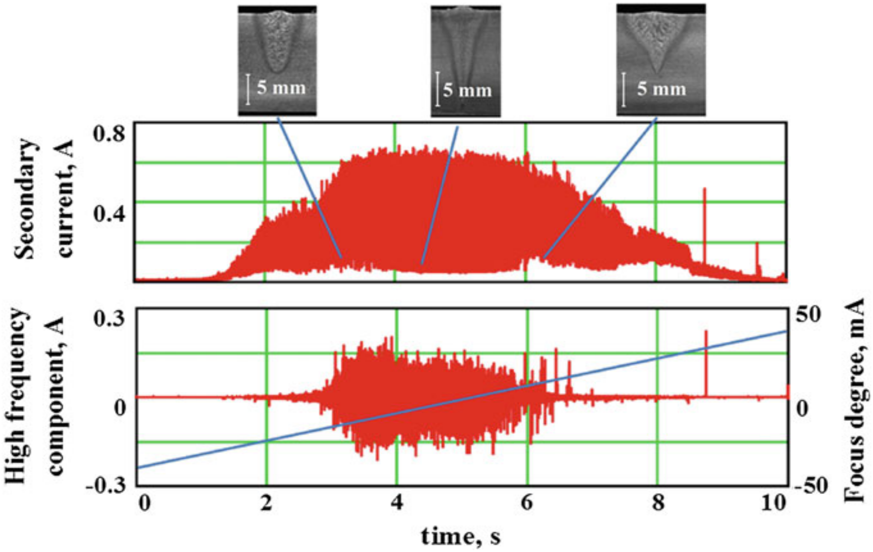

Fig. 6 The high-frequency component of the secondary current during the linear rise of the focus coil current. ($P = 2$ kW, oscillation frequency across the joint $f = 556$ Hz, sweep size 2 A = 1.5 mm)

agreement with the experimentally observed spectrum (Fig. 1) is coincidental. The calculations presented only claim to estimate the order of magnitude.

In the context of the hypothesis described, the observed correlation between the amplitude of the high-frequency component and the focusing mode is obviously dependent upon the fact that the likelihood of the occurrence of ionic-sonic instability grows when the electron drift velocity (magnitude of the secondary current) increases. Given the occurrence of sufficiently large pulse in the secondary current, there is a “blockage” of the plasma gap as a result of anomalous resistance of plasma. The ionic-plasma instability increases and the long pulse of secondary current is interrupted in a series of high-frequency surges. This phenomenon is well-known in the physics of large magnitude pulsed discharges [30].

Thus, possible causes for the observed high-frequency oscillations in the “keyhole-plasma” system are: (a) oscillatory processes of the thermal field in the keyhole caused by the periodic explosive boiling and subsequent defocusing of the electron beam on the products of the discharge; (b) oscillatory ionic-sonic processes in the plasma over the welding zone. In either event, the likelihood of these processes grows with an increase in the thermionic emission from the welding area and thus characterizes the electron beam’s energy density.

Figure 6 shows the secondary current and the high-frequency component ($f > 10$ kHz) during the linear rise of the focus coil current. The signal is appreciable in a certain range, accompanied by deep penetration. The high-frequency component appears in a narrow range. The dependence of the high-frequency

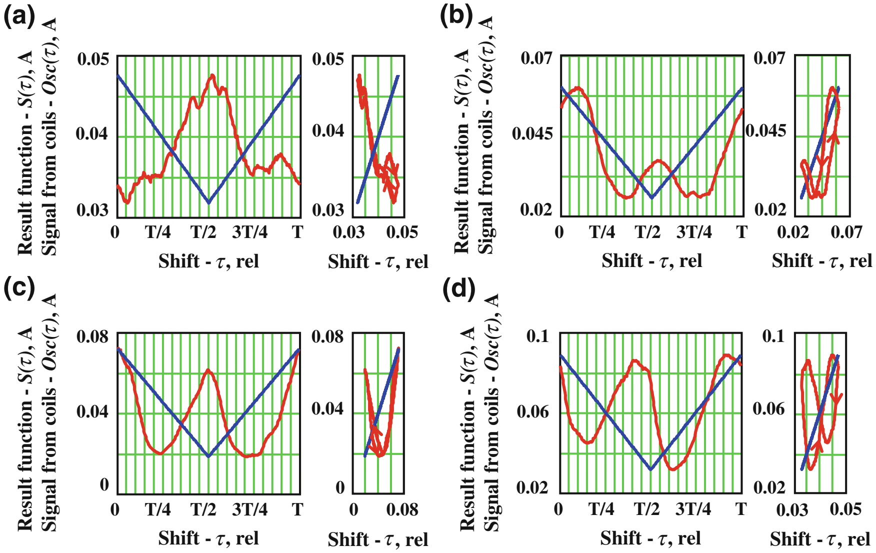

Fig. 7 Function $S(\tau)$, obtained using the coherent accumulation method for the high-frequency component and $Osc(t)$, a record of the deflection coil current during welding along the joint. **a** Under-focused regime ($\Delta I_f = -15$ mA); **b** under-focused regime ($\Delta I_f = -7$ mA); **c** sharp focus regime ($\Delta I_f = 0$ mA); **d** over-focused regime ($\Delta I_f = 10$ mA); ($P = 3$ kW, oscillation frequency $f = 450$ Hz, sweep size 2A = 1.5 mm)

component on the power density (the focus degree) is used to construct operational control methods.

The assertion of the dependence of the probability of high-frequency oscillations on the density of the beam power allows interpretation of the results obtained by the coherent accumulation method for various focus regimes (Fig. 7).

For sharp-focus regimes with maximum penetration depth and over-focused regimes, the beam interacts with the front and back walls almost equally (Fig. 7c, d). The minimum of the high-frequency component signal in this position corresponds to the position at the bottom of the keyhole. The bottom of the keyhole practically coincides with the center of symmetry of the oscillating beam.

As the focus goes down (decreasing the current focus), the minimum of the function of the coherent accumulation method is shifted relative to the center of symmetry of the oscillation beam. This means that the bottom of the keyhole moves relative to the center of symmetry, and the electron beam begins to interact more with the front wall of the keyhole and less with the back one (Fig. 7b).

For strong under-focused regimes (Fig. 7a), when the formation of the keyhole is just beginning, the beam interacts with only the front wall of the keyhole. The high-frequency component signal is maximal at the moment of maximum electron-beam deflection against the welding direction. It appears that at this moment the beam interacts with the bottom of the keyhole. The minimum diameter of the electron beam in this case is below the bottom of the keyhole. Under these conditions, the maximum power density of the electron beam is reached at the bottom of the keyhole. At the top of the keyhole, the power density is less critical, and high-frequency oscillations do not occur there.

We must note that we have still not fully explained the sharp decrease in the secondary current when lowering the area of interaction between the electron beam and the metal deep in the walls of the keyhole. It may be that this is related to the enormous current densities in the keyhole and, as a result, the continuously "blocked" state of the plasma there. It may be that in the keyhole the level of ionization is an order of magnitude less than expected, and the Debye radius is still larger than the lateral dimension of the keyhole. In this case, the plasma does not penetrate the keyhole. The interpretation of this phenomenon will be the subject of future research.

5 Conclusions

1. In this chapter, the ability to study processes in the keyhole (keyhole) during electron-beam welding was demonstrated. A combination of an application of beam deflection oscillation and an analysis of the instabilities of the secondary current in the plasma over the welded samples was used for this purpose.
2. The experimentally obtained secondary current signal in a plasma during electron-beam welding with electron beam oscillation contains a series of high-frequency perturbations, which follow each other at certain frequencies that are multiples of the deflection oscillation frequency.
3. It was shown that the probability of occurrence of these high-frequency perturbations increases with the concentration of energy in the interaction zone. Hypotheses for the emergence of high-frequency oscillating processes in the "beam-keyhole-plasma" structure were considered. Possible causes for the observed high-frequency oscillations in the "keyhole-plasma" system are: (a) oscillatory processes of the thermal field in the keyhole caused by the periodic explosive boiling and subsequent defocusing of the electron beam on the products of the discharge; (b) oscillatory ionic-sonic processes in the plasma over the welding zone. In either event, the likelihood of these processes grows with an increase in the thermionic emission from the welding area and thus characterizes the electron beam's energy density.
4. It was established that during electron-beam welding in a not fully focused mode, the electron beam mainly interacts with the front side and the bottom of the keyhole. In sharp focusing and over-focused modes, the beam interacts practically in the same way with both the front and back sides of the keyhole.
5. It was established that during processing of the high-frequency part of the secondary current in a plasma using the coherent accumulation method, there is a lag of the high-frequency part of the signal in comparison with the deflection coil current signal. The degree of lagging decreases monotonically as the

focusing mode changed from an unfocused to over-focused state, and it is zero for the sharp focusing mode.

6. It must be noted that we have still not fully explained the sharp decrease in the secondary current when lowering the area of interaction between the electron beam and the metal deep in the walls of the keyhole. It may be that in the keyhole the level of ionization is an order of magnitude less than expected, and the Debye radius is still larger than the lateral dimension of the keyhole. In this case, the plasma does not penetrate the keyhole. The interpretation of this phenomenon will be the subject of future research.

Acknowledgments The authors would like to express their thanks to the Russian Foundation for Basic Research No 13-08-00397A and the Ministry of Education of Perm District of the Russian Federation for financial support.

References

1. Chi CT, Chao CG, Liu TF, Wang CC (2008) Relational analysis between parameters and defects for electron beam welding of AZ-series magnesium alloys. J Vac 82:1177–1182
2. Babu NK, Ramana S, Murthy CV, Reddyc GM (2007) Effect of beam oscillation on fatigue life of Ti–6Al–4V electron beam weldments. J Mater Sci Eng 471:113–119
3. Krinberg I, Mladenov G (2005) Formation and expansion of the plasma column under electron beam-metal interaction. J Vac 77–4:407–411
4. Trushnikov DN, Yazovskikh VM, Belenkiy VY (2007) Formation of a secondary-emission signal in electron beam welding with continuous penetration. J Weld Int 21–5:384–386
5. Griskey MC, Stenzel RL (1999) Secondary-electron-emission instability in a plasma. J Phys Rev Lett 82–3:556–559
6. Olszewskaa K, Friedel K (2004) Control of the electron beam active zone position in electron beam welding processes. J Vac 74:29–43
7. Yazovskikh VM, Trushnikov DN, Belenkiy VY (2004) The mechanism of secondary emission processes in electron beam welding with the modulation of the electron beam. J Weld Int 18–9:724–729
8. Trushnikov DN, Belenkiy VY, Mladenov GM, Portnov NS (2012) Secondary-emission signal for weld formation monitoring and control in electron beam welding. J Materialwiss Werkstofftech 43(10):892–897
9. Teng W, Xiangdong G, Katayama S, Xiaoli J (2012) Study of dynamic features of surface plasma in high-power disk laser welding. J Plasma Sci Technol 14–3:245–251
10. Kaplan AFH, Norman P, Eriksson I (2009) Analysis of the keyhole and weld pool dynamics by imaging evaluation and photodiode monitoring. In: Proceedings of LAMP2009, the 5th international congress on laser advanced materials processing, pp 1–6
11. Teresa S, Antonio A, Domenico R, Valentina L, Luigi T, Pietro M (2010) Plasma plume oscillations monitoring during laser welding of stainless steel by discrete wavelet transform application. J Sensors 10–4:3549–3561
12. Peng Y, Chen W, Wang C, Bao G, Tian Z (2001) Controlling the plasma of deep penetration laser welding to increase power efficiency. J Phys D Appl Phys 34–21:3145–3149
13. Rykalin, Uglov A, Zuev I, Kokora A (1985) Laser and electron beam treatment of materials. Mashinostroenie, Russia, Moscow (in Russian)

14. Smurov IY, Uglov AA, Lashyn AM, Matteazzi P, Covelli L, Tagliaferri V (1991) Modelling of pulse-periodic energy flow action on metallic materials. J Int J Heat Mass Transf 34:961–971
15. Trushnikov DN (2013) Using the wavelet analysis of secondary current signals for investigating and controlling electron beam welding. J Weld Int 27(6):460−465
16. Trushnikov D, Belenkiy V, Shchavlev V, Piskunov A, Abdullin A, Mladenov G (2012) Plasma charge current for controlling and monitoring electron beam welding with beam oscillation. J Sensors 12(12):17433–17445
17. Uglov AA, Selishev SV (1987) Autooscillation processes under the action of concentrated energy sources. Science, Russia
18. Kaplan A (1994) A model of deep penetration laser welding based on calculation of the keyhole profile. J Phys D Appl Phys 27:1805–1814
19. DebRoy T (1995) Physical processes in fusion welding. Rev Mod Phys 67–1:85–112
20. Skripov V, Sinitsyn E, Pavlov P, Ermakov G, Muratov G, Bulanov N, Baidakov V (1980) Teplofizicheskie svoistva zhidkostei v metastabil'nom sostoyanii (Thermophysical Properties of Liquids in Metastable State). Atomizdat, Moscow (in Russian)
21. Schumacher B (1964) A review of the (macroscopic) laws for electron penetration through matter. ORF
22. Belen'kii B (1979) The investigation of oscillation processes in the electron beam welding penetration channel. Svar Proizvod 8:6–7
23. Mladenov G, Sabchevski S (2001) Potential distribution and space-charge neutralization in technological intense electron beams—an overview. J Vac 62:113–122
24. Gabovich M, Simonenko L, Soloshenko I, Shkorina N (1974) Excitation of ion oscillations in plasma by a fast beam of negative ions. Zh Eksp Teor Fiz 67:1710–1716
25. Dilthey U, Goumeniouk A, Nazarenko O, Akopjantz K (2001) Mathematical simulation of the influence of ion-compensation, self-magnetic field and scattering on an electron beam during welding. Vacuum 62–2:87–96
26. Galeev A, Sagdeev R (1973) Nonlinear plasma theory. Rev Plasma Phys. Russia, Moscow (in Russian)
27. Kadomtsev V (1976) Collective phenomena in plasma. Russia, Moscow (in Russian)
28. Artsimovich A, Sagdeev R (1979) Plasma physics for physicists. Russia, Moscow (in Russian)
29. Akhiezer A (1974) Ion-acoustic oscillations. Electrodynamics plasma. Russia, Moscow (in Russian)
30. Chen F, Lieberman M (1984) Introduction to plasma physics and controlled fusion. Francis F: Plenum Press, New York

Development in In Situ Observation of Deformation in Semi-solid Alloys Using X-Ray Imaging

Tomoya Nagira and Hideyuki Yasuda

Abstract Casting defects, including macrosegregation and hot tearing, are major issues in a casting process because of the resultant degradation of mechanical properties. Macrosegregation mainly occurs due to fluid flow between dendrite arms and deformation of partially solid alloys, which is induced by solidification shrinkage, thermosolutal convection and external forces applied by several casting processes. An X-ray imaging technique using synchrotron radiation has been developed for in situ observation of deformation at the grain scale in semi-solid Fe–C and Al–Cu alloys. The dynamics of the solid motion showed that impingement between solid particles and rearrangement of solid particles, including translation and rotation, caused the shear-induced dilation. The solid motion was quantitatively analyzed to characterize the deformed microstructures in semi-solid Al–Cu alloys.

Keywords X-ray imaging · Synchrotron radiation · Deformation · Semi-solid alloy

1 Introduction

Casting defects, including macrosegregation and hot tearing, are major issues in a casting process because of the resultant degradation of mechanical properties. Macrosegregation mainly occurs due to fluid flow between dendrite arms and deformation of partially solid alloys, which is induced by solidification shrinkage, thermosolutal convection and external forces applied by several casting processes

---

T. Nagira (✉)
Department of Adaptive Machine Systems, Osaka University, Osaka 565-0871, Japan
e-mail: nagira@ams.eng.osaka-u.ac.jp

H. Yasuda
Department of Materials Science and Engineering, Kyoto University,
Kyoto 606-8501, Japan
e-mail: yasuda.hideyuki.6s@kyoto-u.ac.jp

T. Kannengiesser et al. (eds.), *In-situ Studies with Photons, Neutrons and Electrons Scattering II*, DOI: 10.1007/978-3-319-06145-0_14,

[1]. For example, in high pressure die casting and centrifugal casting, significant stresses act on semi-solid microstructures, resulting in segregation bands containing positive segregation and porosity [2–4]. Figure 1 shows a schematic of shear band formation caused by deformation in semi-solid alloys. When a shear force is applied to semi-solid alloys, the specimen is non-uniformly deformed. At the shear domain, a shear band of increased liquid fraction is often formed, resulting in a segregation band after solidification. However, semi-solid deformation mechanisms are not fully understood. During deformation, the solid/liquid and the solid/solid interactions (i.e., impingement between solid particles) lead to displacement/rotation of solid particles and melt flow [5, 6]. Due to these solid and liquid motions, various mechanical phenomena, including agglomeration/disagglomeration [7], deformation of individual solid particles [5] and dilatancy during rearrangement of the solid particles [2, 3] have been reported. In addition, the rheology of semi-solid alloys [8–10] is influenced by the liquid viscosity, shear rate, and microstructural features including solid fraction, solid particle size, and solid particle shape. It is necessary to study these phenomena to elucidate deformation mechanisms. Observation of deformation in situ is a beneficial approach for understanding the microstructural evolution and for building models of deformation in semi-solid alloys.

In situ observation of solidification and semi-solid deformation behaviors of various alloys have been extensively carried out using X-ray imaging at synchrotron radiation facilities [11–22]. In recent years, in situ observation of deformation at the grain scale in semi-solid Al–Cu and Fe–C alloys has been developed to explore deformation mechanisms [23–30]. Based on these in situ observations, a macroscopic modeling of semi-solid deformation for reproducing segregation bands has also been proposed [31].

This paper overviews the developments in the in situ observation of deformation in semi-solid alloys. Direct evidence for shear-induced dilation and the effect of solid particle shape on dilation are presented to highlight the deformation mechanisms. This paper also characterizes the deformed microstructure including the localization of shear strain and the shear band formation.

2 Development of a Technique for In Situ Observation of Deformation in Semi-solid Alloys

The experiments were carried out at BL20B2 of SPring-8, Hyogo, Japan. A bending magnet was employed as an X-ray source, and the radiation was monochromatized using Si double crystals. Figure 2a shows the setup for the in situ observation of deformation in semi-solid alloys. The observation apparatus consists of an ion chamber, vacuum chamber which holds the furnace, and X-ray detector. An X-ray direct-sensing SATICON video camera tube was used as the image detector [32]. The image signals were converted into a 1,024 × 1,024 pixels, 10-bit format. The pixel size was 5.2 × 5.2 μm^2 and the observation area was 5.2 × 5.2 mm^2. The

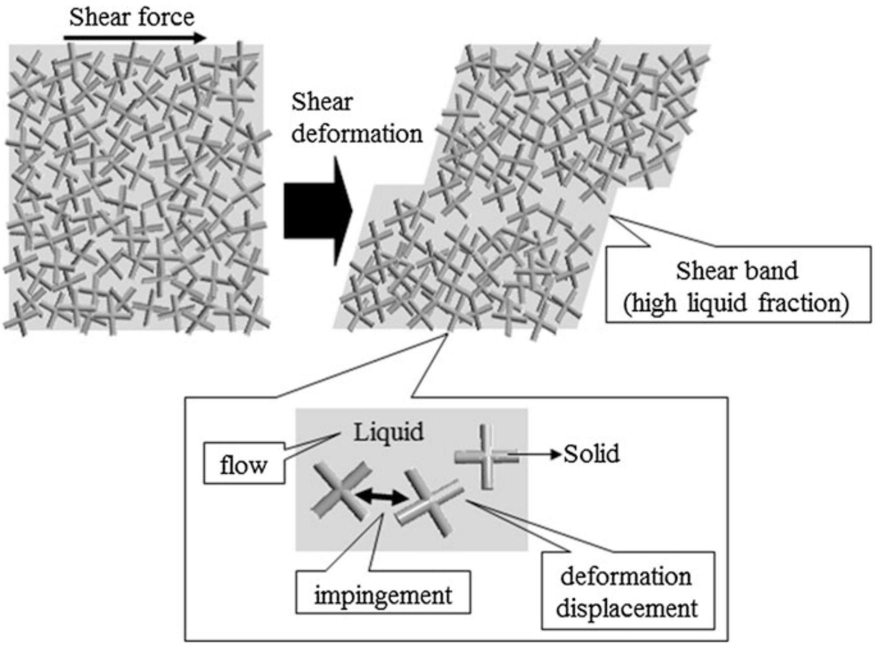

Fig. 1 Schematic of shear band formation [28]

detector acquired 8–32 frames per second and the transmitted images were obtained by integrating a specific number of frames to improve the signal-to-noise ratio.

Figure 2b shows a direct shear cell that is located in the furnace. The specimen, which has dimensions of 10 mm × 10 mm × 0.15–0.2 mm, was placed in the mold consisting of a 200 µm thick Al_2O_3 plate. The mold and Al_2O_3 window plates were retained using BN plates. The specimen was partially remelted in the direct-shear cell under vacuum (10^{-1} Torr) and held at a constant temperature to obtain the desired solid fraction. Direct shear was applied using a stepping motor that pushed the Al_2O_3 push plate upwards at a displacement rate of 30–50 µm/s.

3 In Situ Observation of Shear Deformation in Semi-solid Fe–C Alloys

3.1 Microstructure of Semi-solid Fe–C Alloys

Fe-2.08C-0.87Mn-0.45Si (mass%) ultrahigh carbon steel, which has a wide freezing range and is one of the candidate alloys for semi-solid processing (SSP), was used. The development of SSP of steels has received considerable attention in recent years [33–37]. The SSP has many advantages, including reduced processing force, smaller machines, and reduced porosity over conventional casting processes.

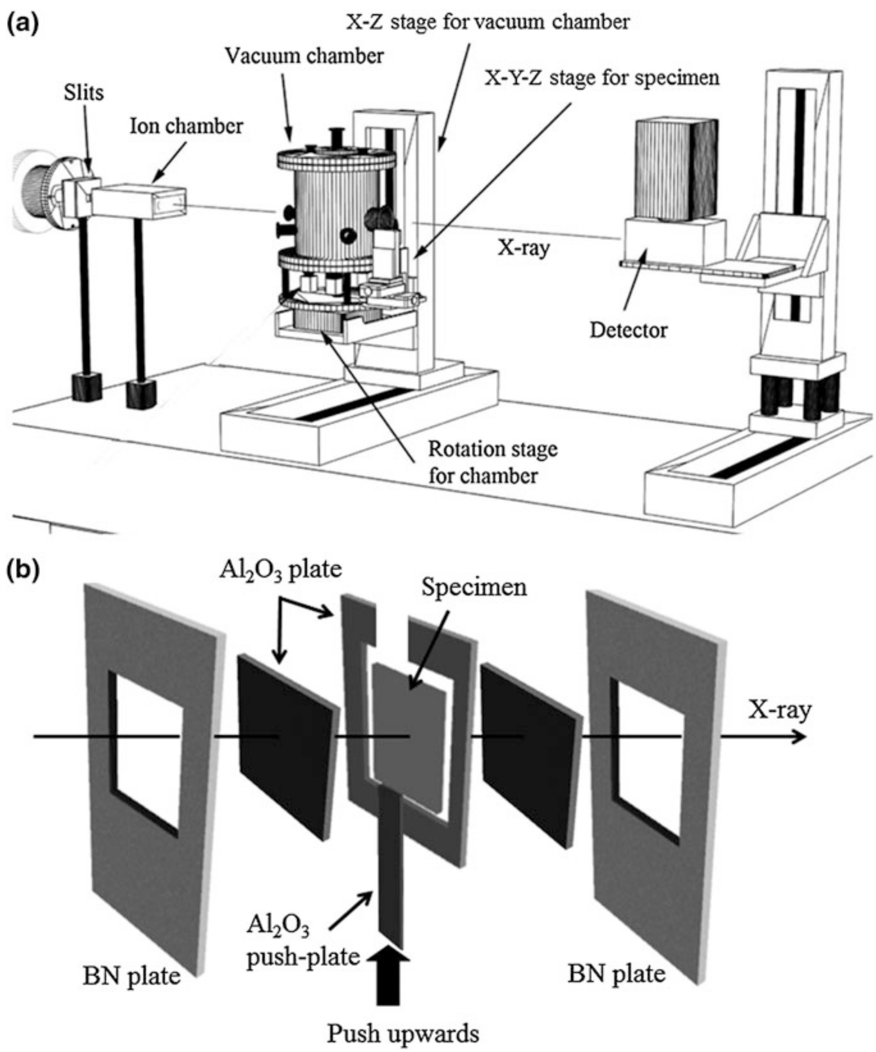

Fig. 2 Setup for the in situ observation experiment: **a** configuration of the experimental apparatus [20] and **b** direct shear cell [28, 29]

Figure 3 shows radiographs of two specimens prior to shear. The average grain size of the specimen in Fig. 3a was 310 μm and a large amount of liquid is entrapped within the solid particles. The sample has a mean thickness of ~0.6 grains. Figure 3b shows an expanded view of a solid particle. Solid particles with a high entrapped liquid fraction are common microstructures that are termed "cloudy-like" [36]. This microstructure is generated by partially remelting a dendritic microstructure with large grain sizes. In contrast, the average grain size of the specimen in Fig. 3c was 120 μm and the sample thickness is slightly thicker

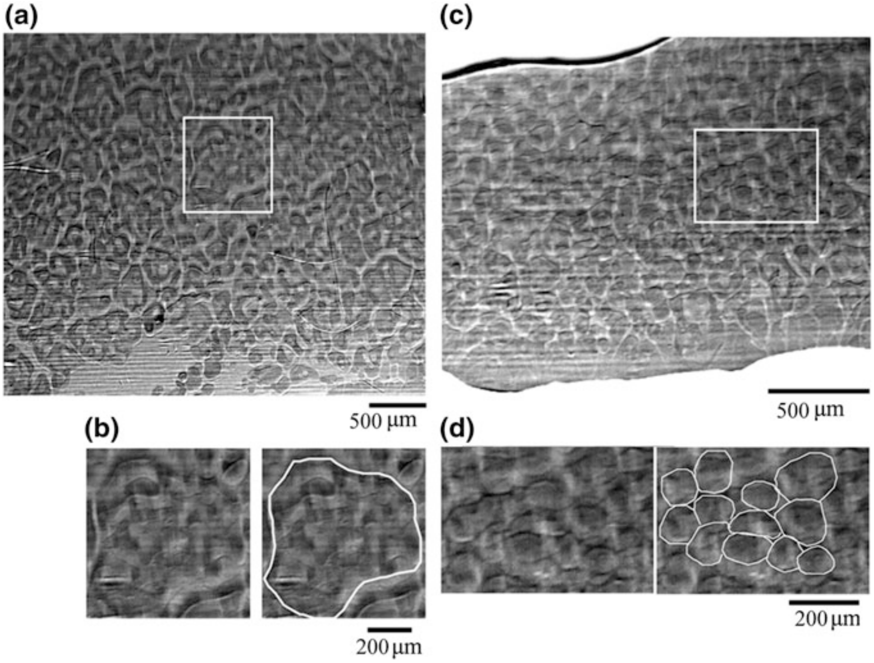

Fig. 3 Semi-solid microstructures prior to shear of the **a** 310 μm specimen and **c** 120 μm specimen [23]. **b** and **d** Expanded views of the *white boxes* in (**a**) and (**c**), respectively. The *outer solid-liquid* interface is traced in *white*

than the grain size. Figure 3d shows an expanded view of the solid particles. The solid particles have a globular morphology without entrapped liquid which are formed by partially remelting a fine equiaxed dendritic microstructure.

The initial solid fraction, g_s, prior to shear was calculated from the intensity of the transmitted X-ray beam through regions of 100 % liquid, I_L, 100 % solid, I_S, and semi-solid, I_{SL}. In a specified region, D, the solid fraction is expressed by the following equation. Further details are given in Ref. [24].

$$[g_S]_D = \frac{\ln I_{SL} - \ln I_L}{\ln I_S - \ln I_L} \tag{3.1}$$

The volume fraction of solid in the 310 μm specimen was calculated to be ~40 %, and the volume fraction of entrapped liquid, g_L^{int}, was calculated to be ~25 % based on image analysis. Therefore, the effective solid fraction, $g_{env}\left(= g_S + g_L^{int}\right)$, is ~65 %. The volume fraction of solid in the 120 μm specimen was calculated to be ~55 %.

The shape factor, F, which indicates the roundness of the solid particles, was calculated using the following equation.

$$F = 4\pi \frac{A}{U^2} \tag{3.2}$$

where, A is the area and U is the perimeter. In the case of a spherical shape (i.e., a circle in radiography), F is equal to 1. The projected-area shape factors of the solid particles are 0.94 and 0.64 for the 120 and 310 μm specimens, respectively. The solid particles in the 120 μm specimen are significantly more spheroidal than those in the 310 μm specimen.

3.2 Deformation of Semi-solid Fe–C Alloys

Figure 4 shows the shear deformation of the 310 μm specimen. The semi-solid microstructure before and after a 2d increment of the Al_2O_3 push-plate motion, where d is the mean particle size, are shown in Fig. 4a and b, respectively. The Al_2O_3 push plate is located in the bottom right corner of Fig. 4a and b. In the upper left region of the Al_2O_3 push plate, which is the shear domain, large liquid-filled spaces were created between the solid particles, which caused a decrease in the solid fraction.

Impingement between solid particles and translation and rotation of solid particles frequently occurred during shear especially at the shear domain. Figure 4c–f show the image sequences, which are expanded views of the white boxes in Fig. 4a and b, during a 2d increment of Al_2O_3 push-plate motion. The image sequences show that the enlargement of liquid-filled spaces between the solid particles was clearly observed during shear. To explain this dilation, five solid particles, labeled a–e, which play an important role in the dilation, are picked up, as shown in Fig. 4g–j. During shear, the Al_2O_3 push plate pushed particle a upwards into particles b and c. The particles were also rotated due to impingement between the solid particles. The forces were transmitted to particles b and c. The rotation and displacement of particle c led to push particles e to the left and d upwards. As a result of the rearrangement of solid particles, a liquid-filled space was produced. In situ observation of the deformation in semi-solid alloys proved that the dilation occurred through impingement between solid particles and rearrangement of solid particles including translation and rotation. The dilatancy caused by impingement and rearrangement of solid particles is similar to the deformation of semi-solid Al–Cu alloys [24] and compacted granular materials including soils [2, 3].

3.3 Effect of Solid Shape on Dilation

The deformation of the elementary volume during shear was examined. It is assumed that the deformation of a semi-solid specimen is consistent with that of a

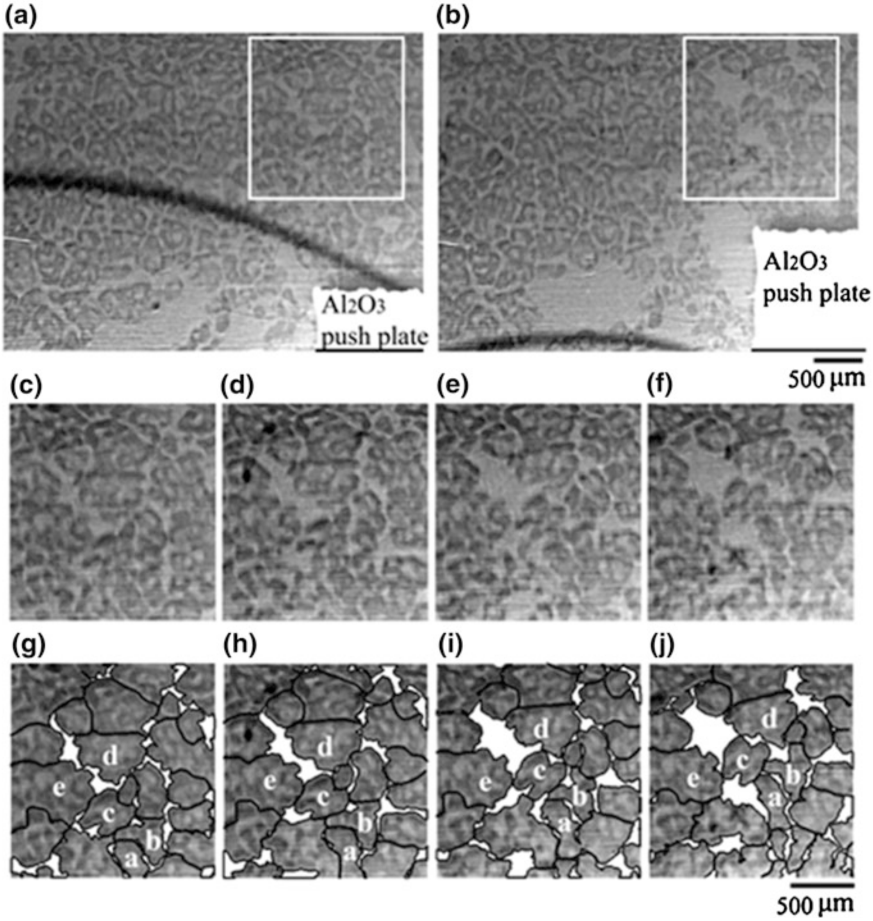

Fig. 4 Deformation of the 310 μm specimen [23]. Semi-solid microstructures **a** before and **b** after a 2d increment of Al_2O_3 push plate motion. **c**–**f** Four frames from the *white boxes* in (**a**) and (**b**). **g**–**j** The five solid particles, labeled (**a**–**e**), that play an important role in the dilation. Liquid regions between solid particles are defined as *white* and the solid particles boundaries are traced *black*

solid specimen. Figure 5a and b show the elementary volume before ($\Delta x \Delta y$) and after ($\Delta x' \Delta y'$) deformation. $\partial U_x/\partial y$ and $\partial U_y/\partial x$ show the angles in the x and y directions, respectively. Figure 5c and d show the 310 μm specimen ($F = 0.64$) before and after a 2d increment of Al_2O_3 push-plate motion. One square as shown in Fig. 5e, which corresponds to the white box in Fig. 5c, was selected as the elementary volume near the shear plane. The sheared element was defined as the best-fit parallelogram region bounding the same grain particles as the original element as shown in Fig. 5f. The liquid fraction remarkably increased from ~1 to ~10 % based on 2D image analysis. The region in Fig. 5e underwent a ~15 %

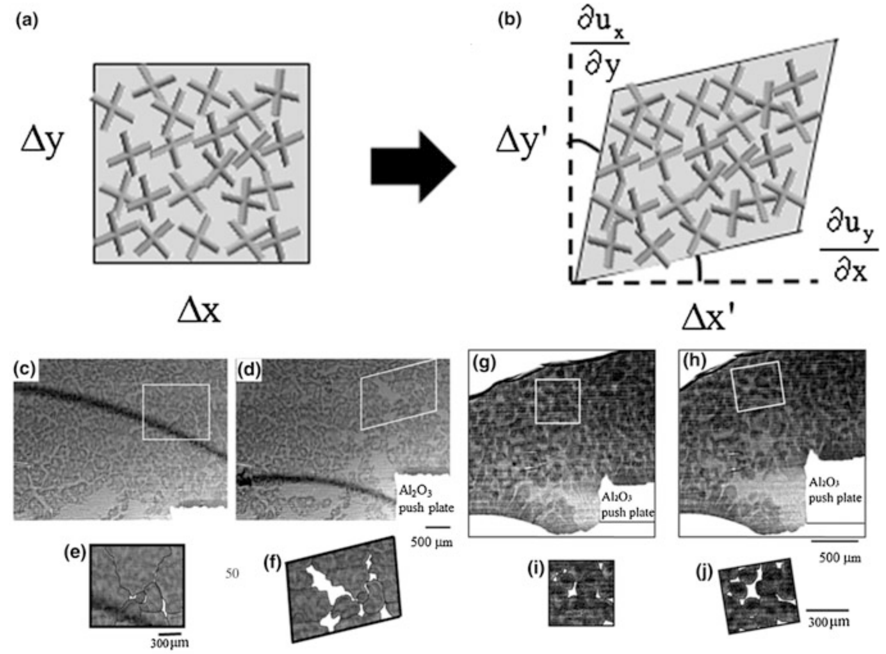

Fig. 5 **a** and **b** schematic of shear deformation in the semi-solid state. **c** and **d** The 310 µm specimen before and after a 2d increment of Al_2O_3 push-plate motion, respectively. **e** and **f** Expanded views of the *white boxes* in (**a**) and (**b**), respectively. **g** and **h** The 120 µm specimen before and after a 2.2d increment of Al_2O_3 push-plate motion, respectively. **i** and **j** Expanded views of the *white boxes* in (**a**) and (**b**), respectively [23, 28, 29]

increase in volume due to liquid being drawn into the grain particle assembly. Note that the thickness of the specimen remains constant during shear.

Figure 5g and h show the 120 µm specimen ($F = 0.94$) before and after a 2.2d increment of Al_2O_3 push-plate motion. One square, as shown in Fig. 5i, which corresponds with the white box in Fig. 5g, was selected as the elementary volume. Figure 5j shows the deformed element bounding the same solid particles as that in Fig. 5i. The liquid fraction increased from ~3.6 to ~7.8 % based on 2D image analysis, and the volume strain is approximately 8 % due to dilation. Comparing the volume strain of the two specimens in Fig. 5e, f, i and j, the irregularly shaped solid particles with a shape factor far from 1 in the 310 µm specimen showed a higher increase in volume strain compared to the spherical solid particles in the 120 µm specimen. Dilation occurs due to rearrangement of solid particles, including rotation and translation, as shown in Fig. 4. If the solid particles are spherical, rotation does not create interstitial space, while, the rotation of irregularly shaped solid particles forms significant interstitial spaces. As a result, the solid fraction of the deformed 310 µm specimen remarkably decreases, as shown in Fig. 5e and f.

4 Localization of Shear Strain and Shear Band Formation

The semi-solid microstructure was characterized by the quantitative analysis of the solid motion in the image sequences during shear. The transmission image was divided into a domain with dimensions of $120 \times 120\ \mu m^2$, which is approximately 1.2 times larger than the average solid particle size. The solid velocities in the x, u_x, and y directions, u_y, were calculated using the correlation pattern between the frames. Further details are given in Ref. [27]. The strain rate in the x direction, ε_{11}, the strain rate in the y direction, ε_{22}, and the shear strain rate, ε_{12}, where 1 and 2 indicate positive x and y directions, are given by

$$\varepsilon_{11} = \frac{\partial u_x}{\partial x} \tag{4.1}$$

$$\varepsilon_{22} = \frac{\partial u_y}{\partial y} \tag{4.2}$$

$$\varepsilon_{12} = \frac{1}{2}\left(\frac{\partial u_x}{\partial y} + \frac{\partial u_y}{\partial x}\right) \tag{4.3}$$

The divergence of the solid rate, $\mathrm{div}(\vec{u})$, is obtained from the following equation.

$$\mathrm{div}(\vec{u}) = \frac{\partial u_x}{\partial x} + \frac{\partial u_y}{\partial y} \tag{4.4}$$

Mass conservation gives the following relationship.

$$\frac{\partial f_s}{\partial t} + f_s \mathrm{div}(\vec{u}) = 0 \tag{4.5}$$

where f_s is the solid fraction. Here, the solid fraction is assumed to be uniform in region of interest. Since the initial solid fraction is close to uniform prior to shear, this assumption is roughly valid.

Past researches on the in situ observation showed that the deformation behaviors, including dilation caused by impingement and rearrangement of solid particles in semi-solid Al–Cu alloys were fundamentally similar to those in semi-solid Fe–C alloys [23, 24]. Image sequences of semi-solid Al–Cu alloys with Al-15Cu-0.5Ti-0.25B (mass%) during shear were used for quantitative analysis. Figure 6a shows the semi-solid microstructure before a 0.5d increment of Al_2O_3 push-plate motion. The average grain size of the specimen was 96 μm. The volume fraction of solid is ~48 %, as calculated with Eq. (3.1). The projected-area shape factor of the solid particles is F = 0.8. The solid motion was quantitatively analyzed during a 0.5d increment of Al_2O_3 push plate displacement. The arrows in Fig. 6b show the solid velocity vectors. At the ahead of the Al_2O_3 push plate, the

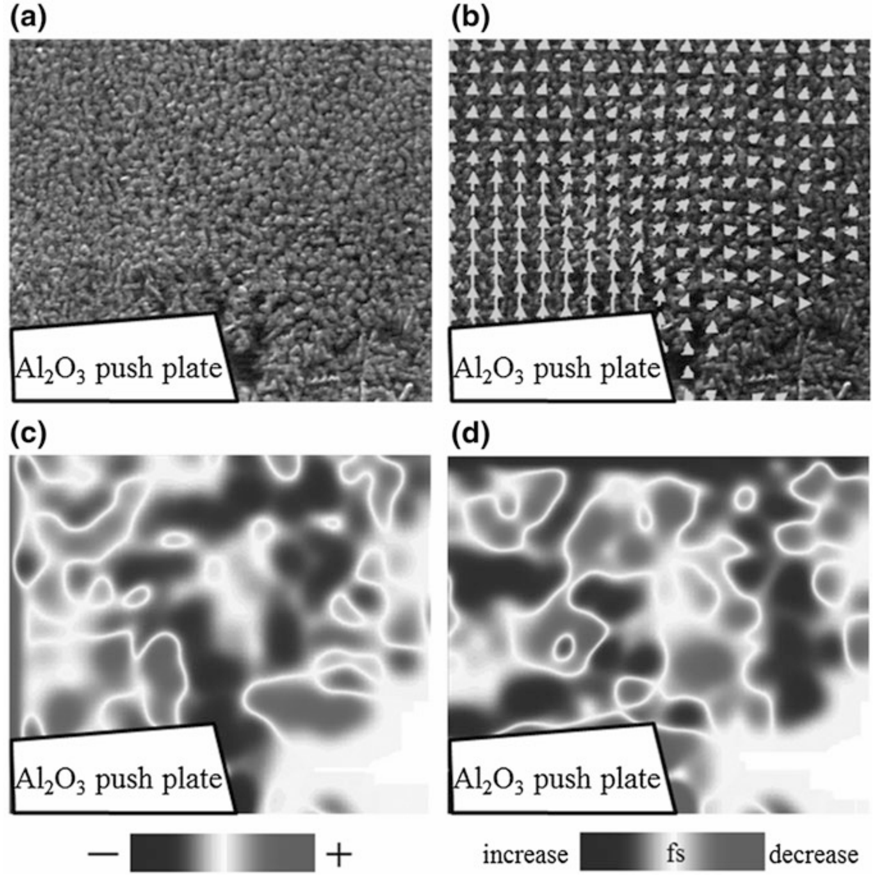

Fig. 6 **a** Semi-solid microstructures of semi-solid Al–15Cu alloy before a 0.5d increment of push-plate motion. **b** Solid velocity vector, **c** distribution of shear strain rate, and **d** divergence of solid velocity in a 0.5d increment of push-plate motion [27]. The divergence corresponds to the change in the solid fraction, f_s

solid particles mainly translated upwards in the direction of the Al_2O_3 push plate motion, and the velocity of the solid particles decreased with increasing distance from the Al_2O_3 push plate front. The right component of the solid velocity vectors became dominant close to the shear plane. The solid velocity vectors turned to the right at the upper right area of the Al_2O_3 push plate. The solid velocity vectors were in the range of 16d from the right side of the Al_2O_3 push plate. The distribution of the solid velocity vectors indicates that the divergence is not equal to zero. In contrast, the divergence of the flow velocity in incompressible Newtonian fluid should be zero at any region because the mass conservation law is always satisfied. Accordingly, the solid motion during shear is characteristic of dense granular flow [2, 3].

Figure 6c shows the distribution of the shear strain rate, ε_{12}, calculated with Eq. (4.3). Shear deformation occurs at the black-shaded region (negative values of shear strain rate). A relatively high shear strain rate is localized at the upper right region of the Al_2O_3 push plate. The mean shear strain rate in the localized shear strain region was estimated to be $-2 \times 10^{-2}\ s^{-1}$. Figure 6d shows the distribution of the divergence of solid velocity, which corresponds to a change in solid fraction. The decrease in solid fraction is represented by the gray-shaded region (positive values of divergence). Compared with the distribution of the shear strain rate (Fig. 6c), the relatively high positive divergence, which corresponds to the decrease in solid fraction, was distributed, at the localized shear strain region. The mean divergence was $1 \times 10^{-2}\ s^{-1}$ at the shear domain. In contrast, negative values of divergence (black-shaded region), which indicate increased solid fraction, were distributed at the Al_2O_3 push plate front. This is caused by the compressive force. The shear band was defined as the region of coupled localized shear strain and decreased solid fraction, as shown in Fig. 6c and d. The shear band width was approximately 10 mean particle diameters. It has been reported that the shear bands are typically 7–18 mean particle diameters in semi-solid metallic alloys, which is similar to those that form in compacted granular materials, such as dense-sand and glass beads [2, 3]. The shear band width of 10 mean particle diameters, as determined by the quantitative analysis of solid motion in semi-solid Al–Cu alloys, is within the range of previous experimental data on the bulk specimen.

Past research on the effect of the solid particle shape on the shear band showed that irregular solid particles resulted in a wider shear band width than spherical solid particles ($F = 1.0$) [27]. The shear band width in semi-solid Al–Cu alloys (10d) was approximately twice as wide as that formed in water-polystyrene particle mixtures. This is because a significant force acts on the surrounding solid particles over a longer distance as they rotate.

5 Summary

An X-ray imaging technique using synchrotron radiation has been developed for in situ observation of deformation at the grain scale in semi-solid Fe–C and Al–Cu alloys. The dynamics of the solid motion showed that impingement between solid particles and rearrangement of solid particles, including translation and rotation, caused the shear-induced dilation. The irregularly shaped solid particles ($F = 0.64$) in semi-solid Fe–C alloys resulted in a higher increase in the volume strain near the shear plane than the spherical solid particles ($F = 0.94$).

The solid motion was quantitatively analyzed to characterize the deformed microstructures in semi-solid Al–Cu alloys. The perpendicular component of solid velocity to the shear plane increased toward the shear plane due to impingement and rearrangement of the solid particles. Localization of shear strain rate was observed at the shear domain where the solid fraction decreased. The shear band, where a high shear strain rate and decreased solid fraction were localized, formed at the shear domain and its width was approximately 10 mean particle diameters for semi-solid Al–Cu alloys.

Acknowledgments Synchrotron radiation experiments were performed at BL20B2 of SPring-8 under proposal nos. 2009A(B)0014, 2010A1420, 2011A1209, 2011B1096, 2012A1110, and 2012B1173 with the approval of the Japan Synchrotron Radiation Research Institute (JASRI). The in situ observation technique was developed with the support of "ISIJ Innovative Program for Advanced Technology," ISIJ Research Promotion Grant. Analysis was carried out under JSPS KAKENHI Grant nos. 24560910, 24246124, and 24226018.

References

1. Dantzig JA, Rappaz M (2009) Solidification, EPFL Press, pp 567–606
2. Gourlay CM, Dahle AK (2007) Dilatant shear bands in solidifying metals. Nature 445:70–73
3. Gourlay CM, Meylan B, Dahle AK (2008) Shear mechanisms at 0–50 % solid during equiaxed dendritic solidification of an AZ91 magnesium alloy. Acta Mater 56:3403–3413
4. Kang I, Ohnaka I (1997) Banded segregation in centrifugal casting of Al–Cu alloys. In: 4th Decennial international conference on solidification processing, Sheffield, pp 346–349
5. Tzimas E, Zavaliangos A (1999) Mechanical behavior of alloys with equiaxed microstructure in the semisolid state at high solid content. Acta Mater 47:517–528
6. Chen CP, Tsao C-YA (1997) Semi-solid deformation of non-dendritic structures-I. Phenomenological behavior. Acta Mater 45:1955–1968
7. Flemings MC (1991) Behavior of metal alloys in the semisolid state. Metall Trans 22A: 957–976
8. Metz SA, Flemings MC (1969) Hot tearing in cast metals. AFS Trans 77:329–334
9. Sumitomo T, StJohn DH, Steinberg T (2000) The shear behavior of partially solidified Al–Si–Cu alloys. Mater Sci Eng A 289:18–29
10. Tzimas E, Zavaliangos A (2000) Evolution of near-equiaxed in the semisolid state. Mater Sci Eng A 289:228–240
11. Mathiesen RH, Arnberg L, Mo F, Weitkamp T, Snigirev A (1999) Time resolved X-ray imaging of dendritic growth in binary alloys. Phys Rev Lett 83:5062–5065
12. Yasuda H, Ohnaka I, Kawasaki K, Sugiyama A, Ohmichi T, Iwane J, Umetani K (2004) Direct observation of stray crystal formation in unidirectional solidification of Sn–Bi alloy by X-ray imaging. J Cryst Growth 262:645–652
13. Mangelinck-Noel N, Nguyen-Thi H, Reinhart G, Schenk T, Cristiglio V, Dupouy MD, Gastaldi J, Billia B, Hartwig J (2005) In situ analysis of equiaxed growth of aluminium-nickel alloys by X-ray radiography at ESRF. J Phys D 38:A28–A32
14. Li B, Brody HD, Black DR, Burdette HE, Rau C (2006) Real time observation of dendritic solidification in alloys by synchrotron microradiography. J Phys D 39:4450–4456
15. Terzi S, Salvo L, Suery M, Limodin N, Adrien J, Maire E, Pannier Y, Bornert M, Bernard D, Felberbaum M, Rappz M, Boller E (2009) In situ X-ray tomography observation of inhomogeneous deformation in semi-solid aluminium alloys. Scr Mater 61:449–462
16. Zabler S, Rack A, Rueda A, Helfen L, Garcia-Moreno F, Banhart J (2010) Direct observation of particle flow in semi-solid alloys by synchrotron X-ray micro-radioscopy. Phys Status Solidi A 207:718–723
17. Phillion AB, Hamilton RW, Fuloria D, Leung ACL, Rockett P, Connolley T, Lee PD (2011) In situ X-ray observation of semi-solid deformation and failure in Al–Cu alloys. Acta Mater 59:1436–1444

18. Yasuda H, Yamamoto Y, Nakatsuka N, Nagira T, Yoshiya M, Sugiyama A, Ohnaka I, Umetani K, Uesugi K (2008) In situ observation of nucleation, fragmentation and microstructure evolution in Sn–Bi and Al–Cu alloys. Int J Cast Met Res 22:125–128
19. Yasuda H, Yamamoto Y, Nakatsuka N, Yoshiya M, Nagira T, Sugiyama A, Ohnaka I, Uesugi K, Umetani K (2009) In situ observation of solidification phenomena in Al–Cu and Fe–Si–Al alloys. Int J Cast Met Res 22:15–21
20. Yasuda H, Nagira T, Yoshiya M, Nakatsuka N, Sugiyama A, Uesugi K, Umetani K (2011) Development of X-ray imaging for observing solidification of carbon steels. ISIJ Int 51:402–408
21. Yasuda H, Nagira T, Yoshiya M, Uesugi M, Nakatsuka N, Kiire M, Sugiyama A, Uesugi K, Umetani K (2011) In situ observation of peritectic solidification in Sn–Cd and Fe–C alloys. In: IOP conference series: materials science and engineering, vol 27, p 012084
22. Yasuda H, Nagira T, Yoshiya M, Sugiyama A, Nakatsuka N, Kiire M, Uesugi M, Uesugi K, Umetani K, Kajiwara K (2012) Massive transformation from phase to phase in Fe–C alloys and strain induced in solidifying shell. In: IOP conference series: materials science and engineering, vol 33, p 012036
23. Nagira T, Gourlay CM, Sugiyama A, Uesugi M, Kanzawa Y, Yoshiya M, Uesugi K, Umetani K, Yasuda H (2011) Direct observation of deformation in semi-solid carbon steel. Scripta Mater 64:1129–1132
24. Gourlay CM, Dahle AK, Nagira T, Nakatsuka N, Nogita K, Uesugi K, Yasuda H (2011) Granular deformation mechanisms in semi-solid alloys. Acta Mater 59:4933–4943
25. Gourlay CM, Nagira T, Dahle AK, Nakatsuka N, Uesugi K, Yasuda H (2011) Synchrotron radiography of direct-shear in semi-solid alloys. In: IOP conference series: materials science and engineering, vol 27, p 012086
26. Nagira T, Morita S, Yasuda H, Gourlay CM, Sugiyama A, Yoshiya M, Uesugi K, Umetani K (2012) In situ observation of shear deformation in semi-solid Al–Cu alloys. In: Proceedings of visual-JW2012, Osaka, pp 215–216
27. Nagira T, Yokota H, Morita S, Yasuda H, Yoshiya M, Gourlay CM, Sugiyama A, Uesugi K, Umetani K (2013) Characterization of shear deformation based on in situ observation of deformation in semi-solid Al–Cu alloys and water-particle mixture. Tetsu-to-Hagane 99:141–148
28. Nagira T, Yasuda H, Gourlay CM, Sugiyama A, Yoshiya M, Uesugi K, Umetani K (2012) In situ observation of shear deformation in semi-solid alloys. J Soc Syn Rad Res 25:275–284
29. Nagira T, Yasuda H, Gourlay CM, Sugiyama A, Yoshiya M, Uesugi K, Umetani K (2012) Direct observation of shear deformation in semi-solid alloys using X-ray imaging. Materia Japan 51:561–568
30. Gourlay CM, Nagira T, Uesugi K, Yasuda H (2013) In situ study of the altering globule packing-density during semisolid alloy deformation. Solid State Phenom 192–193:185–190
31. Morita S, Yasuda H, Nagira T, Gourlay CM, Yoshiya M, Sugiyama A (2012) Macroscopic modeling of semisolid deformation for considering segregation bands induced by shear deformation. In: IOP conference series: materials science and engineering, vol 33, pp 012053
32. Umetani K, Uesugi K, Kobatake M, Yamamoto A, Yamashita T, Imai S (2009) Synchrotron radiation microimaging in rabbit of cancer for preclinical testing. Nucl Instr Meth A 609:38–49
33. Kikuchi M, Kopp R (2002) Mushy/semi-solid metal forming technology—present and future. CIRP Ann Manuf Technol 51:653–670
34. Omar MZ, Palmiere EJ, Howe AA, Atkinson HV, Kapranos P (2005) Thixoforming of a high performance HP9/4/30 steel. Mater Sci Eng A 395:53–61
35. Ramadan M, Takita M, Nomura H, EI-Bagoury N (2006) Semi-solid processing of ultrahigh-carbon castings. Mater Sci Eng A 430:285–291
36. Püttgen W, Bleck W, Hirt G, Shimahara H (2007) Thixoforming of steels—a status report. Adv Eng Mater 9:231–245
37. Sugiyama S, Li J, Yanagimoto J (2007) Semisolid extrusion of low-carbon steel. Mater Trans 48:807–812

Advanced Facility for Parallel Thermo-Mechanical Simulation and Synchrotron X-Ray Diffraction

Guilherme Faria, Leonardo Wu, Thais Alonso, Augusta Isaac, James Piton, Regis Neuenschwander and Antonio J. Ramirez

Abstract In recent years, the number of studies involving in situ measurements experienced an impressive growth in different areas of science. This follows from important advances in several areas of technology, involving precise and reliable sample conditioning, very efficient and fast detectors, and better probe sources. This tendency has been accompanied by the development of new installations specialized on in situ measurements, some of which allow studies involving severe, well controlled, and reproducible thermo-mechanical conditions. Although most of the pioneering experiments were made possible by the customization of pre-existing instrumentation, recently, several beamlines have been built or adapted to work with in situ experiments in synchrotron sources. In order to explore some new areas in materials science, we have developed a new installation in Brazil, named XTMS, or X-ray Scattering and Thermo-Mechanical Simulation station, capable of performing in situ diffraction measurements on samples subjected to extreme and complex thermal and/or mechanical conditions, with excellent versatility and reproducibility. The experimental station has been developed and commissioned by the Brazilian Nanotechnology National Laboratory

---

G. Faria · L. Wu · T. Alonso · A. J. Ramirez (✉)
Brazilian Nanotechnology National Laboratory (LNNano-CNPEM),
PO Box 6192, Campinas, SP 13083-970, Brazil
e-mail: antonio.ramirez@lnnano.cnpem.br

G. Faria · A. J. Ramirez
School of Mechanical Engineering, University of Campinas (FEM-UNICAMP),
Rua Mendeleyev 200, Campinas, SP 13083-860, Brazil

A. Isaac · J. Piton · R. Neuenschwander
Brazilian Synchrotron Light Laboratory (LNLS-CNPEM), PO Box 6192, Campinas,
SP 13083-970, Brazil

A. Isaac
Engineering School, Minas Gerais Federal University, Av. Antônio Carlos,
6627, Belo Horizonte, MG 31270-901, Brazil

T. Kannengiesser et al. (eds.), *In-situ Studies with Photons, Neutrons and Electrons Scattering II*, DOI: 10.1007/978-3-319-06145-0_15,

(LNNano) team in collaboration with the Brazilian Synchrotron Light Laboratory (LNLS), both located at the Brazilian Center for Energy and Materials Research (CNPEM).

Keywords Synchrotron sources · X-ray scattering · Thermo-mechanical simulation · Gleeble-simulator

1 Introduction

In recent years, the number of studies involving in situ measurements experienced an impressive growth in different areas of science. This follows from important advances in several areas of technology, involving precise and reliable sample conditioning, very efficient and fast detectors, and better probe sources. This tendency has been accompanied by the development of new installations specialized on in situ measurements, some of which allow studies involving severe, well controlled, and reproducible thermo-mechanical conditions. Although impressive developments have been made in electron microscopy and neutron scattering areas, it is still the X-ray scattering field which provides the largest amount of results. This is due to the given availability of high flux synchrotron sources and the considerably simpler instrumentation required, when compared to neutron scattering. In fact, a wide variety of materials science in situ studies using X-ray diffraction have been reported on the literature, covering fields such as phase transformation kinetics [1–4], stress induced crystallographic transformations [5, 6], welding [7], etc. Although most of the pioneering experiments were made possible by the customization of pre-existing instrumentation, recently, several beamlines have been built or adapted to work with in situ experiments in synchrotron sources such as the ESRF, APS [8], SPRing-8 [9, 10] and Bessy [11]. In order to explore some new areas in materials science, we have developed a new installation, named XTMS, or X-ray Scattering and Thermo-Mechanical Simulation station, capable of performing in situ diffraction measurements on samples subjected to extreme and complex thermal and/or mechanical conditions, with excellent versatility and reproducibility. This unique setup opens new research possibilities to explore the interrelationships between stress/strain, temperature, chemical elements partition, and crystallography of both diffusion and shear driven transformations. The experimental station has been developed and commissioned by the Brazilian Nanotechnology National Laboratory (LNNano) team in collaboration with the Brazilian Synchrotron Light Laboratory (LNLS), both located at the Brazilian Center for Energy and Materials Research (CNPEM). Here are presented the constructive details and capabilities of this state of the art experimental station.

2 Installation Overview

The XTMS installation has been engineered to be a comprehensive source of information regarding the tested sample, while it is subjected to thermo-mechanical treatment. It provides the sample status during the whole experiment by registering the actual temperature and uniaxial strain/stress conditions at which it is being submitted, while simultaneously acquiring dilatometry and diffraction data revealing how the sample component phases behave throughout the programmed thermo-mechanical test. This allows a unique insight on the fundamentals of phase transformations and their interrelationships with the crystalline structure and the material macroscopic behavior.

The thermo-mechanical simulation and macroscopic properties are controlled and measured using a custom built physical simulator mounted in a X-ray beamline located at the Brazilian synchrotron light source (Fig. 1). The tested sample is contained within a controlled atmosphere chamber, which is equipped with incident and diffracted X-ray beam windows. A heavy duty goniometer, which can hold one or two dimensional X-ray detectors weighting up to 18 kg is mounted around the thermo-mechanical simulator chamber, with its rotation axis parallel to the simulator's uniaxial force application direction. Both the thermo-mechanical simulator and the goniometer are mounted on independent motorized positioning tables, which allow the goniometer rotation axis to be centered at the point of beam incidence on the sample. The incident beam energy selection, positioning, and focusing are performed using the optics shared with the XRD1 beamline, which is a diffraction beamline at LNLS dedicated to polycrystalline samples. In addition, the XTMS installation counts with dedicated equipment for optimized incident beam control such as X-ray attenuators, high resolution slits, and X-ray beam position meter, which also act as an incident beam intensity counter. Further information on the specific systems that comprise the beamline optics can be found on the following sections.

3 Thermo Mechanical Simulator

The thermo mechanical simulator is a custom built Gleeble$^{\text{TM}}$ system, namely a 3S50$^{\text{TM}}$ system, co-developed by the scientific and instrumentation teams from LNNano, LNLS, and Dynamic Systems Inc. (DSI). The physical simulator can control and/or record sample thermal and mechanical history through the experiment, including variables as: programmed and actual temperature, stroke, strain, force and stress. When non contact dilatometry data is acquired, the sample cross section or diameter change with temperature, uniaxial stress and/or time can be recorded to provide an additional insight into the phase transformations undergone by the studied material. The Gleeble thermo mechanical simulator platform was selected due to its well-known flexibility, robust control and penetration on the materials science community.

Fig. 1 XTMS installation at the Brazilian Synchrotron Light Laboratory (LNLS) experiment hall

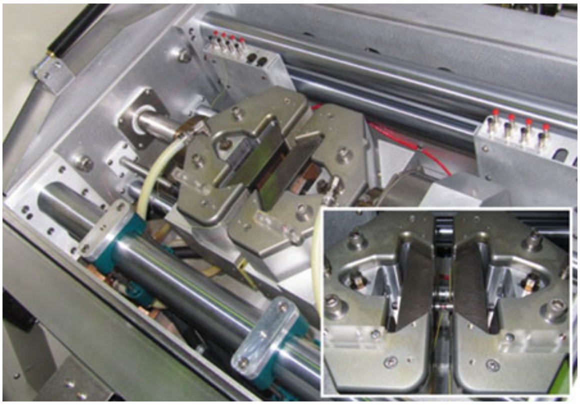

Fig. 2 Interior of the sample chamber and inset showing the jaws, grips, and the sample free span

Taking advantage of the XTMS potential users expertise on Gleeble simulators, its operational philosophy and sample holders were kept as similar as possible to the commercial systems. Thus, the users' learning curve can be shortened and the intended experiment could be pre-developed and optimized in a conventional Gleeble simulator at LNNano or even at the user facilities. Therefore, in the XTMS simulator the samples are tightly hold between Cu-based or stainless steel grips which are supported on mobile and water-cooled jaws, as shown in Fig. 2. Notice in the figure inset that there is a free span between the grips. The sample is heated by Joule effect while passing a high current (low voltage) through it. At the same time, the sample is being cooled by conduction through the grips and water-cooled jaws. Thus, the control system provides the necessary electrical power to obtain the programmed thermal cycle. When more severe cooling rates are necessary the simulator counts with a Liquid Nitrogen (LN_2) cooling accessory, which has been developed by LNNano. The jaws' movement, which provide the stroke/strain/stress, is powered by hydraulic linear actuators. Unlike conventional simulators where only one jaw moves, because of the necessity to keep the sample centered with respect to the synchrotron beam, both jaws move symmetrically on the simulator installed at the XTMS station. Temperature and stroke/strain/stress are controlled by a proportional integral derivative (PID) system, where the PID coefficients can be adjusted to optimize the simulator response for specific tests, for example, to provide a faster response, however, with some loss of resolution.

The sample temperature is measured, controlled and recorded using a thermocouple, which is welded to the sample surface at the center of the free span between the grips. The jaws are kept at room temperature by a closed water cooling cycle, which provides a cooling source for the sample. During heating, this causes a temperature gradient along the free span, which is the physically simulated region. Therefore, due to this thermal gradient, only a specific region near to the sample free span center, where the thermocouple has to be positioned, is submitted to the programmed thermo-mechanical cycle.

Typically, for setups with 20 mm free span and programmed peak temperatures around 1,000 °C, the thermal gradient will be less than 5 °C within approximately 3 mm around the central point of the free span. This 3 mm span, where temperature variation can be disregarded for most experiments, is also the typical width of the used X-ray beam. However, if austenitic stainless steel grips and/or larger free spans are used, the temperature gradient along the sample around its middle length will be less severe, and therefore, the temperature variation within the studied region could be much smaller. Nevertheless, in such condition the maximum cooling rates without the use of LN_2 will be compromised.

Most of the grips used to hold and position the samples were developed by LNNano aiming to the correct positioning of the samples regarding the incident X-ray beam. Among these grips can be highlighted ones that allow adjusting the beam incidence angle during the sample setup. Also, several sample designs have been developed and tested by the XTMS developing group. Thus, depending on the experiment requirements in terms of temperature gradient, cooling rates, applied stress or even tested material availability, different designs can be chosen, as seen in Fig. 3.

Heating rates can go up to 500 °C/s, and the maximum achievable temperature is defined by the type of thermocouples used and the sample melting point. The most commonly used thermocouples are types K, R and S, although other types can also be used. Cooling rates as high as -150 °C/s have been achieved with a long free span and the LN_2 cooling system. However, higher cooling rates can be achieved at high temperature ranges, when a small free span is combined with LN_2 cooling. This system also allows well controlled experiments down to subzero temperatures, where -100 °C can be routinely achieved. Measured temperature resolution depends on the range and used thermocouple, but a value of 0.2 °C is typical for a correctly attached thermocouple. Up to four thermocouples can be welded on the sample, normally being used to monitor the temperature gradient on the volume measured by the X-ray beam. A one color pyrometer is also available and can be used for parallel temperature measurements.

Stroke, strain and stress are applied by the symmetric movement of the jaws that hold the grips which tightly hold the sample. A stroke typical resolution of

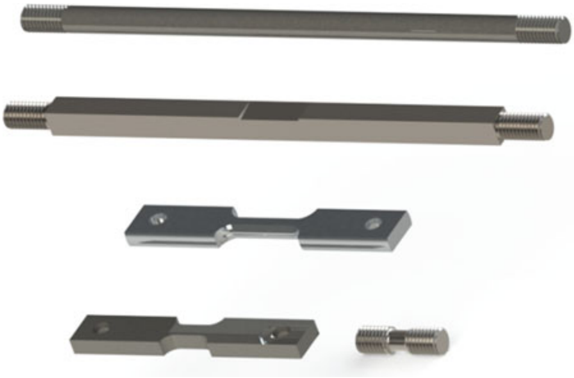

Fig. 3 Basic Sample designs used in XTMS experiments. Sample length range from 120 to 25 mm, and width from 14 to 5 mm

0.01 mm is available. The applied force is measured by a load cell, with 44 kN capability and 0.1 kN resolution. Lower forces load cells can be used, however they are not available at the time. In addition, for very low force values, the resolution will be limited by the system's inherent friction.

Experiments involving stroke/strain/stress are normally performed under tension, whereas, tests requiring elevated accumulated strain may require to be performed under compression mode. However, a methodology for these tests is under development. Strain can be measured/calculated from the sample reduced section length and the jaws stroke assuming that necking is not happening. Unfortunately, this is not case for large strains and/or when the sample is at elevated temperature (due to the thermal gradient). Thus, in such cases, the strain is measured using a non contact laser dilatometer, which is aligned to the center of the free span region, where the peak temperature is located and the thermal cycle is being controlled and recorded. The laser dilatometer provides 10 μm resolution for 2 mm range. Therefore, the strain resolution is defined by the sample geometry and the measuring approach, i.e. jaws stroke or dilatometer. Tests are commonly performed under vacuum, with the lowest achievable pressure being 10^{-3} Torr at the moment. Improvements are being made aiming to reach 10^{-5} Torr. The chamber can also be filled with different gases either for backfilling to reduce oxygen content within the chamber or to run the experiment under a chosen atmosphere, provided that the pressure is below atmospheric pressure. The installation is ready to work with Argon, nevertheless, gas mixtures setup provided by LNLS can be attached to the sample chamber allowing use of artificial air, weld shielding gas mixtures, etc.

4 Beamline

The LNLS Synchrotron is composed of a 1.37 GeV electron storage ring, working with a typical after injection current of 250 mA. The XTMS installation is located at the second hutch of the XRD1 beamline, sharing this beamline with a

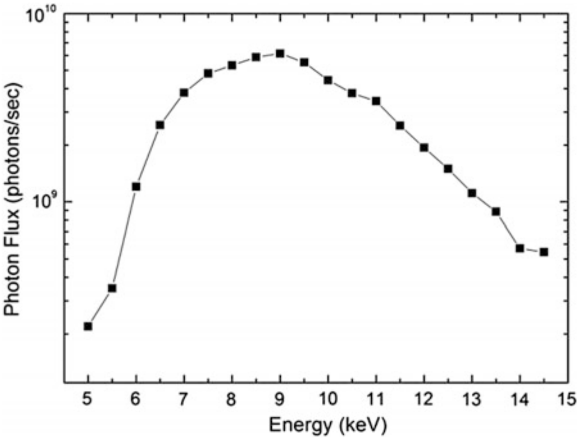

Fig. 4 Photon flux at sample position as a function of energy for a storage ring current of 100 mA

high-resolution powder diffractometer. The XRD1 photon source is a 1.67 T bending magnet followed by optics comprised of a Rh coated silicon X-ray mirror and a double bounce Si(111) monochromator. The optics of this beamline is similar to the ones located at other LNLS diffraction beam lines such as XRD2 [12] and XPD. The first mirror provides vertical focalization whereas the second monochromator crystal is used for horizontal focalization and beam positioning. The sample position inside the thermo-mechanical simulator is located 17 m away from the monochromator's second crystal.

Energy resolution at the beamline is of 5 eV at 8 keV. The energy range of the beamline covers from 5 to 14.5 keV. The X-ray beam size at the sample position has a full width at half maximum of 3.6 mm horizontally and 1.2 mm vertically. Focalization can be adjusted to obtain a shorter and wider beam. In addition, the XTMS has motorized slits that allow for smaller beam size selection, at the cost of reduced flux. Figure 4 shows the photon flux at the sample position for the energy range available at the beamline.

5 X-Ray Measurements

Diffraction data is obtained using position sensitive X-ray detectors mounted on a heavy duty Huber goniometer. The detector distance to the sample can be varied from 360 to 600 mm allowing adjustment of the angular resolution of the detector and angular range that can be acquired simultaneously. Two different detector assemblies are available, the first one being a set of two 1 K Mythen linear detector modules, and the second a Rayonix SX165 CCD area detector.

When a flat surface sample design is used, the X-ray beam incidence angle can be selected either by sample design or by using a specially designed grip set, which allows angle setting with 0.1° resolution. However, this angle setting needs to be

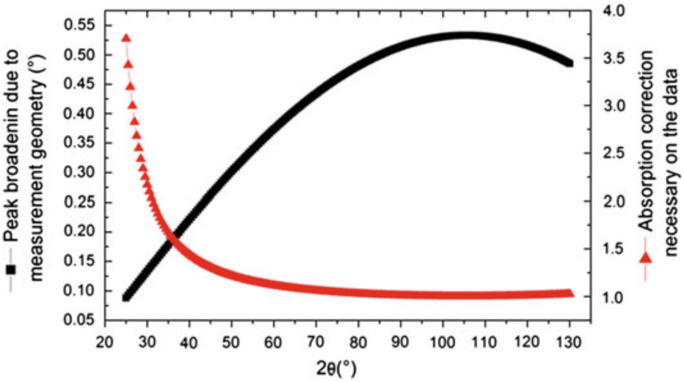

Fig. 5 Peak broadening and absorption correction necessary due to the measurement geometry. Values calculated for 0.5 mm beam height (*vertical direction*) and 15° angle of incidence

predefined and adjusted before starting the experiment, and can only be changed if the termomechanical simulation and X-ray acquisition are interrupted and the sample is removed from the machine. Thus, X-ray diffraction measurements are performed with fixed θ and varying 2θ. Although this geometry is different from the most commonly used $\theta - 2\theta$ scans, it does not greatly affect the data. Major differences are related to peak broadening due to the instrument and the absorption correction variation as a function of 2θ. Figure 5 shows how these two values behave as function of 2θ for commonly used conditions (incidence angle of 15°, 0.5 mm beam height—vertical direction). Thus, careful adjustments of these parameters can greatly reduce both effects, but also compromise the incident beam intensity.

Each Mythen 1 K linear detector module is a silicon strip with 1,280 50 μm × 8 mm channels distributed in a row. It is a fast detector with 0.3 ms read out time suitable for fast in situ experiments. The detector modules were mounted so that when the detectors are 400 mm away from the sample, their center is perpendicular to X-rays coming out of the sample illuminated area, granting the highest possible 2θ angular range in this sample to detector distance. Each module acquires 9.15° angular range with a 0.5° gap between both modules. The sample to detector distance can also be changed, but further tangent corrections are required. For this assembly, the chamber lid used is a cylindrical window located 280 mm away from the sample. The window covers a 130° angular range, from $2\theta = -5°$ to $2\theta = 125°$.

The Rayonix SX165 is a round CCD area detector with 165 mm diameter active area. It has several binning possibilities allowing a compromise between read out time and resolution. Binning choices range from higher resolution with 39 μm pixel size and 5 s readout time to lower resolution with 320 μm pixel size and 0,8 s readout time. Although much slower than the linear detectors, the increased detector area provides much higher statistics, being advantageous in

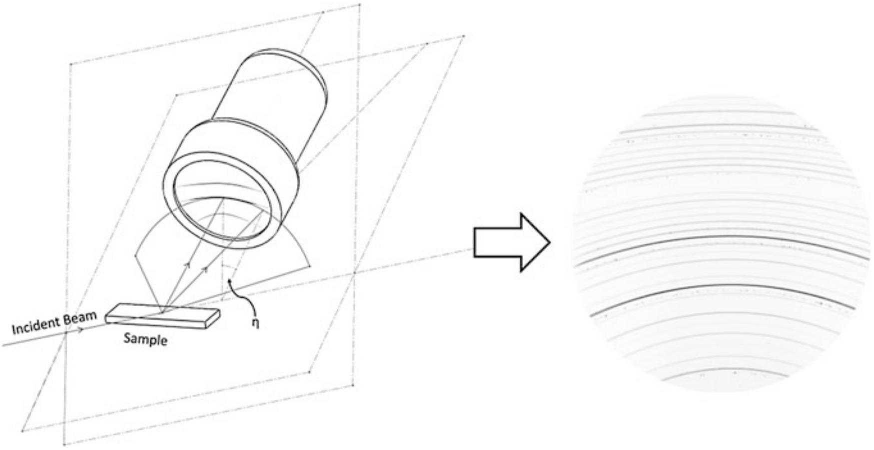

Fig. 6 2D detector measurements schematics. On the inset, an image collected using the detector is displayed. Sample used was Y2O3 deliberately contaminated with CeO2. The center of the detector was positioned at 30°, and its distance to the sample was 350 mm. Beam energy was 10 keV

reducing effects on the diffraction data caused by texture and low number of probed crystallites. The chamber window for the area detector is a 150 × 500 mm flat surface allowing measurements from $2\theta = -5°$ to $2\theta = 125°$, and also ±30° angular range in the azimuth angle (see Fig. 6).

Measurements can be made taking single acquisitions with one of the detectors fixed in a 2θ position, or scanning the detectors through the desired 2θ range. While the second one gives a much higher amount of crystallographic information, it should be used with care given that the time used to move the goniometer may be too long in terms of the studied phase transformation kinetics. Nevertheless, most of the experiments use combinations of both data collection strategies, where detector scans will be performed to provide enough information for example for Rietveld refinement while the studied phase transformation has not started or has slowed down.

6 Operation

Similarly to the typical programming in a Gleeble® thermo-mechanical simulator, experiments are programmed in the XTMS installation by steps, stating the thermal and/or mechanical control variables and their aim values, as well as the other variables that need to be recorded. In addition, for each step it is necessary to state if X-ray diffraction data needs to be recorded and how (scan or single shot). The experiment program is completely specified within SyncSim, a dedicated software developed by the LNNano and LNLS teams for this purpose. Figure 7 shows a graphic representation on how a test would be specified using SyncSim.

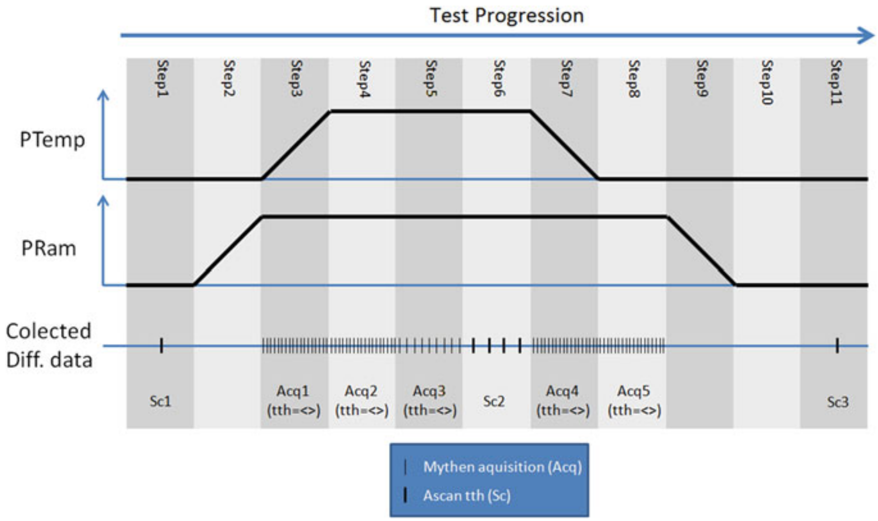

Fig. 7 Example of programmed thermo-mechanical test. PTemp is programmed temperature and PRam can be programmed stroke, strain or stress

7 Applications

As stated previously, the major objective on the designing and construction of the XTMS installation was to build an instrument capable of obtaining high quality data for diverse experiments with different needs without need of major customization. In fact, the installation is ready for experiments requiring high heating or cooling rates, high or low temperatures, long or short temperature dwell times, stress or strain experiments, as well as high acquisition rates or resolution for diffraction data.

In this section we present two experiments performed at the XTMS installation. The first one is a transformation kinetics experiment made on UNS32507 duplex alloy. These materials are formed by a mixture of austenite and ferrite phases, which are stabilized by the careful addition of several alloying elements which, in turn, bring the drawback of potential unwanted phases precipitation, mainly sigma phase (σ), forming at temperatures ranging from 650 to 950 °C [13, 14]. The effect of temperature and time on such phase formation has been widely studied on this and similar materials, including in situ diffraction experiments [15, 16], however, the combined effect of time, temperature and stress on ferrite phase decomposition has not been reported. Using the XTMS installation, time resolved studies on the isothermal decomposition of ferrite (α) in sigma and austenite phases ($\alpha \rightarrow \gamma + \sigma$) have been performed under controlled stress conditions. Samples were heated at a rate of 100 °C/s to a temperature of 850 °C for up to 2 h under uniaxial stresses slightly under the yield strength of these materials at high temperatures. Diffraction data was collected using a linear detector positioned at a

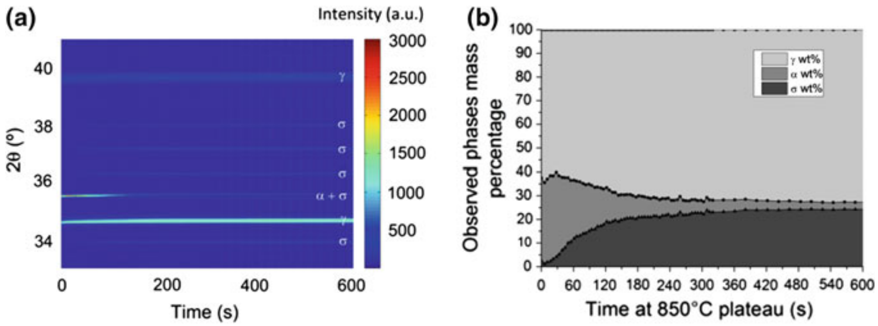

Fig. 8 **a** Measured intensity as a function of the diffraction angle (2θ) and time at 850 °C without load. Peaks are identified as belonging to austenite (γ), ferrite (α), or sigma (σ) phases. **b** Derived mass percentages for the three identified phases as a function of time

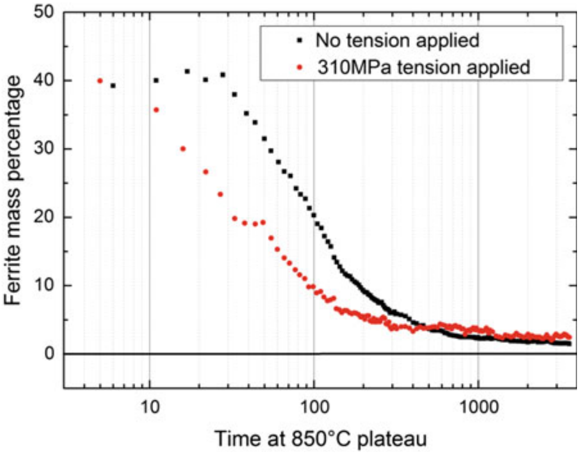

Fig. 9 Ferrite phase percentages as a function of time, for a unstressed and a stressed sample

fixed diffraction angle. Figure 8 shows an example of the diffraction data collected. The data was analyzed by determining the peak intensity of the peaks of each phase as a function of time, and accounting structure factor, multiplicity, etc. of each peak, thus determining the phase mass percentage.

In Fig. 9 we show the results for the determined ferrite phase percentage as a function of time. Due to signal-to-noise features, determined mass percentage for ferrite has an uncertainty of 2 %.

The second experiment is an investigation of the austenite behavior during the transformation induced plasticity (TRIP) effect on Supermartensitic Stainless Steels (SMSS). The SMSS typically have high mechanical and corrosion resistance, but these properties are highly dependent on the present phases in the material. These phases can be martensite (M), tempered martensite (M′), delta ferrite (δ) reversed austenite (γ_r) and carbonates. γ_r is a metastable phase, which is

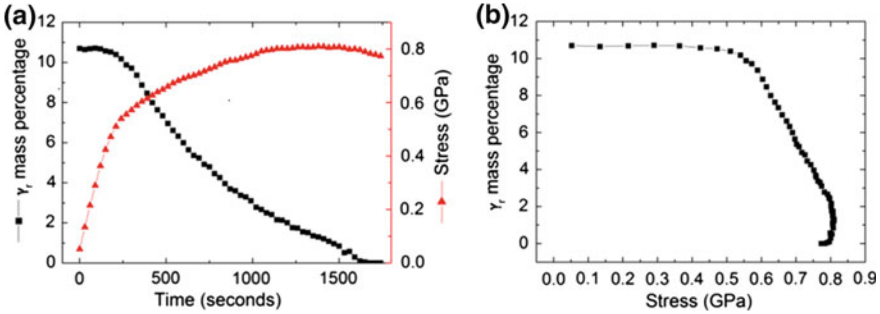

Fig. 10 **a** γ_r mass percentage and stress as a function of time. **b** γ_r mass percentage as a function of stress

stabilized in room temperature by the diffusion of elements such as C, N and Ni during intercritical tempering, in temperatures slightly above the M → γ transformation start temperature (Ac_1). This is the phase responsible for the TRIP effect on these materials. The existence of γ_r in these materials is known as beneficial, since it increases tenacity and conformability. An example is the effect γ_r has on crack growth, where this phase serves as a barrier to crack propagation. In this experiment the effect of applied tension on the $\gamma_r \rightarrow M$ transformation was observed. This observation has been done before using other in situ techniques such as electron microscopy [17], but measurements of bulk behavior for this material have yet to be reported.

In this experiment, samples containing γ_r were strained at a constant rate of 0.24 %/min, while diffraction data was constantly acquired using a linear detector at a fixed diffraction angle, at a rate of 2 images per minute. Figure 10 shows the results for one sample, which had 10.5 wt.% of γ_r. This sample had been pre-stressed at 0.54 GPa. Figure 10a shows the temporal evolution of stress and the derived γ_r mass percentage whereas Fig. 10b shows the correlation between these two variables.

8 Further Instrumentation Developments

Although XTMS is already open for users from the international community, ongoing developments aim to improve the installation's performance, versatility and the reliability of the acquired data. Some of these developments are listed below.

Improvements on atmosphere control and vacuum aim to achieve pressures under 10^{-5} Torr. An oxymeter will be added to the sample chamber. Finally, a mass spectrometer will be engineered to collect data from the chamber in order to provide quantitative data regarding the atmosphere and sample interaction with it.

While the beam must be carefully aligned with the sample surface, in case of elevated strains this alignment will be lost, causing artifacts in the diffraction data due to sample shift. For this reason a position (height) correction system is being developed. This system will use the non contact laser dilatometer reading to retrofit the simulator positioning table, allowing for the whole simulator vertical position to be corrected as the sample cross section is reduced due to necking.

As mentioned before, the thermo-mechanical simulator and the goniometer are mounted in independent positioning tables, implying that after each new sample is mounted, the thermo-mechanical simulator requires a fine goniometer alignment. Although this is not a time consuming task for experienced synchrotron beamlines users, this is a tedious process, which requires constant user input and that could be challenging for newcomers. The XTMS design and construction philosophy is to attract top notch scientist, preferably with some experience on physical thermo-mechanical simulation, disregarding previous experience with synchrotron beamlines. Therefore, tasks such as sample and beamline alignment should be made as simple as possible for them. Thus, using an optical alignment system already mounted in the goniometer arm, this process will soon be done automatically, with little need of user input.

As well as the above listed improvements, future plans include moving the XTMS installation to a second beamline at LNLS, with higher flux and slightly higher energies (30 keV) and in approximately 4 years to the new Brazilian photon source. In fact, the XTMS' major current limitations are the available photon energy range and photon flux. Typical minimum time resolution for diffraction data is limited to approximately 1 s, and this is restricted only by photon flux if linear detectors are used. In addition, higher energies will allow a bigger gauge volume for the diffraction data, increasing statistics and reducing grain size and surface effects.

The new Brazilian synchrotron source, Sirius, currently under construction, will be a third generation machine with low emittance and high brilliance [18]. XTMS will occupy one of this new machine's beamlines, namely JATOBA, dedicated for High energy Tomography and Laue Diffraction. This will be a Wiggler beamline with photon energy range from 30 keV to 250 keV, 10^{-2} ΔE/E energy resolution and a 1 × 1 μm beam size, greatly increasing the possible experiments and versatility of the installation.

9 Contributions

Leonardo Wu, Guilherme Faria and Thais Alonso are part of the XTMS development and operation team. They worked together with the other authors in the design and construction of all features and equipment involved in the installation. Augusta Isaac was instrumental on the selection and funding achievement for the 2D detector. James Piton was fundamental for the developed the control software. Regis T. Neuenschwandern is head of the design and instrumentation group at

LNLS, which contributed enormously to the thermo-mechanical simulator customization, positioning systems design and fabrication. Dr. Antonio J. Ramirez is head of the XTMS development and operation team. He idealized the installation and supervised every step in its construction since the start of the project.

Acknowledgments This installation project, assembly and now operation is being funded by the TMEC-Petrobras research network, FINEP, CNPq, CAPES, LNNano, and LNLS. The authors would also like to thank to all LNNano, LNLS and DSI staff, and specially, to the Materials Characterization and Processing group at LNNano, where most of this installation was developed.

References

1. Elmer JW, Palmer TA, Babu SS, Specht ED (2005) In situ observations of lattice expansion and transformation rates of α and β phases in Ti-6Al-4V. Mater Sci Eng, A 391:104–113
2. Babu SS, Specht ED, David SA, Karapetrova E, Zschack P, Peet M, Bhadeshia HKDH (2005) In situ observations of lattice parameter fluctuations in austenite and transformation to bainite. Metall Mater Trans A 36A:3281–3289
3. Lauridsen EM, Poulsen HF, Nielsen SF, Juul Jensen D (2003) Recrystallization kinetics of individual bulk grains in 90 % cold-rolled aluminum. Acta Mater 51:4423–4435
4. Lauridsen EM, Juul Jensen D, Poulsen HF (2000) Kinetics of individual grains during recrystallization. Scripta Mater 43:561–566
5. Paula S et al (2006) Study of the textural evolution in Ti-rich NiTi using synchrotron radiation. Nucl Instrum Methods Phys Res B 246:206–210
6. Schmahl WW et al (2004) Investigation of the phase evolution in a super-elastic NiTi shape memory alloy (50.7 at.% Ni) under extensional load with synchrotron radiation. Mater Sci Eng, A 378(1):81–85
7. Kannengiesser T, Kromm A, Rethmeier M, Gibmeier J, Genzel C (2008) Residual stresses and in situ measurement of phase transformation in low transformation temperature (LTT) welding materials. Adv X-Ray Anal 52:755–762
8. Haeffner DR, Almer JD, Lienert U (2005) The use of high energy X-rays from the advanced photon source to study stresses in materials. Mater Sci Eng: A 399(1–2):120–127
9. Komizo Y, Terasaki H (2011) In situ time resolved X-ray diffraction using synchrotron. Sci Technol Weld Joining 16:79–86
10. Terasaki H, Komizo Y (2011) Diffusional and displacive transformation behavior in low carbon-low alloy steels studied by a hybrid in situ observation system. Scr Mater 64:29–32
11. Genzel Ch, Denks IA, Gibmeier J, Klaus M, Wagener G (2007) The materials science synchrotron beamline EDDI for energy-dispersive diffraction analysis. Nucl Instrum Methods Phys Res A 578:23–33
12. Giles C, Yokaichiya F, Kycia SW, Sampaio LC, Ardiles-Saravia DC, Franco MKK, Neuenschwander RT (2003) High-resolution X-ray diffraction beamline at the LNLS for the study of charge, orbital and magnetic structures. J Synchrotron Rad 10:430–434
13. Calliari I, Zanesco M, Ramous E (2006) Influence of isothermal aging on secondary phases precipitation and toughness of a duplex stainless steel SAF 2205. J Mater Sci 41(22):7643–7649
14. Michalska J, Sozanska M (2006) Qualitative and quantitative analysis of σ and χ phases in 2205 duplex stainless steel. Mater Charact 56(4–5):355–362
15. Elmer JW, Palmer TA, Specht ED (2007) Direct observations of sigma phase formation in duplex stainless steels using in situ synchrotron X-ray diffraction. Mater Charact 56(4–5): 355–362

16. Palmer TA, Elmer JW, Babu SS (2004) Observations of ferrite/austenite transformations in the heat affected zone of 2205 duplex stainless steel spot welds using time resolved X-ray diffraction. Mater Sci Eng, A 374(1):307–321
17. Karlsen M et al (2009) Microscopy/electron backscatter diffraction-based observations of martensite variant selection and slip plane activity in supermartensitic stainless steels during plastic deformation at elevated. Ambient, Subzero Temp Metall Mater Trans A 40A:310–320
18. Liu L, Resende XR, Rodrigues ARD, Sá FH, Westfahl H (2013) Sirius: a 5BA low-emittance lattice with superbends for the New Brazilian synchrotron light source. Synchrotron Radiat News 26(3):34–38